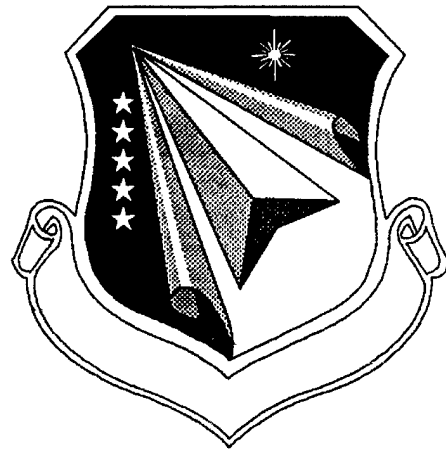


03 JUL 2000

AFOSR Focused Research Initiative:

Low-Emissions, High-Performance Gas Turbine Engines



Hukam C. Mongia et al.

GE AIRCRAFT ENGINES
ONE NEUMANN WAY
CINCINNATI, OH 45215-6301

August 1999

Final Report for 30 September 1995 – 31 August 1999

Addenda A through E

AIR FORCE OFFICE OF STRATEGIC RESEARCH
ARLINGTON, VA 22203-1977

DTIC QUALITY INSPECTED 4

20001109 021

Table of Contents

- Addendum A – The Effect of Gas Turbine Combustor Dome Radial Mixer Geometry On Fuel Spray Distribution and Combustor Performance. (Univ. of California, Irvine)**
- Addendum B – Combustion Dynamics Subtask (Pennsylvania State Univ.)**
- Addendum C – Large-Eddy Simulations of Turbulence-Chemistry Interactions in Low NOx Gas Turbine Engines (Georgia Institute of Technology)**
- Addendum D – Spray Modeling Based Upon Physically Accurate Models at all Scales (California Institute of Technology)**
- Addendum E – Lagrangian Simulation of Gas Turbine Engine Combustion (Massachusetts Institute of Technology)**

REPORT DOCUMENTATION PAGE

AFRL-SR-BL-TR-00-
0595

Public reporting burden for this collection of information is estimated to average 1 hour per response, including the time for reviewing the data needed, and completing and reviewing the collection of information. Send comments regarding this burden estimate or any aspect of this collection of information, including suggestions for reducing this burden, to Washington Headquarters Services, Directorate for Information Operations and Reports, 1215 Jefferson Davis Highway, Suite 1204, Arlington, VA 22202-4302, and to the Office of Management and Budget, Paperwork Reduction Project (0704-0188), Washington, DC 20503.

1. AGENCY USE ONLY (Leave Blank)	2. REPORT DATE <p style="text-align: center;">August 1999</p>	3. REPORT TYPE AND DATES COVERED <p style="text-align: center;">Final - 30 September 1995 through 31 August 1999</p>	
4. TITLE AND SUBTITLE <p>AFOSR Focused Research Initiative: Low-Emissions, High-Performance Gas Turbine Engines</p>		5. FUNDING NUMBERS PE - 61110D PR - 4422 SA - FS C - F49620-95-C-0080	
6. AUTHOR(S) H. Mongia, J. Peters, R. Lucht, R. Dibble, J-Y Chen, S. Menon, J. Bellan, G. Samuelsen, V. McDonell, R. Santoro, D. Santavicca, A. Goniehm		8. PERFORMING ORGANIZATION REPORT NUMBER <p style="text-align: center;">R00AEB</p>	
7. PERFORMING ORGANIZATION NAME(S) AND ADDRESS(ES) GE Aircraft Engines One Neumann Way Cincinnati, OH 54215-6301		10. SPONSORING/MONITORING AGENCY REPORT NUMBER	
9. SPONSORING/MONITORING AGENCY NAME(S) AND ADDRESS(ES) AFOSR/NA Arlington, VA 22203-1977		11. SUPPLEMENTARY NOTES	
12a. DISTRIBUTION/AVAILABILITY STATEMENT <p style="text-align: center;">Approved for public release; distribution is unlimited.</p>		12b. DISTRIBUTION CODE	
13. ABSTRACT (Maximum 200 words) A joint industry/university research and technology program was conducted under AFOSR sponsorship. Participants were GE Aircraft Engines, GE Corporate R&D, California Institute of Technology, Georgia Institute of Technology, Massachusetts Institute of Technology, Pennsylvania State University, University of California at Berkeley and Irvine, and University of Illinois at Urbana-Champaign. The program comprised (1) fundamental research essential to the development of low-emissions, high-performance combustors for commercial and military use and (2) transition of the fundamental knowledge to industry. The objective was to upgrade the state of the art of combustion design methodology and to design and demonstrate an innovative, low-emissions, high-performance gas turbine combustion concept. Fundamental experiments were conducted for (1) a novel coaxial jet flame, (2) a liquid-fuel/air mixing device of radial swirlers (swirlcup), and (3) a natural gas/air mixer using counterrotating axial swirlers (DACRS). Parallel activities included: (1) formulation and validation of semianalytical mechanistic models for predicting performance and emissions of combustors, (2) improved second-order closure based turbulent combustion models, (3) vortex methods, 4) large-eddy simulation with linear eddy subgrid modeling, and (5) an advanced spray model involving macroscales and microscales.			
14. SUBJECT TERMS Gas turbine combustion, combustion modeling, advanced diagnostics		15. NUMBER OF PAGES <p style="text-align: center;">394</p>	16. PRICE CODE
17. SECURITY CLASSIFICATION OF REPORT <p style="text-align: center;">Unclassified</p>	18. SECURITY CLASSIFICATION OF THIS PAGE <p style="text-align: center;">Unclassified</p>	19. SECURITY CLASSIFICATION OF ABSTRACT <p style="text-align: center;">Unclassified</p>	20. LIMITATION OF ABSTRACT <p style="text-align: center;">UL</p>

Addendum A

**The Effect Of Gas Turbine Combustor Dome Radial Mixer Geometry On
Fuel Spray Distribution and Combustor Performance**

AFOSR Focused Research Initiative
Low Emissions, High Performance Gas Turbine Engines

Contract 200-IQ-14N44080
General Electric Aircraft Engines
Cincinnati, Ohio

Principal Investigator
Dr. G. S. Samuelsen, Professor

Co-Principal Investigator
Dr. V. G. McDonell

Researchers
L. Arellano
A. Ateshkadi
J. Torres
J. M. Williams

UCI Combustion Laboratory
University of California
Irvine, California 92697-3550

UCICL-ARTR-96-2(f)

September, 1999

Table of Contents

	<u>Page</u>
Table of Contents	iii
List of Illustrations	v
List of Tables	vii
1.0 Summary	1
2.0 Objectives	3
3.0 Approach	4
4.0 Results	5
4.1 Task 1 – Test Plan Development	5
4.2 Task 2 – Hardware/Condition Selection	5
4.2.1 Condition Selection	5
4.2.2 Dome Hardware	6
4.2.3 Radial Mixer Interface.	6
4.3 Task 3 – Facility Refinement	8
4.3.1 Atmospheric Test Facility	8
4.3.2 Elevated Pressure Facility	10
4.4 Task 4 – Diagnostic Development	10
4.4.1 Laser Anemometer / Phase Doppler Inferometry	10
4.4.2 Planar Liquid Laser Induced Fluorescence	11
4.4.3 Digital Particle Image Velocimetry	11
4.5 Task 5 – Experimental Testing	12
4.5.1 Subcomponent Experiments	12
4.5.1.1 Injector Only	12
4.5.1.2 Injector/Swirler Assembly	13
4.5.1.3 Hardware Assembly Effect	14
4.5.1.4 Summary of Subcomponent Tests	15

Table of Contents

	<u>Page</u>
4.5.2 Screening Tests	15
4.5.2.1 Fuel Distribution	16
4.5.2.2 Reaction Structure and Stability	18
4.5.2.3 Lean Blowoff	18
4.5.2.4 Emissions	20
4.5.2.5 Sooting Propensity	21
4.5.2.6 Summary of Screening Tests	23
4.5.3 Comprehensive In Situ Measurements	24
4.5.3.1 Scattering Images	24
4.5.3.2 Continuous Phase Velocities	24
4.5.3.3 Dispersed Phase Characteristics	26
4.5.3.4 Dispersed Phase Characteristics – Reacting and Confined	31
4.5.4 Summary	33
4.6 Task 6 – CFD Modeling	35
4.7 Task 7 – Design Tool Development	35
4.7.1 Semi–Emperical Analytical Models	35
4.7.2 Lean Blowout Model	37
4.7.3 CFD Model Refinements	52
5.0 References	53
6.0 Relevant Papers and Presentations	54
6.1 Relevant Papers	54
6.2 Miscellaneous Papers	54

List of Illustrations

Figure	Title	Page
1.	Program Plan Schematic.	6
2.	Program Plan.	7
3.	Test Hardware Amenable to Statistically Designed Experiments.	8
4.	Full-Scale Radial Hardware Effective Areas.	9
5.	Data Acquisition System.	9
6.	LA/PDI Test Setup.	10
7.	PLLIF and Nonreacting Experiment Setup.	11
8.	Digital Particle Image Velocimeter System Schematic.	12
9.	PLLIF Image of Fuel Nozzle Air Without Atomizing Air.	13
10.	Cube Plot of Fuel Distribution Response for Swirl Strength, Swirl Sense, and Venturi.	17
11.	Effect of Venturi and Swirl Sense on Spray Distribution (Primary Swirl 35°, Secondary Swirl 65°)	18
12.	Reaction Structure for Target 2 Condition Equivalence Ratio of 0.6. (Primary Swirl 35°, Secondary Swirl 65°) – Same Exposure	19
13.	Lean Stability Limit and Associated Reaction Structure Near Blowout.	19
14.	Average Exit Plane Emissions for Cases Shown in Figures 11 through 13.	20
15.	Photos of Exit Plane Particulate for 0.5 sec. Sampling Time (F+1.5).	22
16.	Non-Reacting Spray Image, Radial Velocity Vector and Turbulent Kinetic Energy Profile for the 35° Primary Swirl Vane Angle and 65° Secondary Swirl.	25
17.	Radial Profile of Azimuthal Velocity (M/S) for the 35° Primary Swirl Vane Angle and 65° Secondary Swirl Angle.	27
18.	Droplet Distribution D32 Profiles for the 35° Primary Swirl Vane Angle and 65° Secondary Swirl Vane Angle.	28
19.	Droplet Volume Flux Profiles for the 35° Primary Swirl Vane Angle and 65° Secondary Swirl Vane Angle.	30
20.	3D IGES File Rendering for Full Domain Mesh Generation in Fluent UNS. ...	36
21.	Prediction vs. Measured Axial Velocity Profile for Primary Swirler 35°, Secondary Swirler 65°, Co-Swirl Without Venturi.	38
22.	Prediction vs. Measured Axial Velocity Profile for Primary Swirler 35°, Secondary Swirler 65°, Counter-Swirl Without Venturi. .	39
23.	Prediction vs. Measured Axial Velocity Profile for Primary Swirler 35°, Secondary Swirler 65°, Co-Swirl With Venturi.	40

List of Illustrations (concluded)

Figure	Title	Page
24.	Prediction vs. Measured Axial Velocity Profile for Primary Swirler 35°, Secondary Swirler 65°, Counter-Swirl With Venturi.	41
25.	Range of Aii Values for Various Hardware Configurations.	45
26.	Comparison of Predicted Values of A'' (ANOVA Model) and the A'' Values Determined from Experimental Fit of QLBO Data (Table 10).	46
27.	Comparison of Measured and Predicted Values of OLBO for all 12 Mixer Configurations at 294K Inlet Air Temperature.	47
28.	Comparison of Measured and Predicted Values of OLBO for all 12 Mixer Configurations at 366K Inlet Air Temperature.	48
29.	Comparison of Measured and Predicted Values of OLBO for all 12 Mixer Configurations at 294K Inlet Air Temperature.	49
30.	Main Effects Normal Probability Plot for LBO.	50
31.	Time-Averaged Image (50 Images) of Reaction Near Lean Blowout at 477K Inlet Air Temperature for 25° Primary Swirler and 75° Secondary Swirler.	50
32.	Average Effects of Mixer Parameters and Interactions on LBO at 366K and 477K.	51
33.	Time-Averaged Image (50 Images) of Reaction Near Lean Blowout at 294K Inlet Air Temperature for Optimum LBO Mixer Configuration (45° Primary Swirler and 55° Secondary Swirler, Counter-Swirl With Venturi).	52

List of Tables

Table	Title	Page
1.	Targeted Operating Conditions.	6
2.	Comparison of 0.5 and 1.35 FN Fuel Nozzle Distribution.	13
3.	Mixer Component Orientation.	14
4.	PLLIF Images for Three Hardware Alignments.	15
5.	Half Factorial Study.	16
6.	Primary Particle Diameters.	22
7.	TPSD Results for Soot Concentration.	23
8.	Summary of Observations – Four Cases 35/65 Primary/Secondary Swirl, Target 2.	34
9.	Predictive Model of the Axial Velocity Profile in the Radial Direction.	37
10.	Half-Fraction Two-Level Test Matrix of Experiments.	45

1.0 Summary

A comprehensive research program to develop efficient design tools for liquid-fueled gas turbine combustors featuring radial inflow swirl was conducted at the University of California, Irvine Combustion Laboratory (UCICL). To achieve this goal, a detailed test plan was developed in cooperation with GE Aircraft Engines that consisted of the following steps:

- Identification of Hardware and Operating Conditions
- Preparation of Test Facilities
- Preparation and Development of Diagnostics
- Conducting of Experiments at the subcomponent, screening, and detailed levels
- Conducting CFD modeling to extend the Experiments
- Development and Validation of Design Tools

The first four and last tasks were completed during the program. Significant progress was made on the remaining tasks. Key deliverables produced by the program include:

- The development of flexible, unique test hardware
- Diagnostic methods extending capabilities from time-averaged to instantaneous
 - the development and application of planar laser induced fluorescence to quantify the fuel distribution provided by the mixers
 - the development of a digital particle image velocimetry system
 - the development of a spatially resolved method for measuring combustion radicals including OH, CH, and C₂ in the presence of droplets
- Identification of key factors affecting performance for radial inflow mixers.
 - The simplex fuel injector characteristics play little to no role in the performance of the mixer
 - Swirl strength had no statistically significant effect in the performance of the mixer
 - Swirl Sense and the Venturi did have significant effects upon fuel distribution, stability, emissions, and reaction structure.
 - No single configuration yielded optimum performance, though the co-swirl case with venturi has promise, especially if fuel can be placed at the centerline.
 - The detailed measurements provide the reasons for some of the behavior observed
- Collection of detailed data for model verification for four configurations.
- Development of methodology for modeling the behavior within the mixer via CFD

- Development of initial analytical models for use in design efforts.

Additional work should be conducted to extend the measurements to other conditions and to acquire planar measurements of scalars and velocities. More temporally resolved measurements should be obtained to fully explain the results from the screening tests. In addition, the CFD work started to resolve the flow within the mixer should be completed and used to bring additional physics into the analytical model developed for aerodynamics. Other models should be developed and verified for stability, fuel distribution, and emissions.

2.0 Objectives

The goal of the UCICL program was to develop efficient design tools for liquid-fueled gas turbine combustors featuring radial dome swirl. While one goal was to develop Semi-Analytical (mechanistically correct) design tools based on Advanced Diagnostic measurements (SAM-AD), other types of efficient tools were to be developed as intermediate steps. The program was founded primarily on the experimental strengths of the UCICL, nevertheless, numerical studies were also conducted to both guide the experiments and to provide additional insight into the complex mechanisms occurring within radial-dome swirl systems. Conditions ranging from atmospheric pressures and room temperatures to inlet temperatures and pressures approaching practical conditions were considered.

3.0 Approach

To meet the program goal delineated above, the following approach was established as part of the overall program:

- Establish a Test Plan
- Identify Hardware and Operating Conditions for Testing
- Refine the Test Facility to Provide the Operating Conditions Desired
- Prepare/Develop Necessary Diagnostics
- Conduct Experiments (Subcomponent, Screening, Detailed)
- Conduct CFD Modeling
- Develop and Validate Design Tools

For convenience, *Tasks* are utilized to delineate the major research approach areas:

<u>Task</u>	<u>Title</u>
1	Test Plan Development
2	Hardware/Condition Selection
3	Facility Refinements
4	Diagnostic Development
5	Experimental Testing
6	CFD Modeling
7	Design Tool Development

4.0 Results

The results from the program are summarized in this section. Discussion is provided on each Task delineated above, although the majority of the section is dedicated to deliverables associated with Tasks 2, 5, and 7.

Specifically the following key results were produced by the program:

- the development of flexible, unique test hardware
- development of diagnostic methods for extending measurement capability from time-averaged to instantaneous
- identification of key factors affecting performance for radial inflow mixers.
- collection of detailed data for model verification for four configurations.
- development of methodology for modeling the behavior within the mixer via CFD
- development of initial analytical models for use in design efforts.

With relatively small additional effort, additional models can be developed along with extension of the databases to cover other operating conditions and configurations. Further, the goal of obtaining results to support LES model development can be accomplished through the use of planar and temporally resolved diagnostic methods developed through this program.

4.1 Task 1 – Test Plan Development

It was decided early in the program that the UCI Combustion Laboratory would emphasize mixers derived from radial inflow swirlers. In addition, the UCICL would give emphasis to liquid fuel injection. For the purpose of the current program, experiments that isolate one combustor dome from interaction with either jets or other adjacent domes were identified. Figure 1 summarizes the test plan developed and the associated deliverables. Whereas the bulk of the plan illustrates the strategy for accomplishing Task 7, the *EXPERIMENT* box represents Task 5, and the *CFD* box represents Task 6. Task 2 “Hardware Selection”, Task 3.0 “Facility Refinements”, and Task 4.0 “Diagnostics Development” are pre-requisite to the conduct of Tasks 5–7. Figure 2 provides the overall schedule for the program. Details regarding efforts made in support of each Task during the current reporting period are described in the following sections.

4.2 Task 2 – Hardware/Condition Selection

4.2.1 Condition Selection

Extensive discussions were held with GEAE to define suitable operating conditions. Table 1 shows the conditions and the rationale for their selection. For the scope of work for the current program, the emphasis of the efforts were directed at Targets 1 and 2.

The following conditions were agreed upon by GEAE and UCICL on April 18, 1996 at a meeting in Cincinnati, Ohio.

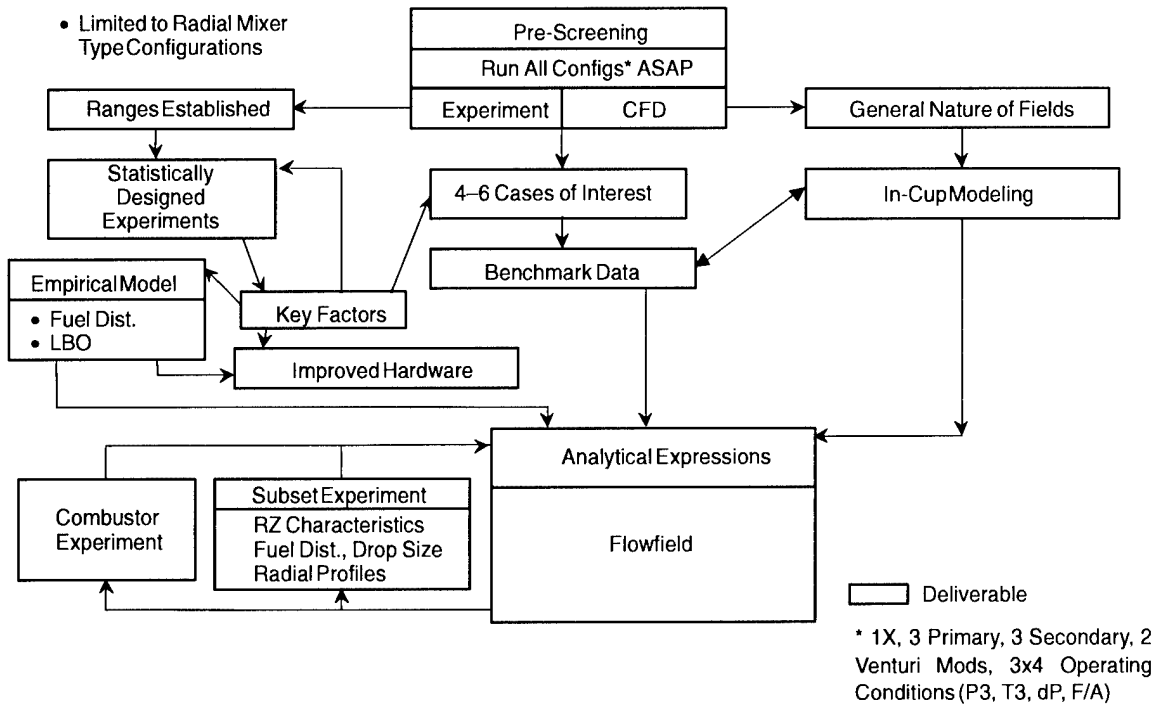


Figure 1. Program Plan Schematic.

Table 1. Targeted Operating Conditions.

Target	P3, atm	T3, °F	Conditions
1	1	70	Ignition
2	1	400	Relight
3	4	400	Idle
4	10	800	Approach (30% power), light cruise (50% power)
5	10	1000	Takeoff

4.2.2 Dome Hardware

A set of dome hardware based on radial inflow swirlers was developed specifically for the current program. The resulting dome hardware provided a unique ability to mix and match any of the components while maintaining effective area constant. This provided the ability to conduct many statistically designed experiments without adding pressure drop or flow rate changes. Figure 3 illustrates the developed hardware. The radial mixer hardware developed makes possible full parametric studies involving 1) the primary swirler angle at three levels, 2) the secondary swirler angle at three levels, 3) the swirl sense in two directions, and 4) the presence or absence of a venturi structure. As proof of concept, Figure 4 illustrates the variation in effective area for all combinations of the hardware and reveals the extent to which effective area has been successfully maintained.

4.2.3 Radial Mixer Interface.

A new plenum for the atmospheric spray studies was designed and fabricated. A plenum was also developed for elevated pressure testing, but was not utilized due to the limited work scope.

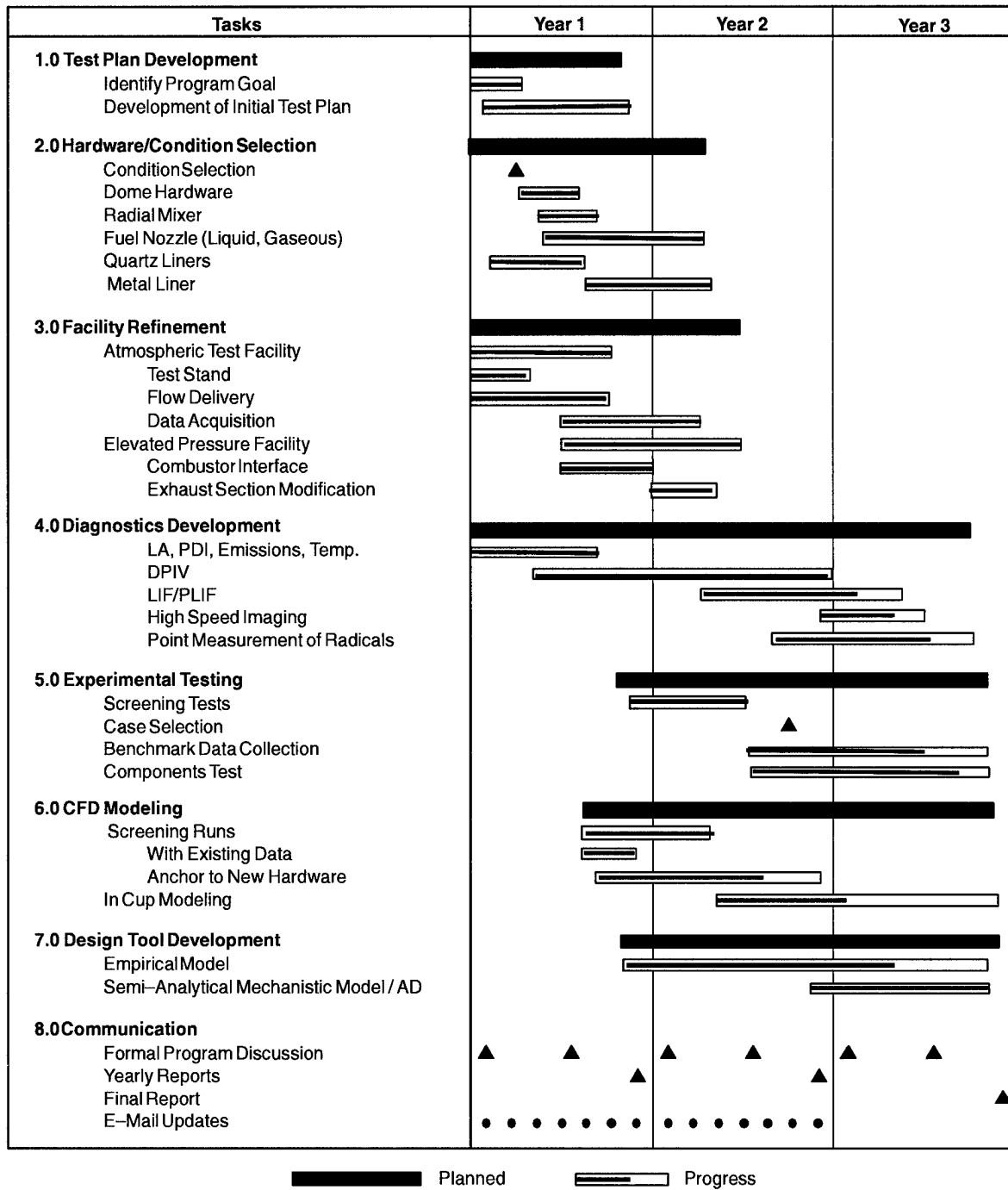


Figure 2. Program Plan.

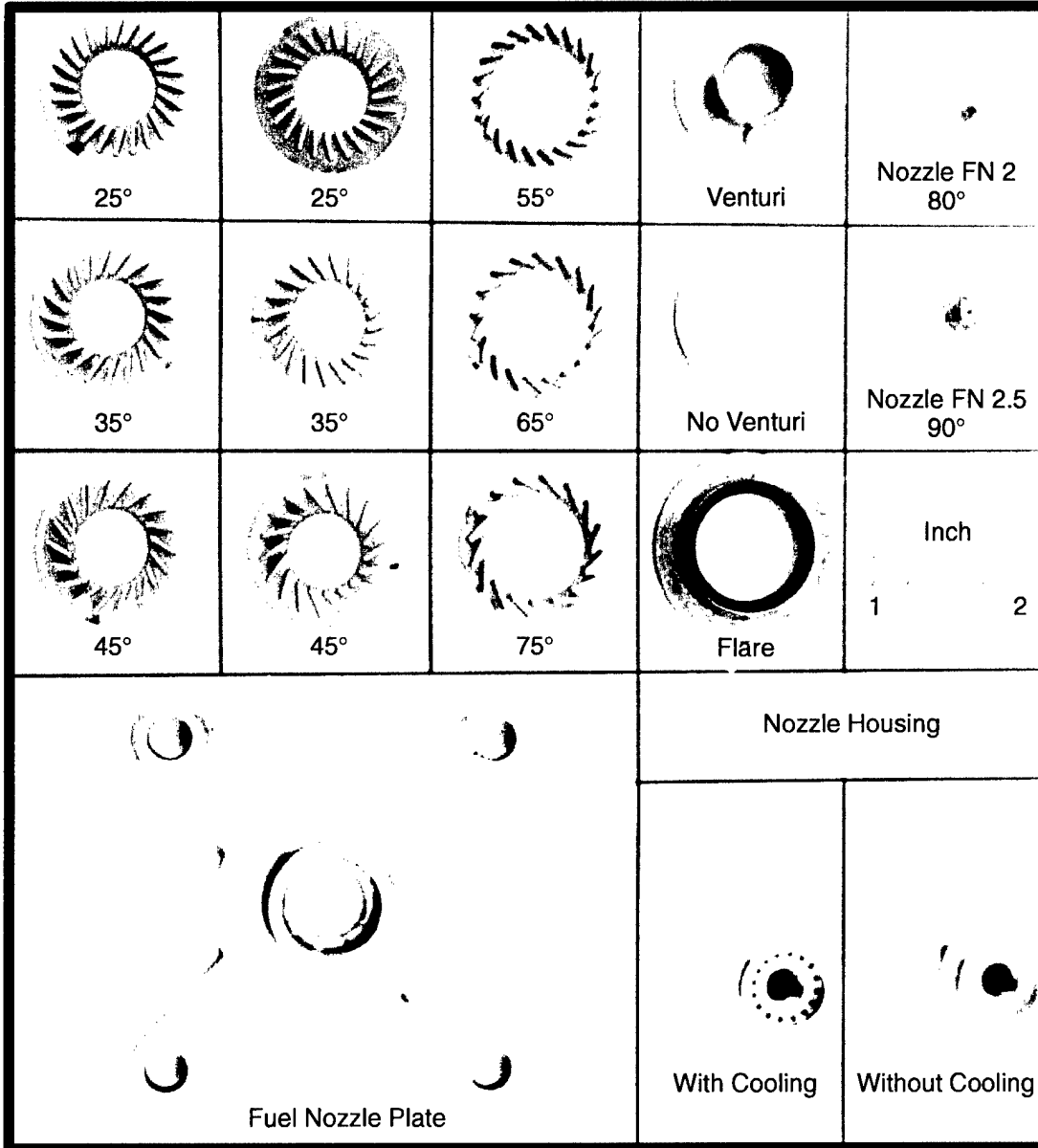


Figure 3. Test Hardware Amenable to Statistically Designed Experiments.

4.3 Task 3 – Facility Refinement

The majority of Task 3 was completed during the first year. However, refinements were made throughout the program as needed.

4.3.1 Atmospheric Test Facility

An existing facility was upgraded and modified specifically to support the program. In particular, the facility was outfitted with electronic sensors and control devices to allow to be fully instrumented. Figure 5 shows the overall system. In addition, an existing atmospheric spray stand was modified to support sub-component studies described in Section 3.5.

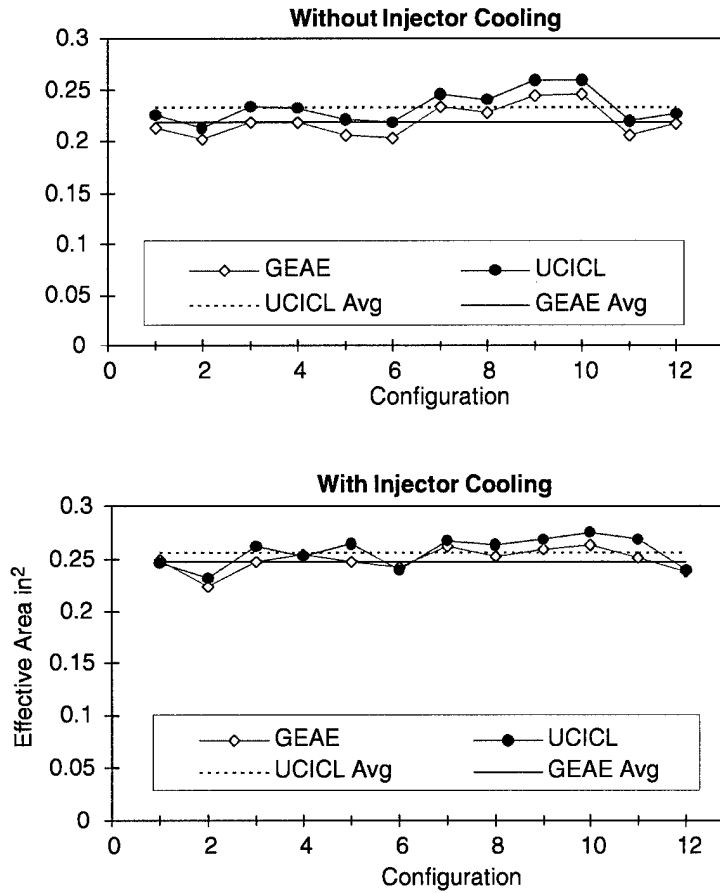


Figure 4. Full-Scale Radial Hardware Effective Areas.

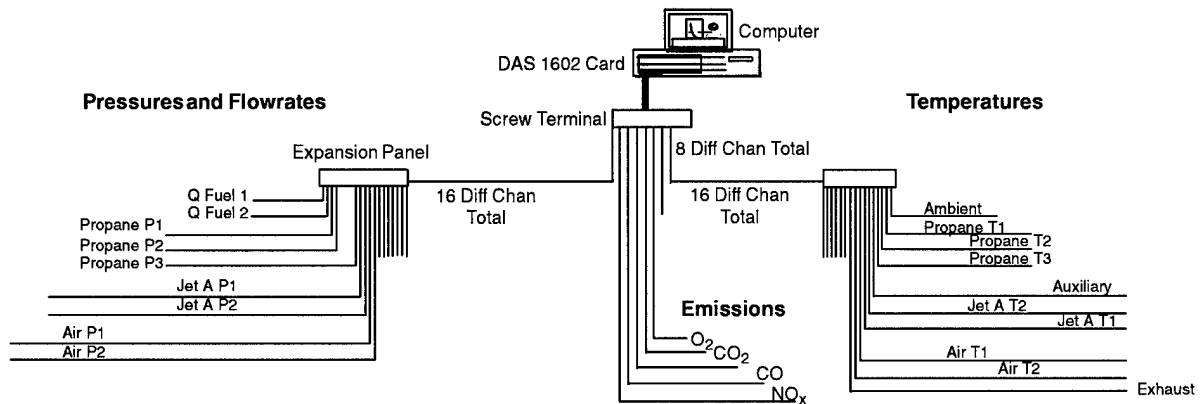


Figure 5. Data Acquisition System.

4.3.2 Elevated Pressure Facility

The elevated pressure facility at the UCI Combustion Laboratory can provide 1 lbm/sec of air at 1000 °F and 15 atm. A wide range of conditions can be covered by this facility for the full-scale hardware including Targets 3–5 (Table 1). The interfacing designed for the atmospheric facility was designed to interface to the high-pressure vessel with minimal modifications.

4.4 Task 4 – Diagnostic Development

To meet the goals of the program, several diagnostics were required. In particular, existing methods including laser anemometry (LA), phase Doppler interferometry (PDI), and various thermocouple and extractive probes were required for point measurement methods. The setup for LA and PDI on the dedicated atmospheric facility is illustrated in Figure 6.

To obtain temporally resolved information, a method for obtaining spatially resolved measurements of radial species in the presence of droplets was developed using Cassegrain optics and a polychromator following the approach of Akamatsu et al. (Reference 1). Of particular interest were planar methods, including Digital Particle Image Velocimetry (DPIV), Planar Laser Induced Fluorescence (PLIF), and high speed imaging methods. To this end, a PLIF system for imaging fuel distribution was developed. Also, a DPIV system was developed. The radial measurement and PIV systems successfully developed during the current program were not extensively applied due to time constraints. The optical systems are described below except the radial species measurement method which is described in (Reference 1).

4.4.1 Laser Anemometer / Phase Doppler Interferometry

An existing fiber optic-based LA/PDI system was utilized for measurement of gas phase velocities and droplet characteristics within the combustor. For LA applications an alumina seeder was integrated into the plenum air circuit. Quartz liners were designed to allow optical access at the exit plane of the mixer. This system allowed for the point measurement of velocity for either droplets or gas phase. In addition, the PDI diagnostic resolved the droplet size and mass distribution at a point.

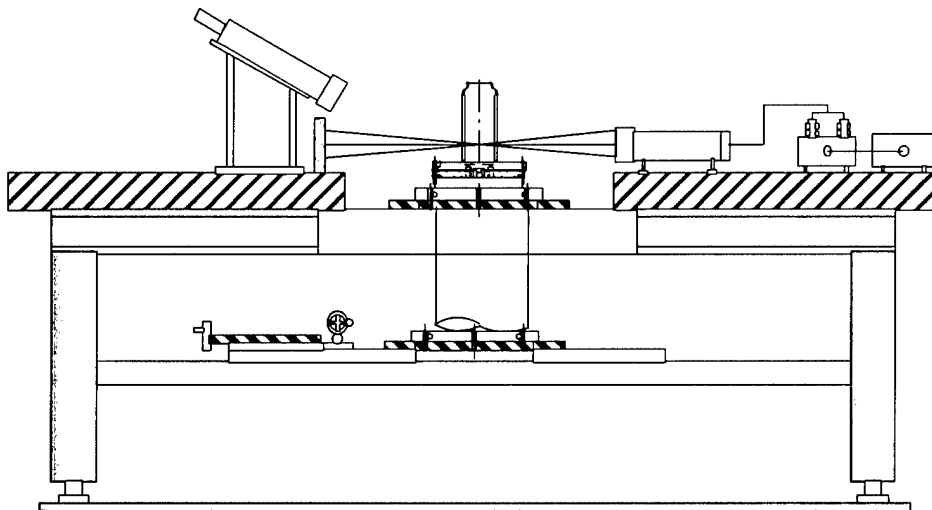


Figure 6. LA/PDI Test Setup.

4.4.2 Planar Laser Liquid Induced Fluorescence

Planar Laser Liquid-Induced Fluorescence (PLLIF) was employed to characterize the planar distribution of fuel downstream of the mixer. In the setup utilized, a laser sheet passed through the fuel spray at a distance equivalent to one and two (mixer) flare diameter (25 mm and 50 mm) downstream (Figure 7). The laser energy induced fluorescence from fluorescein molecules doped in the liquid fuel, which in turn was proportional to the fuel mass (Reference 2). An Ar⁺ laser operating at a wavelength of 0.4880 μm was used to generate a laser sheet, and gray scale images of the spray were captured on a computer using an intensified CCD camera. A total of 32 images of the fuel spray were captured and averaged for the analyses conducted. Being a planar imaging technique, PLLIF was relatively quick to apply to assess the distribution of fuel in the spray.

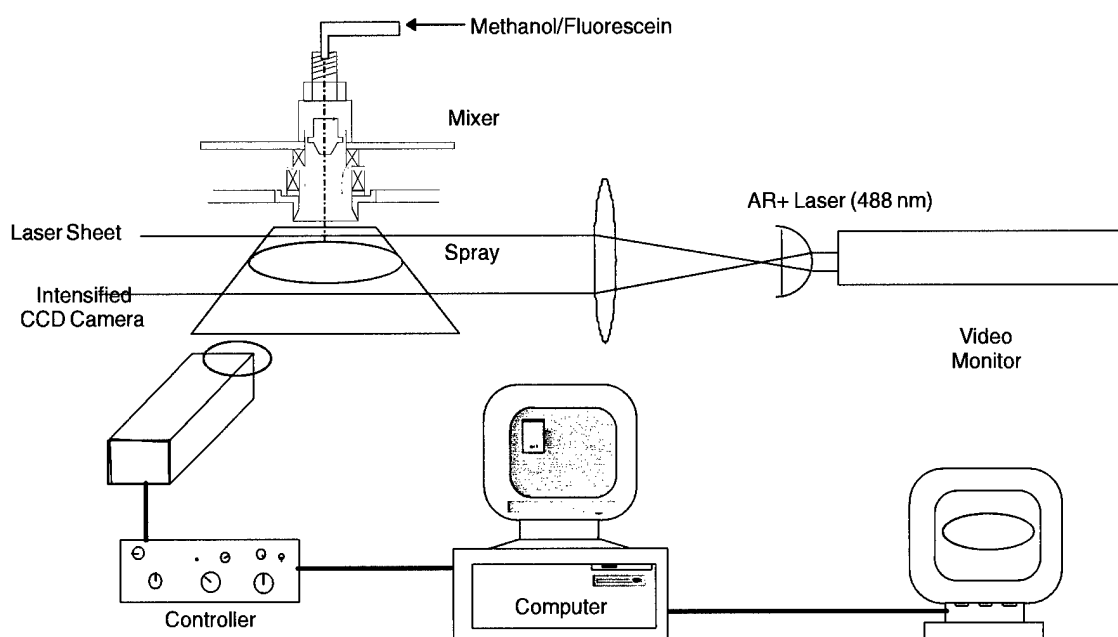


Figure 7. PLLIF and Nonreacting Experiment Setup.

4.4.3 Digital Particle Image Velocimetry

A Digital Particle Image Velocimeter (DPIV) system was developed as part of the program, though has yet to be extensively utilized. The system consists of two Nd:YAG, pulsed, Q-switched, lasers, a unique video camera, a frame grabber board, a delay generator, various optics, a personal computer, and DPIV software. These components were carefully selected and integrated together to form the DPIV system. Each component was based on the latest technology in the field, in fact, the camera and frame grabber were the first units ever produced. The overall DPIV system schematic is shown in Figure 8.

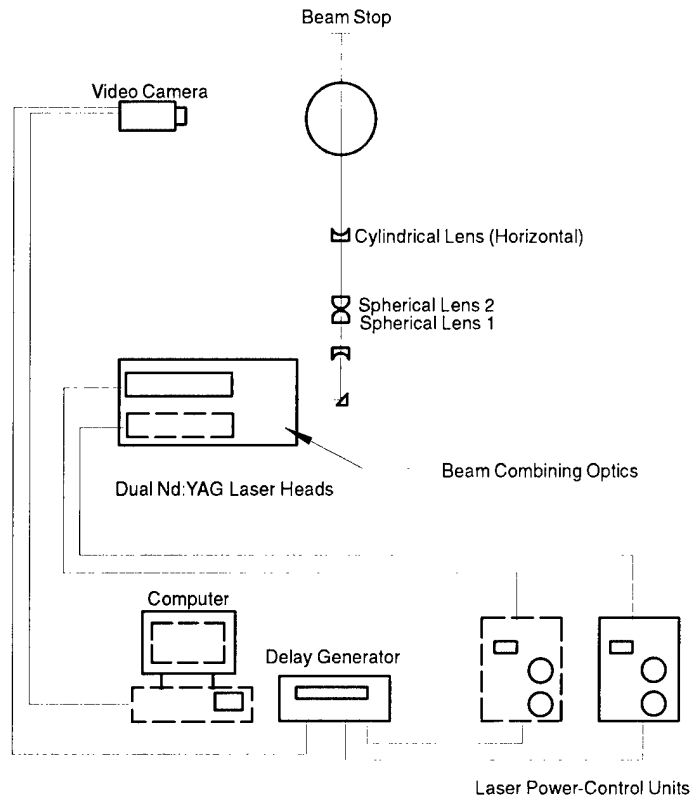


Figure 8. Digital Particle Image Velocimeter System Schematic.

4.5 Task 5 – Experimental Testing

The testing strategy was broken up into three types: subcomponent experiments, screening, and comprehensive measurements. Highlights from the results obtained from each type are described in this section.

4.5.1 Subcomponent Experiments

The PLLIF technique was employed to study the sensitivity of the fuel distribution to the fuel injector and hardware assembly protocol. This was required to ensure repeatability of the system upon breakdown and reassembly. Also, the results could allow reduction of parameters (e.g. if the fuel injector is not important to the performance, it could be dropped from the list of test parameters, thereby saving time for other types of testing.)

4.5.1.1 Injector Only

As a first step, the effect of fuel nozzle was examined by comparing a 90-degree macrolaminate injector with $FN = 0.5$ and a 90-degree conventionally machined injector with $FN = 1.35$. The fuel injectors were tested in the absence of the swirler hardware as a baseline. The fuel flow rate was the same for each case (corresponding to an equivalence ratio of 0.6 for the reacting flow studies). The pressure drop for the 1.35 FN injector is less than for the 0.5 FN injector due to the difference in flow number. This results in a wider area for the lower FN injector. The objective was to identify the

presence of any gross nonuniformity in the spray field. Figures 9a and 9b illustrate the PLLIF image of the fuel distribution one flare diameter downstream of the mixer exit (25.4mm). The results do not reveal any gross spray nonuniformities.

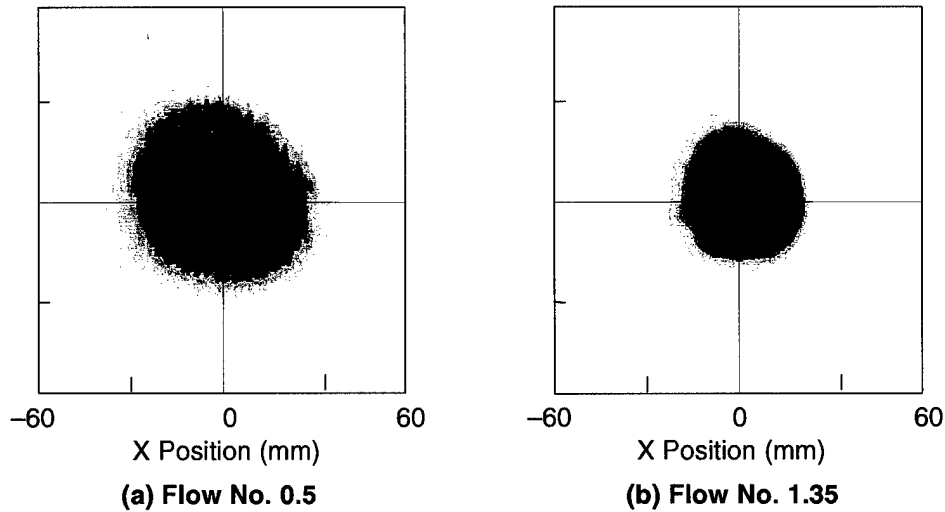


Figure 9. PLLIF Image of Fuel Nozzle Air Without Atomizing Air.

4.5.1.2 Injector/Swirl Assembly

The spray distributions for each nozzle were then compared for four different swirler geometry configurations 1) 35/65/Counter-Swirl/With Venturi, 2) 25/55/Co-Swirl/With Venturi, 3) 45/55/Co-Swirl/Without Venturi, and 4) 45/55/Counterwhirl/With Venturi. In each case, a 4% pressure loss was set for the air flow. The PLLIF images collected are shown in Table 2.

Table 2. Comparison of 0.5 and 1.35 FN Fuel Nozzle Distribution.





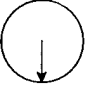
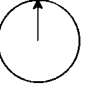
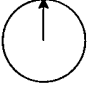
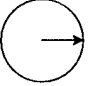
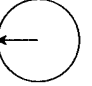
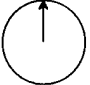
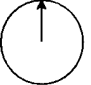
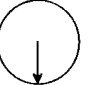
Geometry	1	2	3	4
Primary Swirl	35°	25°	45°	45°
Secondary Swirl	65°	55°	55°	55°
Venturi	With	With	Without	With
Swirl Sense	Counter-Swirl	Co-Swirl	Co-Swirl	Counter-Swirl
Flow Number				
0.5				
1.35				


FN has little impact when the airflow is present. However, a difference in the high mass concentration distribution is noted between the two different fuel nozzles used. The smaller flow number nozzle (0.5) has better flow symmetry compared to the conventional flow nozzle (FN=1.35). The lower injection pressure drop for the 1.35 nozzle may result in poor atomization thereby reducing the interaction between the fuel and swirling air. In addition, the macrolaminate methodology may offer a superior spray in general, despite the difference in pressure. Regardless, for the current program, the macrolaminate nozzle (FN=0.5) is considered to be a better performer in terms of symmetry of fuel distribution and it was adopted for the screening tests.


4.5.1.3 Hardware Assembly Effect


To assess the importance of the hardware assembly protocols in determining fuel distribution, a study was conducted. The mixer hardware was disassembled and the components were rotated according to three types of orientations (A, B and C) as shown in Table 3. Orientation A was the baseline. In orientation B the primary swirler was rotated 180°, the venturi plate rotated 90° clockwise and the secondary swirler was kept at the original position. In orientation C the primary swirler was rotated to the original orientation (A), the venturi plate was rotated 90° counter-clockwise relative to the orientation A and the secondary swirler was rotated 180° with respect to orientation A.

Table 3. Mixer Component Orientation.

	A	B	C
Fuel Nozzle			
Primary Swirler			
Venturi			
Secondary Swirler			



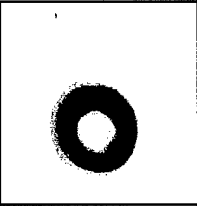
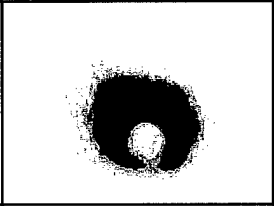
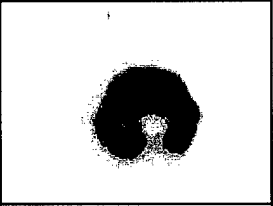
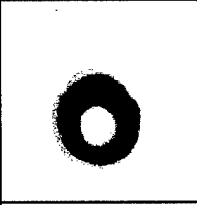
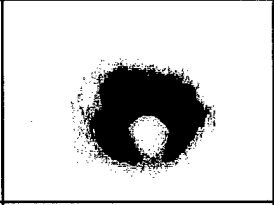
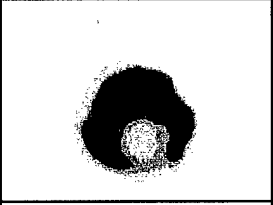
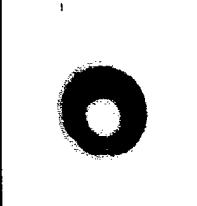
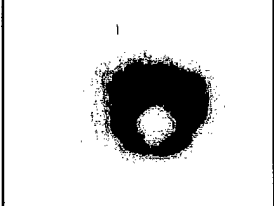
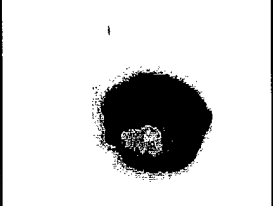




PLLIF images were taken with each of the three orientation of the hardware assembly and compared (Table 4). Three swirler configurations were tested: 1) Primary swirler 35°, Secondary swirler 65°, Co-Swirl, With Venturi, 2) Primary swirler 35°, Secondary swirler 65°, Co-Swirl, Without Venturi, and 3) Primary swirler 45°, Secondary swirler 75°, Counter-Swirl, Without Venturi. The FN 0.5 nozzle was used in these experiments. In these images, no correction for laser sheet intensity variation (Gaussian profile) was done, so the comparison should be based only on differences in the sprays produced for each geometry (1,2, or 3).

In Geometry 1 and 2, no change in the spray area is observed when swirler components are rotated. In Geometry 3, when only the Venturi and the Secondary swirler are rotated a shift in the spray distribution in the clockwise direction is observed. However, the changes are minor.

Table 4. PLLIF Images for Three Hardware Alignments.

Geometry	1	2	3
Primary Swirl Angle	35°	35°	45°
Secondary Swirl Angle	65°	65°	75°
Venturi	With	Without	Without
Swirl Sense	Co-Swirl	Co-Swirl	Counter-Swirl
Configuration			
A			
B			
C			

4.5.1.4 Summary of Subcomponent Tests

The results revealed that changes in flow number from 0.5 to 1.35 has little impact on the fuel distribution produced. It was also later observed (not shown in the present results) that the lean stability limit was also not affected strongly by nozzle flow number or spray angle. Since the injector appeared to play a small role in the performance of the system, this allowed this parameter to be dropped from the list of variables, thereby allowing more time for other types of experiments.

The results also revealed that the research hardware is relatively insensitive to orientation and alignment. Apparent asymmetry is attributed primarily to the images not being corrected for laser intensity variation. Thus the hardware is well suited for testing with statistically based designed which require frequent breakdown and reassembly of the parts

4.5.2 Screening Tests

Once subcomponent tests were conducted to understand basic behavior and sensitivity to variations in factors of interest, formal screening tests were also conducted using statistically designed experiments. Table 4 presents one of the matrices utilized. In this case, four parameters are studied: 1) the primary swirler vane angle, 2) the secondary swirler vane angle, 3) the relative swirl direction between the two swirlers (swirl sense) and 4) the presence of the venturi. Note that fuel injector angle/FN is not included due to the findings of the sub-component tests. The matrix shown in Table 5 represents a statistically designed experiment on four factors at two levels with centerpoints. For these screening studies supporting the program, a half fraction was conducted for efficiency. It is

noteworthy that, for screening tests to be effective, the parameter studied should be something that can be quickly determined. Thanks to the PLLIF system developed, fuel distribution was one such parameter. Reaction structure, lean blowout, exit plan emissions are others. It was planned to also conduct such tests using DPIV to rapidly characterize the mean and instantaneous flow field, but has not yet been completed.

Highlights from the screening studies are presented in this section.

Table 5. Half Factorial Study.

Run	Primary Swirl Angle (degrees)	Secondary Swirl Angle (degrees)	Swirl Sense	Venturi
1	25	75	CO	W/
2	25	75	CC	W/
3	35	65	CO	W/O
4	25	55	CC	W/O
5	35	65	CC	W/
6	45	55	CO	W/O
7	45	75	CO	W/
8	35	65	CC	W/O
9	25	55	CO	W/
10	45	75	CC	W/O
11	35	65	CO	W/
12	45	55	CC	W/

4.5.2.1 Fuel Distribution

Table 5 lists the mixer configurations experimented with under non-reacting conditions to identify the key factors affecting the fuel distribution.

Figure 10 presents a collection of the PLLIF images for the test matrix presented in Table 5. The images shown reflect the fuel distribution 25 mm downstream of the exit plane of the mixer. A “cube plot” has been generated with the three primary axes being the swirl sense, the primary and the secondary swirl vane angle. It is evident that the venturi consistently reduces the spread of the fuel spray. A more subtle factor is also noted, namely the swirl sense. Careful comparison reveals that co-swirl creates a larger spray area than does counter swirl. This is evident from Figure 11 which summarizes the main effects.

Perhaps of equal interest is the result that swirl strength has no impact on the fuel distribution. This is a surprising result given the range of swirl strengths considered for both the primary and secondary swirlers. This results implies that either (1) the range of swirl strength is not wide enough to reveal an effect given the impact of venturi and swirl sense or (2) the swirl angle is not a good indicator of the actual swirl strength. This observation is worth of further study. Regardless, for the purpose of this program, the results reveal that the venturi and swirl sense are the only two important factors which dictate fuel distribution.

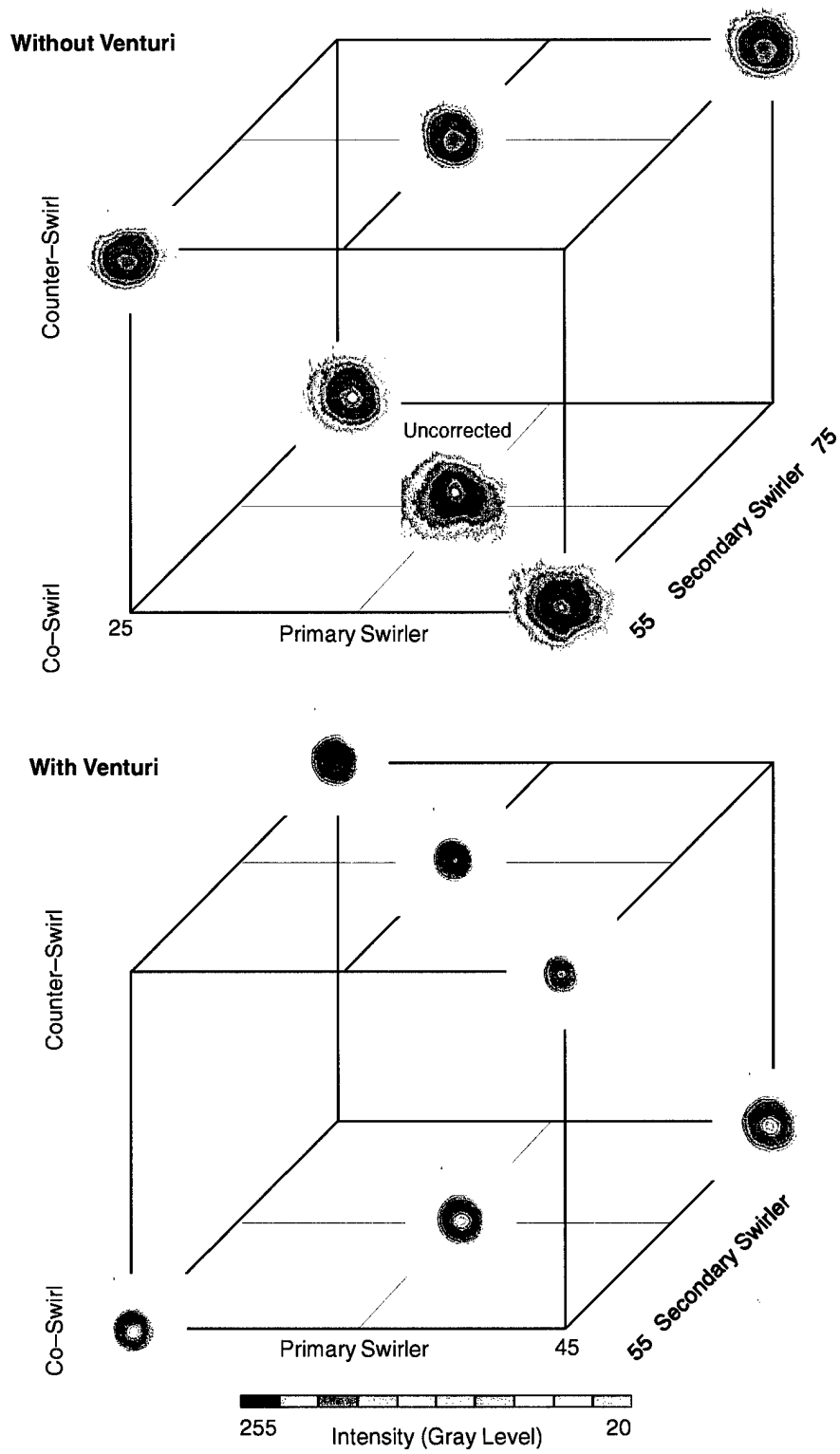


Figure 10. Cube Plot of Fuel Distribution Response for Swirl Strength, Swirl Sense, and Venturi.

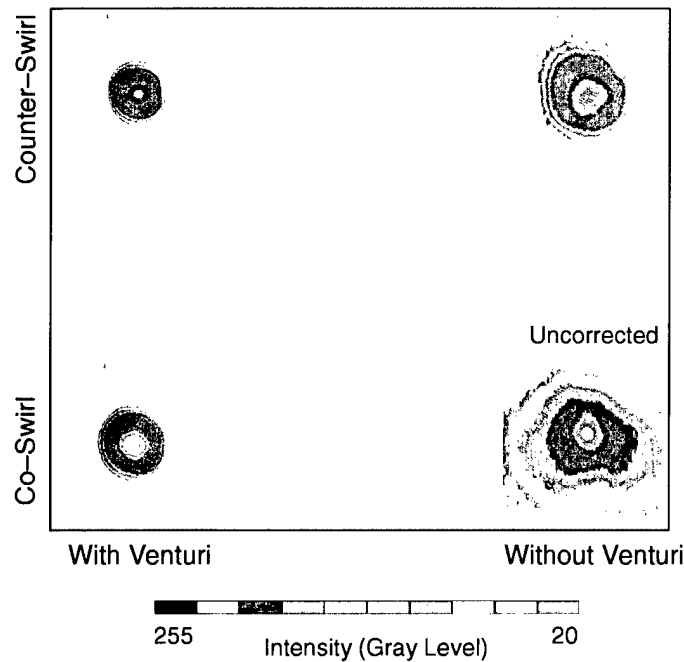


Figure 11. Effect of Venturi and Swirl Sense on Spray Distribution (Primary Swirl 35°, Secondary Swirl 65°)

Based on fuel distribution, swirl sense and presence of the venturi were identified as being of importance to study in more detail in the comprehensive measurements.

4.5.2.2 Reaction Structure and Stability

Like the fuel distribution, reaction structure was another good candidate for screening tests. Figure 12 presents photographs for the time-averaged reaction structure for Target 2 condition at an equivalence ratio of 0.6 in a format similar to Figure 11.

It is noted that much more extensive evaluation of these images has been presented in the Year 2 Annual Report. Based on this evaluation, conclusions regarding the important factors were drawn (i.e., venturi and swirl sense important again). As a result, Figure 12 provides a representative result from the images of reaction structure illustrating the role of swirl sense and the venturi. It is noted that the case of Counter-Swirl with venturi has a reaction structure at an equivalence ratio of 0.6 that differs from the other three cases. This is the case with the narrowest fuel distribution.

4.5.2.3 Lean Blowoff

Another screening effect examined was the lean stability limit. In this case, the stability limits for the four cases shown in Figures 11 and 12 are summarized in Figure 13. In this case, the images of the reaction structure are obtained at a point just prior to lean blowout.

In the case of stability, Figure 13 reveals that the Counter-Swirling cases have the best stability regardless of whether or not the venturi is present. The Counter-Swirl case with venturi has a narrow reaction structure compared to any of the other cases—consistent with the observations discussed relative to Figure 12.



Figure 12. Reaction Structure for Target 2 Condition Equivalence Ratio of 0.6. (Primary Swirl 35°, Secondary Swirl 65°) – Same Exposure

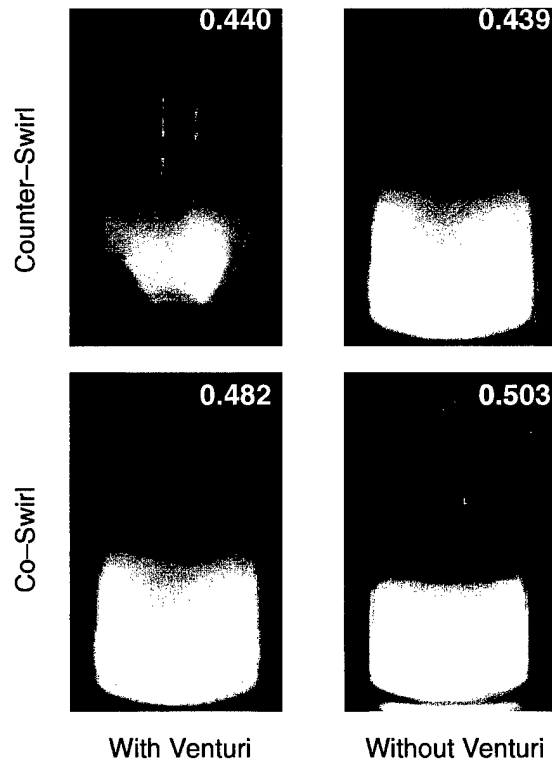


Figure 13. Lean Stability Limit and Associated Reaction Structure Near Blowout.

4.5.2.4 Emissions

Another effect used for screening was emissions. In this case, factorial experiments were again conducted. The bulk of these results for Target Conditions 1 and 2 were presented in detail in the Year 2 Annual Report. For the purpose of illustrating the findings, the results presented here focus upon the four cases which have been the subject of current discussion. For the emissions results presented here, the Target 2 conditions were utilized.

Figure 14 presents the exit plane emissions results for the four cases presented in Figures 11 through 13. These results were obtained by area weighting three measurements along a radial profile at the exit of the combustor. In general, the radial gradients in the emissions were fairly small, with the exception of CO which tended to be highest near the wall as expected.

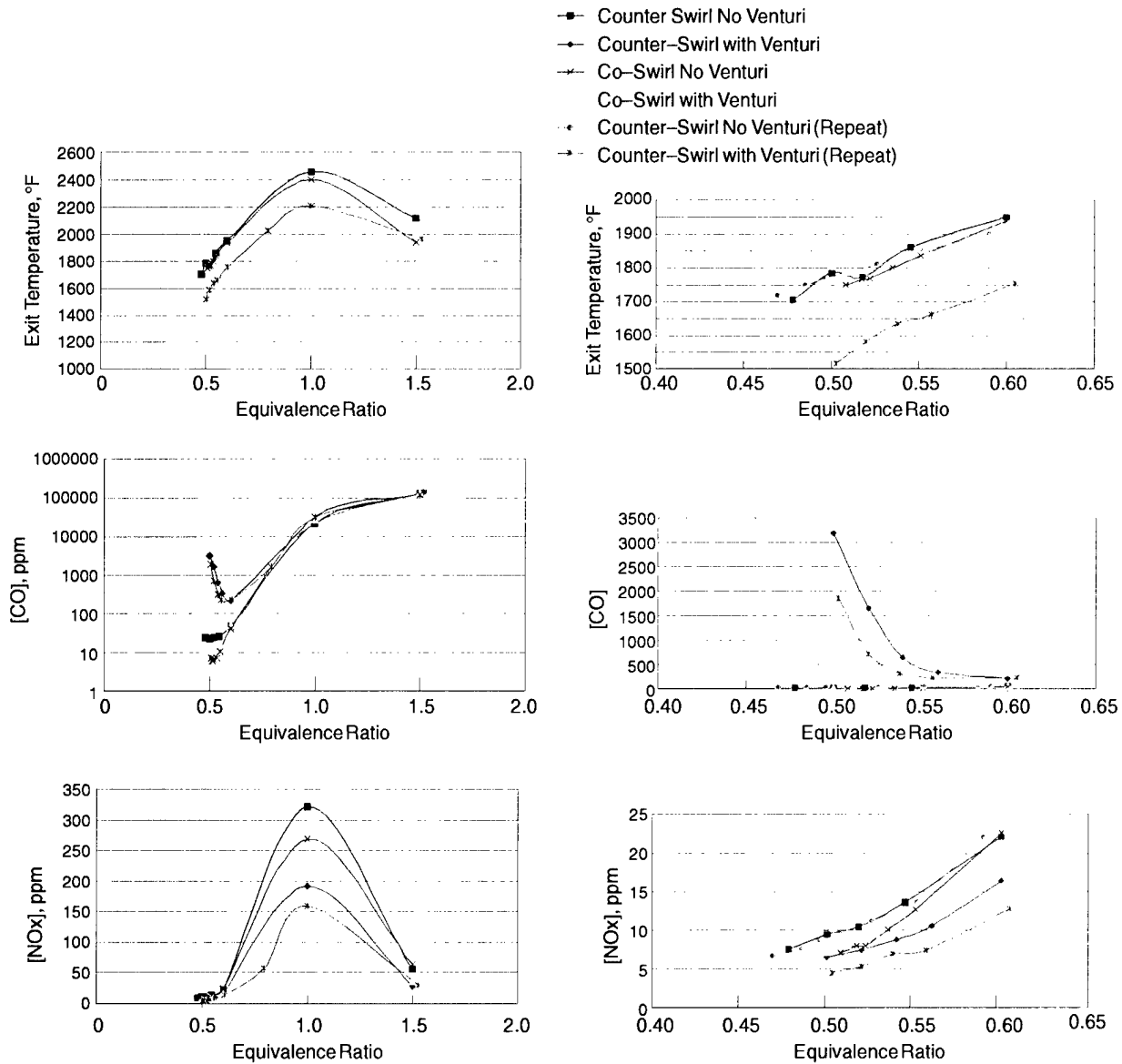


Figure 14. Average Exit Plane Emissions for Cases Shown in Figures 11 through 13.

Figure 14 reveals some interesting behavior relative to the CO at low equivalence ratios. In this case, the counter-swirl with venturi case exhibits a *bucket* in the CO profile, whereas the other three cases show no bucket. This same case also has the lowest temperatures and lowest NO_x concentrations, which may be directly related to the lack of oxidation of the CO.

4.5.2.5 Sooting Propensity

The particulate emissions from each the four cases were evaluated using a thermophoretic sampling technique. Thermophoretic sampling methodology has proven to be a successful method for characterizing the morphology of soot (Reference 3). Furthermore, previous work in combustor type environments using thermophoretic sampling techniques (Reference 4) has shown great promise for the characterization of soot in complex systems. As a result, this same methodology was applied to the present combustor configurations.

The soot characterization results include morphological observations and population data obtained from the thermophoretic sample. Particulate samples obtained were imaged via Transmission Electron Microscope (TEM).

Samples were obtained for equivalence ratios of 0.6, 1.0, and 1.5. Sampling times of 0.5 seconds were used for the equivalence ratio of 1.5. A sampling time of up to 5.0 seconds was used for equivalence ratios of 0.6 and 1.0, but no soot was visible on the grids for any of these cases. The sampling time could not be extended since the fragile grids would have been destroyed if exposed to the hostile combustion environment for any more time. Soot samples were obtained at an equivalence ratio of 1.5 for three conditions. The counter-swirl with venturi case required a 5.0 second sampling time to obtain significant quantities of soot. These samples were analyzed and the results are presented here. The primary results include soot morphology and soot volume fraction.

To provide a fair visual comparison of the sooting propensity, images of the soot obtained from each of the configurations at an equivalence ratio of 1.5 and a sampling time of 0.5 seconds were obtained. The results are presented in Figure 15. The counter-swirl with venturi sample did not contain enough soot to image for the 0.5 second sampling time.

Soot Morphology – From visual observation of the images above it is evident that soot agglomerates were captured within the flame zone of the combustor. The aggregates ranged in size up to 1 micron, but the majority of aggregates were less than 0.5 micron. The smallest aggregates contained only a couple of primary particles while the largest aggregates contained hundreds, and possibly, thousands of primary particles. The largest aggregates and the greatest soot coverage can be seen in the two cases not containing a venturi. The two configurations containing venturis produced considerably less soot. The soot captured from the co-swirl with venturi cases consisted primarily of individual primary particles. Very few small aggregates were observed (<0.2 microns in length). The counter-swirl with venturi case produced interesting and surprising results. A very minute amount of soot was captured on the grid for a sampling time of 0.5 seconds. Only two small primary particles were observed on the entire grid and therefore the image was not included in Figure 15. A sampling time of 5.0 seconds finally yielded enough soot for analysis. Evidently, the rate of deposition is not linear in time, at least not at early times.

In addition to visual observation and measurement of aggregate lengths, the diameters of primary particles within the aggregates were measured. Approximately 75–100 primary particle diameters were measured in each sample and the measurements were used to calculate an average and standard deviation of the diameters. The results are included in Table 6.

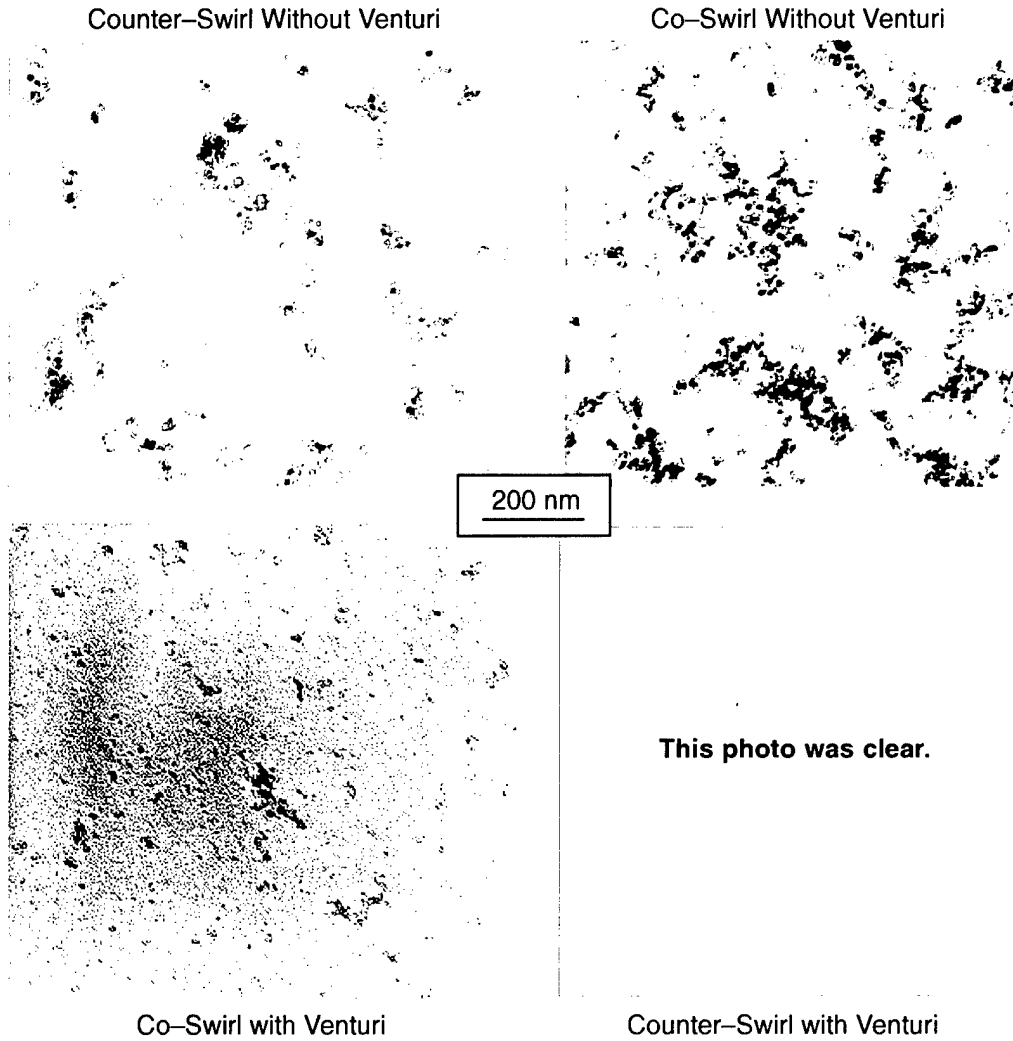


Figure 15. Photos of Exit Plane Particulate for 0.5 sec. Sampling Time ($\Phi+1.5$).

Table 6. Primary Particle Diameters.

Configuration	Diameter (nm)
COUNTER WITH	16.2 \pm 4.8
COUNTER WITHOUT	16.4 \pm 3.6
CO WITH	17.2 \pm 4.1
CO WITHOUT	15.8 \pm 3.7

The range of primary particles observed was very narrow. The standard deviation within each sample was also very small. It is believed that the particles being emitted from the combustor are monodisperse for these conditions. The monodisperse nature of soot particles in the 10–20 nm size range has previously been observed in various reacting conditions (Reference 4). This suggests that the particles all experienced a similar history in these types of intensely mixed reactions.

From these samples it can be concluded that the venturi has the most effect on the soot morphology. Soot produced in configurations containing a venturi consists mainly of individual primary particles. Configurations lacking a venturi produce much more soot and it is highly agglomerated. To a lesser extent the counter-swirl also influences soot formation. Up to this point, the actual amount of soot produced, in terms of a soot volume fraction, has not been discussed. This will be addressed in the following section to see if these qualitative results are accurate.

Soot Population – The soot volume fraction for different combustor configurations were determined using the soot sample along with the TSPD method (Reference 5). Enlarged photographs of the soot were scanned and analyzed to determine the soot coverage including the primary particle size, aggregate size, and projected area of the aggregate. The results presented here focus on the amount of soot produced at the experimental conditions. The amount of soot will be presented as a mass fraction and the volume fraction of soot contained in the reacting condition at 1400K.

The results obtained from the theory support the visual observations of the reactions and the non-reacting spray data. Several samples were taken for each configuration. The results presented include the average and standard deviation for the samples obtained during the configuration. The results are shown in Table 7.

Table 7. TSPD Results for Soot Concentration.

Configuration	fv (TSPD) 1400k
COUNTER WITH	0.56 ±0.07
COUNTER WITHOUT	0.64 ±0.07
CO WITH	0.08 ±0.03
CO WITHOUT	0.013 ±0.002

The trends of soot production by the configurations are obvious. The trends are not masked by the experimental variation. The amount of soot (at 1400K) ranges from 0.026 to 0.44 ppm. The cases not containing a venturi clearly produce the most soot. Both the counter-swirl and the co-swirl are approximately 0.5 ppm or 500 ppt. The average amount of soot produced is greater in the co-swirl without venturi case but the variation prohibits making the conclusive statement that this case produces more soot than the counter-swirl case. It is evident that the uncertainty and variation does not prohibit concluding that the cases with venturis produce less soot. The amount of soot produced in the cases with a venturi is at least 75% less than the amount of soot produced in cases without a venturi. The counter-swirl with venturi case produced considerably less soot than the co-swirl with venturi case.

It is clear that the soot production is greatly effected by the hardware geometry. This provides indication that by incorporating particular design aspects, the sooting propensity for this type of combustor dome geometry can be reduced.

4.5.2.6 Summary of Screening Tests

Based on the results from the screening tests, several key conclusions can be drawn. In particular, the swirl strength plays a relatively small role in the behavior of these mixers compared to the venturi and swirl sense. The counter-swirl case with venturi seems to stand apart relative to the other cases. It is this case that has the narrowest fuel distribution, highest CO, lowest NO_x, lowest particulate emission, and best stability. It also has a reaction structure at lean equivalence ratios which is

significantly different from the other three cases. It is noteworthy that the configuration with co-swirl and with venturi also was relatively stable, but produces very low CO and relatively low NO_x and particulate. To make a proper determination, however, the importance of each of these performance aspects must be weighted by the desired outcome. Once this *desirability* has been formulated, optimization can be conducted.

The next steps after the screening are to try and understand why the configurations perform the way they do. To answer this question, detailed measurements, comprehensive modeling, and development of analytical models were conducted as described in the next sections.

4.5.3 Comprehensive In Situ Measurements

Based on screening tests for the Target 2 condition, four combustor configurations were identified for detailed measurements of velocity, temperature, species, droplet characteristics, etc. in a manner that will allow CFD calculations to be evaluated. They are: 1) Primary Swirl angle 35° and Secondary Swirl angle 65°, Co-Swirl, Without Venturi; 2) Primary Swirl angle 35° and Secondary Swirl angle 65°, Co-Swirl, With Venturi; 3) Primary Swirl angle 35° and Secondary Swirl angle 65°, Counter-Swirl, Without Venturi; and 4) Primary Swirl angle 35° and Secondary Swirl angle 65°, Counter-Swirl, With Venturi.

4.5.3.1 Scattering Images

Figures 16a and 16b present sheet scattering results for the Co-Swirling cases. The scattering images reveal that the Venturi confines the spray toward the centerline. The case without venturi (Figure 16b) reveals large isolated drops that are flung to the outer periphery of the spray. Comparing the co-swirl images (Figures 16a, b) to the counter-swirl (Figures 16c, d), an absence of droplets at the centerline is observed for the co-swirl case, attributed to the greater centrifugal force in this case. In all four cases, the most intense scattering comes from the area at the edge of the exit flare, suggesting most of the liquid spray is present in this region.

4.5.3.2 Continuous Phase Velocities

The velocity vector plots for the two Co-Swirl configurations (Figure 16a and 16b) indicate *no substantial difference* between the mean continuous phase flows for the case with and without venturi. The case with venturi has lower levels of turbulent kinetic energy (TKE) near the exit plane of the mixer ($Z = 0.55 R_f$) implying weaker shear in this case. The reduced shear is attributed to the physical separation between the primary and secondary swirler in the case with the venturi. The interaction between the co-flowing air circuits is delayed as compared to the case without venturi. The case without venturi also exhibits the highest radial diffusion of this turbulent kinetic energy.

The velocity vector plots indicate the presence of a recirculation zone at the centerline for both Counter-Swirl cases (Figures 16c, d) near the nozzle exit. In contrast to the co-swirl case, for the Counter-Swirling case, the venturi does impact the general structure, namely reducing the radial spread of the flow. Like the co-swirling case, the venturi reduces the local TKE, presumably for the same reasons give above. The Co-Swirling cases have a stronger recirculation zone compared to the Counter-Swirling cases.

The magnitude of the TKE is higher for Counter-Swirl cases compared to Co-Swirl cases which might be expected given the opposing direction of flow with Counter-Swirl (compare Figure 16a

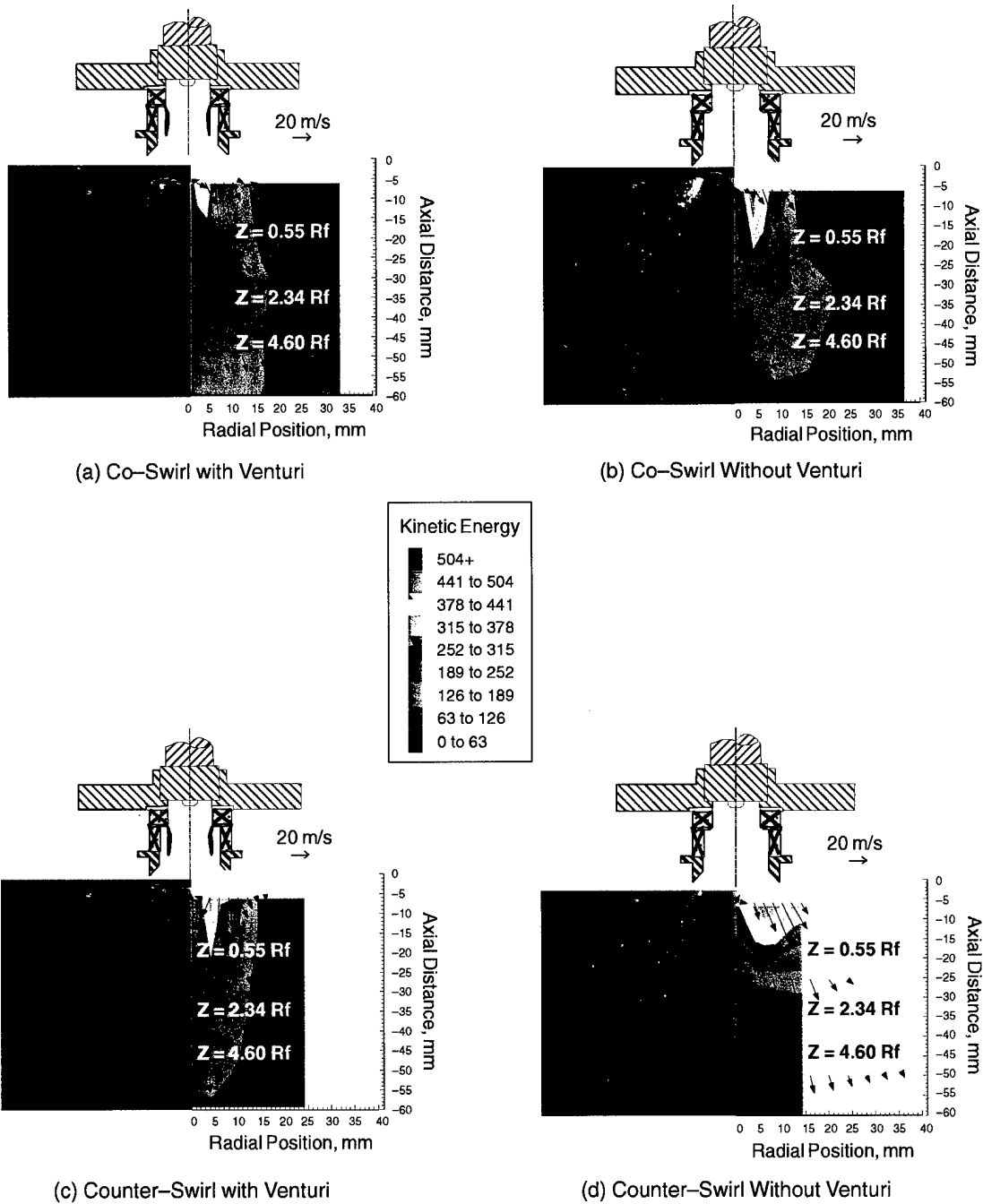


Figure 16. Non-Reacting Spray Image, Radial Velocity Vector and Turbulent Kinetic Energy Profile for the 35° Primary Swirl Vane Angle and 65° Secondary Swirl.

and 16b with 16c and 16d). TKE dissipation occurs most rapidly near the mixer exit in all cases. At $4.60 R_f$, the TKE has completely dissipated for the case Without Venturi and Counter-Swirl (Figure 16d). Whereas, in all other cases higher radial dissipation than axial dissipation occurs indicated by the higher TKE values at the downstream measurement location.

Figure 17 presents the azimuthal (or tangential) velocity component (W) of the non-reacting continuous phase for: (a) Co-Swirl With Venturi, (b) Co-Swirl Without Venturi, (c) Counter-Swirl With Venturi and (d) Counter-Swirl Without Venturi. The azimuthal velocity component was taken for the full radial traverse at three axial plane locations. Positive values of W on the negative side of centerline and negative values of W on the positive side of centerline correspond to clockwise flow (i.e., swirl produced by the secondary swirler).

The azimuthal velocity for all four hardware configurations dissipates at the far downstream measurement location ($Z = -50$ mm). The radial profiles vary substantially between Co-Swirl and Counter-Swirl configurations.

For the Co-Swirl arrangement, the highest tangential velocity near the mixer exit plane ($Z = -6$ mm) is achieved without venturi. The peak azimuthal velocity occurs at a radius of 10mm for the case Without Venturi compared to a radius of 5mm for the case With Venturi at the axial location $Z = -6$ mm. This can be explained by the fact that the venturi acts as a physical barrier between the primary and secondary flow circuit until the two eventually mix near the mixer exit. This separation of the two flows delays the mixing of the two streams. In the Co-Swirl case Without Venturi more of the fluid is allowed to mix and spread to a farther radial distance. Farther downstream ($Z = -25.4$ and -50 mm) the dissipation of the azimuthal velocity becomes independent of the venturi as indicated by similar profiles of azimuthal velocity at downstream planes.

In the Counter-Swirl cases, azimuthal velocities are much lower (Fig. 17c and 17d). The opposed air flow of the primary and secondary swirler leads to reduced overall swirl. For the case With Venturi (Figure 17c) both counter-clockwise and clockwise swirling flow were measured. The azimuthal components at inner radii indicate counter-clockwise swirl from the primary swirler, while those at the outer radii indicate clockwise swirl from the secondary swirler. Since the mass flow split between the secondary and primary swirler is 60/40, respectively, the magnitude of tangential velocity is higher for the secondary swirler. In the absence of the Venturi, the distinct peaks caused by the two swirlers are no longer delineated as more intense mixing between the two swirler circuits occurs prior to the mixer exit. In both Counter-Swirl cases, the dissipation of tangential velocity occurs much more quickly than the Co-Swirling cases.

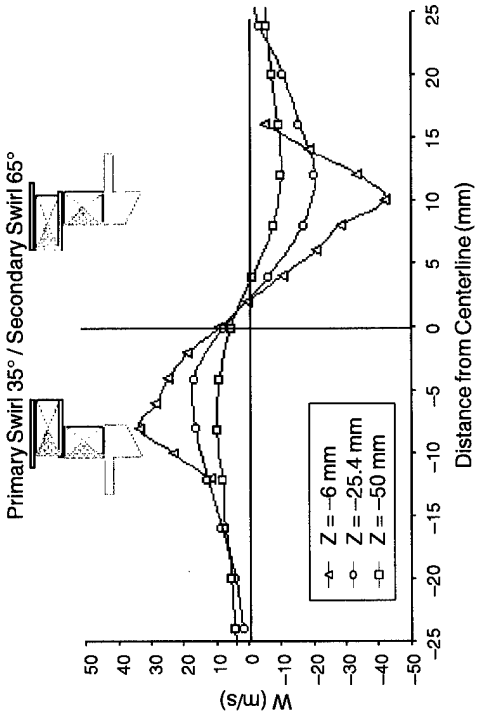
4.5.3.3 Dispersed Phase Characteristics

In this section the structure of the non-reacting spray in terms of average fuel drop size and spatial distribution (i.e., volume flux) is presented.

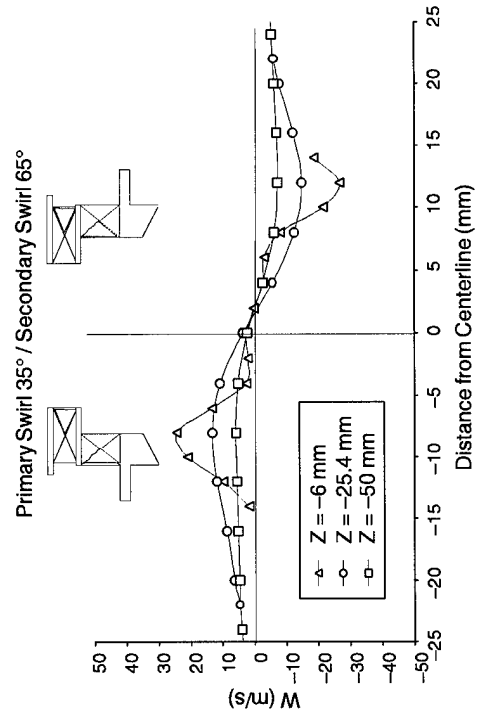
Droplet Distribution D_{32}

Figure 18 presents radial profiles of the Sauter mean diameter (SMD), or D_{32} , for the four configurations. The figure has been split so that only half of the radial D_{32} profile of each configuration is shown. The bar-values at each point represent the range of D_{32} measured at that radial distance and four circumferential locations, thereby reflecting the symmetry of the spray.

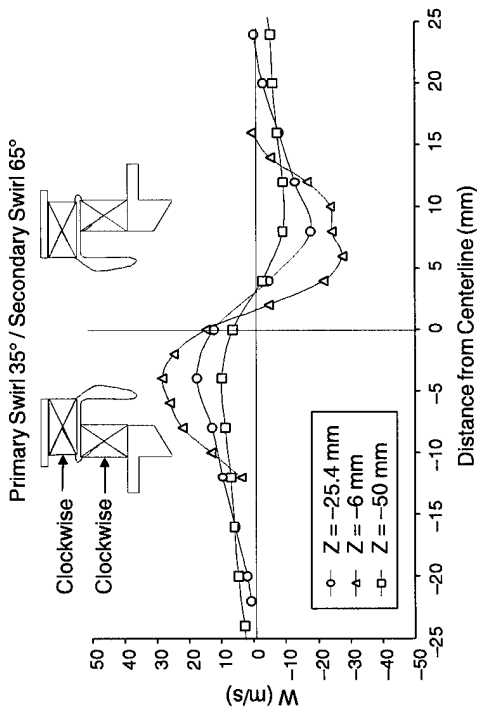
For the Co-Swirl configurations (Figure 18a) the Venturi reduces drop size by a factor of 3 at the exit plane. Smaller D_{32} values are measured, especially at the $Z = -6$ mm plane, because the Venturi



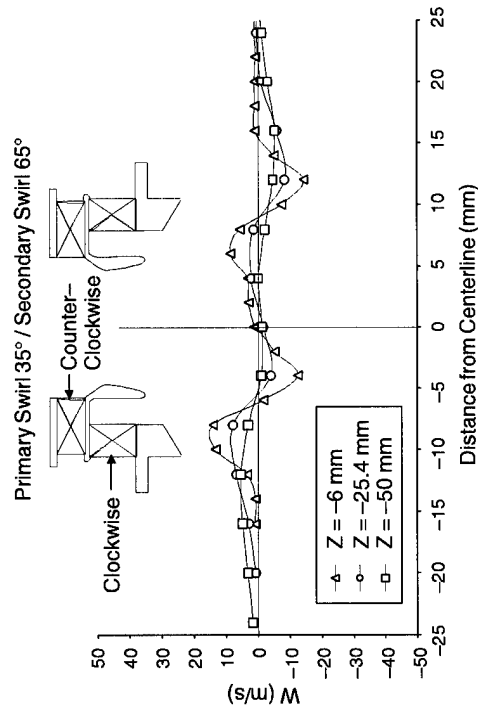
(a) Co-Swirl with Venturi



(b) Co-Swirl Without Venturi

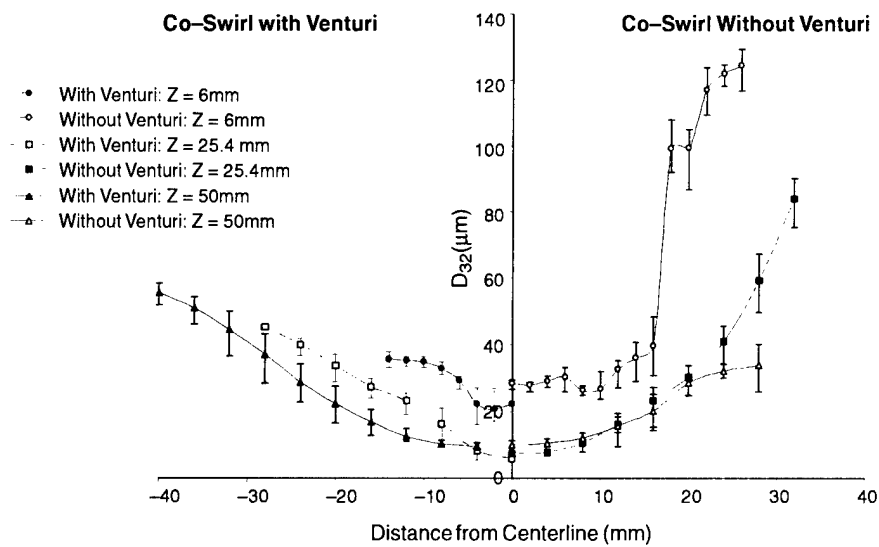


(c) Counter-Swirl with Venturi

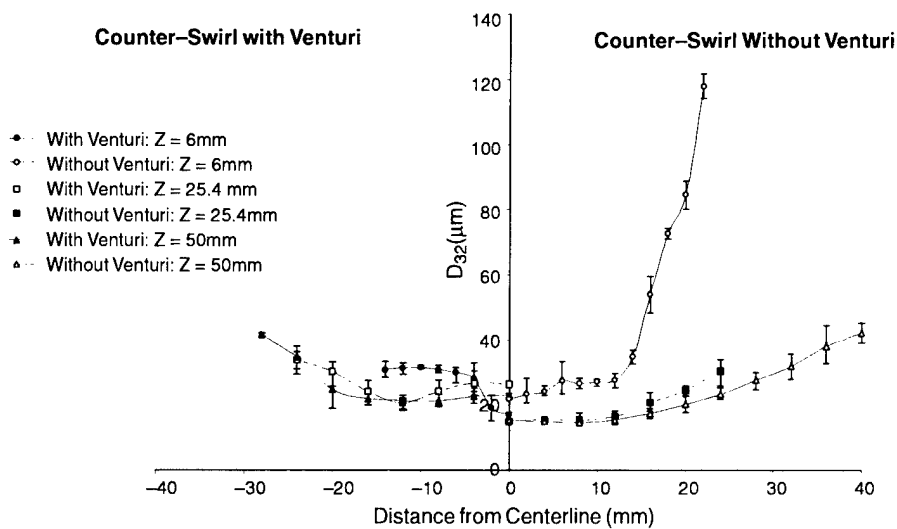


(d) Counter-Swirl Without Venturi

Figure 17. Radial Profile of Azimuthal Velocity (M/S) for the 35° Primary Swirl Vane Angle and 65° Secondary Swirl Vane Angle.



a) Co-Swirl with and Without Venturi



b) Counter-Swirl with and Without Venturi

Figure 18. Droplet Distribution D_{32} Profiles for the 35° Primary Swirl Vane Angle and 65° Secondary Swirl Vane Angle.

acts as a prefilming surface for the liquid spray and enhances the atomization process. The Venturi also confines the droplet distribution to the centerline region near the mixer ($Z = -6\text{mm}$ and -25.4mm). The case Without Venturi illustrates that the inertia of the largest droplets produced allows penetration through the flow (consistent with images in Figure 15). Farther downstream, the distribution in the near centerline region looks similar for the case With and Without Venturi, but more large drops can be found Without Venturi in the outer periphery of the spray. The greatest difference between the two Co-Swirl configurations is the near field drop size and distribution. In general, the Venturi enhances the atomization process and produces a much more uniform drop size distribution near the mixer exit.

Counter-Swirl results in similar trends compared to the Co-Swirl cases. Finer atomization again occurs with the Venturi. The case Without Venturi reveals that Counter-Swirl produces smaller drop sizes than the Co-Swirl case. This is attributed to the more intense shear that occurs with the opposed-swirling air streams (recall TKE values in Figure 16) in the Counter-Swirl configuration which leads to finer atomization. In general, drops in the outer periphery of the spray with Counter-Swirl are 65% smaller than those for the Co-Swirl.

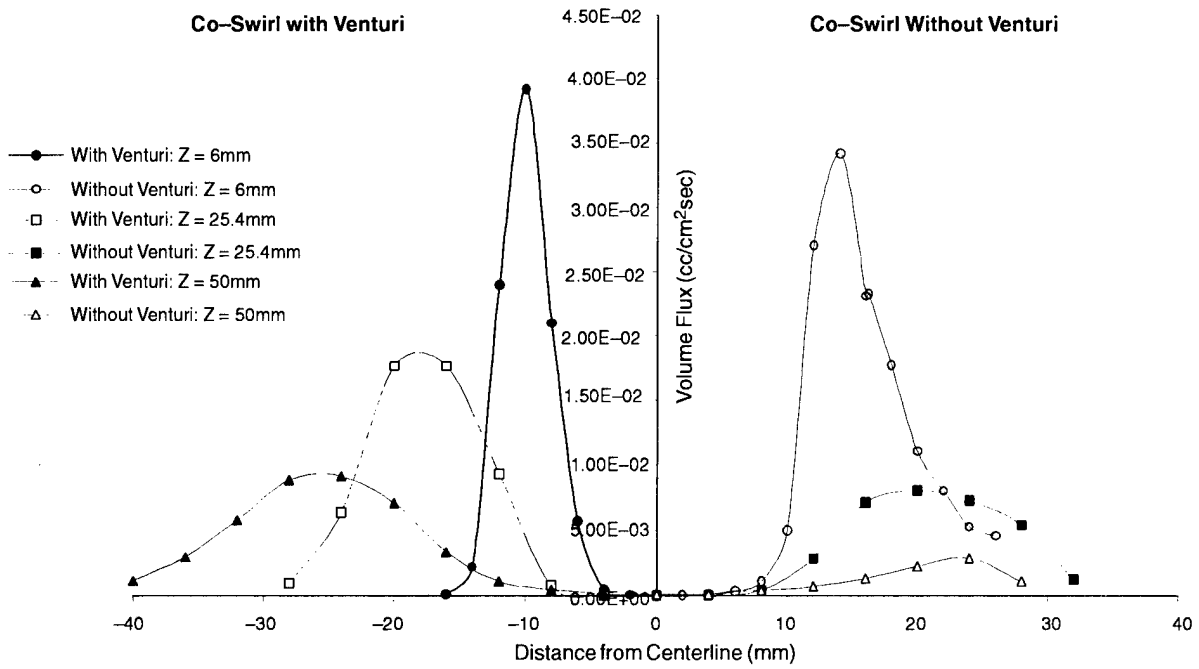
Comparing all the four configurations in Figure 17 it is found that Counter-Swirl With Venturi produces the smallest droplets and has the most uniform drop size profile. All droplets formed with this configuration ranged from $D_{32} = 18\text{--}32\ \mu\text{m}$, for a region that extended 30mm in the radial direction and 40mm in the axial direction.

A qualitative analysis of the spray structure photographs in Figure 15 confirms that the net effect of the venturi is to confine the flow and minimize the large drop formation and penetration through the outer periphery of the spray.

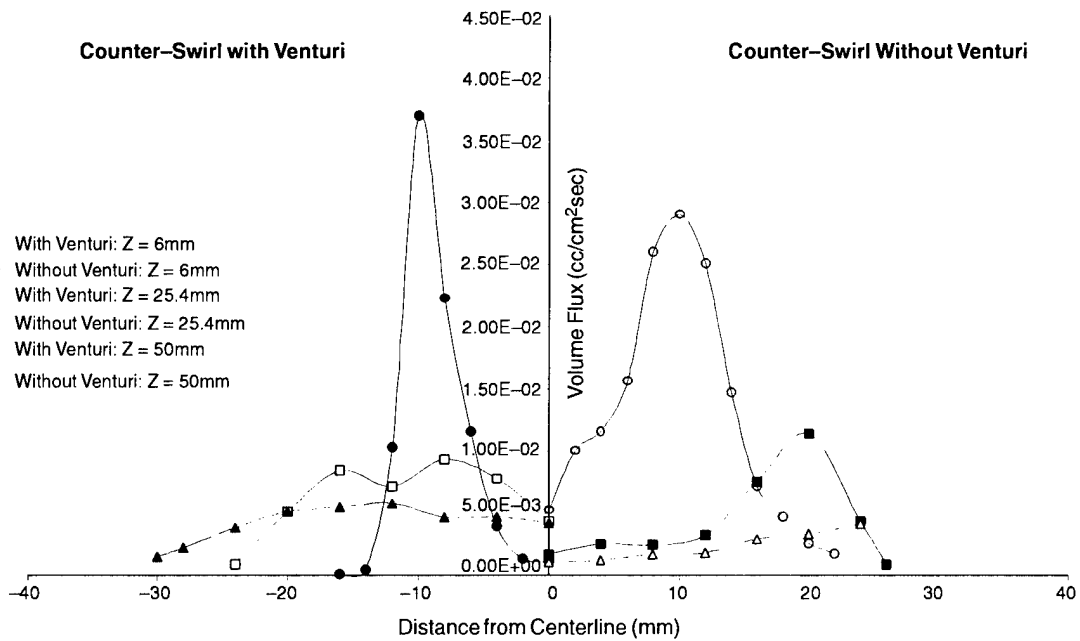
Droplet Volume Flux

Figure 19 presents radial profiles of local volume flux (volume of liquid passing through the interferometric probe volume cross section per unit time) in the spray under non-reacting conditions at three axial plane locations. Figure 19 quantifies the degree to which the Venturi confines the flow towards the centerline in the near mixer exit region. A higher volume flux occurs closer to the centerline of the flow in the case With Venturi with most of the fuel concentrated in a small annular ring. In the case Without Venturi the peak volume flux is pushed out radially and is more diffused than With Venturi. Note that, in the centerline of the flow, very little fuel exists. The drop sizes in the high concentration region are uniform (Figure 17), indicating that the volume flux gradients are attributed more to droplet population than droplet size. For the case Without Venturi very large average drop sizes were found (Figure 17). Up to the radial location of 10mm drop size distribution was uniform at $30\ \mu\text{m}$ (Figure 17) with a very low volume flux (Figure 18). Farther out where drops get larger with radius the volume flux also increases as larger drops contribute more to the volume. However, past the 15mm radial location where drops continue to get larger as radius increases there is a sudden drop in the flux indicating a small number of very large drops are present at this location. This is indicated in the images in Figure 15.

Figure 19b presents the Counter-Swirl case. Again, the Venturi concentrates the spray to a relatively narrow annulus near the mixer exit region. Since the D_{32} is relatively uniform (Figure 19) with Venturi it is concluded that a large drop population exists near the mixer exit region. For the case Without Venturi, a uniform D_{32} profile is found up to radial location 12mm followed by a sudden rise in droplet size (Figure 18). The volume flux at $Z = -6\text{mm}$ increases up to radial location followed



a) Co-Swirl with and Without Venturi



b) Counter-Swirl with and Without Venturi

Figure 19. Droplet Volume Flux Profiles for the 35° Primary Swirl Vane Angle and 65° Secondary Swirl Vane Angle.

by a sudden drop in volume flux (Figure 18) as drop size begins to increase (Figure 17). Although large drops are formed Without Venturi, Counter-Swirl minimizes their population.

4.5.3.4 Dispersed Phase Characteristics – Reacting and Confined

In this section the structure of the reacting confined spray in terms of average fuel drop size, spatial distribution (i.e., volume flux), and velocities is presented.

Droplet Distribution D_{32}

The droplet size distribution for the 35° Primary Swirler / 65° Secondary Swirler *Co-Swirl* With Venturi measured within the reaction at three axial planes within the combustor ($z=6, 25$ and 50mm) were as follows. Large droplets ($35\text{--}50\ \mu\text{m}$) were found in the near field of the reaction ($z=6\text{mm}$). Farther downstream smaller drops sizes were found – reflecting the vaporization of the larger drops at a downstream location. At this location more drops were also found at the outer periphery of the spray within the reaction. Generally, the measurements of SMD within a reacting flow were larger than the measurements for non-reacting unconfined conditions (Figure 19). In the reacting case smaller drops that were produced within the mixer and near the mixer exit vaporizer much quicker as compared to the non-reacting condition. As such, in the reaction small drops were not found and most drops entering the probe volume have an associated SMD leaning more towards larger drops. In non-reacting cases, the SMD leaned more towards smaller drops present due to absence of any substantial vaporization.

The droplet size distribution for the 35° Primary Swirler / 65° Secondary Swirler *Counter-Swirl* With Venturi measured within the reaction at three axial planes within the combustor ($z=6, 25$ and 50mm) were as follows. Here, with the Counter-Swirl configuration a more narrow range of droplets were found ($35\text{--}45\ \mu\text{m}$). However, the SMD gets larger with downstream distance. This can be explained by the complete evaporation of the smaller droplets that occur farther downstream and resulting in only larger droplets being detected.

Droplet Velocity

With the *Co-Swirl* configuration it was found that the peak axial velocity of the droplets moves farther towards the outer periphery with axial distance. No negative velocity of droplets were measured near the recirculation zone. This could be the result of small drops that tend to be present within the recirculation zone, exhibiting negative velocity, vaporize much more rapidly, mix and react within the recirculation zone.

The azimuthal velocity component of droplets with the highest velocities was clearly seen near the mixer exit and reducing in velocity farther downstream. In the case with Counter-Swirl, near the mixer exit, the droplets ($15\text{--}35\ \mu\text{m}$) possess both positive and negative azimuthal velocity as the two counterrotating streams were separated by the Venturi and the presence of which was seen at the $z=6\text{mm}$ plane. Farther downstream the droplets follow the direction of the Secondary Swirler which comprises 60% of the total combustor flow and the Primary Swirler 40%.

Droplet Flux

The dense fuel spray at the $z=6\text{mm}$ axial plane (near mixer exit) precluded accurate measurements with the optical configuration utilized. However, measurements were made at the $z=25$ and 50mm plane.

The *Co-Swirl* With Venturi configuration issues a hollow spray cone from the mixer. The highest liquid fuel concentration is at the 15mm radial location.

At a farther downstream location ($z=50\text{mm}$) the reduction in flux shows the narrowing of the liquid fuel spread, indicative of the evaporation process. Though the peak flux value and the location of it remains constant between the two planes of measurements.

Flux values for the Counter-Swirl With Venturi configuration. The liquid fuel concentration was more towards the center as opposed to the Co-Swirl configuration. At the $z=25$ axial plane location little fuel is present at the outer periphery of the combustor. At the 50mm downstream location the reduction in fuel volume flux indicated much more rapid vaporization with the Counter-Swirl as opposed to the Co-Swirl. This was consistent with the smaller drops that were produced with the Counter-Swirl (~20% less than Co-Swirl) enhancing the complete vaporization of the fuel.

Mean Temperature Field

In each of the four baseline configurations of the 35° Primary Swirler- 65° Secondary Swirler, in situ temperature measurements were taken in order to demonstrate how the Swirl Sense and Venturi affect the temperature distributions within the combustor. An inlet air temperature of 400°F was used.

Temperature measurements were made with a Type-R thermocouple mounted to a water-cooled probe used as a support structure. Radiation effects of the thermocouple to the combustor wall were taken into account and temperature correction scheme was calculated.

Mean temperatures were measured as close to the combustor wall as possible ($\pm 20\text{ mm}$) and as far downstream as the length of the combustor (165 mm). Measurements were made in both the positive and negative radial direction to check for symmetry. Once it was shown that good symmetry exists ($\pm 15^\circ\text{F}$) only one side of the radial direction were measured and the mirror image presented on the other side to show the general flow temperature profile within the entire combustor. Since the effect of Venturi and Swirl Sense was studied each will be discussed separately.

Venturi Effects

Co-Swirl – As shown in Figure 23 the venturi moves the low temperature region into the center of the combustor. The cool temperatures were attributed to fuel rich regions exceeding the flammability limits.

The cusp in the centerline temperature profile in the near mixer exit region is evidence of the recirculation that brings hot gases back into the primary zone. Note that, near the wall region and especially in the corner of the combustor wall at the mixer exit, very high temperatures ($\sim 2000^\circ\text{F}$) were observed. This could be the result of a recirculation zone that is anchored in that region that either sustains a local reaction (if enough fuel is supplied to that region) or where hot gases from downstream region get pulled back into that region. Up to 35 mm downstream of the mixer exit high temperature gradients exist – after which the high temperature region becomes much more radially and axially uniform. This would not suggest that a reaction exists, however, since temperature is a transporative property and could simply be diffusing into the downstream region.

Without Venturi a much more compact high temperature region is formed in the primary zone very close to the mixer exit. The high temperature gradient region extends only 15–20 mm downstream. High temperatures ($\sim 2000^\circ\text{F}$) were found in the corner wall and along the wall of the combustor. The centerline recirculation zone convects high temperature gases back upstream. This configuration also shows how the mixer hardware itself is subjected to higher temperatures than the case With Venturi. The lowest temperature measured in the near mixer exit region was 900°F . Though the absence of the Venturi has shown to impede atomization, it may be that the hot gases can conduct,

convect and also radiate some of the high temperature within the mixer region where fuel is initially injected, thereby, enhancing vaporization. Detailed droplet size and volume flux measurements will provide more insight into how droplets are transported between the two configurations. If no change in droplet size is noticed between the case With and Without Venturi it may suggest that the Venturi does increase the atomization rate, whereas, no Venturi produces larger drops which were subjected to higher initial temperatures, their subsequent prevaporization may be providing the same droplet size distribution as the case with Venturi.

Counter-Swirl – The Venturi effects were similar with the Counter-Swirl configuration as with the Co-Swirl configuration. However, the effect the Venturi has on the temperature is much more pronounced with the Counter-Swirl configuration. A low temperature region extends 50mm downstream of the mixer exit. Near the wall region very high temperature gradients exist in the radial direction.

High temperatures exist in the corner wall of the combustor regardless if the Venturi is present or not. Without Venturi a high radial and axial temperature exists in the near mixer exit region. With Venturi an axially and radially uniform temperature profile exists after 90mm downstream. Without Venturi this is achieved after 60mm.

Though the Venturi has shown to enhance the atomization process it clearly creates a no-reaction zone within a good part of the primary zone due to the low temperatures that exist there. This low temperature region could be filled with fuel/air mixture within the flammability limits but were at too low of a temperature for the activation energy to convert chemical energy into thermal. It could also be that this low temperature region is a very fuel-rich region that can not sustain the reaction due to the equivalence ratio being outside the flammability limit. However, the Lean Blowout measurements showed the most stable reaction is with this configuration. The reaction-stabilizing mechanism may not be related to the centerline fuel distribution but rather fuel being injected into a corner recirculation zone. The high temperatures at the wall would certainly support very intense corner reaction zones.

Swirl Sense Effects

With Venturi the Co-Swirl configuration kept the low temperature region of the mixture to a much more compact region at the mixer exit as opposed to the Counter-Swirl configuration. Also with Co-Swirl the presence of hot gas recirculation is seen clearly at a mixer exit, whereas, no effect of recirculation is clearly visible with the Counter-Swirl configuration. Counter-Swirl injects a low temperature fuel/air mixture well into a third of the total length of the combustor.

Without Venturi the difference between the two swirl senses is more subtle. Here the Co-Swirl configuration exhibits a more radial spread of the hot gases towards the outer wall and clearly shows evidence of recirculated hot gases very near the mixer exit. In a Counter-Swirl arrangement much lower temperatures exist near the mixer exit. With Co-Swirl radially and axially uniform temperatures were achieved at the 30mm downstream plane. However, with Counter-Swirl such uniformity is not achieved until 60mm downstream. Here, the Co-Swirl shows a more intense reaction throughout the combustor with minimal low temperature regions.

4.5.4 Summary

Armed with screening results as well as detailed measurements, some mechanistic understanding of the behavior of the radial mixer device can be derived. To aid in this effort, Table 8 presents a summary of observations just presented.

Table 8. Summary of Observations – Four Cases 35/65 Primary/Secondary Swirl, Target 2.

Config	Counter-swirl Venturi	Counter-swirl No Venturi	Co-swirl Venturi	Co-swirl No Venturi
Result				
Sheet Scatter Image	Low Spread "less hollow"	Wide Spread "less hollow"	Med. Spread Hollow	Med. Spread Hollow
LA Gas TKE profile	High shear Narrow region	High shear, Wide region	Low shear Narrow region	High shear, Narrow region
LA Gas Mean Velocity Profile	Short RZ Low Spread	Short RZ Wide Spread	Med RZ Med. Spread	Med RZ Med. Spread
PDI Vol. Flux Profile (Nonreacting Unconf)	Narrow Spread Fuel @ CL	Medium Spread Fuel @ CL	Medium Spread No Fuel @ CL	Wide Spread No Fuel @ CL
PDI Drop Size Profile (Nonreacting Unconf)	Flat 50 Micron Max	Gradient 120 Micron Max	Flat 50 Micron Max	Gradient, 120 Micron Max
Stability	Best	Best	Medium	Worst
NO _x Emissions	Low	High	Medium	Medium
CO Emissions	High	Low	Low	Low
Combustor Thermal Field	Large Low Temp. Core	Short Low Temp. Core	Short Low Temp. Core Recirc. Hot Gas	No Low Temp. Core. Compact High Temp. Reg.
Soot Aggregation	Lowest	High	Low	High
Soot Volume Fraction	Lowest	High	Low	High
Turbine Inlet Temp	Low	High	High	High
Reaction Structure	Narrow	Wide	Wide	Wide

Before drawing conclusions from Table 8, it is important to summarize findings from the screening tests. The screening tests indicated:

- The fuel injector flow number has no effect on performance when operated in the mixer at nominal pressure drops. This attributed to the much greater momentum of the air flow.
- Swirl Strength did not affect fuel distribution, stability, or *emissions for the conditions studied*.
- Swirl Sense and the Venturi have a major impact on fuel distribution, stability, and *emissions for the conditions studied*.

Based on these findings, the mid points of swirl strength were selected for detailed study, resulting in the additional observations provided in Table 8. Table 8 suggests a few important conclusions relative to the general performance of radial inflow mixers.

- **Fuel Distribution:** Co-Swirl without a Venturi results in the widest distribution of fuel resulting in a more uniform presentation of fuel to the combustor. This might be expected to lead to poor stability and low NO_x at lean conditions.
- **Reaction Stability:** Counter-Swirl is a critical aspect providing stability. This is due to the ability of the Counter-Swirl to provide fuel to the centerline region regardless of whether or not a venturi is present. As expected from the fuel distribution, the Co-Swirling case with no venturi had the poorest stability.
- **NO_x Emissions:** The Counter-Swirl with Venturi results in the minimum NO_x levels which were consistent with the associated turbine inlet temperatures.

Interestingly, the co-swirl case with no venturi did not have the lowest NO_x, indicating that something other than the presentation of fuel is playing a role in the formation of NO_x. Detailed measurements of temperature and better understanding of the reacting two-phase flow is required to explain the NO_x observations. The Counter-Swirl case with no venturi had the highest NO_x levels.

- **CO Emissions:** The Counter-Swirl with venturi case with the lowest temperature and NO_x also exhibited high CO levels. It is likely that the low NO_x and temperature is due to the lack of heat release from the remaining CO. For some reason, this particular case has a reaction that is quenched somewhere prior to full oxidation of the CO. Again, additional in-situ measurements of temperature and the flow field structure were required to explain this fully.
- **Particulate:** Counter-Swirl With Venturi produced very little particulate compared to the other cases.

From the results obtained to date, no one configuration provides the best overall performance. The cases with best stability (Counter-Swirl) suffer from high CO (with Venturi) or high NO_x (without Venturi). It could be that the NO_x levels would be similar for these two cases if the CO conversion was completed. The cases with the lowest CO levels and corresponding moderate NO_x level have the poorest stability. The results suggest that, if fuel can be maintained at the centerline for either of the co-swirling cases, improved performance may be achieved relative to the Counter-Swirling cases. It is interesting that the large variation in droplet size appears to have no consistent affect on the performance (e.g., low CO can still be achieved even with large droplets in the case of co swirl without venturi). Planar and time resolved measurement may be needed to fully explain the results.

4.6 Task 6 – CFD Modeling

To provide results to support Task 7 and to drive the experimental effort, CFD modeling of the various configurations was initiated and reported in the Year 1 Annual Report. The lack of understanding of the detailed flow within the swirl cup required the CFD effort to be redirected to a methodology to allow these details to be resolved. The full geometry of the swirlers was recreated and output to an IGES file format. Using Gambit, a preprocessor packaged with Fluent UNS, the geometry file was imported and meshing was initiated. An example of the geometry file and mesh is shown in Figure 20. Additional effort is now needed to conduct actual CFD runs of the domain. These efforts are being continued and should be completed within a year. In parallel, with the data acquired, the modeling results can be anchored.

4.7 Task 7 – Design Tool Development

4.7.1 Semi-Empirical Analytical Models

The goal of this effort is to produce analytical expressions that can be used for design purpose. While expressions for emissions, stability, and pattern factor are ultimately desired, intermediate models for the parameters affecting these must be developed (e.g., fuel distribution, drop sizes, aerodynamic fields, etc.). Purely empirical models of the fuel distribution were provided by the TASK 5 screening results (Reference 7). For the scope of the current program, the aerodynamic field was selected for

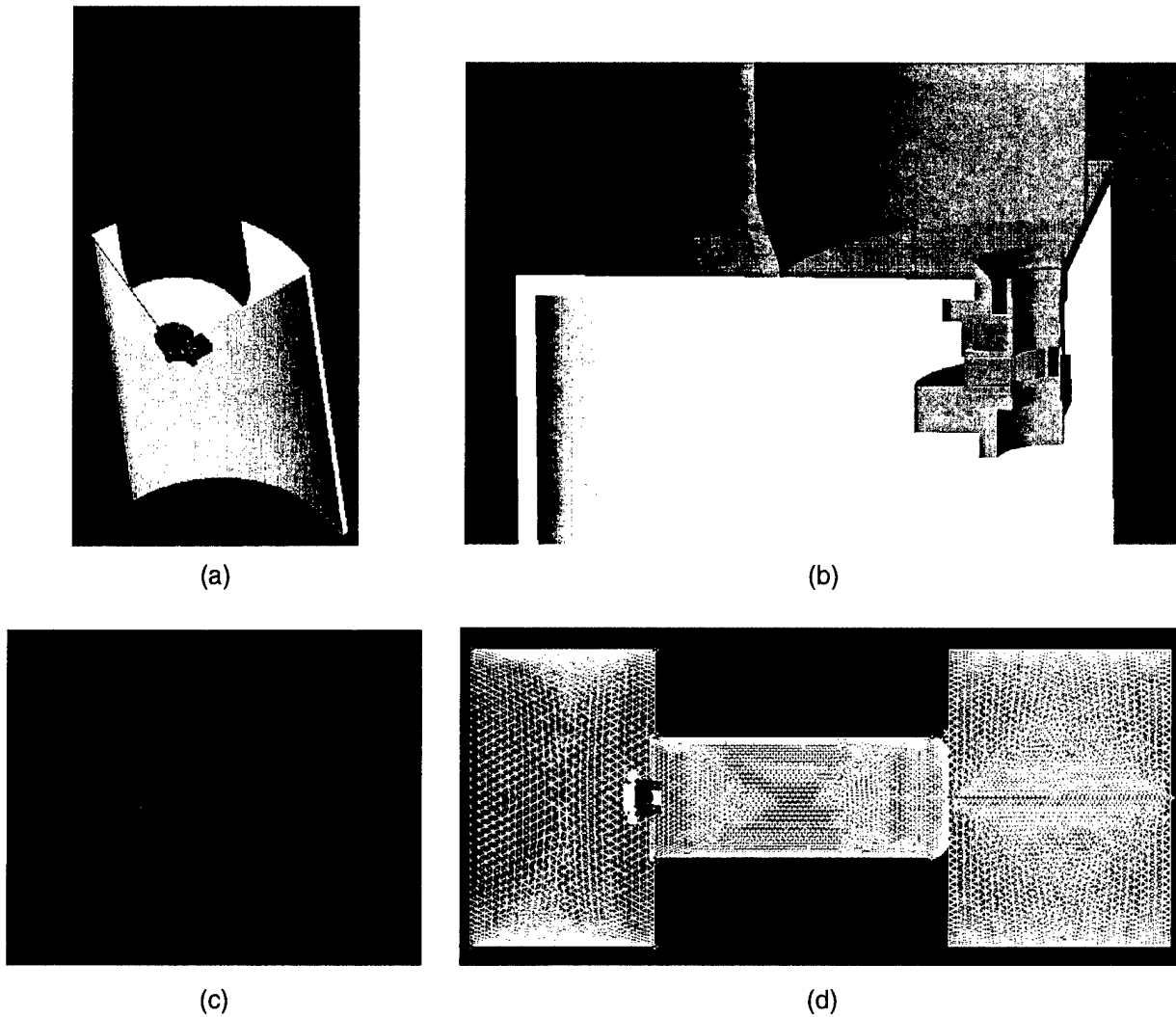


Figure 20. 3D IGES File Rendering for Full Domain Mesh Generation in Fluent UNS.

the development of more mechanistically correct analytical expressions. It might be argued that this field should be handled by CFD which is well suited to bring physics into the expressions. However, since previous work had been done in this area, it was explored in the current program.

The model used for the flow field is described in detail by (Reference 8). The relationship used to predict the axial velocity profile in the radial direction is shown in Table 9.

Both measured and predicted values of the axial velocity were determined for both confined and unconfined flow. Figures 21 and 22 illustrate the predicted vs. the measured normalized axial velocity profile vs. normalized radial location ($\xi=r/(x+a)$) for the case of Co-Swirl Without Venturi and Counter-Swirl Without Venturi configuration of the $35^\circ/65^\circ$ Primary/Secondary swirler geometry. Figures 23 and 24 illustrate the same plot for the Co-Swirl With Venturi and Counter-Swirl Without Venturi, respectively. The profiles for three axial locations away from the mixer flare exit are shown (6mm, 25.4mm and 50mm). The measured values were collected from the LA measurements of the continuous phase in Task 5. Both *confined* and *unconfined* measurements are illustrated for each configuration

Table 9. Predictive Model of the Axial Velocity Profile in the Radial Direction.

$$\frac{U_m}{U_{mo}} = 3.93 S^{0.8} \left(\frac{d}{x+a} \right)^c \quad \text{Equation 1}$$

$$\frac{U}{U_m} = \left(\frac{r}{r_o} \right)^2 \exp(-k_u) \left[\left(\frac{r}{x+a} \right)^3 - \left(\frac{r_o}{x+a} \right)^3 \right] + A \quad \text{Equation 2}$$

$$A = \left(0.65 - 2S \left(\frac{r_o}{x+a} \right) - \left(\frac{r}{x+a} \right) \right) \left(1 - \frac{r}{r_o} \right) \quad \text{Equation 3}$$

$$k_u = 0.667 \left(\frac{x+a}{r_o} \right)^3 \quad \text{Equation 4}$$

Where:

- U_m Peak Axial Velocity
- U_{mo} Peak Axial Velocity at Nozzle Exit
- c 1.52S^{0.64}
- r Radial Distance
- r_o Radial Location of Maximum Axial Velocity
- x Axial Distance, m
- a 2.3d : Distance from nozzle exit to origin of the flow
- d Atomizer exit diameter, m
- S 0.9

The model used based on the equations in Table 9 were modified for the all the configurations tested to provide the best curve fit. Mainly the swirl number value (S) and the radius at which the maximum velocity occurs were adjusted to provide the best curve fit.

For the Co-Swirl Without Venturi the best agreement between the predicted model and the measured value is achieved for the Unconfined condition. In the Confined condition, the general trend of the velocity profile is predicted well but the magnitude was under-predicted. Important to note the higher negative velocities attained within the recirculation zone with the Confined configuration and the model's capability to predict that.

The Counter-Swirl Without Venturi configuration showed the best match between the measured and predicted values of axial velocity. In the Confined configuration the presence of the recirculation zone is very evident.

The Co-Swirl With Venturi configuration had good prediction as well, except in the near mixer exit region where only satisfactory agreement was obtained.

The Counter-Swirl With Venturi configuration had good agreement for the predicted velocity profile for the Confined situation. The Unconfined predicted negative velocities that the measured values did not indicate.

4.7.2 Lean Blowout Model

An LBO predictive model, based on an existing model, was improved to account for a heterogeneous swirl-stabilized reaction. The model, which also included terms specific to mixer components, predicted to within 14% of the measured value, the LBO fuel-air ratio at three different operating

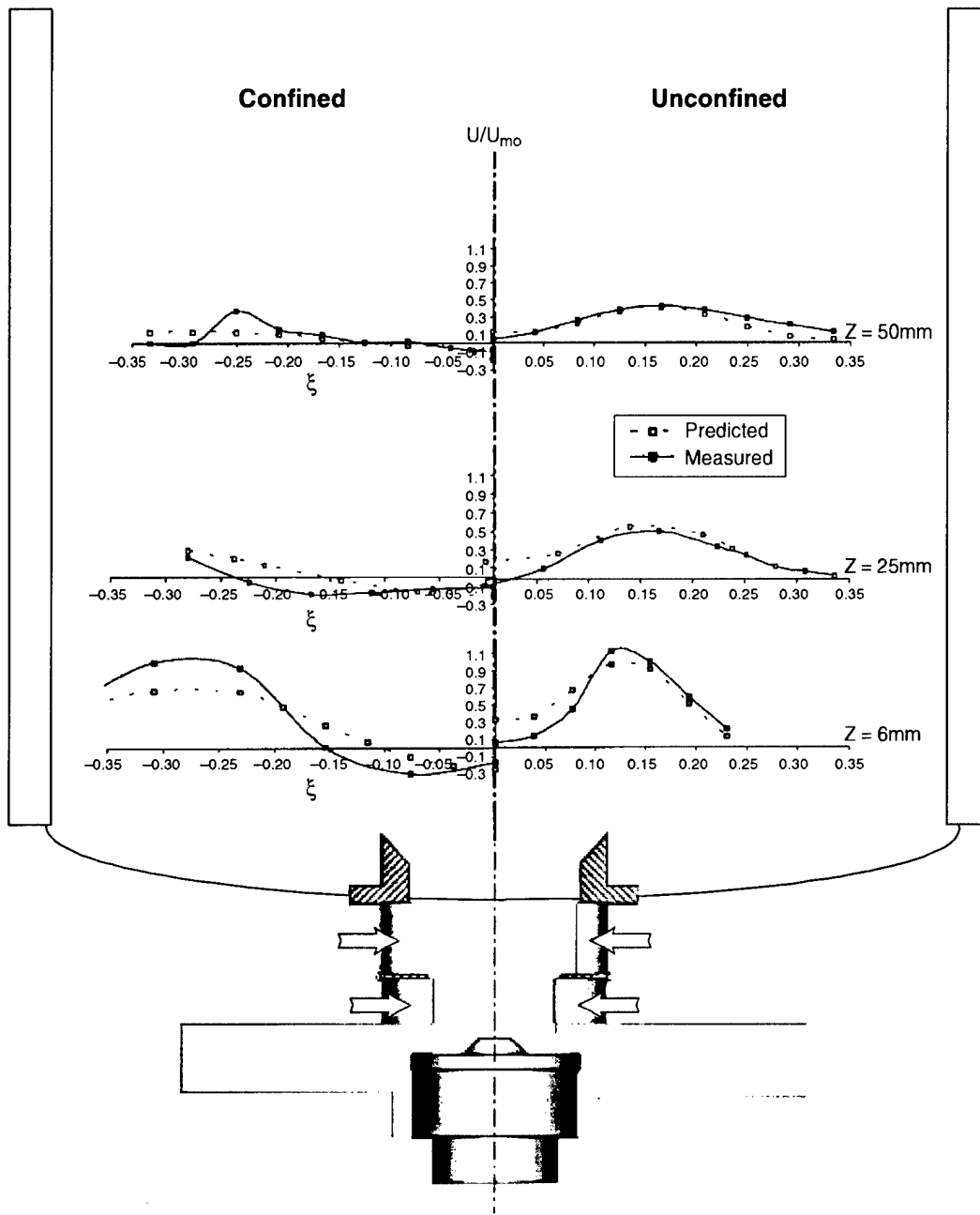


Figure 21. Prediction vs. Measured Axial Velocity Profile for Primary Swirler 35°, Secondary Swirler 65°, Co-Swirl Without Venturi.

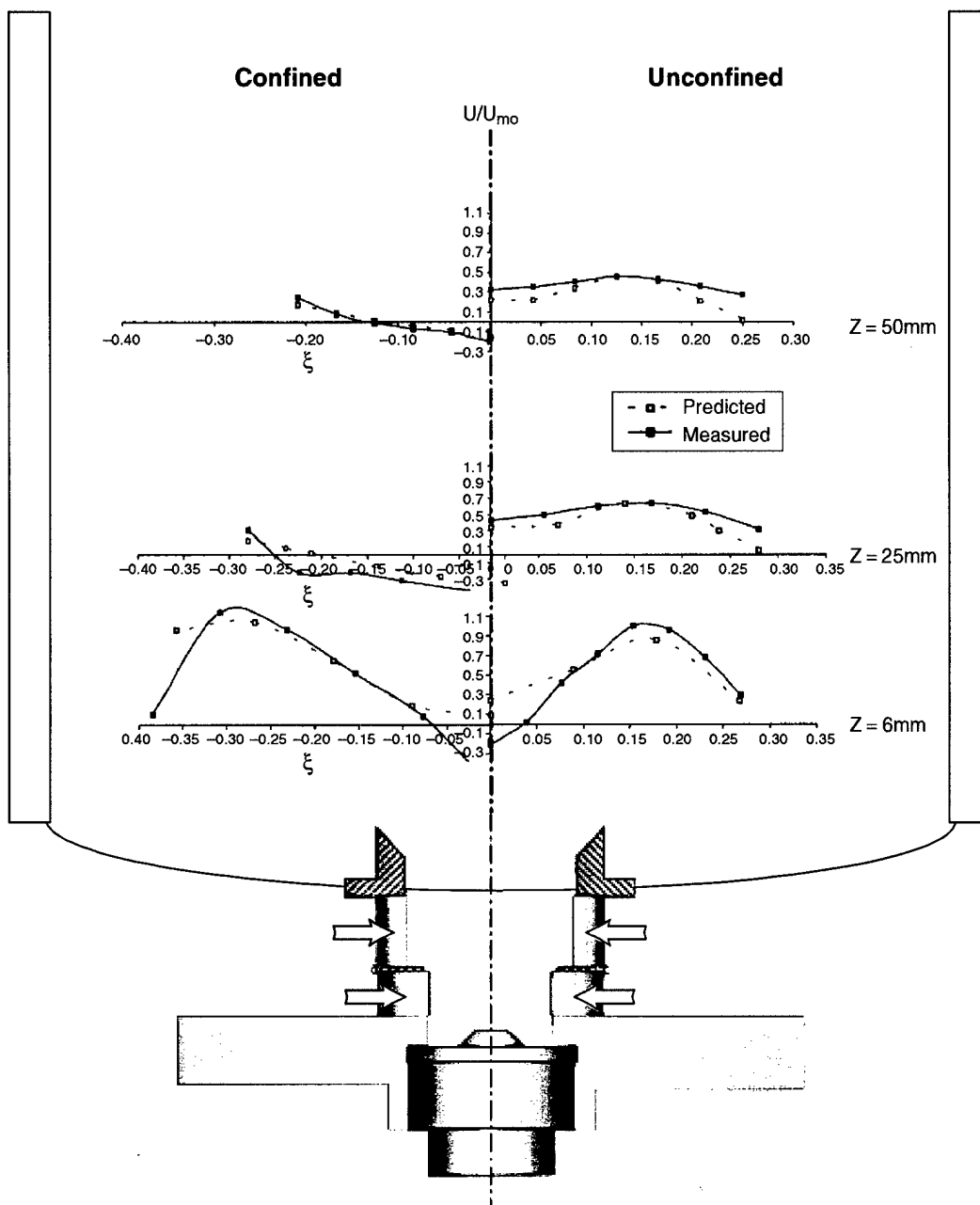


Figure 22. Prediction vs. Measured Axial Velocity Profile for Primary Swirler 35°, Secondary Swirler 65°, Counter-Swirl Without Venturi.

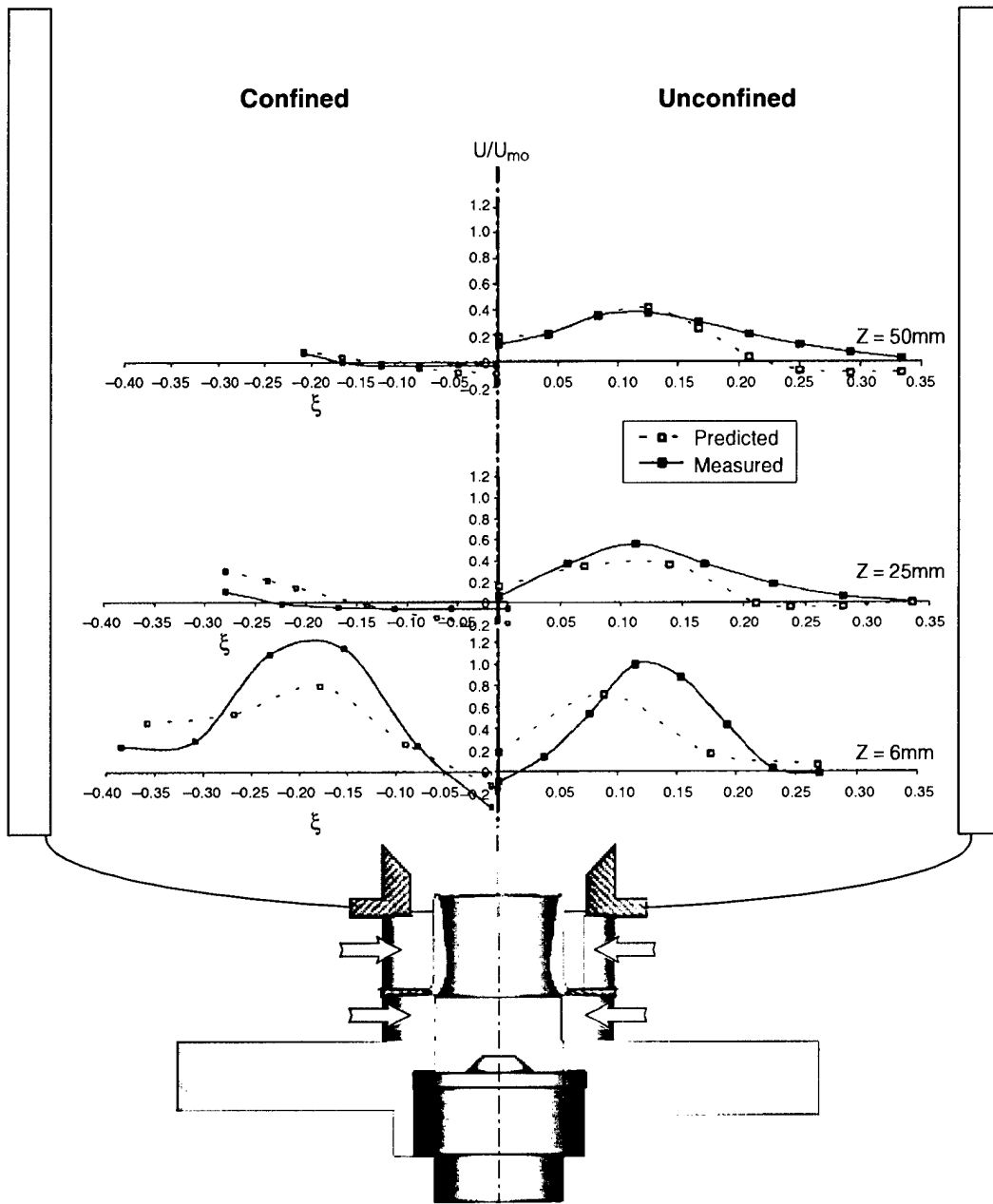


Figure 23. Prediction vs. Measured Axial Velocity Profile for Primary Swirler 35°, Secondary Swirler 65°, Co-Swirl With Venturi.

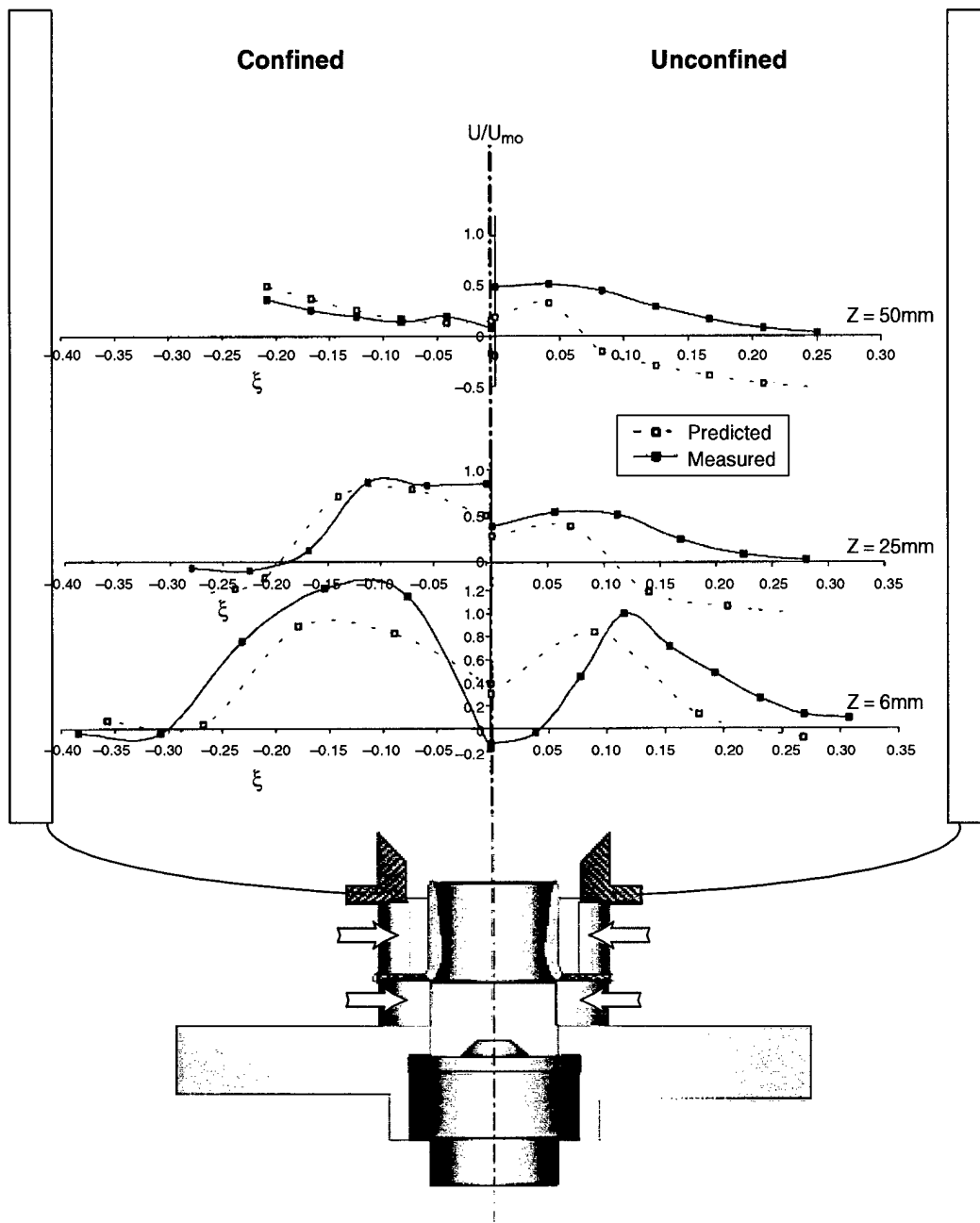


Figure 24. Prediction vs. Measured Axial Velocity Profile for Primary Swirler 35°, Secondary Swirler 65°, Counter-Swirl With Venturi.

temperatures. Based on the principle of multivariate experiments main effects of mixer parameters on LBO were identified. Specifically, the Venturi and Swirl Sense (Co- vs. Counter-Swirl) were parameters affecting LBO at lower air inlet temperatures (294 and 366K). The Venturi and Counter-Swirl enhance the atomization and mixing process and, as a result, improve stability. At a higher inlet air temperature (477K) the Secondary Swirl Vane angle also plays a role in determining LBO – with larger angles (75°) generating better stability. The hardware configuration with the best LBO performance was identified (45° Primary Swirler, 55° Secondary Swirler, Counter-Swirl With Venturi). This configuration exhibited a uniform reaction throughout the primary zone.

The correlation used utilizes an expression derived for fuel-air ratio at Lean Blowout as a function of the air loading parameter. For homogeneous mixtures, it has been shown that at Lean Blowout fuel-air ratio depends on the inlet air velocity, pressure, and temperature, and on the size of the combustion zone. The relationship is of the form:

$$q_{LBO} \alpha \left| \frac{m_A}{VP_3^n \exp(T_3/b)} \right|^x \quad \text{Equation 5}$$

where n is the reaction order, and x is a constant determined experimentally. Equation 5 was used by Lefebvre to correlate measured values of weak extinction equivalence ratio for propane-air flames stabilized on bluff-body flameholders, using experimental data to determine optimum values of n , b and x .

Equation 5 may also be used to predict the Lean Blowout limits of combustion chambers supplied with heterogeneous fuel-air mixtures, provided that the rate of fuel evaporation is sufficiently high to ensure that all the fuel is fully vaporized within the primary combustion zone. If the fuel does not fully burn vaporize, then the effective fuel-air ratio will be lower than the nominal value. However, if the fraction of fuel that is vaporized is known, or can be calculated, it can be combined with Equation 5 to yield fuel-air ratio at Lean Blowout, i.e.,

$$q_{LBO_{\text{heterogeneous}}} = q_{LBO_{\text{homogeneous}}} \cdot f_f^{-1} \quad \text{Equation 6}$$

where f_f is the fraction of fuel that is vaporized within the primary combustion zone. From analysis of the factors governing the rate of evaporation of a fuel spray (Ballal and Lefebvre, 1980), it was found that:

$$f_f = 8(\rho_g / \rho_f)(k / c_p)_g \ln(1 + B)(V_{pz} / m_{pz} D_o^2)(1 + 0.22 \text{Re}_{D_o}^{0.5}) \quad \text{Equation 7}$$

Substituting the value of an effective evaporation constant,

$$\lambda_{\text{eff}} = \frac{8(k / c_p)_g \ln(1 + B)(1 + 0.22 \text{Re}_{D_o}^{0.5})}{\rho_f} \quad \text{Equation 8}$$

$$f_f = \frac{8\rho_g V_{pz} \lambda_{\text{eff}}}{f_{pz} m_A D_o^2} \quad \text{Equation 9}$$

An additional term incorporated into the expression for Lean Blowout fuel–air ratio is the heating value of the fuel. Fuels with high heat content should be capable of burning down to weaker mixture strengths than fuels having a lower heat content. With this modification and substitution of

$q_{\text{homogeneous}}$ from Equation 5 and f_f from Equation 9 into Equation 6 gives:

$$q_{LBO} \propto \left[\frac{f_{PZ}}{V_{PZ}^{(1+x)}} \right] \left[\frac{m_A^{(1+x)}}{P_3^{(1+nx)} \exp(xT_3/b)} \right] \left[\frac{D_o^2}{\lambda_{\text{eff}} LCV} \right] \quad \text{Equation 10}$$

The first term on the right hand side of Equation 10 is a function of combustor design. The second term represents the combustor operating condition and the third terms embodies the relevant fuel–dependent properties.

Not enough experimental data exists to accurately determine the exponents $(1+x)$ and n . However, to simplify the expression the order of V_{PZ} and m_A is the same with the order of the pressure term somewhat higher based on the reaction order, n . Ballal and Lefebvre have found that the pressure exponent is about 30% larger than that of the air mass flow rate. Also, the temperature dependence was found to correspond to the relationship:

$$q_{LBO} \propto \exp-(T_3/300) \quad \text{Equation 11}$$

This observation will be modified, however, in the analysis for swirl–stabilized reaction. Thus the simplest form in which Equation 10 can be expressed is:

$$q_{LBO} = \left(\frac{A'' f_{PZ}}{V_{PZ}} \right) \left(\frac{m_A}{P_3^{1.3} \exp(T_3/300)} \right) \left(\frac{D_o^2}{\lambda_{\text{eff}} LCV} \right) \quad \text{Equation 12}$$

where Lefebvre defined A'' as a constant whose value depends on the geometry and mixing characteristics of the combustion zone and was arrived at experimentally.

There are some drawbacks to this model posed by Lefebvre that need improvements prior to developing a model that expresses LBO performance for the liquid fuel–fired swirl–stabilized reaction. Mainly, 1) The value of the constant, A'' , does not allude to any mixer parameter(s) and its role in determining LBO is unknown; 2) Assigning appropriate values of V_{PZ} to all the combustor configurations tested by Lefebvre was challenging. To surmount this problem, as a first step approach, it is decided to substitute the geometrical volume, V_c , which is more easily attainable, into Equation 12 instead of V_{PZ} ; 3) Values of f_{PZ} , the fraction of the total combustor airflow entering the primary zone, is difficult to attain for various combustor geometry. For the quartz combustor studies f_{PZ} is assigned the value of unity since no jets interact with the main dome flow. This will increase the accuracy of the model; 4) A more serious drawback to Equation 12 is that it demands an accurate knowledge of mean drop size D_o over the entire range of operating conditions. In the study by Ballal and Lefebvre, drop sizes were not measured nor estimated with sufficient accuracy. In order to attain a better accuracy on the model, a first step approach is to use a representative Sauter Mean Diameter (SMD) from correlations for airblast atomizers. However, a representative SMD is not the only solution for an expression for a initial drop size. Within the stabilizing region in the combustor dome an SMD distribution may be found which will decrease the accuracy of the model.

However, as a first approach the correlation for SMD is a marked improvement to the LBO model first developed by Ballal and Lefebvre. Future in-situ measurements within the stabilizing region will provide more insight into a representative drop diameter that is more conducive to stability analysis.

The model used to describe and predict LBO will be modified and will utilize a new approach in determining the direct role of specific combustor mixer geometry parameters on LBO. The strength of this approach lies in the use of a statistical tool to both design the experiment and to determine the role of mixer parameters on LBO. An Analysis of Variance will be conducted to understand the importance of the underlying parameters affecting weak extinction of swirl-stabilized reactions.

The model used to predict LBO was based on measured values of LBO fuel-air ratio inside an 80mm diameter combustor. Lean Blowout was induced by attaining a steady-state operation at $\Phi=0.8$ until the combustor components reached a steady-state temperature. By gradually reducing the fuel loading until the reaction became extinct the fuel-air ratio at that point was recorded. Images of the reaction near extinction were also taken using a Redlake high speed Motionscope CCD camera. A sample of 50 still images were collected and averaged to show reaction structure near LBO.

For the purpose of simplifying the final expression for the LBO model as a function of mixer geometry coded values of the ranges of hardware variations are used. Table 10 also illustrates coded values assigned to each hardware parameter.

Sauter Mean Diameter (SMD) Correlation

To further improve the model for predicting LBO, a more accurate representative initial droplet diameter will be sought by using a correlation for SMD developed by El Shanawany and Lefebvre (Reference 9) for an airblast atomizer:

$$\frac{SMD}{D_h} = \left(1 + \frac{m_L}{m_A} \right) \left(0.33 \left(\frac{\sigma}{\rho_A U_A^2 D_p} \right)^{0.6} \left(\frac{\rho_L}{\rho_A} \right)^{0.1} + 0.068 \left(\frac{\mu_L^2}{\sigma \rho_L D_p} \right)^{0.5} \right) \quad \text{Equation 13}$$

This correlation is a function of both air and liquid fuel fluid properties and the operating condition and geometrical configuration of the injector. Incorporating these parameters from the experiments conducted at or near Lean Blowout, values of SMD for each experiment were obtained. The range of SMD values calculated were from 39 – 54 μm . Assumptions made were Jet-A fuel properties are similar to Kerosene. Gas properties were taken for air at 1400 K. And turbulent fluctuation velocity, u' , used in calculating Reynolds number is ten percent of mean velocity determined from continuity equation and geometrical area of the injector used.

The calculated SMD value is substituted for D_o into Equation 12 as the initial drop diameter of the spray. Though this SMD value may not be the representative diameter to represent the evaporation characteristics conducive to promoting stability, it is a marked improvement to the model used by Lefebvre for heterogeneous mixtures.

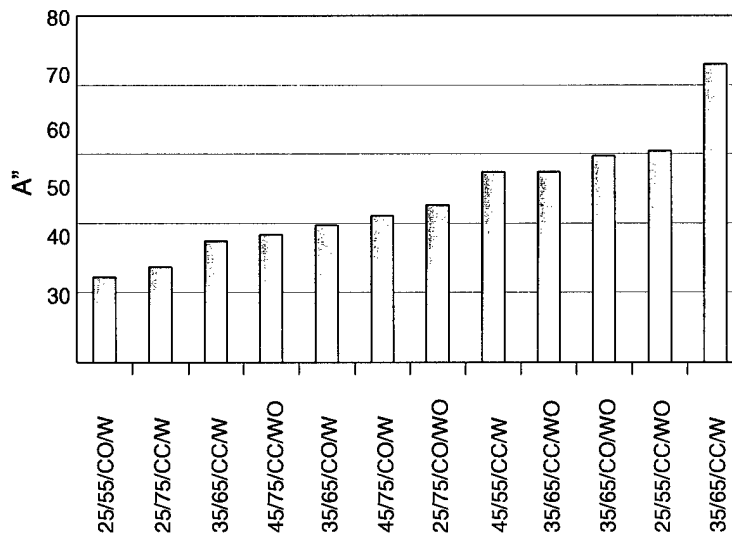
Mixer Coefficient, A''

In Equation 12 the value of A'' coefficient was varied until the calculated values of q_{LBO} match the measured values of q_{LBO} . The value of A'' that provided the best fit of these two values are tabulated in Table 10.

Table 10. Half-Fraction Two-Level Test Matrix of Experiments.

<i>Run</i>	<i>Primary Swirl Angle</i>	<i>Secondary Swirl Angle</i>	<i>Swirl Sense</i>	<i>Venturi</i>	<i>Measured A''</i>
1	25	75	CO	W/O	53.6
2	25	75	CC	W	42.7
3	35	65	CO	W/O	64.5
4	25	55	CC	W/O	56.4
5	35	65	CC	W	56.1
6	45	55	CO	W/O	74.0
7	45	75	CO	W	55.3
8	35	65	CC	W/O	77.7
9	25	55	CO	W	46.4
10	45	75	CC	W/O	44.2
11	35	65	CO	W	53.3
12	45	55	CC	W	56.4
<i>Coded Value</i>	<i>Primary Swirl Angle</i>	<i>Secondary Swirl Angle</i>	<i>Swirl Sense</i>	<i>Venturi</i>	
Lo-Value	-1	-1	CO:-1	W/=-1	
Mid-Value	0	0	CC:+1	W/O=+1	
Hi-Value	1	1			

The range of values of A'' calculated was between 42–78. Since this coefficient is a function of mixing characteristics of the various hardware configurations, values of A'' between hardware configurations which are similar may be leading to a mixing characteristic which may be similar in nature as it pertains to stability. Figure 25 shows the various groups of A'' values in the experiments

Figure 25. Range of A'' Values for Various Hardware Configurations.

conducted. The lowest value of A'' can be attributed to better mixer performance which will lead to lower Lean Blowout fuel–air ratios (q_{LBO}) (increase in stability). Figure 25 alludes to one group of low A'' values. Two of the lower A'' values are found with Counter–Swirl configurations with Venturi. The higher values of A'' are found with cases Without Venturi. Referring to Equation 12 the lower the value of A'' result in lower LBO fuel–air ratio (better stability).

A much more detailed analysis was conducted on the hardware parameters which affect the mixing coefficient, A'' . Values of A'' determined to best match the calculated q_{LBO} with the measured q_{LBO} were inputted into the test matrix response for all 12 experiments to determine the effect of mixer parameter(s) on A'' .

Following the ANOVA the statistical design tool used lists the least squares (a method by which data is fitted to a mathematical model) coefficients for the model with a test of their significance. It is outside the scope of this study to describe the detail of the model development; however, the results shown below are of the model used to predict the value of the mixing coefficient, A'' .

$$A'' = \alpha_1 + \alpha_2(A) + \alpha_3(B) + \alpha_4(C) + \alpha_5(D) + \alpha_6(AB) + \alpha_7(AC) + \alpha_8(AD) \quad \text{Equation 14}$$

The value of α_n ($n=1, \dots, 8$) is given as:

$$\alpha_1 = 53.61; \alpha_2 = 3.85; \alpha_3 = -4.68; \alpha_4 = -1.13; \alpha_5 = 5.00; \alpha_6 = -3.06; \alpha_7 = -3.47; \alpha_8 = -1.82$$

The coded values of A (primary swirl vane angle), B (secondary swirl vane angle), C (swirl sense) and D (venturi) are used in Equation 14 and are listed in Table 10.

Figure 26 illustrates how well the ANOVA model predicted the A'' values as compared to the values listed in Table 10. As can be seen, the model does a good prediction of the A'' values for almost all hardware configurations. This supports the use of the expression for the mixing coefficient (Equation 14) in predicting the LBO fuel–air ratio.

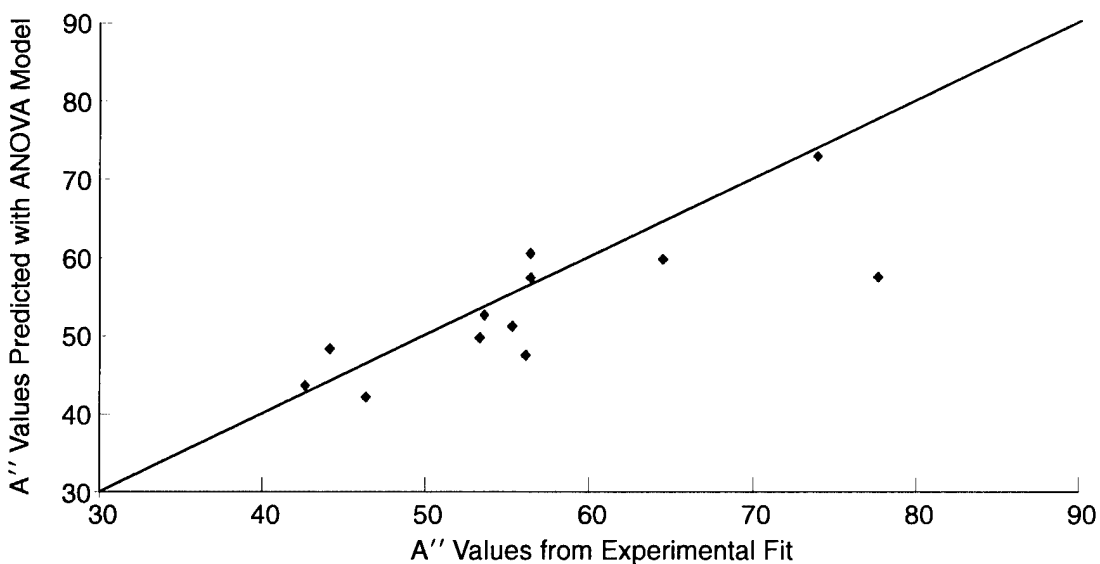


Figure 26. Comparison of Predicted Values of A'' (ANOVA Model) and the A'' Values Determined from Experimental Fit of Q_{LBO} Data (Table 10).

Model Verification

With an expression derived for A'' as a function of mixer configuration, Equation 12 has been transformed into one which relates LBO performance to specific mixer configuration, operating condition and fuel properties.

To predict the Lean Blowout fuel-air ratio, q_{LBO} , modifications were made to Equation 12 to reflect the LBO performance for this particular radial mixer. Mainly the temperature dependence term was changed according to:

$$q_{LBO} \propto \frac{B''}{\exp(T_3 / 600)}; \text{ where } B'' = 7 \times 10^{-6} T^2 - 3.6 \times 10^{-3} T + 1.424 \quad \text{Equation 15}$$

This dependence on temperature differs from the one suggested by Lefebvre (Equation 11). The new model for predicting q_{LBO} then becomes,

$$q_{LBO} = \left[\frac{A'' f_{PZ}}{Vc} \right] \left[\frac{m}{P_3^{1.3} \exp(T_3 / 600)} \right] \left[\frac{D_o^2}{\lambda_{eff} LCV} \right] B'' \quad \text{Equation 16}$$

with the expression for A'' given in Equation 14 and B'' given in Equation 15. The predicted q_{LBO} is then calculated and compared to the measured values of q_{LBO} in the experiments. Results of the model validity is illustrated in Figure 27. The agreement between the predicted and measured value of LBO is satisfactory. The average difference between the measured and predicted value of q_{LBO} is $\pm 9.2\%$.

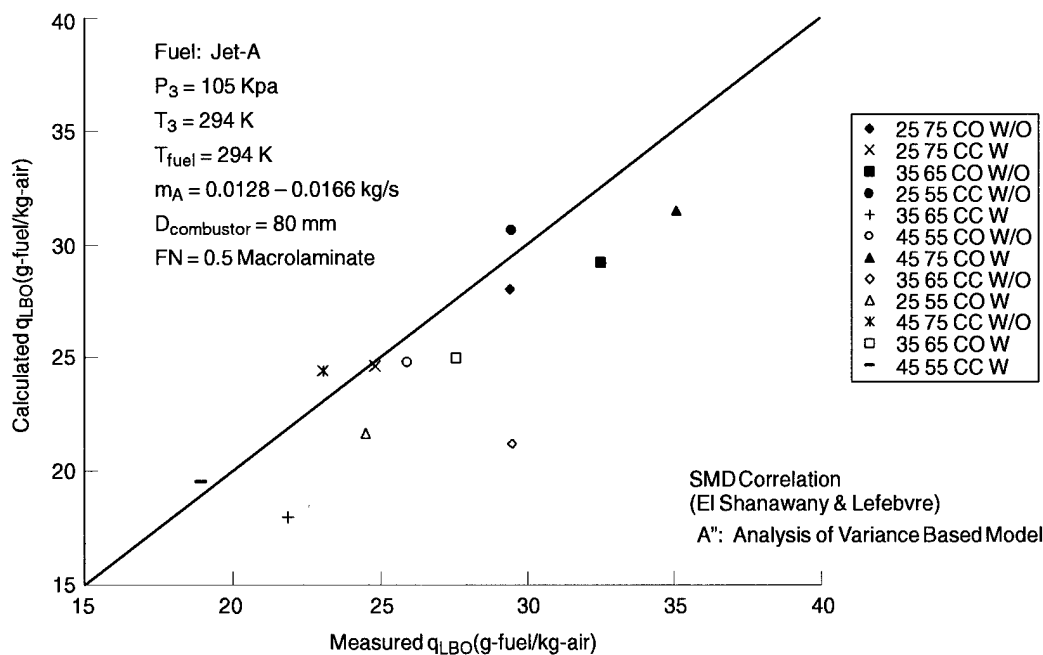


Figure 27. Comparison of Measured and Predicted Values of q_{LBO} for all 12 Mixer Configurations at 294K Inlet Air Temperature.

The expression for q_{LBO} shows that with the improvements made to the model by: 1) incorporating an SMD to represent the initial droplet size diameter, 2) relating the mixer coefficient (A'') to specific mixer configuration and 3) modifying the temperature dependence of LBO fuel-air ratio, the new model provided a good agreement to the measured value of LBO.

As a second step to verify the model the expression in Equation 16 can be used to predict LBO fuel-air ratio for each hardware configuration tested at other operating conditions. This verification of the model was done and described in the following section.

Temperature Effects

Lean Blowout fuel-air ratio was also measured at two different inlet air temperatures, $T_3 = 366K$ and $T_3 = 477K$, to verify if the LBO model can accurately predict LBO performance at other operating conditions. Using the same expressions of A'' as in the base model the calculated q_{LBO} were compared to the measured values in the experiments. Figures 28 and 29 illustrate the results for $T_3=366K$ and $T_3=477K$, respectively. The agreement here between the measured and predicted values is also satisfactory with the average difference between the measured and predicted value of q_{LBO} at 366K being $\pm 13.5\%$ and at 477K the average being $\pm 14.0\%$. Here the model has shown to do an adequate calculation of predicting the LBO performance at other operating conditions as well.

Though this model of LBO performance for various mixer configurations is useful as a design tool to predict performance for all the possible combinations of mixer configurations (128 total) a more detailed analysis, based on statistical analysis is needed to determine main effects of specific mixer parameter, or interaction between parameters on LBO performance.

Main Effects

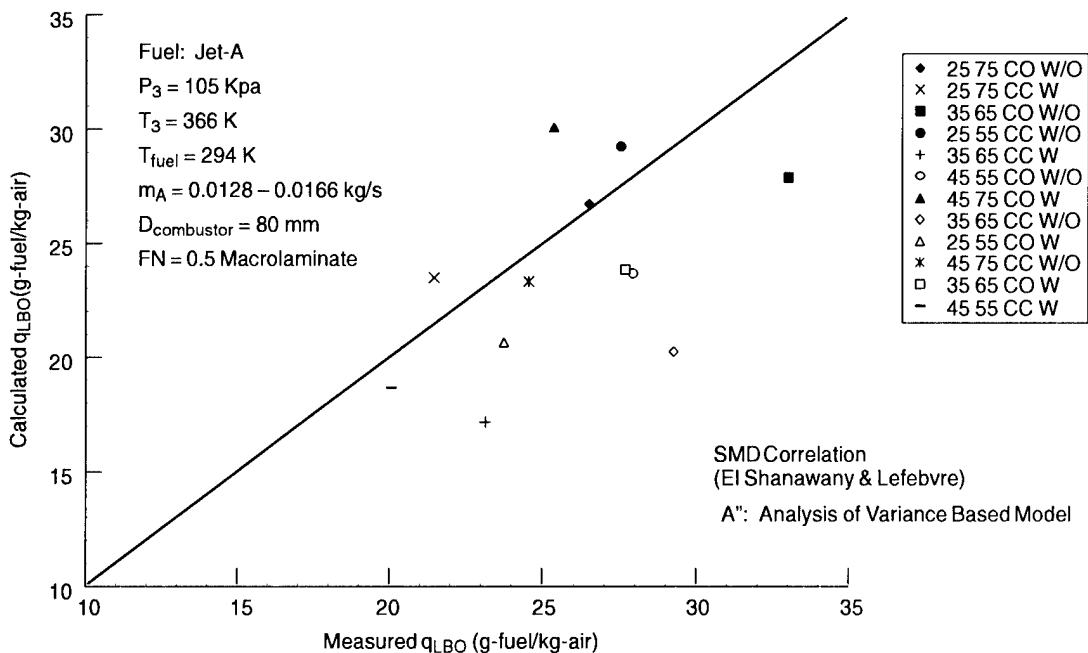


Figure 28. Comparison of Measured and Predicted Values of q_{LBO} for all 12 Mixer Configurations at 366K Inlet Air Temperature.

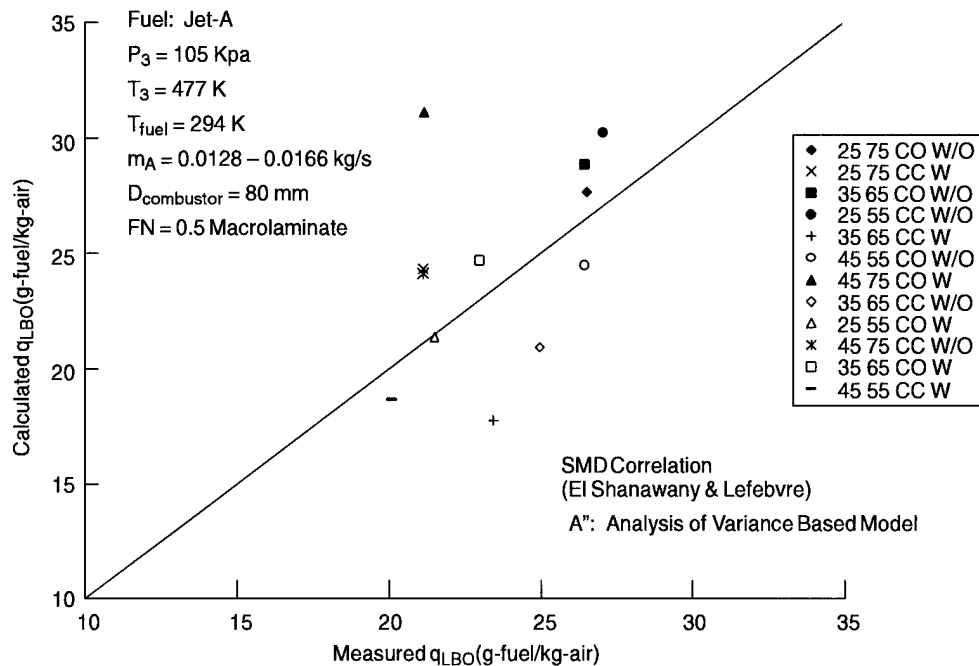


Figure 29. Comparison of Measured and Predicted Values of O_{LBO} for all 12 Mixer Configurations at 294K Inlet Air Temperature.

To isolate the effect a mixer parameter (or a combination of parameters) has on a LBO equivalence ratio (Φ) the same approach is taken as when main effects for A'' were calculated.

Through the *Central Limit Theorem*, it is expected that as a sample size increases, the distribution of averages becomes normal. Hence, if the effects on a response by hardware parameters (or combinations of parameters) are truly random, their distribution will be normal. To explore any deviation from this, a probability plot can be generated for the effects on responses (Reference 10). Figure 30 shows the normal probability plot of the effects calculated for the LBO at three different inlet air temperatures (294K, 366K and 477K). As seen in Figure 30a the effect caused by the Swirl Sense (C) and Venturi (D), at the baseline operating condition of 294K inlet air temperature, deviate from a normal distribution (hence, its effect is not random). The deviation signifies that Swirl Sense and Venturi play a role in determining Lean Blowout in the configurations tested. Figure 30b identifies the same parameters showing a stronger effect on LBO at 366K.

At higher inlet air temperature (477K) Figure 30c shows that main effects on LBO are Venturi (D), Secondary Swirl Vane Angle (B) and an interaction between the Primary Swirl Vane Angle and Swirl Sense (AC). These parameters allude to the critical role mixer geometry plays in dictating LBO performance. The effects of mixer configuration become more distinct as inlet air temperature increases and more fuel is vaporized and readily available to mix and react.

Figure 31a shows the reaction structure for Co-Swirl Without Venturi configuration and Figure 31b shows one for Counter-Swirl With Venturi for a 25° Primary Swirl and 75° Secondary Swirl.

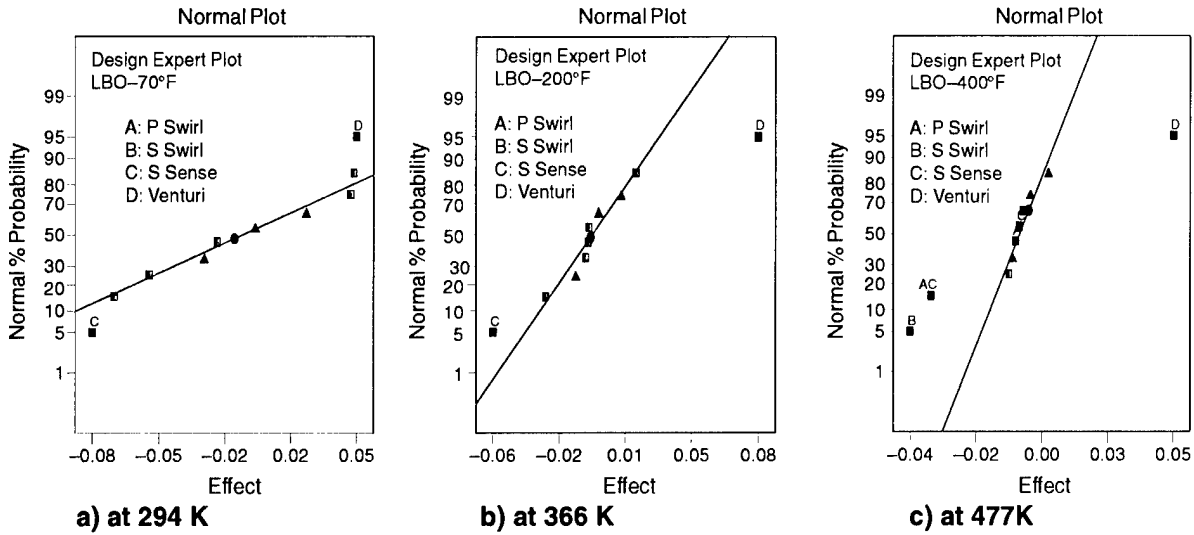


Figure 30. Main Effects Normal Probability Plot for LBO.

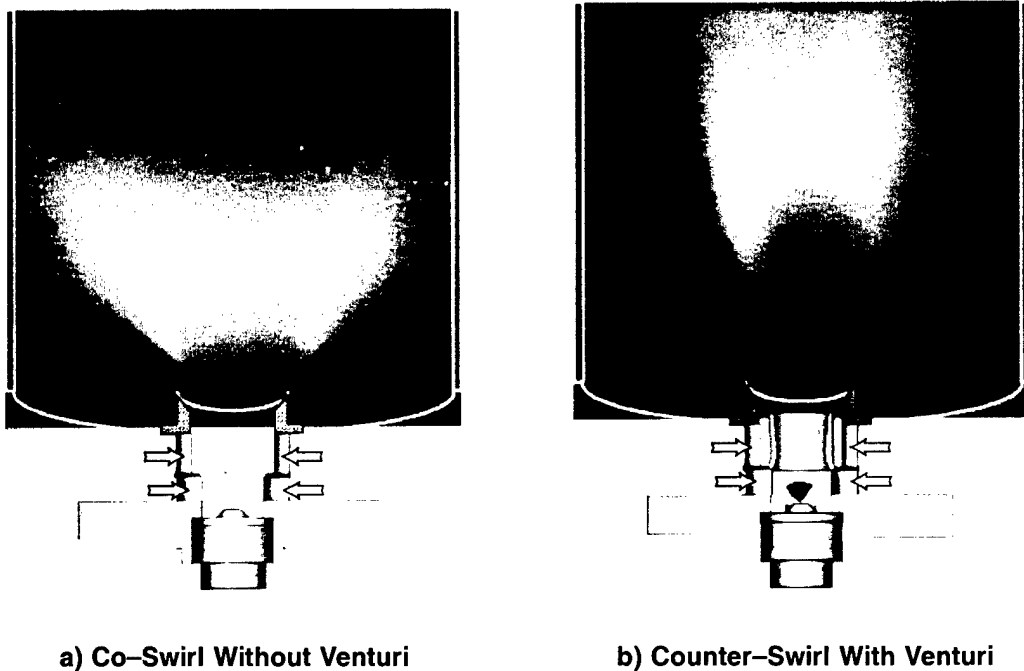


Figure 31. Time-Averaged Image (50 Images) of Reaction Near Lean Blowout at 477K Inlet Air Temperature for 25° Primary Swirler and 75° Secondary Swirler.

Figure 32 illustrates the *average* effect the Venturi and Swirl Sense have at 366K. The average effect of the Secondary Swirler and the interaction between the Primary Swirler and Swirl Sense at 477K are also shown. At 366K Co-Swirl reduces stability and Counter-Swirl increases stability marked by the higher and lower LBO observed, respectively. Counter-Swirl imposes a great velocity gradient near the liquid fuel surface. Hence, greater shearing and atomization occurs which improves the overall potential for a reaction to be sustained.

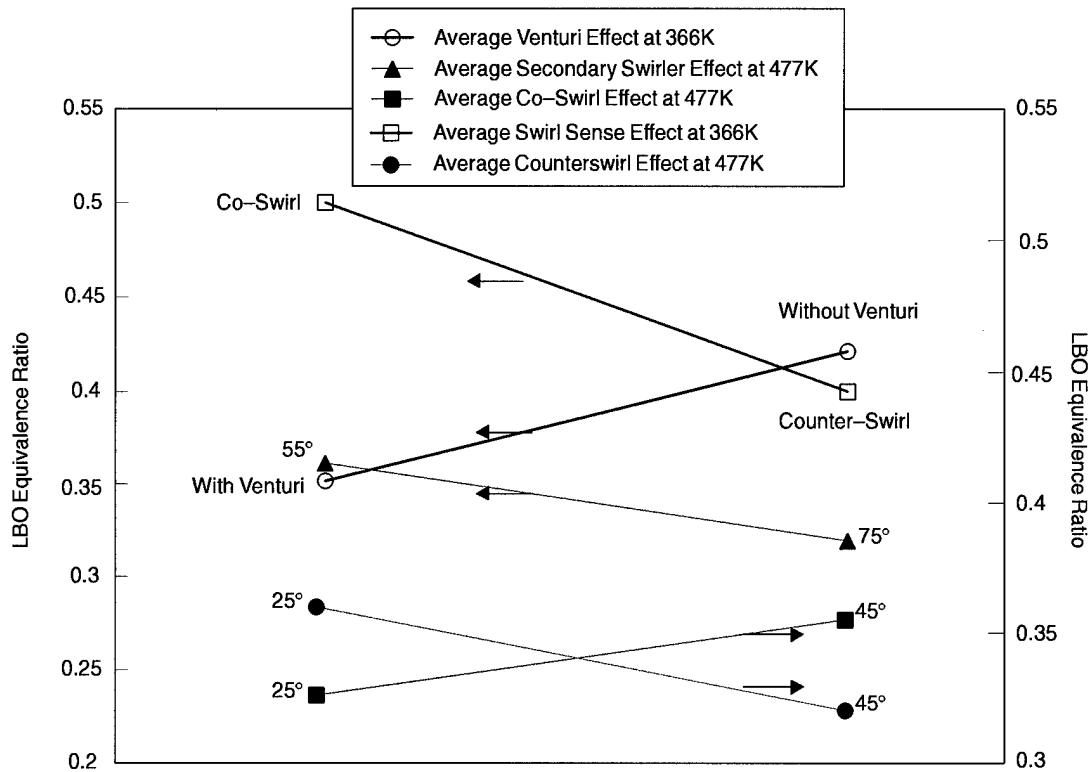


Figure 32. Average Effects of Mixer Parameters and Interactions on LBO at 366K and 477K.

The presence of Venturi increases stability (low LBO Φ) by prefilming the fuel surface to enhance atomization and mixing. Also the Venturi acts a reaction lifting mechanism preventing direct exposure of the mixer components to the reaction front. This is evident in the sample image of the reaction in Figure 31b.

At 477K the Venturi was found to have the same effect on LBO. In addition, the interaction between Primary Swirler and Swirl Sense (AC) shows that with a 25° Primary Swirler, Co-Swirl Swirl Sense, as opposed to Counter-Swirl, had better stability. However, with a 45° Primary Swirler Counter-Swirl achieved the better stability (lower LBO Φ) (Figure 32).

At 477K the Secondary Swirler was also shown to affect LBO. Mainly, with a 75° Secondary Swirler better stability was achieved. This could be due to the fact that the higher tangential velocity created by the 75° swirler generates greater shear on the liquid fuel surface and improves mixing. The higher swirl strength is also expected to create a stronger recirculation zone to ignite the fresh fuel-air mixture – hence enhancing stability.

Figures 33a and 33b show the most stable reaction structure with the configuration: 45° Primary Swirler and 55° Secondary Swirler Counter-Swirl With Venturi for 294K and 477K, respectively. It is observed that the reaction is uniform throughout the primary zone and becomes much less luminous as inlet air temperature is increased. The lowest LBO Φ achieved was with this configuration.

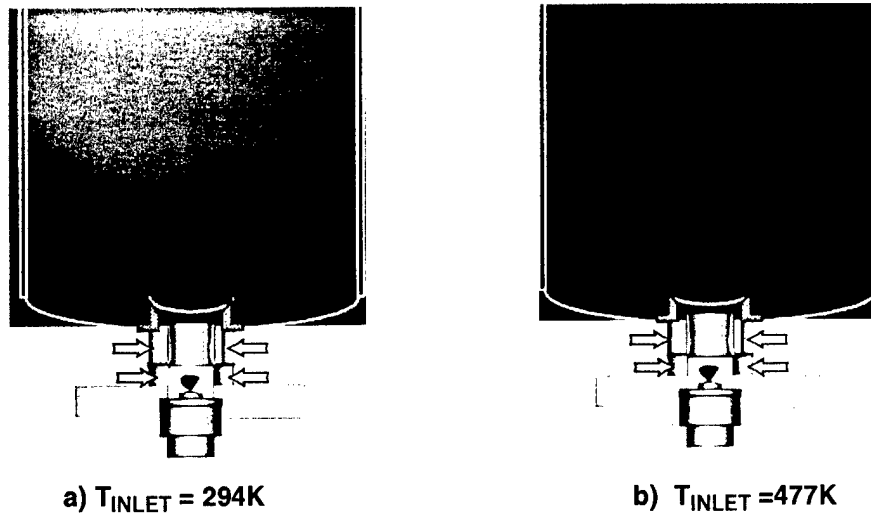


Figure 33. Time-Averaged Image (50 Images) of Reaction Near Lean Blowout at 294K Inlet Air Temperature for Optimum LBO Mixer Configuration (45° Primary Swirler and 55° Secondary Swirler, Counter-Swirl With Venturi).

4.7.3 CFD Model Refinements

Once semi-analytical models have been developed, they can be utilized in the existing CFD calculations to refine the predictions. To this end, FLUENT has evolved and a refined version focusing upon non-structured strategies is now available with improved models for spray behavior and turbulence.

5.0 References

- 1 Akamatsu, F., Wakabayashi, T., Tsushima, S., Katsuki, M., Mizutani, Y., Ikeda, Y., Kawahara, N. and Nakajima, Y. (1998). *Development of a Light Collecting Probe with High Spatial Resolution and its Performance for the Detection of Flame Chemiluminescence*, presented as a Work in Progress poster, 27th Symposium (International) on Combustion.
- 2 McDonell, V.G., Lee, S.W., and Samuelsen, G.S., *Interpretation of Spray Behavior in Complex Aerodynamic Flows Using Phase Doppler Interferometry and Planar Liquid Laser Induced Fluorescence*, Proceedings of The International Society for Optical Engineering (SPIE), Optical Techniques in Fluid, Thermal and Combustion Flows, Vol. 2546, pp. 530-539, 1995.
- 3 Dobbins, R.A. and Megaridis, C.M., *Morphology of Flame-Generated Soot as Determined by Thermophoretic Sampling*, Langmuir, 1987. 3:254-259.
- 4 Fang, T.C., Megaridis, C.M., Sowa, W.A. and Samuelsen, G.S., *Soot Morphology in a Liquid-Fueled Swirl-Stabilized Combustor*. Combustion and Flame, 1998 Vol.112, pp.312-328.
- 5 Koylu, U.O., McEnally, C.S., Rosner, D.E., Pfefferle, L.D. *Simultaneous Measurements of Soot Volume Fraction and Particle Size / Microstructure in Flames using a Thermophoretic Sampling Technique*, Combustion and Flame 1997 V.110 494-507.
- 6 Ateshkadi, A., McDonell, V. G., and Samuelsen, G. S. (1997). *The Effect of Gas Turbine Combustor Dome Geometry on fuel Spray Distribution*. Paper 97F-106, presented at the Fall Meeting of the Western States Section of the Combustion Institute, Diamond Bar, CA.
- 7 Arellano, L., Ateshkadi, A., Fukushima, H., McDonell, V.G., and Samuelsen, G.S. (1997). *Multivariate Experiments to Assess the Effect of Combustor Dome Geometry on Fuel Distribution and Stability*, presented at 42nd ASME IGTI Meeting, Orlando, FL.
- 8 Rizk, N. K. and Mongia, H. C., 1991, *Model for Airblast Atomization*, Journal of Propulsion and Power, Vol.7, Number 3, pp. 305-311.
- 9 El Shanawany, M.S.M.R., and Lefebvre, A.H. *Airblast Atomization - The Effect of Linear Scale on Mean Drop Size*, Journal of Energy, Vol.4 No.4, pp. 184-189, 1983.
- 10 Box, G. E. P., Hunter, W. G., and Hunter, J. S., 1978, *Statistics for Experimenters: An Introduction to Design, Data Analysis, and Model Building*, New York, Wiley & Sons.

6.0 Relevant Papers and Presentations

6.1 Relevant Papers

Eight papers were produced during the program:

Ateshkadi, A., McDonell, V. G., & Samuelsen, G. S. (1997). *The Effect of Gas Turbine Combustor Dome Geometry on Fuel Spray Distribution*. Paper 97F-106, presented at the Fall Meeting of the Western States Section of the Combustion Institute, Diamond Bar, CA.

L. Arellano, A. Ateshkadi, H. Fukushima, V.G. McDonell, and G.S. Samuelsen (1997). *Multivariate Experiments to Assess the Effect of Combustor Dome Geometry on Fuel Distribution and Stability*, presented at 42nd ASME IGTI Meeting, Orlando, FL.

L. Arellano, A. Ateshkadi, H. Fukushima, V.G. McDonell, and G.S. Samuelsen (1997). *Multivariate Experiments to Assess the Effect of Combustor Dome Geometry on Fuel Distribution and Stability*, submitted to *ASME J. Gas Turbines and Power*.

Ateshkadi, A., McDonell, V. G., & Samuelsen, G. S. (1998a). *Effect of Hardware Geometry on Gas and Drop Behavior in a Radial Mixer Spray*. Accepted for publication, *27th Symposium (International) on Combustion*, Boulder, CO:

Ateshkadi, A., McDonell, V. G., & Samuelsen, G. S. (1998b). *Effect of Mixer Geometry on Fuel Spray Distribution, Emissions and Stability*. Paper 98-0247, presented at *36th Aerospace Sciences Meeting*, AIAA 98-0247 Reno, NV.

Ateshkadi, A., McDonell, V. G., & Samuelsen, G. S. (1998c). *Role of Combustor Dome Geometry on Spray Structure and Combustion Performance*. Presented at 11th ILASS-Americas Conference, Sacramento, CA.

Ateshkadi, A., V. G. McDonell, and G. S. Samuelsen, *Lean Blowout Model for a Liquid Fuel-Fired Swirl-Stabilized Combustor*. Submitted for Publication. *Combustion and Flame*.

L. Arellano, A. Ateshkadi, H. Fukushima, V.G. McDonell, and G.S. Samuelsen (1997). *Effect of Mixer Geometry on Spray Distribution: A Multivariate Experiment Approach*, presented at 10th ILASS-Americas Conference, Ottawa, Ontario, Canada.

In addition, the program generated four theses and one dissertation:

Arellano, L., *Multivariate Experiments to Assess the Effect of Combustor Dome Geometry on Fuel Distribution and Stability*, M.S. Thesis, 1999

Ateshkadi, A., *The Effect of Fuel/Air Mixer Design Parameters on the Continuous and Discrete Phase Structure in the Downstream Reaction-Stabilizing Region*, Ph.D. Dissertation, 1999.

Dudik, M.J.: To be completed Spring 2001.

Torres, J.: To be completed Fall 2001.

Williams, J.M., *Characterization of Soot and Gaseous Emissions from a Practical Combustor with Variable Operating Configurations*, M.S. Thesis, 1998

6.2 Miscellaneous Papers

Arellano, L., Ateshkadi, A., Fukushima, H., McDonell, V.G., and Samuelsen, G.S., (1997). *Multivariate Experiments to Assess the Effect of Combustor Dome Geometry on Fuel Distribution and Stability*, submitted to *ASME J. Gas Turbines and Power*.

Addendum B

Combustion Dynamics Subtask

**AFOSR Focused Research Initiative:
Low Emissions, High Performance Gas Turbine Engines**

**Prepared by
Robert J. Santoro and Domenic A. Santavicca
Propulsion Engineering Research Center
and
Department of Mechanical and Nuclear Engineering
The Pennsylvania State University
University Park, PA 16802**

**Submitted to
General Electric Aircraft Engines
Cincinnati, OH**

October 1999

Table of Contents

	<u>Page</u>
1.0 Summary	1
2.0 Objectives	2
3.0 Approach	4
3.1 1X Dual-Annular Rotating-Swirl Injector	4
3.1.1 Fuel and Air Supply System	4
3.1.2 Injector and Combustion Chamber	5
3.1.3 Data Acquisition Systems	9
3.1.3.1 Low-Frequency Sampling System for Flow System Monitoring	9
3.1.3.2 High Frequency Sampling System	11
3.1.4 Diagnostic Techniques	11
3.1.4.1 Dynamic Pressure Measurement	11
3.1.4.2 Detection of CH* Chemiluminescence Using a Photo Multiplier Tube	11
3.1.4.3 Timing System for Phase-Resolved Imaging	12
3.1.4.4 Images of Chemiluminescence	14
3.1.4.5 Images of OHV Planar Laser-Induced Fluorescence ..	15
3.1.4.6 Acetone PLIF for Mixing Studies in Non-reacting Flows	16
3.1.4.7 Exhaust Gas Sampling System	17
3.2 3X DACRS Injector Experimental Setup and Procedures	18
4.0 Results and Discussion	21
4.1 1X DACRS	21
4.1.1 Characterization of Instability Modes	21
4.1.2 Stability Map	23
4.1.2.1 235 mm Chamber Results	23
4.1.2.2 350 mm Chamber Results	27
4.1.3 Acetone PLIF for Mixing Studies in Non-reacting Flows	32
4.1.4 Phase-resolved Images of Unstable Combustion	34

Table of Contents

	<u>Page</u>
4.1.5 Emissions	37
4.2 3X DACRS	37
4.2.1 Stability Regimes	37
4.2.2 Flame Chemiluminescence Measurements	42
5.0 Summary and Conclusions	46
5.1 1X DACRS Injectors	46
5.2 3X DACRS Injectors	48
6.0 References	49
6.1 Cited References	49
6.2 Relevant Papers	50
6.3 Contributing Professionals	50
6.4 Publications, Meetings, and Presentations	51

List of Illustrations

Figure	Title	Page
1.	Facility Schematic.	4
2.	Dual Annular Counterrotating Swirl Injector Schematic.	6
3.	Dual Annular Counterrotating Swirl Injector Photo.	6
4.	Plan and Cross Section Drawings of Flat Vane Swirler.	7
5.	Model Gas Turbine Natural Gas Injector Photo. (Simple single swirl: 45° angle, X _{inj} = 36.8 mm)	7
6.	PSU and DACRS Injector Schematics.	8
7.	Combustion Chamber Cutaway View.	9
8.	Customized Data Acquisition Software Window Display Example.	10
9.	Dynamic Pressure and CH* Chemiluminescence Measurement Arrangement Drawing.	12
10.	Signal Timing Sequence Take Phase-Resolved Images of Flames.	13
11.	Schematic of Optical Setup for OH LIF Experiment.	14
12.	Spectral Characteristics of the Premixed Natural Gas Flame.	15
13.	Exhaust Gas Sampling System Schematic.	18
14.	Schematic of Combustor Setup with DACRS-3X Injector.	19
15.	High Speed Pressure Transducer Locations.	21
16.	Identification of First and Second Longitudinal Modes of Observed Combustion Instability.	22
17.	Calculated and Experimentally Observed Frequencies for 1L Mode.	24
18.	Typical Upstream Manifold Pressure Profile.	25
19.	Theoretical Amplitude Profiles of 1L and 2L Modes for a Standing Wave in a Closed Chamber	25
20.	Photographs of Stable and Unstable Flames with DACRS 45°/55° Swirler.	26
21.	Phase-resolved CH Chemiluminescence Images (DACRS 45°/55°).	27
22.	Absolute and Relative Amplitudes of Dynamic Pressure as a Function of Equivalence Ratio (Short Chamber Configuration).	28
23.	Equivalence Ratio and Chamber Pressure Effects on Strength of Instabilities.	28
24.	Stability Map for DACRS Injectors.	29
25.	Inlet Air Temperature Effect on Instabilities.	30

List of Illustrations (concluded)

Figure	Title	Page
26.	Inlet Air Temperature Effect on Strength of Instabilities (PSU Swirler).	31
27.	Stability Map as a Function of Chamber Pressure (PSU Swirler).	31
28.	Unmixedness at $x=5.5\text{mm}$ from Dump Plane (DACRS Injectors).	33
29.	Unmixedness Profiles of DACRS Injectors.	33
30.	Pressure Drops Across DACRS Injectors.	34
31.	Phase-locked Average OH PLIF Images.	35
32.	Phase-resolved Chemiluminescence Images (DACRS $45^\circ/55^\circ$).	36
33.	NO _x and CO Emissions of DACRS Injectors.	38
34.	Pressure Fluctuation vs. Equivalence Ratio.	39
35.	Pressure Signal Frequency at the Dump Plane and Fuel Line – Equivalence Ratio 0.65.	40
36.	Pressure Signal Frequency at the Dump Plane and Fuel Line – Equivalence Ratio 0.72.	41
37.	Time Trace of Pressure and Total Flame Cumiluminescence Fluctuation at Equivalence Ratio of 0.72.	42
38.	Flame Intensity Variations During a Pressure Oscillation Cycle – Equivalence Ratio 0.65, $U_{\text{Comb}} = 5 \text{ m/s}$, $T_{\text{inlet}} = 400^\circ\text{C}$	44
39.	Flame Intensity Variations During a Pressure Oscillation Cycle – Equivalence Ratio 0.72, $U_{\text{Comb}} = 5 \text{ m/s}$, $T_{\text{inlet}} = 400^\circ\text{C}$	44
40.	Flame Intensity Variations During a Pressure Oscillation Cycle – Equivalence Ratio 0.65, $U_{\text{Comb}} = 5 \text{ m/s}$, $T_{\text{inlet}} = 400^\circ\text{C}$	45
41.	Flame Intensity Variations During a Pressure Oscillation Cycle – Equivalence Ratio 0.72, $U_{\text{Comb}} = 5 \text{ m/s}$, $T_{\text{inlet}} = 400^\circ\text{C}$	45

1.0 Summary

The Low Emissions, High Performance Gas Turbine Engines Focused Research Initiative, initiated on September 1, 1995, had as its goal to provide a new mechanism by which state-of-the-art research developed at universities in critical areas would be transferred rapidly to industry. Specifically, a major objective was to reduce the time for basic research to impact actual hardware from the current time period of fifteen years to seven. To achieve this goal, a five-year research effort bringing industry and universities in partnership was envisioned. As part of a research team assembled by General Electric Aircraft Engines (GEAE), researchers at Penn State focused on the understanding and control of pressure oscillations in gas turbine combustors, a phenomenon commonly referred to as combustion instability. A state-of-the-art injector design was selected for study by GEAE and provided to Penn State. The major objective of the program was to provide a set of well-characterized data that would anchor models concurrently under development at GEAE. These detailed measurements of the combustion instability process required optical access to the combustion chamber. The state-of-the-art design selected for study was the Dual Annular Counter-rotating Swirl (DACRS) injector. Since sub-scale studies were conducted, the effect of injector scale on combustion instability was another objective of the research. Consequently, two injectors were fabricated by GEAE that differed in scale by a factor of three (referred to as the 1X and 3X DACRS injectors throughout this report). For simplicity, the injectors were designed to operate on natural gas as the fuel.

The major objective of the combustion instability study was achieved in that an extensive set of detailed measurements of the stability characteristics of the DACRS injectors under well-controlled conditions was obtained. A data set representing the stability behavior over a wide range of conditions resulted that specifically addressed injector stability behavior as a function of equivalence ratio, inlet air temperature, operating pressure and chamber configuration. Additionally, phase-resolved measurements of the energy release process with respect to the observed pressure oscillations were obtained from global and spatially resolved measurements using chemiluminescence and planar laser-induced fluorescence techniques. These measurements provided detailed understanding as to the coupling mechanisms between heat release and pressure oscillations that were observed during unstable operation. Analysis of the data allows evaluation of the role of mechanisms responsible for the initiation and sustenance of the combustion instability including the fluid mechanic effects of swirl, the role of fuel-air unmixedness and fuel feed system coupling. Both the data and these mechanistic insights provide a rich data set from which to develop and validate models intended to describe combustion instability in gas turbine combustors.

2.0 Objectives

The Low Emissions, High Performance Gas Turbine Engines Focused Research Initiative was initiated on September 1, 1995 after a peer review process by the U.S. Air Force of proposals submitted by Industry/University teams in the gas turbine engine field. The goal of the Focused Research Initiative was to provide a new mechanism by which state-of-the-art research developed at universities in critical areas would be transferred rapidly to industry. Specifically, the goal was to reduce the time for basic research understanding to impact actual hardware from the current time period of fifteen years to seven. To achieve this goal, a five-year research effort bringing industry and universities in partnership was envisioned. The topics for focused research initiatives were selected based on critical technology areas for future U.S. Air Force military aircraft that also had significant potential for commercial impact on U.S. industry. High performance gas turbine engines remain the key to military jet aircraft superiority, and commercial aircraft development traditionally benefits considerably from research and development efforts in the military arena. Furthermore, commercial aircraft sales make up a considerable fraction of the foreign export market for the United States and U.S. industries are increasingly challenged by foreign competition to produce high efficiency and environmentally clean engine technology. Additionally, domestic emphasis on environmental quality is motivating the military increasingly to be "good neighbors" with respect to air quality. Consequently high performance, low emission gas turbine technology clearly represented a critical area worthy of a focused research effort by appropriate research teams.

In response to this challenge, General Electric Aircraft Engines (GEAE) assembled a team of leading researchers from six universities and a national laboratory to address the combustion research issues critical to future gas turbine engine development. Research efforts were also coordinated with a major Air Force Research Laboratory, Wright Patterson Air Force Base. An integrated experimental and theoretical approach was adopted to provide both an appropriate data base and analysis tools to develop the next generation of design tools needed to rapidly incorporate new basic understanding into practical applications. Because the results of the studies are in the public domain wide ranging benefits to the aerospace community can be anticipated.

The Penn State effort focused on the understanding and control of pressure oscillations in the combustor, which represents one of the most challenging and least understood phenomena potentially limiting the development of future high performance gas turbine engines. This phenomenon is commonly referred to as combustion instability. In order to address combustion instability studies under realistic conditions applicable to actual current gas turbine engine technology, a state-of-the-art injector design was selected for study by GEAE and provided to Penn State. The objectives of the program also required that the experimental conditions replicate to as high a degree as possible the operating conditions typical of modern gas turbine combustors. Furthermore, as the studies were intended to anchor models concurrently under development at GEAE, detailed measurements of the combustion instability process were desired, which required optical access to the combustion chamber. Since by necessity sub-scale studies would be conducted, the effect of injector scale was one of the objectives of the research. Consequently two injectors were fabricated by GEAE that differed in scale by a factor of three. The state-of-the-art design selected for study was the Dual Annular Counterrotating Swirl (DACRS) injector. These injectors are referred to as the 1X and 3X

DACRS injectors throughout this report. For simplicity in the initial phase of the study, the injectors were designed to operate on natural gas as the fuel.

The major objective of the combustion instability study was to provide detailed measurements of the stability characteristics of the DACRS injector under well-controlled conditions that could be used to validate combustor models developed by GEAE. In particular, the stability behavior as a function of equivalence ratio and inlet air temperature was a major research objective. Additionally, phase resolved measurements of the energy release process with respect to the observed pressure oscillations were also to be obtained. Both global and spatially resolved measurements were desired using chemiluminescence and planar laser-induced fluorescence techniques. Finally, it was desired to obtain these results under elevated pressure conditions. To this end, the 1X DACRS injector was studied in a facility assembled for this research contract that was capable of operation at pressures up to ten atmospheres while the 3X DACRS injector was studied in an existing two-atmosphere facility.

3.0 Approach

3.1 1X Dual-Annular Rotating-Swirl Injector

3.1.1 Fuel and Air Supply System

The high-pressure combustion facility used in the current study is schematically represented in Figure 1. Two available air compressors operating in parallel delivered about 270 g/s (0.6 lbm/s) of air at 2.4 MPa (350 psia) or 180 g/s (0.4 lbm/s) at 3.8 MPa (550 psia). Hence, allowing for pressure drop across the flow system, the air supply allows combustion pressures up to 2.5 MPa (360 psia). The compressed air passed through an air filter and dryer (pressure dew point 3.3°C) before flowing into the main airflow metering system. The air metering system consisted of a dome loader and a set of four critical flow venturis connected in parallel. Throat diameters of these four metering venturis were 2.34 mm (0.092"), 2.84 mm (0.112"), 4.95 mm (0.195") and 7.39 mm (0.291"), respectively. Since each venturi was connected to its own shut-off ball valve, a desired range of flow rates for cooling and combustion air was obtained by a selected combination of the venturis. Flow coefficients, C_d , for each of the venturis were calibrated by means of a critical orifice with a known C_d . The upstream pressure of the metering venturis was remotely adjusted in the control room using the dome loader of the lab, and the upstream air temperature was measured using a K-type thermocouple. Using these two values, exact mass flow rates through each choked air-metering venturi could be calculated.

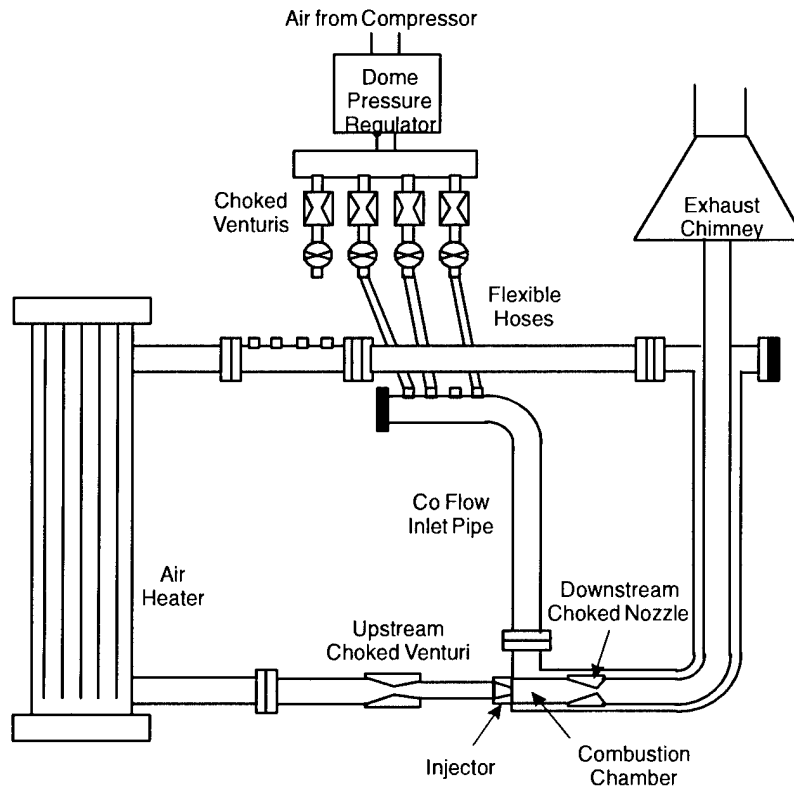


Figure 1. Facility Schematic.

A high capacity, air circulation heater was used to preheat the inlet air to temperatures as high as 811 K (1000°F) at maximum flow rates, thus providing the capability of simulating the effects of real gas turbine compressor stages. Hot air from the heater was introduced into a model combustor through a venturi with a throat diameter of 7.39 mm (0.291-in.), which leads to the 24-mm (0.945-in.) inner diameter inlet section. Since this upstream venturi was designed to be choked at test conditions, any pressure wave generated in the combustion chamber cannot travel upstream across the venturi. As a result, the location of this venturi sets the upstream acoustic boundary of the combustor.

A natural gas compressor was used for charging a bank of natural gas tanks manifolded together for a total capacity of 113 scm at 20 MPa (3990 scf at 3000 psia). A desiccant dryer (pressure dew point 4.4°C) and a particulate inline filter remove moisture and particles from the natural gas, respectively. Since the composition of natural gas delivered from the local supplier changes depending on the season, samples of natural gas have been taken for composition analysis for one year. The typical composition of the natural gas analyzed by a gas chromatograph (HP 5890 series II) equipped with a thermal conductivity detector (TCD) and a flame ionization detector (FID) was methane 95.52% ($\pm 1.48\%$), ethane 3.99% ($\pm 1.42\%$), propane 0.25% ($\pm 0.12\%$), and higher hydrocarbons and other species, 0.24% ($\pm 0.11\%$).

3.1.2 Injector and Combustion Chamber

The primary injector investigated in this study was the Dual Annular Counterrotating Swirl (DACRS) injector designed and fabricated by GEAE. This injector consisted of two swirl rings that counterrotate air at a specified swirl angle. The rings were made of curved vanes for better aerodynamics and smaller pressure losses. Before burning, the air was swirled and mixed with natural gas at a given equivalence ratio. Two combinations of swirl angles were studied: a 45°/55° and a 55°/65° swirl combination, where the angles represent the outer and inner ring angles respectively. The natural gas fuel was introduced through the outer swirl vanes using three injection holes on each of the ten swirl vanes. The swirl rings were attached to a centerbody that was tapered to point at the dump plane. The centerbody was cooled using air that was directed through the centerbody from the back of the injector. A schematic showing the dimensions of the DACRS injector is shown in Figure 2 while a photograph of the injector is shown in Figure 3.

Comparison of the combustion instability behavior obtained with a simple single swirler designed and fabricated at Penn State was also made to help understand the advantages of the counterrotating geometry. A generic axial air swirler with swirl angle of 45° with respect to the oncoming air was designed and fabricated for the companion studies (Reference 1). This swirler was composed of eight straight flat vanes. The vanes were aligned between a hub and an outer ring so that the incoming flow does not see any open area in the axial direction of the swirler. An angle measured between the axis of the swirler and the plane of a straight vane defines a swirl angle, ϕ , as shown in Figure 4. The thin hub of the swirler slides onto the injector centerbody, and taper edges on both sides of the hub minimize flow disturbance. The average pressure drop across the swirler was 7.2%. The swirler was located 38 mm (1.5 in.) from the dump plane for all the experiments reported here.

The simple single swirler was attached to a central bluff body that was 9.53 mm (0.375 in.) in diameter and mounted flush with the dump plane, providing an effective flame anchoring system. Natural gas was injected radially from the bluff body downstream of the swirler through ten 0.75-mm diameter holes located at a variable distance, X_{inj} , upstream of the dump plane. For the

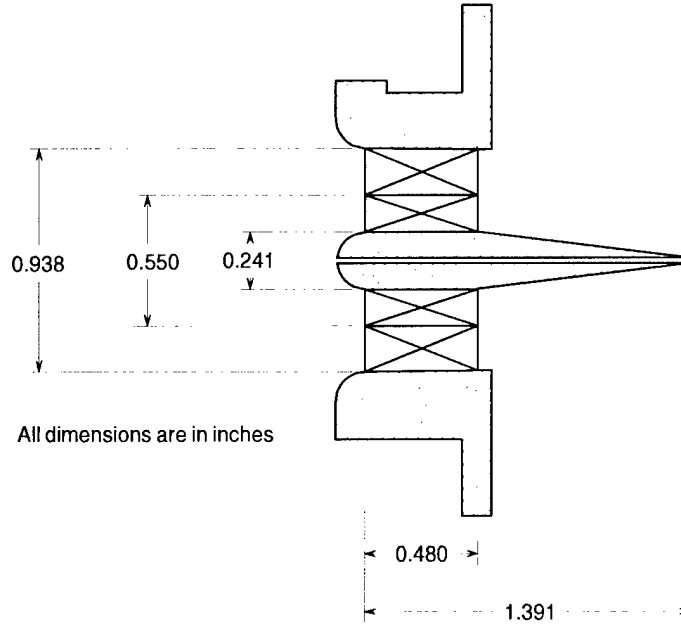


Figure 2. Dual Annular Counterrotating Swirl Injector Schematic.

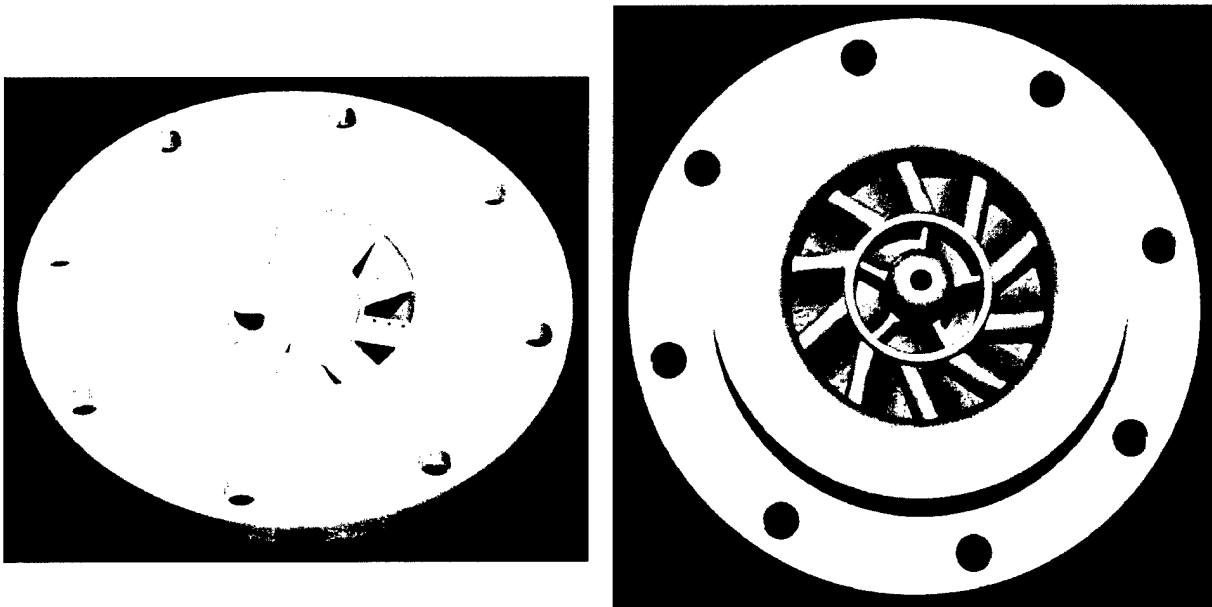


Figure 3. Dual Annular Counterrotating Swirl Injector Photo.

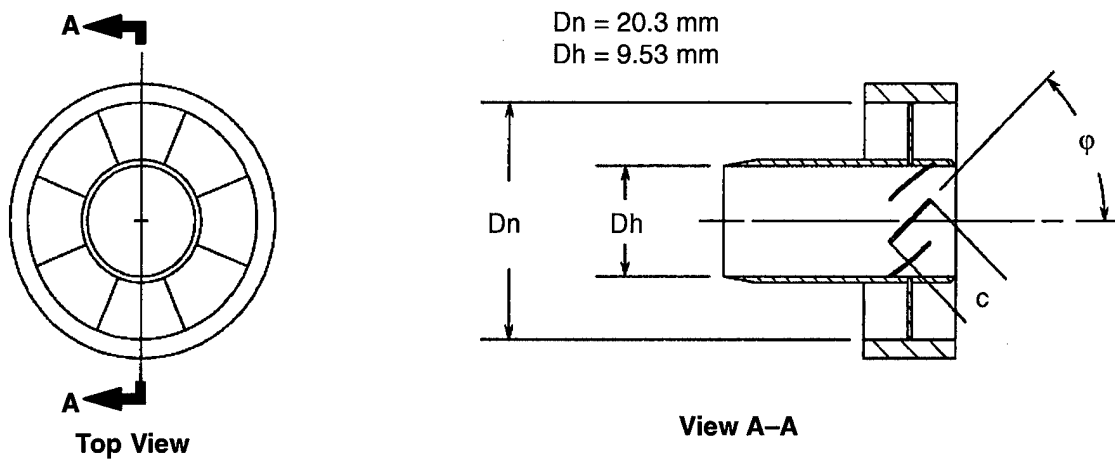


Figure 4. Plan and Cross Section Drawings of Flat Vane Swirler.

present comparisons X_{inj} was maintained at 36.8 mm (1.45 in.) from the dump plane. Figure 5 presents the photograph of the fuel injection head set up with the 45° swirler and $X_{inj} = 36.8 \text{ mm}$ (1.45 in.). Set-ups for both DACRS and Penn State injectors can be compared on Figure 6.

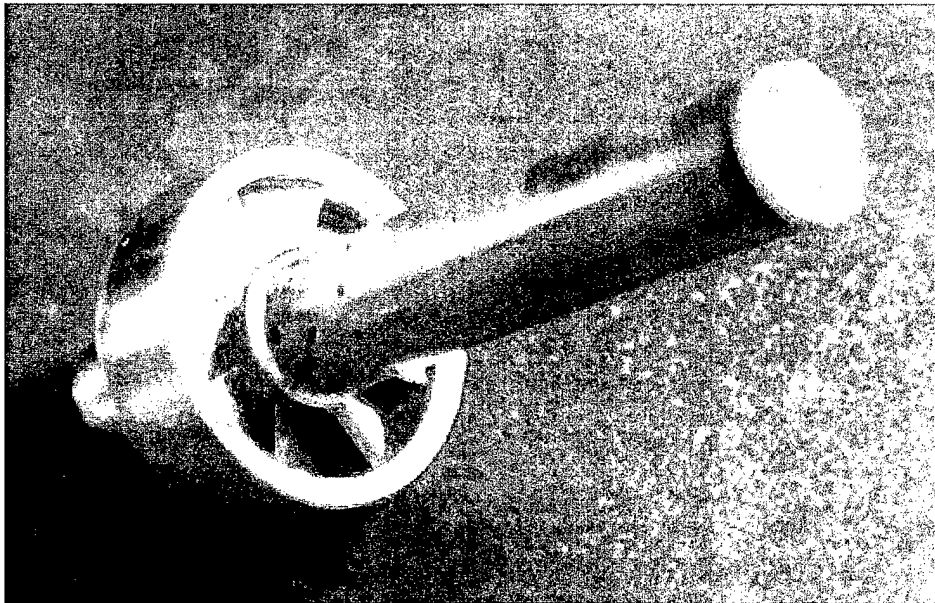
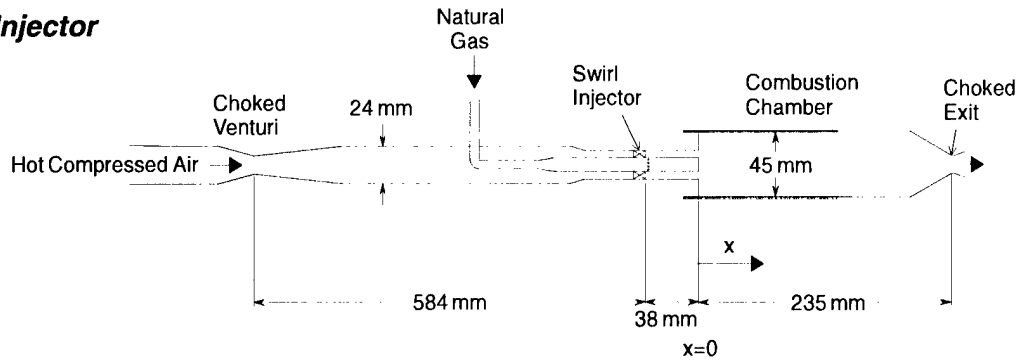


Figure 5. Model Gas Turbine Natural Gas Injector Photo.
(Simple single swirl: 45° angle, $X_{inj} = 36.8 \text{ mm}$)

PSU Injector



DACRS Injector

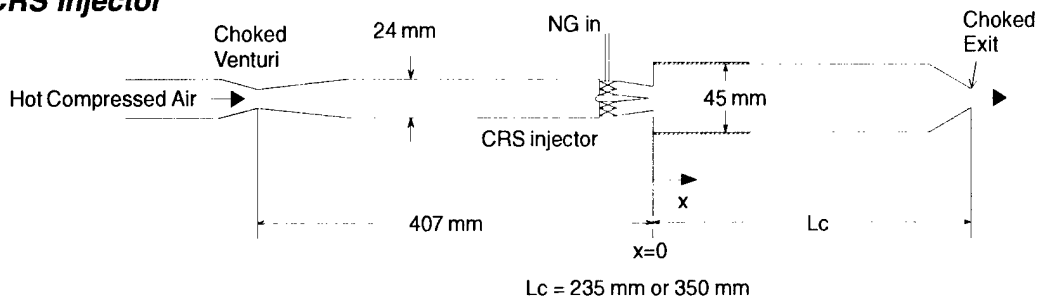


Figure 6. PSU and DACRS Injector Schematics.

The combustion chamber had a modular design such that the chamber length and the order of the test sections could be changed. A cutaway view of the combustion chamber is presented in Figure 7. The inside diameter of the cylindrical combustion chamber was 45 mm (1.77 in.) with an expansion ratio of 7.8, which was based on the ratio of the area of the combustion chamber to that of the tapered inlet section at the dump plane. Eight high frequency pressure transducers, located axially along the injector and the combustion chamber were monitored in order to determine the mode structure for any instability observed. The combustion chamber was composed of several independent sections that were held together by a hydraulically pressurized assembly. Each stainless steel section houses one or more transducers and could be added to or removed from the overall chamber. This arrangement provided useful flexibility, not only to position the transducers in the most appropriate way, but also to vary the total chamber length from 140 to 370 mm (5.51 to 14.6 in.) and study chamber length effects on combustion instability behavior. Chamber lengths of 235 mm (9.25 in.) and 350 mm (13.78 in.) were chosen for study. Also visible on the cutaway view of Figure 7 is the fully optically accessible cylindrical quartz section used in the study to image the heat release zone and correlate it to pressure fluctuations. The quartz cylinder was protected during hot-fire experiments by impingement of cooling air pressurized to match the chamber pressure to equalize the forces across the quartz section. Some of the air-cooling vanes are shown in Figure 7.

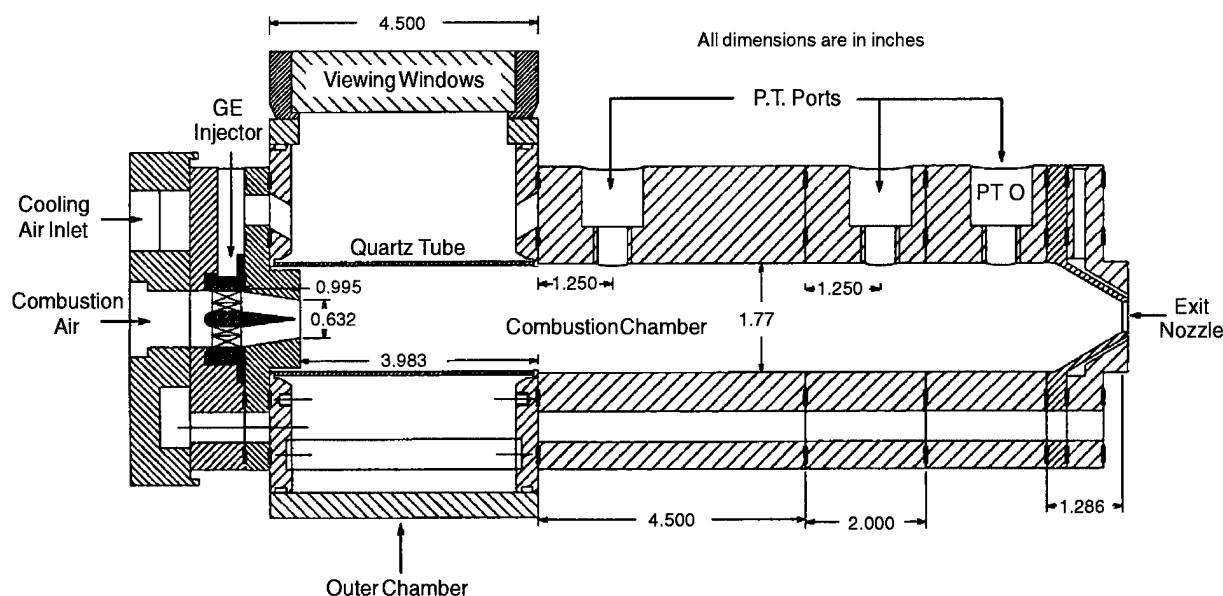


Figure 7. Combustion Chamber Cutaway View.

To acoustically isolate the combustor and the injector from the airflow supply and the exhaust sections, the combustor design includes two sonic choked points. The first was upstream of the injector in the air circuit as described earlier, and the second was located at the exit nozzle of the combustor. These two choked points represent well-defined boundary conditions for studying combustion instabilities.

To protect the exit nozzle from the severe thermal loading resulting from the combusting flow, a cooling system was employed using compressed air to atomize water introduced at the nozzle. A throat-area-controlling valve (Masoneilan) adjusted the amount of water supplied into the gap made by the exit nozzle and the downstream heat exchanger. The amount of cooling water was adjusted to keep the exhaust gas temperature below 533K (500°F). Since samples of the exhaust gases were extracted after cooling, the amount of cooling air delivered into the exit nozzle was metered in order to compensate for the dilution of the exhaust gases by the cooling air.

3.1.3 Data Acquisition Systems

3.1.3.1 Low-Frequency Sampling System for Flow System Monitoring

For the safe and successful control of the test rig, all pressures, temperatures, and emission concentration signals were monitored and logged throughout an experiment. Thermocouples and piezo-electric pressure transducers were used for measuring temperatures and pressures, and gas analyzers for species concentrations of exhaust gases. All of the thermocouples used in the flow system were K-type except one R-type thermocouple located 305 mm (12") downstream of the exit nozzle. The R-type thermocouple measures the exhaust gas temperature and was displayed on a

LED readout mounted on the control panel in the control room that was monitored by the operator. Pressure transducers (Setra models 204 and 205) actuated by a 28 VDC power supply return voltage outputs proportional to the pressure. All temperature and pressure signals were transmitted into the control room via thermocouple wires and four-wire cables.

Pressure and temperature measurements at every section of the various flow subsystems were continuously monitored during a test as stated earlier in this section. Continuous monitoring and logging of all pressure and temperature data during each experiment was achieved utilizing customized data display-and-log software along with an analog-to-digital (A/D) conversion board (Keithley, DAS1401) installed in an IBM compatible Pentium-90 computer. The sampling board had four expansion boards (Keithley, EXP-16) in a daisy chain arrangement that provided 64 individual channels for pressure, temperature, and concentration measurements. The Pentium-90 computer was solely dedicated to processing pressure and temperature signals, and displaying appropriate values at each stage of the flow system. Figure 8 shows the appearance of a process display window.

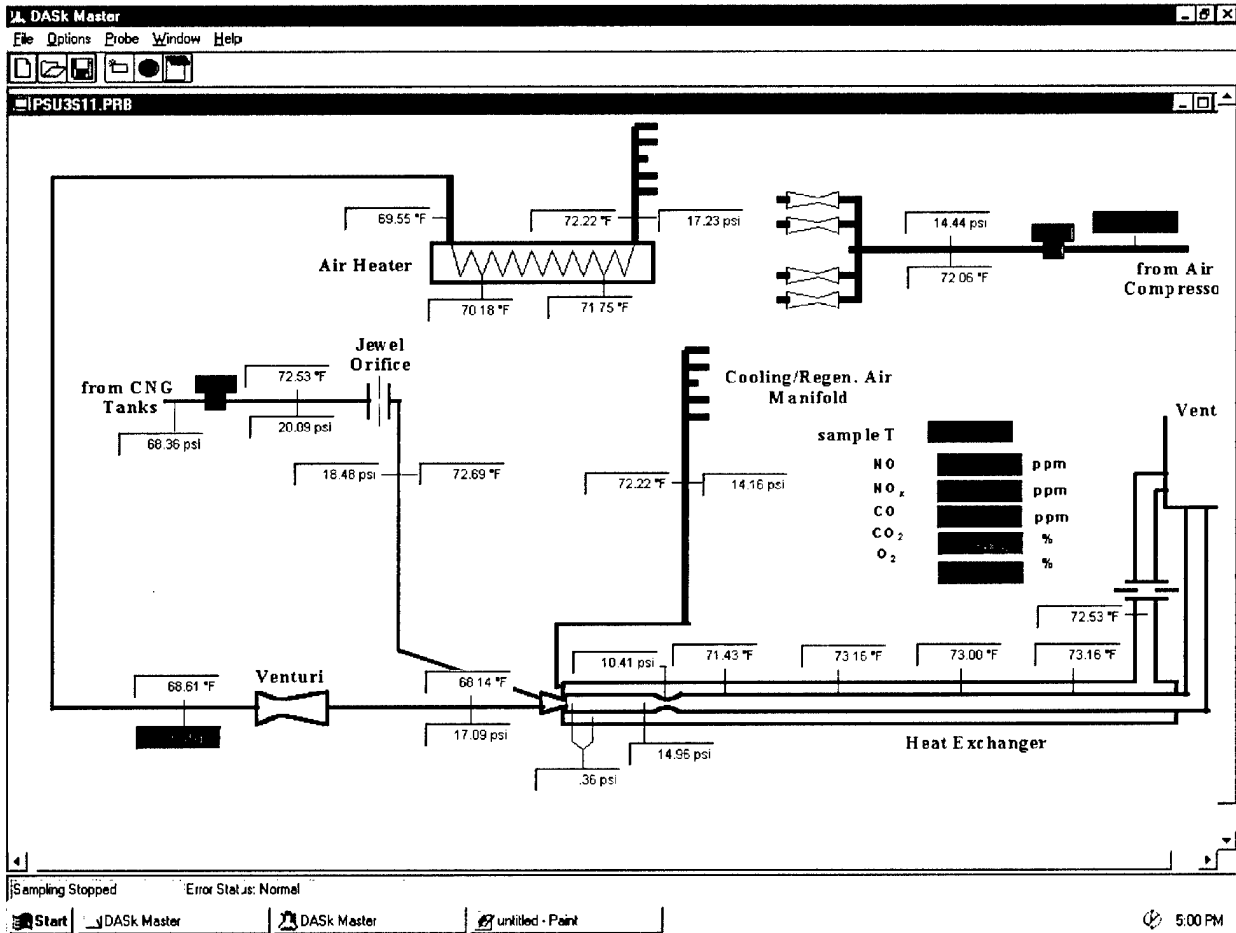


Figure 8. Customized Data Acquisition Software Window Display Example.

3.1.3.2 High Frequency Sampling System

High-frequency sampling of the dynamic pressure and photo multiplier tube (PMT) signals could be accomplished with an eight channel A/D sampling board (National Instrument, AT-MIO-16E-1) installed in an IBM compatible Pentium-200 computer. Along with the A/D sampling board, a sample and hold board (National Instruments, SC-2040) made it possible to simultaneously sample input signals at sampling rates greater than 30 kHz for each individual channel. All signals sampled by the board were monitored on the Pentium-200 computer display and, if necessary, stored. The typical sampling rate per channel was 30 kHz, and the number of data points in one file was 4096 per channel.

3.1.4 Diagnostic Techniques

To understand the characteristics of combustion instability, experimental information related to dynamic pressure and flame structure has been taken and analyzed in this study.

3.1.4.1 Dynamic Pressure Measurement

The measurement of dynamic pressure was a common diagnostic technique for the study of combustion instabilities since dynamic pressure data could provide information characterizing the acoustic waves propagating in the combustion chamber. Water-cooled dynamic pressure transducers (PCB model 113A21) were flush mounted along the combustor to measure dynamic pressure fluctuations at the combustor wall. The natural frequency and rise time of the pressure transducers were 500 kHz and 1 μ s respectively, which were well above the characteristic time scales needed to resolve the instability phenomena of interest in the present study. The exact locations of each dynamic pressure transducer is shown in Figure 9. The constant current excitation required for the dynamic pressure transducers was provided by a signal conditioner (PCB model 483A), and voltage outputs from the signal conditioner were sent to the high frequency sampling system for monitoring and storing of pressure measurement signals.

3.1.4.2 Detection of CH* Chemiluminescence Using a Photo Multiplier Tube

The electronically excited CH* radicals were produced from the highly exothermic chemical reactions involving oxidation of the fuel. A major reaction channel for the production of CH* was $C_2 + OH = CO + CH^*$, which yielded significant radiative emission at 431.5 nm ($A^2\Delta \rightarrow X^2\Pi$). The emission of excited CH* radicals were very strong in the reaction zone of hydrocarbon flames and, thus, was argued to be a marker of the flame heat release zone. The radiative lifetime of this unstable CH* radical was about 0.6 ns, which was shorter than the fluid mechanical and acoustical characteristic times of the reacting flow in the combustion chamber (Reference 2). From these characteristics of CH* chemiluminescence, the measurement of the intensity of CH* chemiluminescence has been conducted to infer the rate of chemical reactions in numerous experimental studies (Reference 3, 4, 5, and 6).

CH* chemiluminescence signals from the combustor were monitored through the top section of the quartz window test section and stored simultaneously with the measurements of the dynamic pressure. The optical setup for collecting the CH* chemiluminescence signals is shown in Figure 9. A bi-convex lens (focal length of 50.2 mm) collected light emissions from a projected area in the

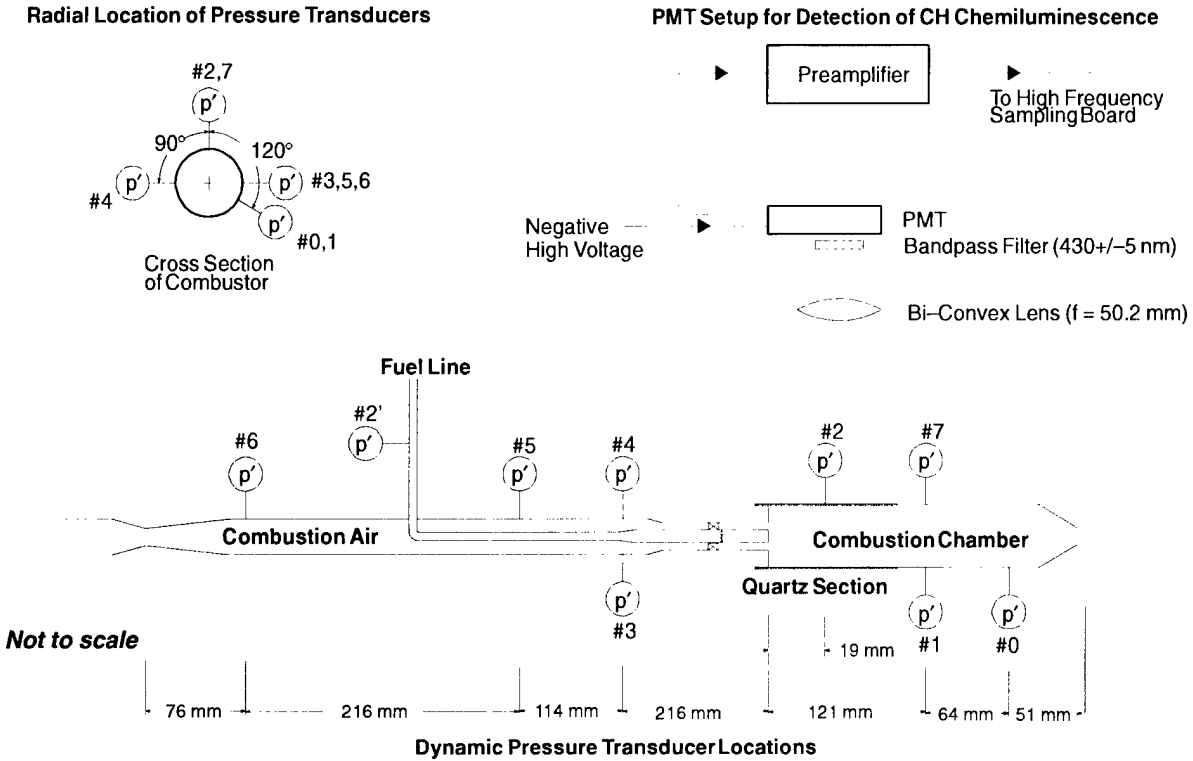


Figure 9. Dynamic Pressure and CH* Chemiluminescence Measurement Arrangement Drawing.

combustor having a 45-mm (1.77 in) diameter. This light emission was focused onto the detection area of a photo multiplier tube (HAMAMATSU, R928) through a band pass filter (430nm with FWHM of 10nm), which helped reject background flame luminosity not associated with the CH* emission. The photo multiplier tube was biased with a high negative voltage (-800 VDC) and its output, which was terminated with a 50 Ω resistor, was connected to a preamplifier (Stanford Research SR560) for signal conditioning and amplification. An amplified voltage output signal, including any DC offset, was monitored using the high frequency sampling system previously described. These measurements were simultaneously saved with pressure signals for later analysis.

3.1.4.3 Timing System for Phase-Resolved Imaging

The quartz test section of the experimental setup allowed the observation of flame structures in the combustor. Due to the periodic nature of the flame structure relative to the pressure fluctuations, it was necessary to temporally resolve the flame structure associated with the dynamic pressure. Images of the flames were captured under phase-locked conditions with the pressure fluctuations using the signal from the dynamic pressure transducer PT#0 ($x/L_c = 0.78$) shown in Figure 9 as a reference. The timing system used for triggering the intensified CCD camera system was used for both the chemiluminescence and OH- PLIF experiments.

The timing sequence for obtaining phase-locked images of the flames is shown in Figure 10. Typical traces of the signals similar to the ones shown in Figure 10 were monitored on a digitizing oscilloscope (HP model 54512B) to verify that proper timing for obtaining phase-locked images with respect to the dynamic pressure was achieved. The raw pressure signal shape from the signal

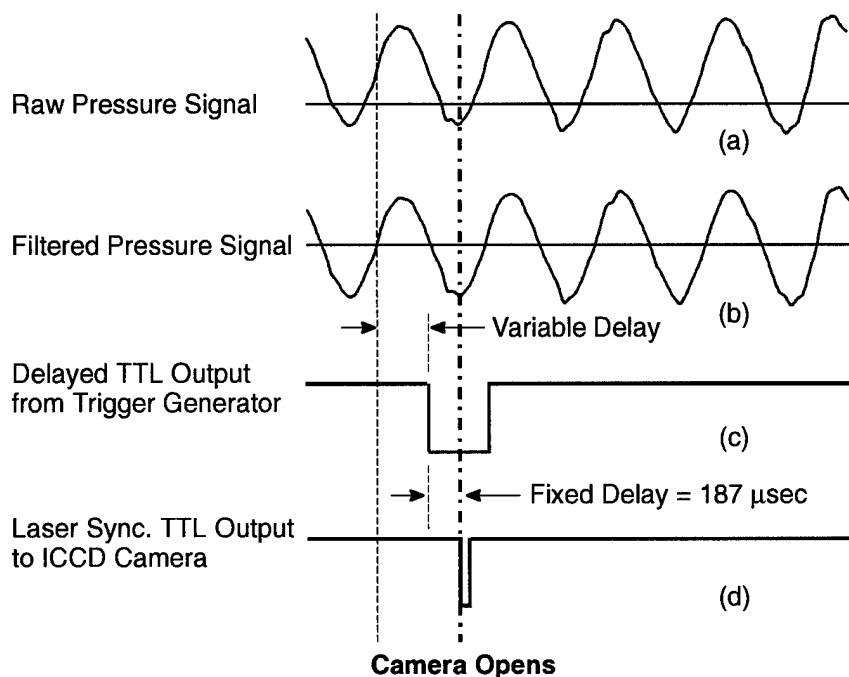


Figure 10. Signal Timing Sequence Take Phase-Resolved Images of Flames.

conditioner (PCB model 483A) was similar to the one shown in Figure 10(a). This signal contains both a DC offset and high frequency noise, which needs to be removed before inputting the signal to a trigger generator. A preamplifier (Stanford Research model SR560) was used to remove the DC offset and to filter the high frequency noise to provide filtered pressure signals for reliable triggering. The output of the preamplifier removes all signals outside its bandpass of 300 Hz to 30 kHz and introduced a negligible phase delay between the input and output signals, approximately 5 μ s. The filtered signal appeared similar to the trace shown in Figure 10(b). This filtered signal provided a threshold level for generating the trigger signal sent to the intensified CCD camera. The threshold level was usually set at zero with a positive gradient on the trigger pulse generator (Stanford Research DG 535). The negative TTL signal output from the trigger pulse generator is shown in Figure 10(c). The timing setting on the trigger pulse generator limits the trigger pulse frequency to around 10 Hz since the Nd:YAG laser (Continuum SURELITE II) achieved maximum pulse energies at a 10 Hz repetition rate. The time delay of the output TTL signal from the instant when the threshold value was reached by the input pressure signal was adjusted on the trigger pulse generator to take images at the different phases of the reference pressure signal. After a fixed time delay from the falling edge of a trigger signal, approximately 187 μ s, a negative TTL signal from the laser was delivered to the pulse generator of the intensified CCD camera system to initiate image acquisition. Since the time delay between the laser trigger signal (shown in Figure 10(d)) and the actual intensified CCD gate opening was negligible (~ 65 ns), the moment that the laser trigger signal was generated corresponded to acquiring an image. The timing of the laser TTL signal relative to the pressure signal was monitored on an oscilloscope during the image acquisition process. A schematic of the optical setup and timing arrangement is shown in Figure 11.

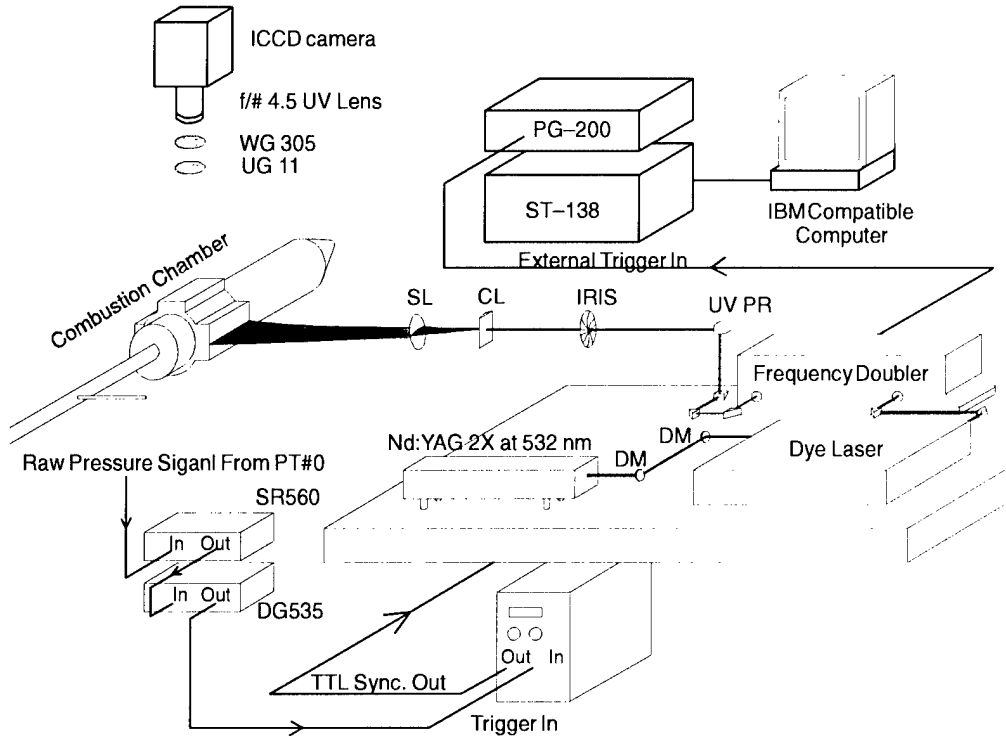


Figure 11. Schematic of Optical Setup for OH LIF Experiment.

As mentioned earlier in this section, the same timing system was used for taking chemiluminescence and OH- PLIF images. For chemiluminescence images, the shutter in the laser remained closed to prevent the propagation of any laser light generated.

3.1.4.4 Images of Chemiluminescence

The intensity of chemiluminescence has been often interpreted as an indicator of heat release from flames. Therefore, the detection of chemiluminescence signals has been considered a common experimental technique for assessing heat release rates in the study of combustion instability for many years. The most commonly used species for this purpose were CH^* and OH^* in hydrocarbon flames. A recent numerical study by Samaniego *et al.* (Reference 7) suggested that the detection of CO_2^* emission in hydrocarbon flames can also be used to infer the heat release rate. They note that CO_2^* emission was characterized by a broad band light emission extending across the region of the emission spectrum (see Figure 12). Images of CO_2^* emissions were also taken to compare with the results from emissions from CH^* and OH^* species.

To spectrally isolate the chemiluminescence for each species of interest in the flame, spectral filters were used corresponding to: 310nm (FWHM 10nm) for OH^* , 430nm (FWHM 10nm) for CH^* , and 460nm (FWHM 10nm) for CO_2^* . The detection bandpass for the CO_2^* emission was determined from the measurement of spectral characteristics of the flames as shown in Figure 12 to avoid emission peaks due to OH^* and CH^* species.

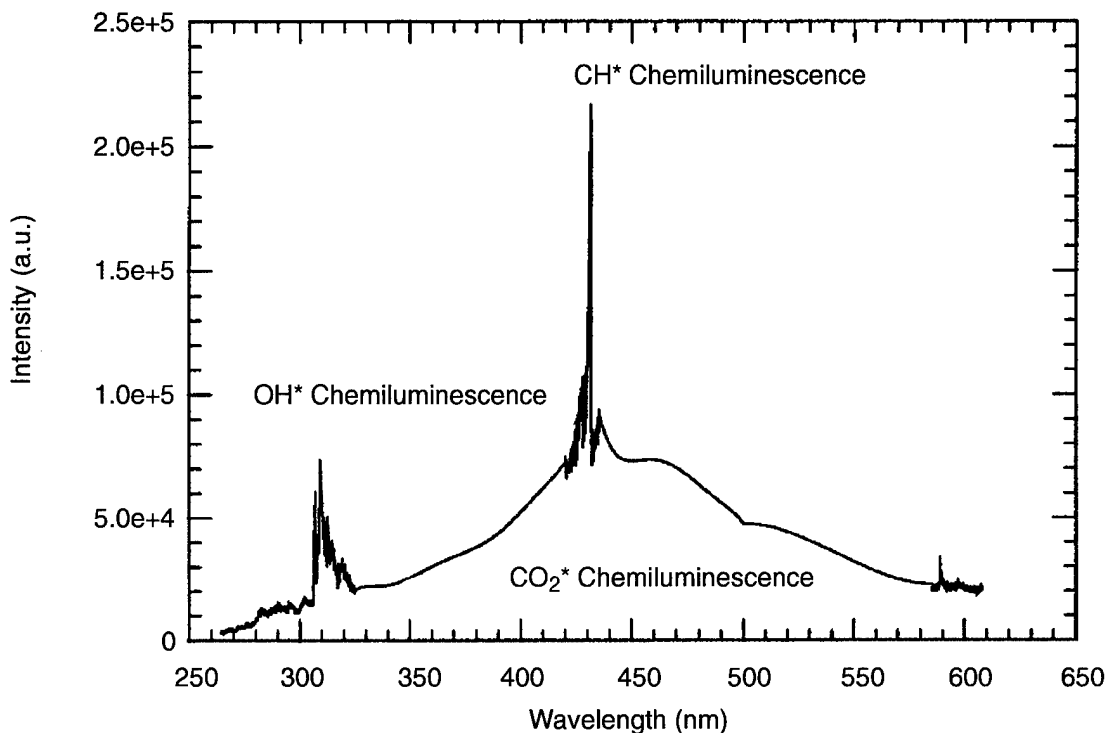


Figure 12. Spectral Characteristics of the Premixed Natural Gas Flame.

The intensified CCD camera (Princeton Instruments ICCD-576) used throughout the study has a photocell with 576 x 384 pixels. The gain for the intensifier of the camera was set at 8.5 out of a maximum of 10. For UV transmission of OH* chemiluminescence, an UV Nikkor camera lens with f-number 4.5 was used. The opening of an electronic gate of the intensified CCD camera was achieved using a pulse generator (Princeton Instruments PG200), and the image data processing and transfer to the computer were accomplished using the detector controller (Princeton Instruments ST-138). The gate width applied to the camera for detection was varied from 5 to 20 μ s depending on the intensity of emission signals. For each image at the fixed phase relative to the dynamic pressure oscillations, 100 images were accumulated.

3.1.4.5 Images of OH· Planar Laser-Induced Fluorescence

The application of laser-based techniques in measurements of properties in combustion environments became popular because of the non-intrusive nature of these diagnostic approaches. Among the many available laser diagnostic techniques, planar laser-induced fluorescence (PLIF) techniques have been popular due to their advantage of providing instantaneous two-dimensional information (Reference 8). Two-dimensional images provide detailed cross section information of the flame structure whereas chemiluminescence images show line-of-sight, that was volume averaged, information regarding flow structures.

OH· was chosen as the species for the study due to its well-known optical properties, and it was frequently reported as a marker of the flame zone. For the excitation of OH· molecules to an upper electronic energy level, a laser pulse at a wavelength of 283.55 nm was selected. The schematic of OH· PLIF setup is shown in Figure 11 and a detailed description follows.

A frequency doubled Nd:YAG laser (Continuum SURELITE II) producing a laser output at 532 nm was used to pump a dye laser (Spectra Physics PDL-3). The nominal pulse energy from the Nd:YAG laser at 532 nm was around ~300 mJ/pulse, and the pulse width was ~8ns at FWHM. The dye (Rhodamine 590, Exciton) was dissolved in methanol (HPLC grade) to give a maximum conversion efficiency around 560 nm. A frequency extender (Spectra Physics Quanta-Ray WEX) converted the wavelength of the output pulse from the dye laser through a frequency doubling process to yield a UV beam output at 283.55 nm for excitation of the $Q_1(8)$ line of the $A^2\Sigma-X^2\Sigma(1,0)$ band of OH. The energy of this UV laser beam was about 3 mJ/pulse. All optical components following the frequency extender were made of UV grade fused silica to transmit the UV laser beam. A combination of cylindrical and spherical lenses transformed the Gaussian input beam into a sheet beam. The thickness of the sheet beam was ~300 μm . The sheet beam intersected the centerline of the quartz tube inside of the window test section to provide two-dimensional flame structure information from the center cross section of the combustor. The camera viewed the centerline plane of the combustion chamber directly after the dump plane corresponding to an area 45 mm \times 67.5 mm, and the spatial resolution for the image after 3 \times 3 binning was 350 μm \times 350 μm .

The intensified CCD camera was mounted on a three-axis traversing system and viewed the entire section of quartz tube through the top of quartz section as illustrated in Figure 11. The onset of the gate pulse for the intensified CCD camera was delayed at 50~100 ns with respect to the laser pulse. For fluorescence measurements in the UV wavelength range, an UV Nikkor, $f/\#$ 4.5 camera lens was used. Two Schott[®] glass filters (UG-11 and WG-305) were employed to restrict transmission of fluorescence emission to wavelengths between 300 and 400 nm.

3.1.4.6 Acetone PLIF for Mixing Studies in Non-reacting Flows

Before conducting reacting flow tests for different setups involving different natural gas injection locations, it was necessary to assess the degree of mixing between fuel and air before combustion. Since the harsh environment of the reacting flow makes it exceedingly difficult to measure any mixing property at the actual test conditions, information about the degree of premixing was obtained from the non-reacting flow tests that simulate the reacting flow case.

Acetone has been considered one of the best tracers satisfying the requirements of mixing studies for gaseous flows and has been applied as a PLIF tracer for studies of mixing in many cases (Reference 9, 10, 11, and 12). To simulate the fuel injection process, acetone was seeded into a helium flow, and the ratio of acetone flow rate was selected to achieve a mixture molecular weight that was the same as that of methane.

The acetone flow rate was metered using a critical orifice, and acetone was vaporized before being seeded into the helium flow. The helium flow was metered using the fuel delivery system described earlier. The mixture of helium and acetone was then injected into the cross flow of heated air.

For excitation of the acetone molecules, the fourth harmonic output of the Nd:YAG laser at a wavelength of 266 nm was used. The laser beam after passing through the fourth harmonic generator installed in the Nd:YAG laser, was diverted 90 degrees by a Pellin-Broca prism that spatially isolates the fourth harmonic beam from other wavelength beams. This UV laser beam was then directed through a series of two prisms that changed the direction of polarization as shown in Figure 11. The same optical setup as employed for OH PLIF measurements was used for forming a sheet beam. Only one glass filter (WG-305) was used to filter the UV fluorescence signals since the spectrum

of fluorescence for acetone ranges between wavelengths of 350 to 550 nm. The dye laser and frequency doubler were not used for the acetone PLIF experiments.

The fluorescence signal generated was proportional to the input laser intensity and the number density of the species molecules of interest in the lower energy state under excitation conditions corresponding to the linear regime (Reference 13). Based on calibrations obtained from measurements of laser power and fluorescence signal using several known concentrations of acetone under complete mixing conditions, the spatial concentrations of acetone was estimated from the intensity of acetone PLIF images. Using this information, the degree of premixing was described by the introduction of an unmixedness parameter, which is defined as,

$$U = \frac{\overline{C_{ac}^2}}{\overline{C_{ac}}(1 - \overline{C_{ac}})}$$

where C_{ac} is the concentration of acetone. According to the definition of the unmixedness parameter, U , its value must range between 0 and 1. A value of zero for the unmixedness parameter means that perfect mixing was achieved while a value of one indicates no mixing has occurred (Reference 14).

3.1.4.7 Exhaust Gas Sampling System

It was crucial to assess the performance of the present model gas turbine combustor in terms of the exhaust gas emissions characteristics if truly relevant results were to be achieved. In this subsection, a description of the exhaust gas sampling system is provided.

Cooling water atomized by compressed air was injected downstream of the exit nozzle after flowing through the exit nozzle gap. Thus, cooling of the nozzle and hot exhaust gases can be accomplished at the same time. Since cooling air was mixed with the exhaust gas before the sampling gas extraction location, concentration readings of each species will be different from the actual concentrations of exhaust gases without dilution by cooling air. The effects of the cooling air and water spray on the species formation or destruction were assumed to be negligible because the temperature of cooled exhaust gases were kept below 533K (500°F) throughout the experiment to prevent any further chemical reaction.

Sample gases were drawn into the sampling system by means of a metal bellows pump that has wetted parts made of Teflon and stainless steel for eliminating any chemical contamination (see Figure 13). The sampling probe was a simple stainless steel tube with an outside diameter of 6.25 mm (0.25 in.) protruding into the centerline of the inside pipe of the heat exchanger. Water vapor in the sample gases was condensed using a stainless steel coil immersed in an ice bath, and the condensed water was trapped in a glass impinger. The output temperature of the dry sample gases was around 4°C.

The sampling system consisted of nondispersive infrared CO (Horiba model VIA-510) and CO₂ analyzers (Beckman Industries model 864) and a paramagnetic O₂ analyzer (Beckman Industries model 755) along with a chemiluminescence NO_x analyzer (Thermo Environmental Instruments model 42H). All analyzers operated at atmospheric pressure except for the NO_x analyzer, which was conditioned at its own flow settings. Calibration of the analyzers experiment, using zero and span calibration gases, was done before and after each test at the same flow conditions at which the tests were conducted. Sample gases were metered before going through each analyzer. Any excessive amount of sample gas was bypassed to the exhaust system. Analog voltage outputs from the

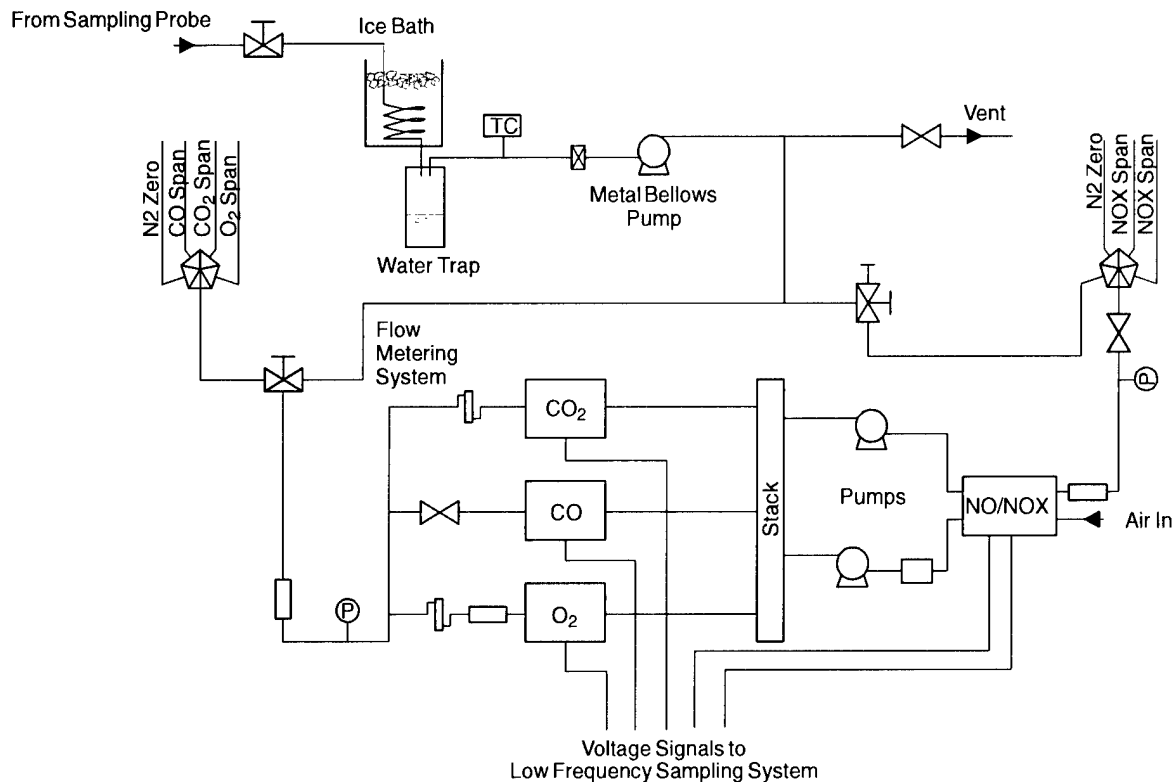


Figure 13. Exhaust Gas Sampling System Schematic.

analyzers were sampled by the low frequency sampling board and converted to their concentrations using the software running on the Pentium-90 computer. The concentration data were stored in the data log file with the pressure and temperature data corresponding to test conditions.

3.2 3X DACRS Injector Experimental Setup and Procedures

The schematic of the combustor with the GE-DACRS 3X injector is shown in Figure 14. The injector was attached to a converging section that was designed to specifications provided by GEAE. The combustor was 63.5 cm long and was made up of two sections. The first section, downstream of the dump-plane, was an optically accessible quartz-tube, 12.7 cm in diameter and 22.9 cm long, and the second section was a 40.6-cm long stainless-steel pipe with an inner diameter of 10.2cm. The quartz-steel interface was water-cooled, and sealed with a high-temperature silicone rubber compound. The length was based on studies by Sivasegaram and Whitelaw (Reference 15), who were able to obtain combustion instabilities for combustors with a restricted exit with $L/D \leq 5$. The combustor exit was restricted, to provide an acoustic boundary, so that the fundamental longitudinal mode in the combustor was a half-wave mode. The combustor exit diameter was 3.2 cm in diameter and was designed so that the combustor operating pressure was still nominally one atmosphere. The diffuser section, immediately upstream of the injector, was a 12.7 cm diameter by 99 cm long, stainless-steel pipe. Air was preheated up to 450°C using a 88 kW electric heater, and was choked at the diffuser inlet. Combustor inlet air temperatures were measured near the injector inlet. Air flow rates were measured using a rotameter (Fischer Porter Model 10A45575), and the fuel flow rates were measured using a digital mass flow controller (Hastings Model NAHL-25P). The fuel used was natural gas with a nominal methane content of 96%.

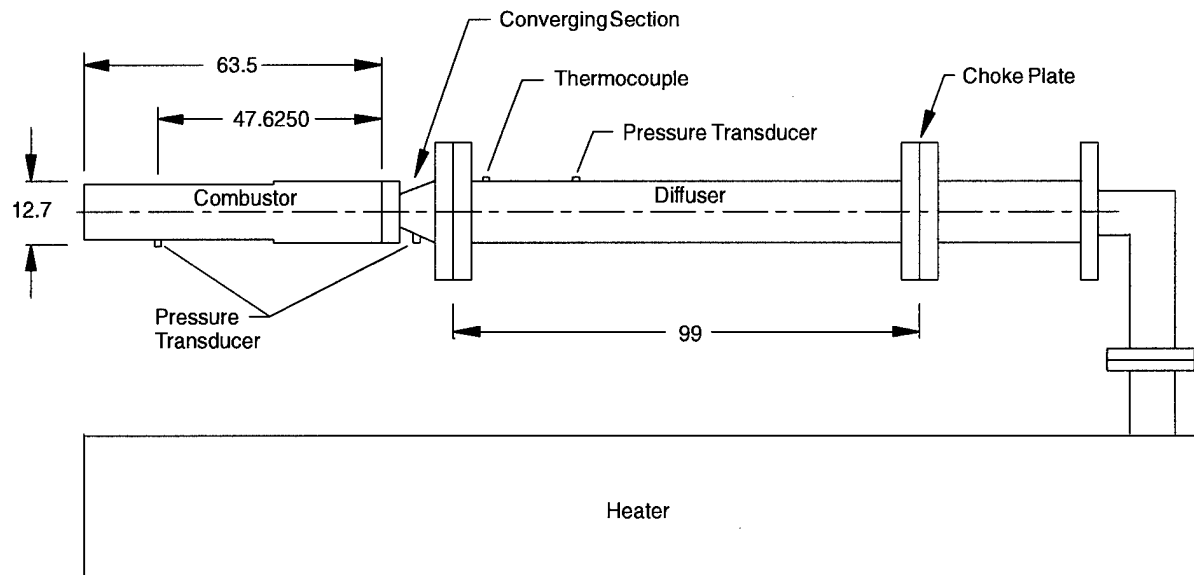


Figure 14. Schematic of Combustor Setup with DACRS-3X Injector.

High frequency, piezo-electric, pressure transducers (PCB Piezoelectronics Model P112A), housed in water-cooled jackets, were used to make pressure fluctuation measurements. Three pressure transducers were used, and they were located at the dump-plane, three-quarters the combustor length from the dump-plane, and in the fuel line located close to the injector. The dump plane transducer was actually mounted in the nozzle converging section and measures the dump-plane pressure through a 5 cm long duct with a diameter of 0.48 cm. Although this arrangement was not optimum for measurement of the dump-plane pressure fluctuations, the quartz-steel interface arrangement mandated such a compromise. The length of the duct was much less than the combustor length, and hence has a resonant frequency which was much greater than the frequency of the fundamental half-wave longitudinal mode in the combustor. Similarly, the phase difference between the dump-plane pressure and the pressure recorded by the transducer should be negligible. Pressure data was acquired over 5 seconds at 10 kHz sampling rate per channel.

Phase-averaged flame chemiluminescence images were taken using an intensified CCD camera (Princeton Instruments) and a 60 mm UV lens (Nikkor, $f=4.5$). A 350–600 nm broadband filter was used to collect chemiluminescence emitted by CO_2^* and CH radicals in the flame. The broadband filter was used to obtain sufficient signal-to-noise ratio. These images provide a qualitative measure of the heat release from the flame (Reference 7), and help determine the variation in the flame structure during the pressure fluctuation cycle inside the combustor. The imaging area was 18.75 cm by 12.5 cm. Each of the phase-averaged images was an accumulation of 20 instantaneous images. The trigger circuits used for the phase averaged measurements were the same as those used by Shih (Reference 16). Dump-plane pressure was used as the reference signal for acquiring the flame images. A low-pass filter was used to provide a clean signal to the camera triggering circuits. The phase-averaged images captured were line-of-sight images and therefore depict a distorted picture of the flame's actual heat release structure. A three-point Abel deconvolution scheme was used to extract the 2D flame brush data from the line-of-sight images (Reference 17).

In addition to phase-averaged, flame chemiluminescence images, total flame intensity fluctuations were also measured using a photomultiplier tube (PMT). The PMT was mounted 137 cm away from the combustor axis. A 430 nm bandpass filter (± 5 nm bandwidth) was used to collect CH chemiluminescence flame emission. These measurements provide a measure of the phase relationship between combustor pressure and heat release fluctuations.

4.0 Results and Discussion

4.1 1X DACRS

As part of the research program involving the 1X DACRS injector, parameters expected to have an effect on combustion instability were systematically varied, which included inlet temperature, combustion chamber length and swirl vane combination. Modes of instability were then identified and the corresponding stability maps produced. In an attempt to learn more about the mechanism responsible for the initiation and sustenance of combustion instability, efforts also focused on correlating combustion heat release with the observed pressure oscillations.

4.1.1 Characterization of Instability Modes

In any study of combustion instability, it was instrumental to know the acoustic pressure field, $p'(x,y,z,t)$ and to be able to correlate it to local heat release fluctuations through, for example, global response factors,

$$R = \frac{\int_V \int_T p'(V,t) \cdot q'(V,t) dV dt}{\int_V \int_T p^2(V,t) dV dt}$$

and other local Rayleigh indices. In the above expression for the global response factor, p' is the dynamic pressure, q' is the unsteady heat release, V is the volume and T is the period of the oscillation associated with the combustion instability. Hence, much effort was devoted, in the early stages of the project, to identify the modes of instability encountered and characterize $p'(x,y,z,t)$. This task was successfully achieved using the eight high-speed pressure transducers described in the previous section and shown in Figure 15. The high-speed pressure transducers and model combustor geometry were designed to allow flexibility in terms of positioning of the pressure

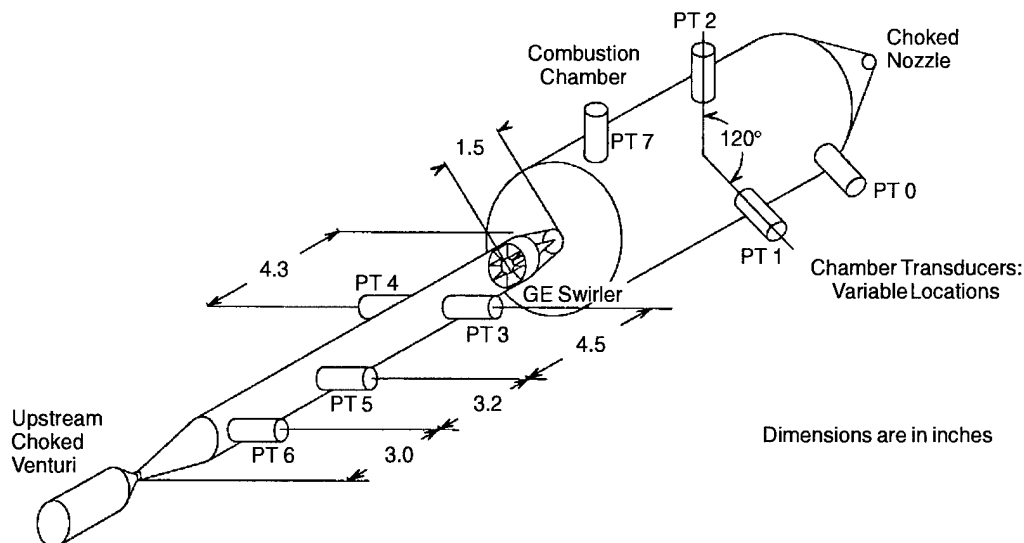


Figure 15. High Speed Pressure Transducer Locations.

transducers to assist in identification of the mode of the observed combustion instability. Whereas the four pressure transducers upstream of the injector remained at fixed locations, three or four pressure transducers were placed at locations in the combustor that were chosen for an optimum resolution of the instability modes. One pressure transducer (PT 0) was always placed at the same location to serve as a reference and comparison for all experiments. This pressure transducer was the most downstream of the eight transducers and was located 52 mm (2.05 in.) upstream of the exit nozzle. All experiments were conducted with sonic choked conditions at the exit nozzle and upstream venturi.

Almost every instability encountered displayed the same characteristic properties in terms of the observed modes and corresponding frequencies. A typical example is represented in Figure 16 for $\phi = 0.709$, $P_c = 0.304$ MPa (3 atm.), $L_c = 350$ mm (13.77 in) and $T_0 = 425^\circ\text{C}$ (800°F). The pressure records clearly show a strong mode around 1200 Hz superimposed with its much weaker first harmonic (see windows w1 and w2 of Figure 16). Pressure profiles from transducers located at the same axial but different angular locations were always nearly identical (see window w3 of Figure 16). Therefore circumferential modes can be ruled out. Since radial modes were very unlikely in such a small combustor, the two modes present were either bulk or longitudinal ones. Furthermore, pressure measurements from transducers located at different axial locations were always clearly out of phase (see window w4 of Figure 16), indicating that the two modes must be longitudinal. A simple 1-D analysis of the acoustics in the chamber indicates that the modes present were the first longitudinal mode of the combustion chamber and its harmonic. Using equilibrium properties of the flame

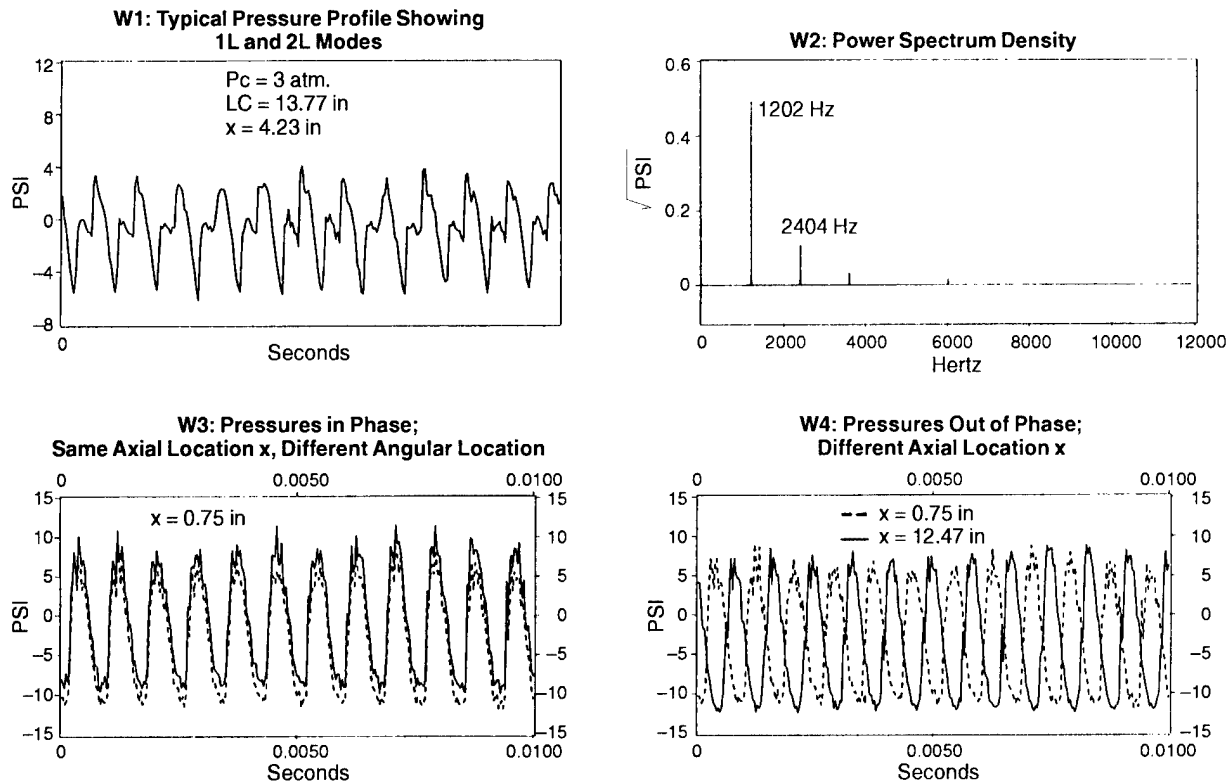


Figure 16. Identification of First and Second Longitudinal Modes of Observed Combustion Instability.

and taking L_c as the acoustic chamber length, the calculated frequencies for the 1L mode were in excellent agreement with the experimental values in the case of the 235 mm (9.25 in.) long chamber configuration. For this case, the calculated frequencies were always within 3.5% of the experimental observed values (see Figure 17a). Agreement was still reasonable but not as good for the longer 350 mm (13.78 in.) long chamber configuration where differences of between 7 and 19% were observed with the calculated frequencies being always higher than experimental observations (see Figure 17b). These differences could be due to higher heat losses through the cooled quartz and chamber walls, which lower the gas temperature and reduce sound speed and consequently the frequencies. Another and more probable cause was the fact that the dump plane was not a completely hard acoustic boundary. Some acoustical energy propagates upstream past the injector up to the choked venturi. This fact was confirmed by the four upstream transducers which pick up the same 1L+2L modes of the chamber, only somewhat attenuated (see Figure 18). Therefore a weak coupling was possible between the combustion chamber and the upstream manifold which could slightly shift the frequencies.

In any case, the important point was that the pressure profile in the combustor was well known and closely resembles that of a pure 1L (and 2L) standing wave in the combustor, between the dump plane and the exit nozzle (see Figure 19). It is important to note that the 2L mode was negligible compared to the 1L mode everywhere in the chamber, except in the middle part. In particular, only the 1L mode was of significance in the region of the heat release zone, whatever the flow conditions and chamber configuration employed. This was an important point that simplified the correlation between heat release and pressure instability. It should also be noted that although the modes and their associated frequencies were similar for the two chamber lengths, the amplitude of the observed pressure oscillations differed greatly for the two chambers.

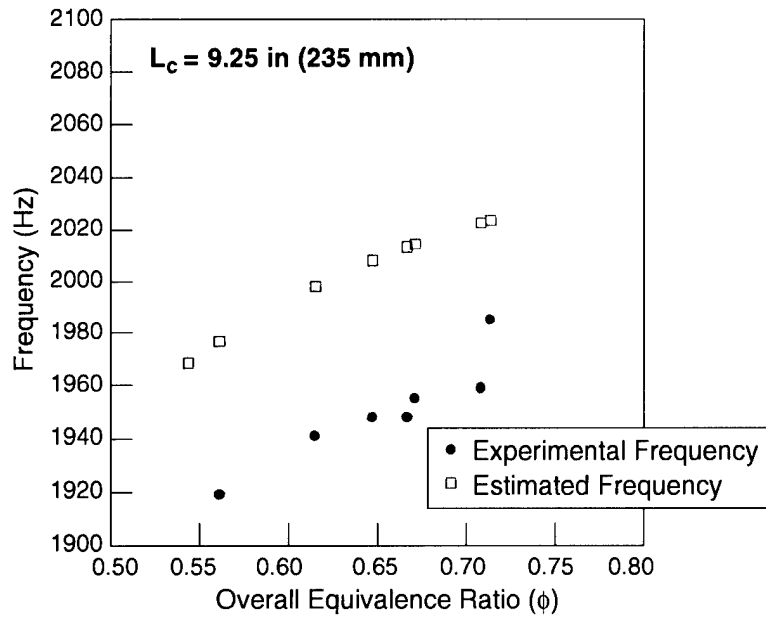
4.1.2 Stability Map

In conjunction with the systematic characterization of dynamic pressure fluctuations, stability maps have been constructed which plot the amplitude of the acoustic pressure signal from pressure transducer PT0, normalized by the mean chamber pressure, as a function of the equivalence ratio. Such maps show the influence of the different operating parameters on the amplitude of the observed instabilities.

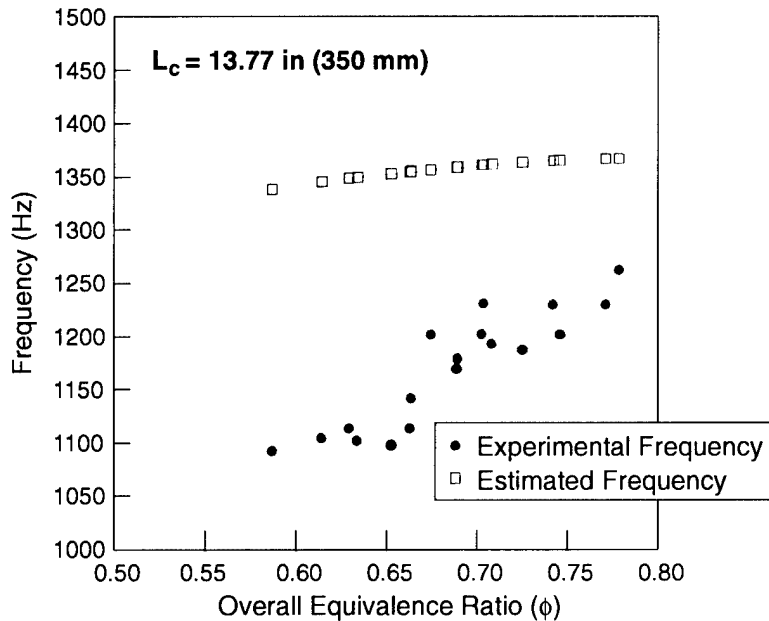
These instabilities have been reliably obtained under specific fixed operating conditions. They were characterized by significant fluctuations in chamber pressure recorded by the pressure transducers (see Figure 16) as well as a change in flame shape and luminosity detected by both a video (see Figure 20), an intensified CCD camera (see Figure 21), and a photo multiplier tube (PMT). Based on the results of the current study, the following parameters were found to influence the occurrence of combustion instability significantly: inlet air temperature T_0 , equivalence ratio, ϕ , chamber length, L_c , and the swirler configuration of the two DACRS injectors studied ($45^\circ/55^\circ$ and $55^\circ/65^\circ$).

4.1.2.1 235 mm Chamber Results

Using the $45^\circ/55^\circ$ 1X DACRS injector, tests have been conducted using the shorter ($L_c=235$ mm) of the two chamber lengths studied. For this chamber length, it was quite difficult to produce instabilities. In particular, higher chamber pressures and richer mixtures were needed, in fact, no instabilities were found at pressures equal to or less than 0.355 MPa (3.5 atm). Even when instabilities were present, the amplitudes were always fairly small with maximum values corresponding to



(a) 235 mm Long Chamber Configuration



(b) 350 mm Long Chamber Configuration

Figure 17. Calculated and Experimentally Observed Frequencies for 1L Mode.

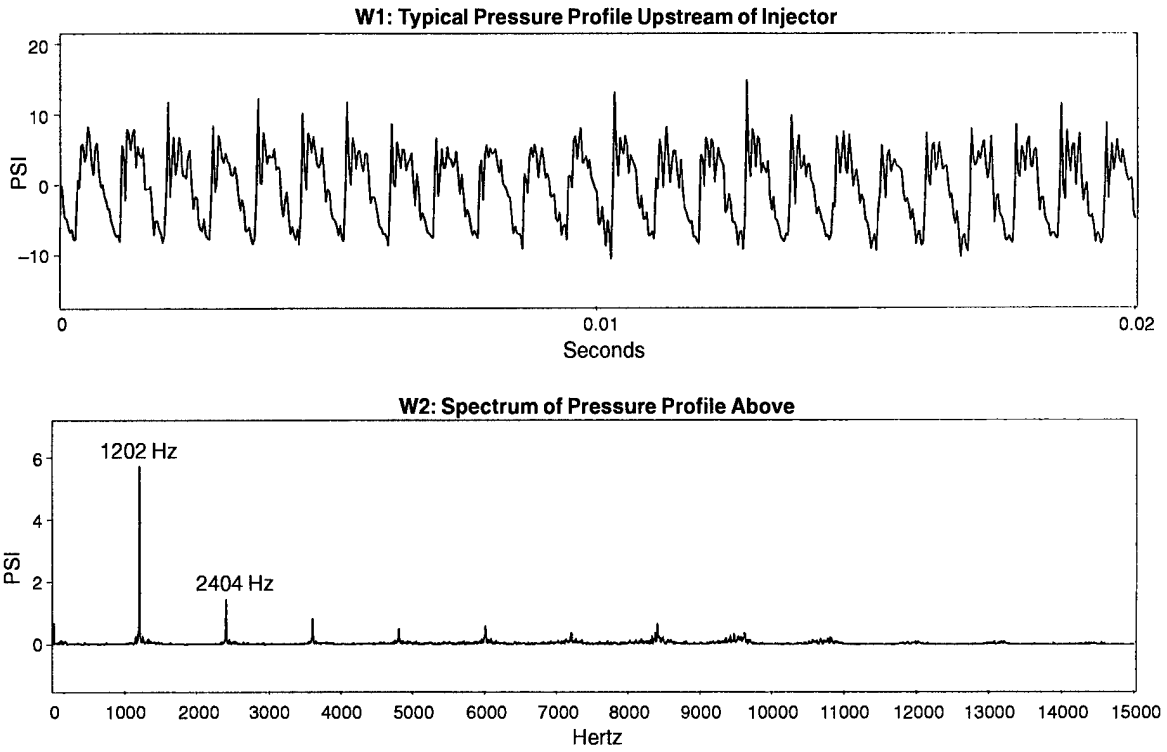


Figure 18. Typical Upstream Manifold Pressure Profile.

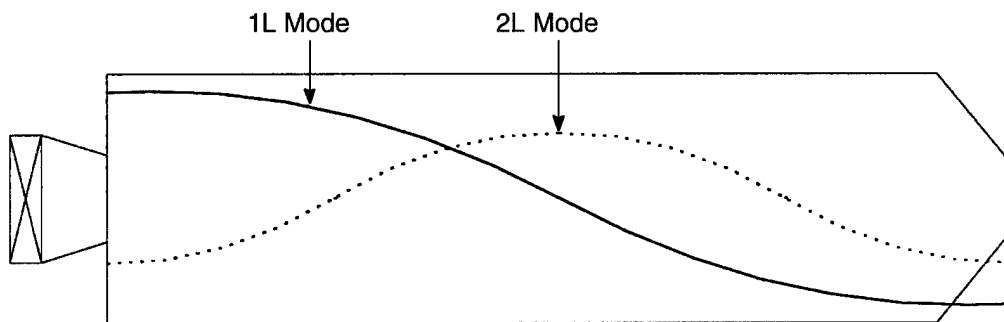
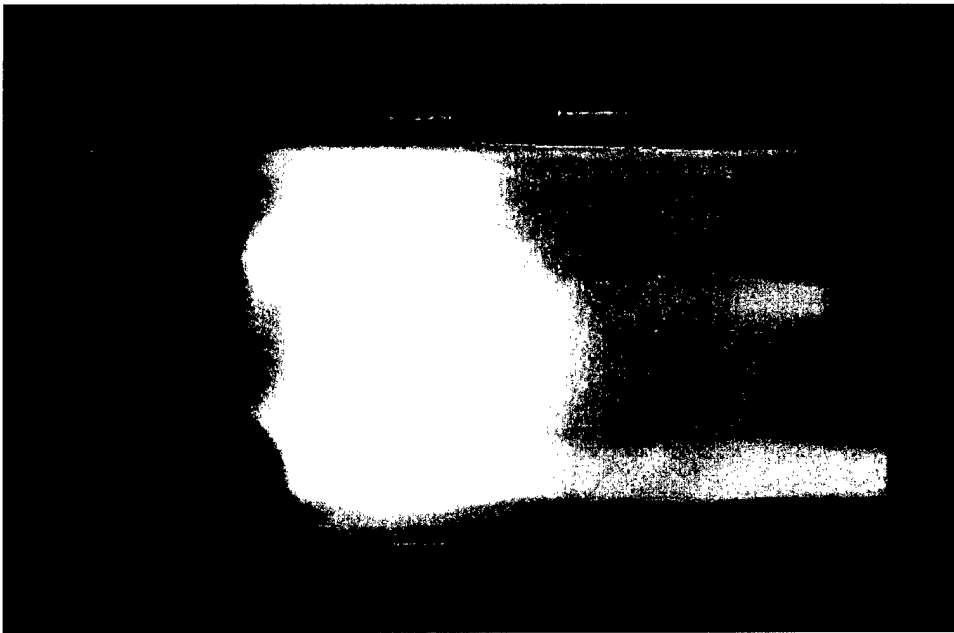


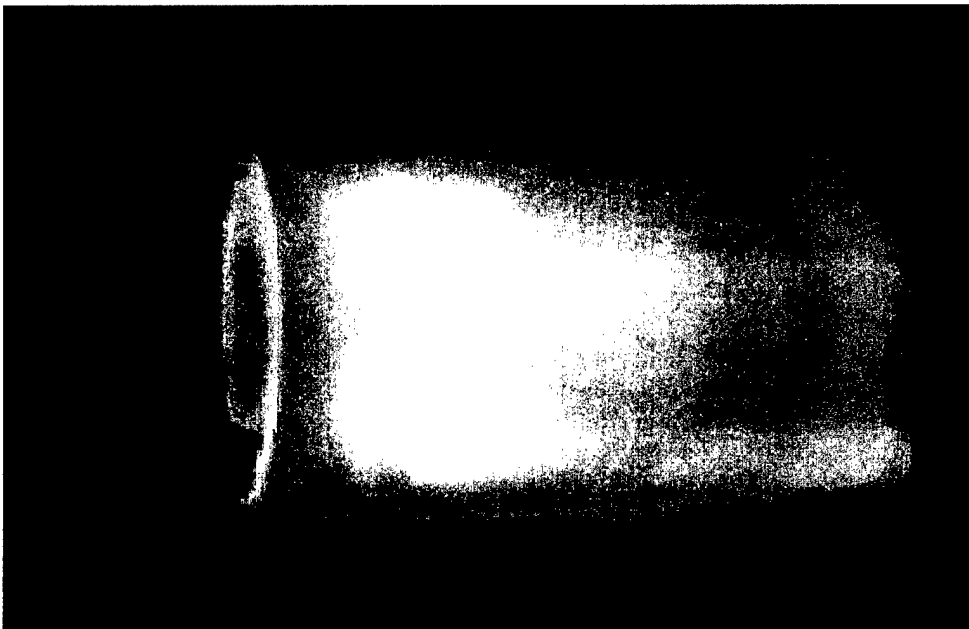
Figure 19. Theoretical Amplitude Profiles of 1L and 2L Modes for a Standing Wave in a Closed Chamber;

Stable Flame



$T_0 = 679\text{K}$, $P_c = 0.443\text{ MPa}$, $\phi = 0.58$, $\dot{m}_{\text{air}} = 50\text{g/s}$, and $L_c = 235\text{ mm}$

Unstable Flame



$T_0 = 715\text{K}$, $P_c = 0.443\text{ MPa}$, $\phi = 0.63$, $\dot{m}_{\text{air}} = 50\text{g/s}$, and $L_c = 350\text{ mm}$

Figure 20. Photographs of Stable and Unstable Flames with DACRS 45°/55° Swirler.

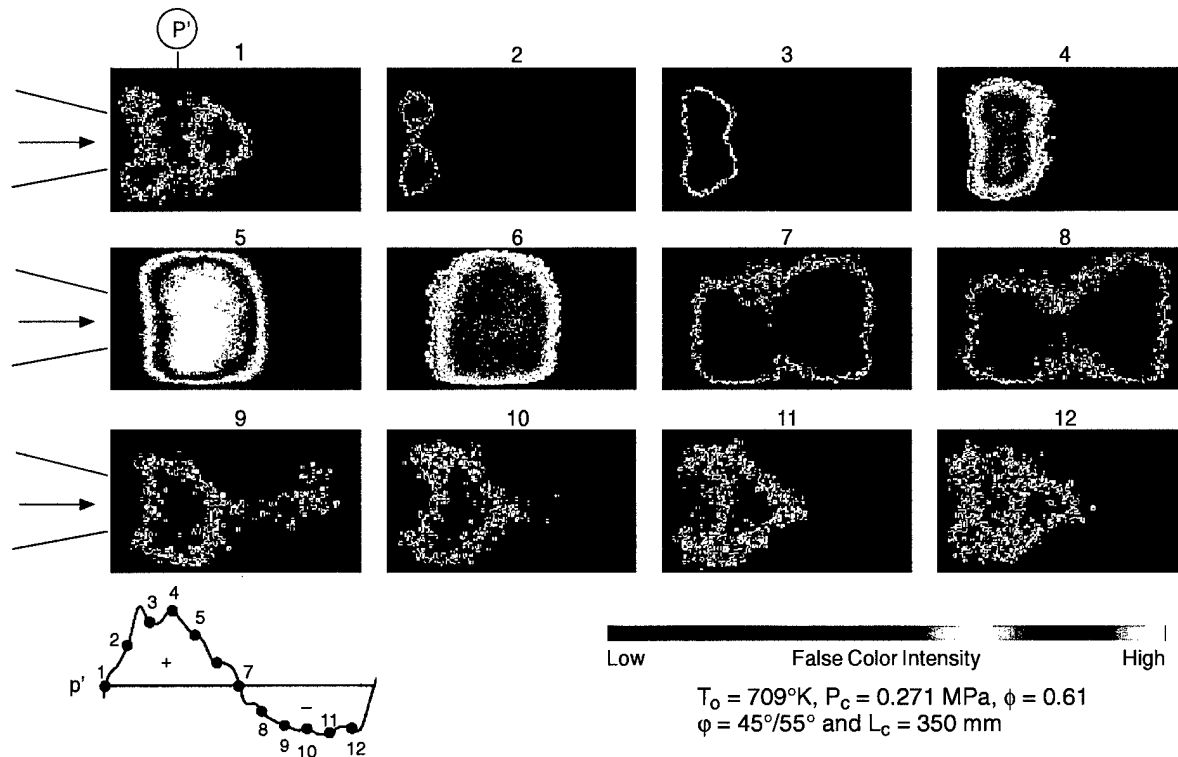


Figure 21. Phase-resolved CH Chemiluminescence Images (DACRS 45°/55°).

5% of P_c (see Figure 22). Please note that the RMS values of the pressure fluctuations have been multiplied by $\sqrt{2}$ to represent real amplitude values.

This result was in stark contrast with the behavior of a generic, straight vane, 45° single swirl injector fabricated in-house at Penn State and studied extensively under the same operating conditions. Figure 6 shows a schematic representation of the combustors used for both the PSU single swirl injector and the DACRS injector while Figure 23 shows the stability map of that PSU single swirl injector at three operating pressures. Unlike the DACRS injector, strong instabilities with absolute amplitudes of up to 18% of the chamber pressure ($\approx 12.5\%$ rms) can be repeatedly obtained at inlet air temperatures above 672 K (750°F). A possible explanation for that difference observed between the stability behavior of the two injectors was that the flame from the DACRS appears to be much more uniformly distributed and longer than the flame produced by the PSU single swirl injector. Therefore the local heat release was not able to couple to the maxima of pressure fluctuations p' (close to the dump plane) as effectively for the DACRS injector case and, consequently, combustion remains stable.

4.1.2.2 350 mm Chamber Results

Since only relatively weak instabilities were produced for the DACRS injectors with the short chamber ($L_c=235 \text{ mm}$), it was decided to install a longer chamber ($L_c=350 \text{ mm}$) and study the effect of chamber length on the instabilities. This longer chamber produced, indeed, drastically different instabilities with the following general trends. For both DACRS injectors, the flame becomes unstable if the inlet air temperature T_0 was higher than a threshold value $T_{0\text{min}} \approx 672 \text{ K}$ (750°F) and if the equivalence ratio ϕ was greater than $\phi_{\text{min}} \approx 0.59$. If those two conditions were not met simulta-

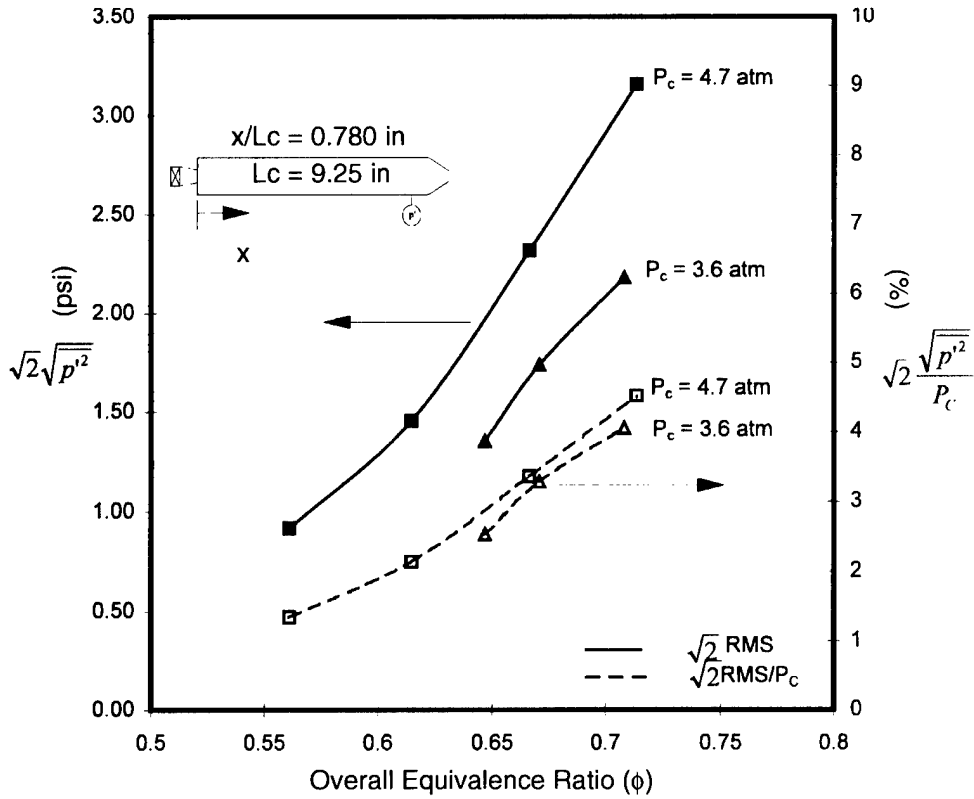
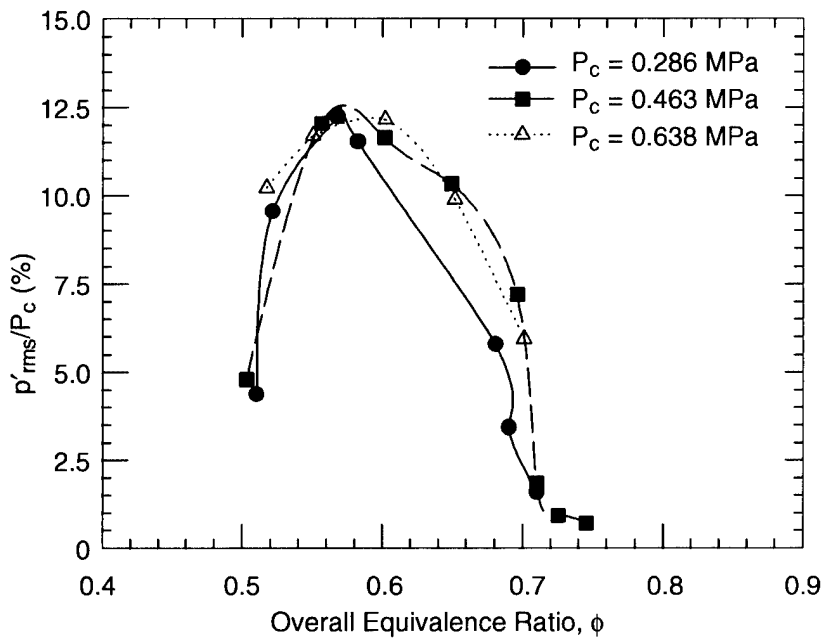


Figure 22. Absolute and Relative Amplitudes of Dynamic Pressure as a Function of Equivalence Ratio (Short Chamber Configuration).



$X_{inj} = 36.8$ mm, Swirl Angle = 45° , $T_0 = 670$ K

Figure 23. Equivalence Ratio and Chamber Pressure Effects on Strength of Instabilities.

neously, the flame will usually remain stable. The stability maps for both swirler configurations for the DACRS injectors were quite similar, with that for the 55°/65° swirler being slightly shifted towards leaner conditions (see Figure 24). Both curves showed very high maxima with respect to amplitudes of the observed combustion instabilities (18% rms of the chamber pressure P_C , i.e. more than 25% absolute amplitude). At higher values of ϕ , the instabilities became weaker but were still substantial. Another important trend was that the instabilities die out at the leanest conditions well before LBO, which typically occurs around 0.48–0.50. This was particularly interesting to note since combustion instabilities were commonly thought to occur (or at least worsen) towards the leanest conditions.

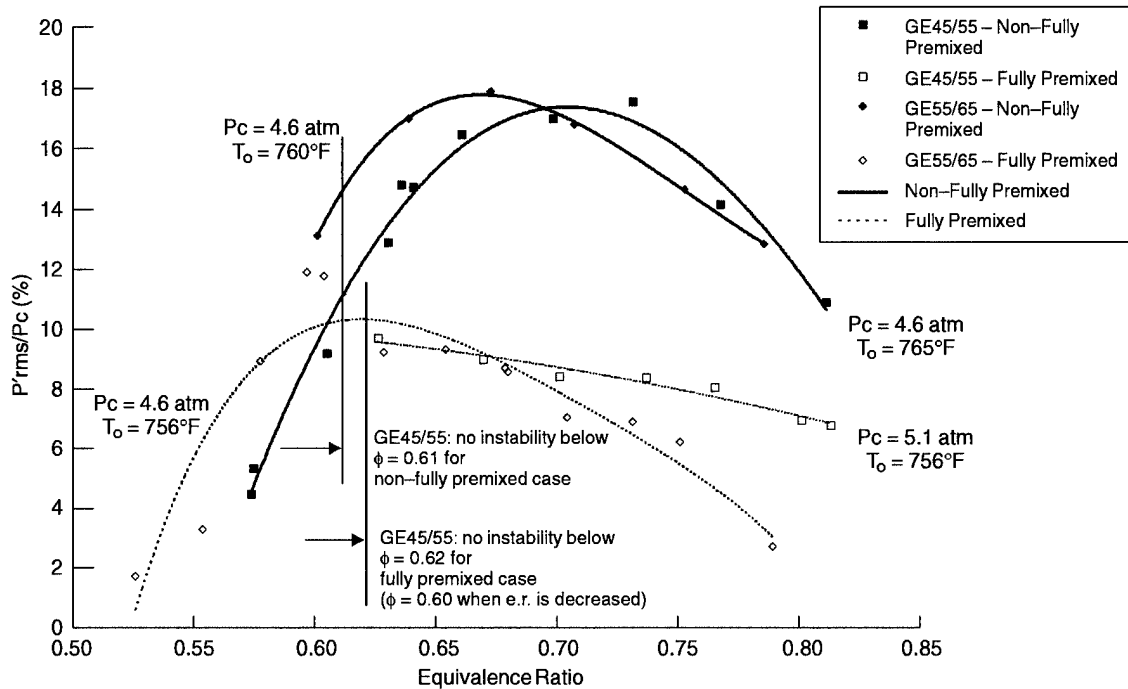


Figure 24. Stability Map for DACRS Injectors.

For a fixed $\phi > \phi_{min}$, inlet air temperatures higher than T_{0min} did not appear to alter the strength of the instabilities significantly (see Figure 25). However, if T_0 is reduced below T_{0min} once the flame was unstable, the instabilities generally weakened but did not disappear until T_0 was significantly reduced below T_{0min} , sometimes to levels as low as 616–628K (650–670°F). This important hysteresis effect with respect to temperature has also been observed for equivalence ratio, that is flames remain unstable even below the minimum equivalence ratio ϕ_{min} at which they initially became unstable.

It should be noted that T_{0min} has a slight dependence on equivalence ratio. Specifically, it decreases slowly with ϕ , for example $T_{0min} \propto 678 \text{ K (760}^\circ\text{F)}$ at $\phi=0.59$ and $T_{0min} \propto 655 \text{ K (720}^\circ\text{F)}$ at $\phi=0.70$. Hence, richer mixtures will tend to go unstable slightly before leaner mixtures. This same trend was also observed and even amplified with the hysteresis effect mentioned above, i.e.; unstable flames at richer conditions remain unstable at a lower T_0 , which was lower than the corresponding T_{0min} , than lean flames. This explains why, in Figure 25, the flame at $\phi=0.68$ was still unstable at $T_0=633 \text{ K (680}^\circ\text{F)}$ while it was already much less unstable at $\phi=0.62$.

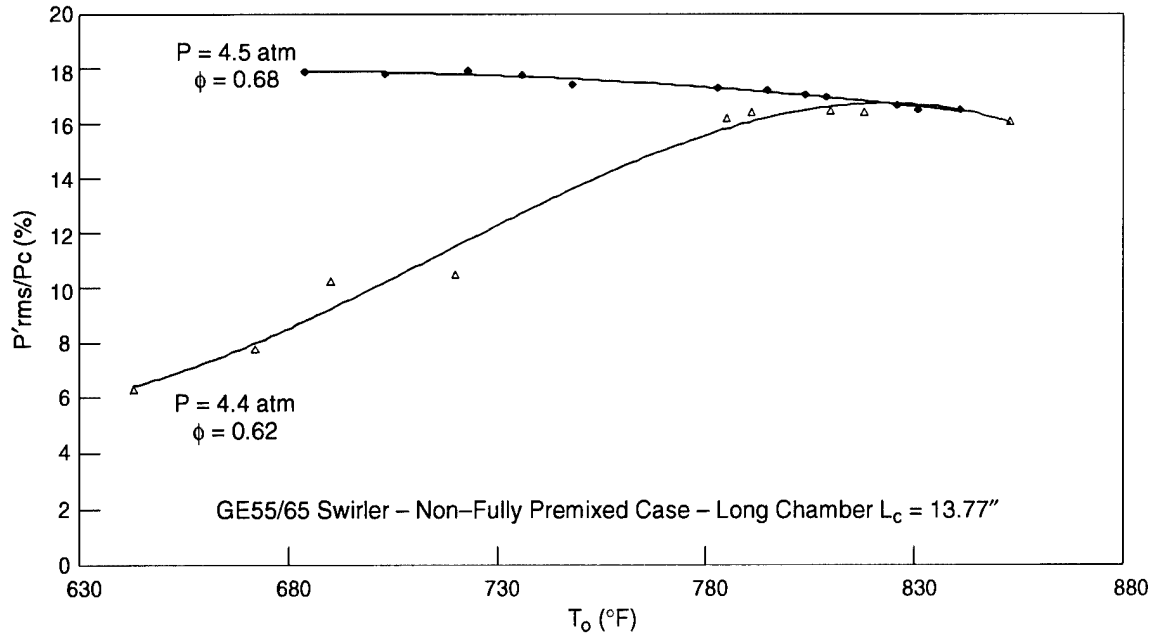


Figure 25. Inlet Air Temperature Effect on Instabilities.

All the results obtained for the DACRS injectors were in stark contrast with those obtained with the PSU single swirl injector for the same longer chamber length ($L_c=350$ mm). The most obvious difference was the effect of T_0 . With the PSU single swirl injector, combustion was always unstable below a threshold temperature $T_{0max} \approx 689$ K (780°F) and becomes stable if T_0 is increased above T_{0max} . Moreover, for a fixed ϕ , the amplitude of the instability increases sharply as T_0 is decreased, until the flame blows out (see Figure 26). Just before blow out, the amplitude was very high (17% rms of P_c). Therefore, T_0 has opposite effects on the PSU single swirl and GE DACRS injectors in the 350 mm long chamber. Furthermore, for $T_0 < T_{0max}$, instabilities were produced at much leaner conditions for the PSU single swirl injector, especially at higher chamber pressures (see Figure 27), with the maximum pressure amplitudes occurring between LBO ($\alpha \approx 0.50$) and 0.55. Again, these drastically different behaviors were probably due to the very different swirler configurations as well as the different combustor inlets. Recall that the PSU single swirl injector had a straight inlet with a bluff body while the DACRS injector had a tapered inlet with a very small centerbody as shown in Figure 6. These differences produced, in turn, very different flame patterns and anchoring characteristics and therefore different flame responses to combustion instability mechanisms.

Some experiments were conducted in a fully premixed mode with both GE DACRS injectors. Instead of injecting the natural gas normally through the swirl vanes, it was decided to cap the swirler fuel manifold and to inject the fuel upstream of the inlet choked venturi. The goal of this procedure was to ensure a completely uniform premixed combustible mixture entering the combustor and also to provide a fixed, constant equivalence ratio independent of the presence of any combustion instability. It was actually possible to produce strong instabilities in this manner even though these instabilities were always significantly lower in amplitude than those observed for the normal injection case. The corresponding stability maps for both DACRS injectors were represented by the dashed lines shown in Figure 24. The maximum amplitude of the observed combustion instabilities under these fully premixed conditions was about the same for both DACRS injectors (about 10%

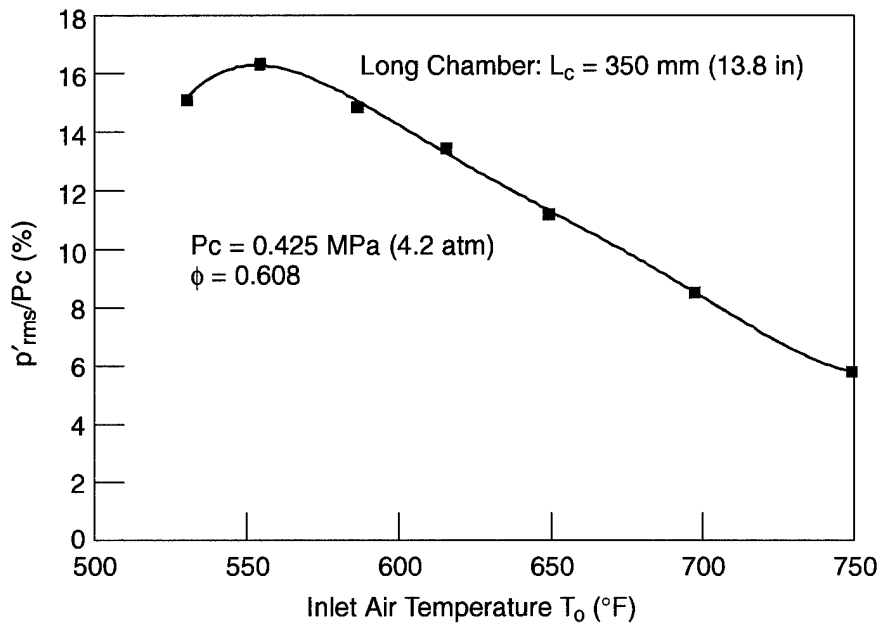


Figure 26. Inlet Air Temperature Effect on Strength of Instabilities (PSU Swirler).

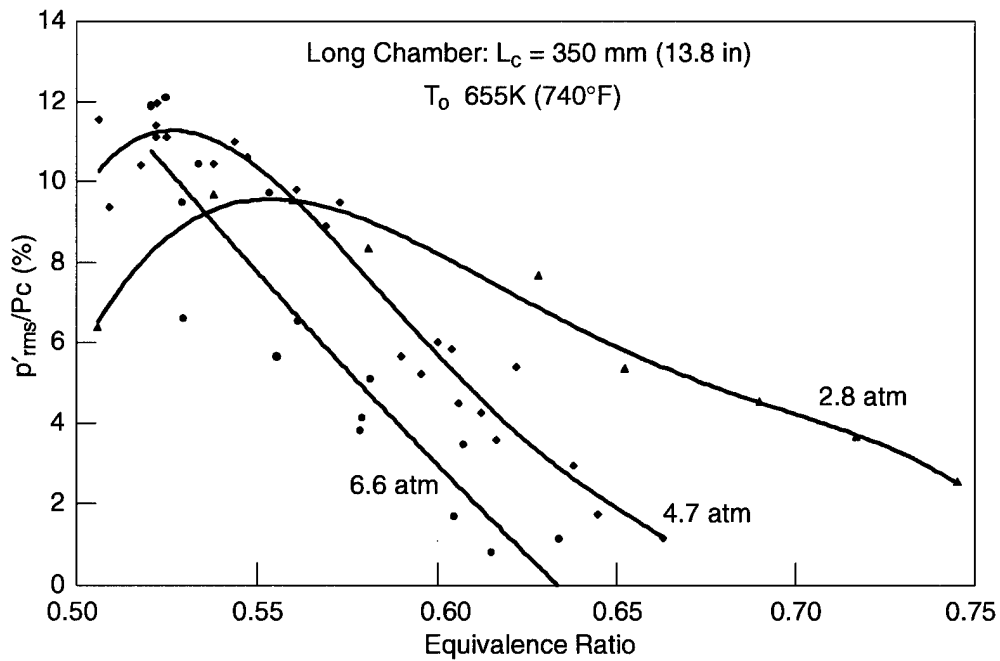


Figure 27. Stability Map as a Function of Chamber Pressure (PSU Swirler).

rms of P_c), but the shape of each stability curve was quite different. For the $45^\circ/55^\circ$ DACRS swirler, no instabilities were observed for $\phi < \phi_{\min} \approx 0.62$ or $\phi_{\min} \approx 0.60$ for decreasing ϕ due to hysteresis effects again. However, when ϕ was increased above ϕ_{\min} , instabilities set-in suddenly and then decreased only slowly at richer conditions. For example, p'_{rms}/P_c was still about 7% when ϕ was beyond 0.8. For the $55^\circ/65^\circ$ DACRS swirler, the stability curve follows a more classic dome shape, with unstable conditions occurring only when $0.53 < \phi < 0.80$.

A possible explanation for the lower pressure amplitudes observed for the combustion instabilities obtained during fully premixed operation (nearly half the amplitude of those observed when the fuel was injected through the swirl vanes) was the absence of one mechanism often seen as playing a major role in driving instabilities, namely, equivalence ratio modulation (Reference 18 and 19). Since all experiments were conducted with a choked upstream venturi, pressure oscillations could not propagate upstream past the venturi. Hence, by injecting the fuel before the upstream choked venturi, the equivalence ratio was kept constant, decoupled from and independent of any instability occurring downstream. Under these conditions, there cannot be any equivalence ratio modulation. The fact that combustion instabilities occur anyway, although at a lower strength, indicates that in these fully premixed experiments, other mechanisms were responsible for the sustenance of the observed instabilities. This result was not really surprising since combustion instabilities were often the result of several mechanisms coupled together. One such mechanism could be a total mass flow rate modulation.

4.1.3 Acetone PLIF for Mixing Studies in Non-reacting Flows

One of the program goals was to quantify the quality of the natural gas/air premixing at the entrance of the combustor for both DACRS injectors. Hence, cold flow experiments were carried out using acetone PLIF seeded in the air. These experiments were conducted by carefully matching the conditions of a corresponding combustor case to insure the relevance of the results. In particular, the air mass flow rate, pressure, inlet air temperature and velocity were kept the same (≈ 50 g/s, 0.47 MPa, 670K and 46 m/s at the swirler, respectively). Moreover, the liquid acetone was fully prevaporized and mixed with helium in the proper proportions to match the natural gas injection momentum as closely as possible. This procedure provided the best approach in terms of maintaining the same fuel and air mixing dynamics while yielding satisfactory concentrations of acetone for laser-induced fluorescence (LIF) measurements.

For the LIF measurements, the fourth harmonic of an Nd:YAG laser operating at a wavelength of 266 nm was used to excite the broad band acetone fluorescence. An ICCD camera was focused on the entrance region of the combustor, directly after the dump plane, to record the 2D fluorescence image with satisfactory resolution. The degree of premixing of the fuel with air was calculated using the unmixedness parameter, U , defined as $U = \overline{C'^2} / (\overline{C}(1-\overline{C}))$ where C denotes the acetone concentration. A plot of U across the cylindrical chamber at the dump plane is presented in Figure 28 for both DACRS injectors. The unmixedness was calculated based on the intensity fluctuations of single-shot acetone PLIF images. Hence, at any point in the spatial profile, the lower the value of the unmixedness, the better the premixing between fuel and air. The same measurements carried out at varying axial locations in the combustor are presented in Figure 29. As could be expected, the higher swirl injector configuration ($55^\circ/65^\circ$) mixes the fuel and the air better and the unmixedness profile was essentially flat for that injector very close to the dump plane ($x/D_c = 0.18 \Rightarrow x = 8$ mm), indicating excellent mixing downstream of that location. For the $45^\circ/55^\circ$ swirler configuration, the

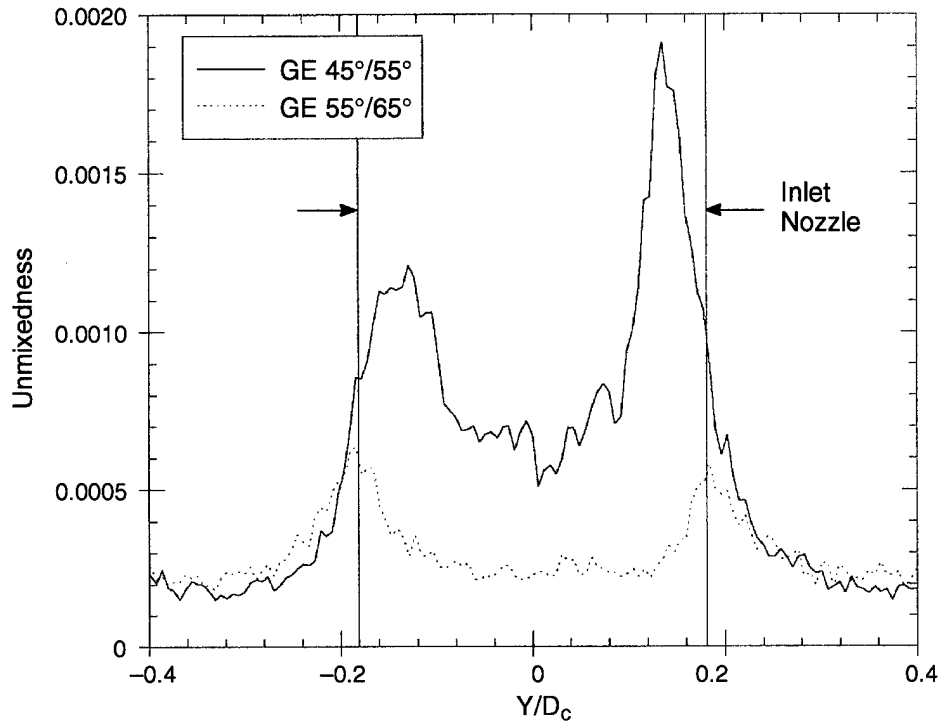


Figure 28. Unmixedness at $x=5.5\text{mm}$ from Dump Plane (DACRS Injectors).

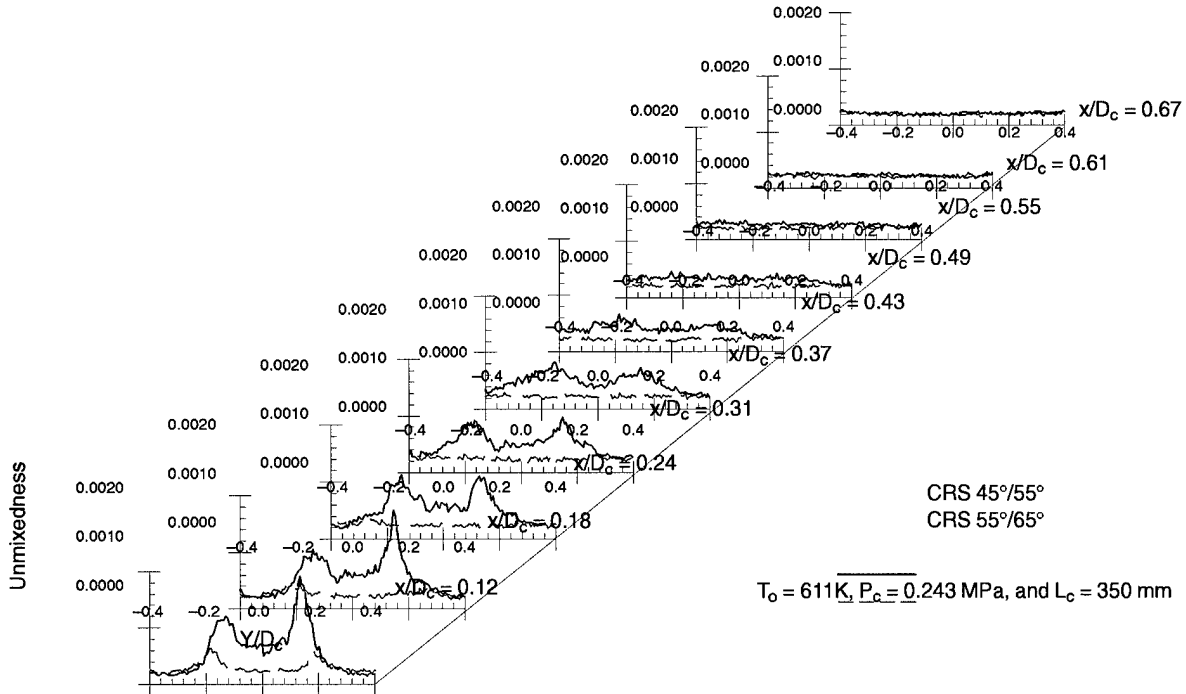
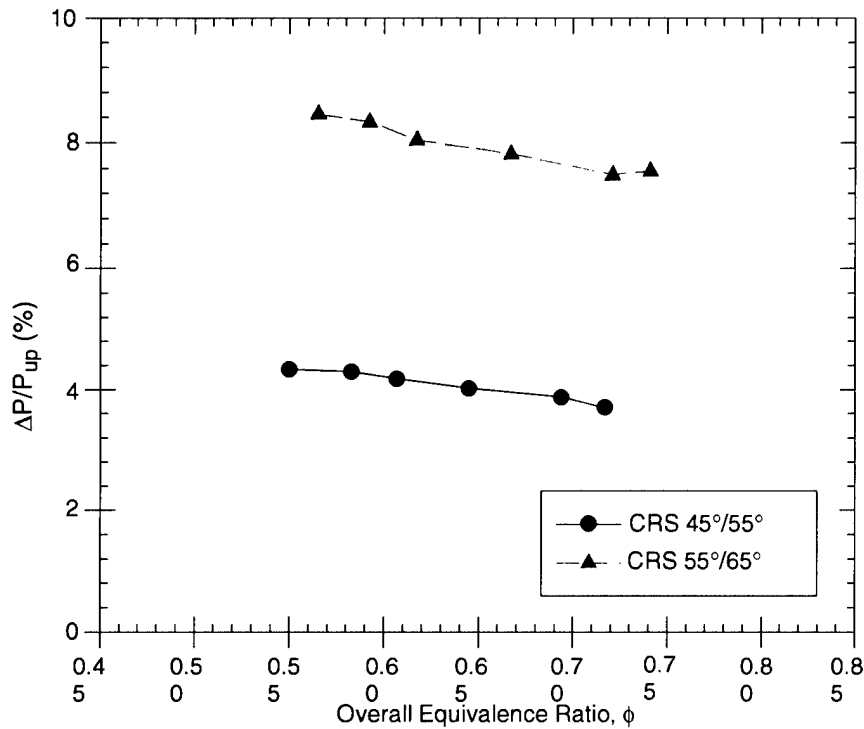


Figure 29. Unmixedness Profiles of DACRS Injectors.

mixing was not quite as good but the low values of U (0.002 max.) even at an $x/D_c = 0.12$ ($x = 5.5$ mm) after the dump plane indicate that mixing was still good. Of course, the better mixing produced by the $55^\circ/65^\circ$ swirler configuration comes with a higher penalty in terms of the pressure drop ($\Delta P \approx 8\%$ versus only 4% for the $45^\circ/55^\circ$ configuration, see Figure 30). Finally, the stability maps obtained for both DACRS swirler configurations were very similar, which indicates that the difference in mixing performance in both cases was negligible as far as combustion instability behavior was concerned. It may therefore be concluded that the $45^\circ/55^\circ$ swirler configuration was better suited since it produces a much less pressure drop without sacrificing combustion stability and, as will be shown below, this injector also produces very similar levels of pollutant emissions to the $55^\circ/65^\circ$ configuration.



$T_o = 710K$, $P_c = 0.454$ MPa, $\bar{m}_{air} = 50g/s$, $U_o = 47$ m/s, and $L_c = 235$ mm

Figure 30. Pressure Drops Across DACRS Injectors.

4.1.4 Phase-resolved Images of Unstable Combustion

As mentioned earlier, the relationship between heat release and pressure oscillations was instrumental in understanding combustion instabilities. Thus, another ongoing priority of the project was to improve the heat release visualization and its correlation to the local pressure fluctuations during unstable combustion. Several phase-resolved imaging techniques were employed involving imaging of some key intermediate radicals at different instants of the dynamic pressure cycle. Since pressure transducers can obviously not be mounted on the quartz section, the experiments were carried out in two steps. First, the quartz section was placed at the heat release location (between 2 and 7 cm from the dump plane), and images of an unstable flame were taken in reference with the pressure cycle given by pressure transducer PT0. Between 20 and 50 images were taken and averaged for each of 12 phase angles corresponding to 30° , 60° , 90° , 120° , 150° , 180° , 210° , 240° ,

270°, 300°, 330° and 360° of the cycle. In the second step of the study, the quartz chamber was then moved downstream and replaced by two stainless steel chambers in such a way that pressure transducer PT1 was then located at the heat release zone (this location is indicated in the first image of Figure 31). The experiment was then duplicated but this time the pressure signals PT0 and PT1 were simultaneously recorded. Thus, the emission images taken during the first step can be indirectly, but accurately, compared as a function of time with the pressure fluctuations at the same location.

First, OH LIF images were taken at different phases of the local (1L mode) pressure cycle (see Figure 31). The images clearly show the presence of OH intermediate radicals not only near the heat release location (near the dump plane) but also quite a bit further downstream. This result was expected since the OH radical was involved in slow recombination reactions and was therefore usually spread throughout the post flame zone as well as in the flame reaction zone. For this reason, OH LIF does not seem very well suited for precise heat release visualization.

It was then decided to take phase-resolved CH chemiluminescence images of the unstable flame. The CH radical has been extensively used as a marker of heat release since it was believed to be a short lived, intermediate radical produced only during strong exothermic reactions accounting for most of the heat release. These CH images are shown in Figs. 32(a) and 32(b) and correspond to the 45°/55° and 55°/65° DACRS injectors respectively. They clearly indicate a strong temporal correlation between the dynamic pressure and the CH chemiluminescence and reveal a much better resolved heat release signal both from a temporal and spatial point of view than the OH LIF images. During the minimum of the local pressure fluctuations, the flame was particularly weak but when the pressure fluctuation rose and approached its maximum value, the flame became quite intense. Hence, the heat release occurs precisely during the maximum of the pressure amplitudes corresponding to images 2 through 6, which satisfies the Rayleigh criterion.

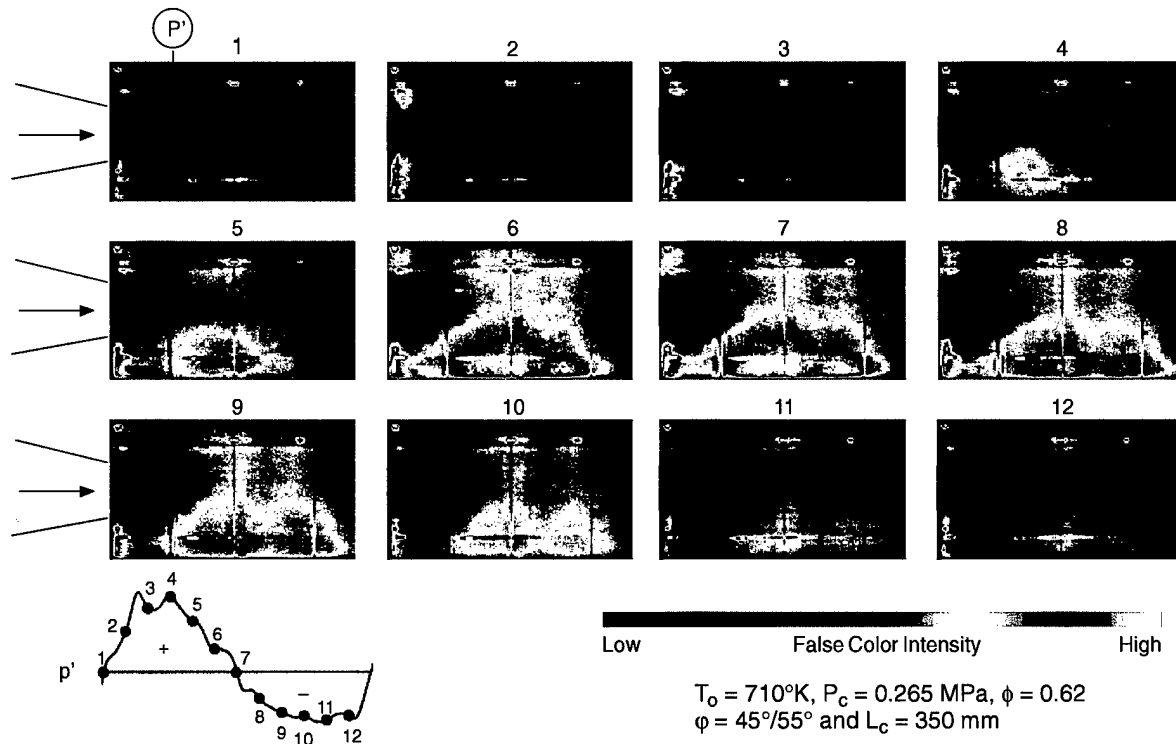
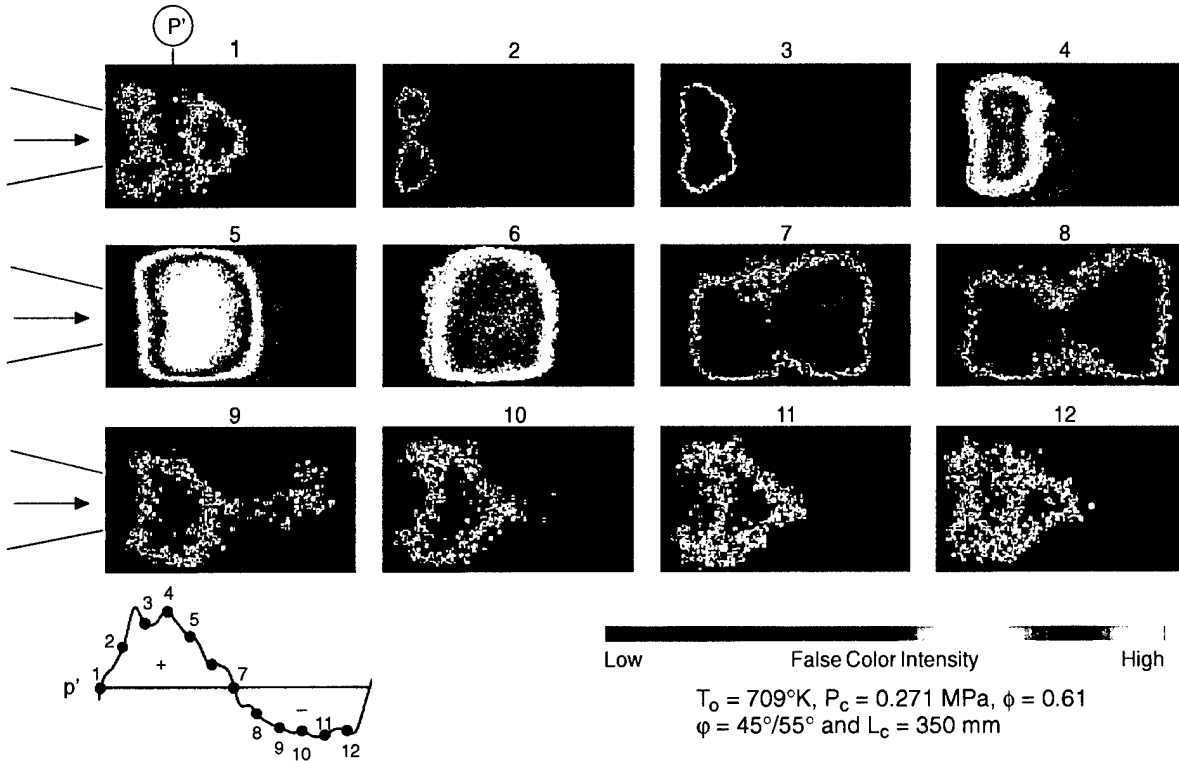
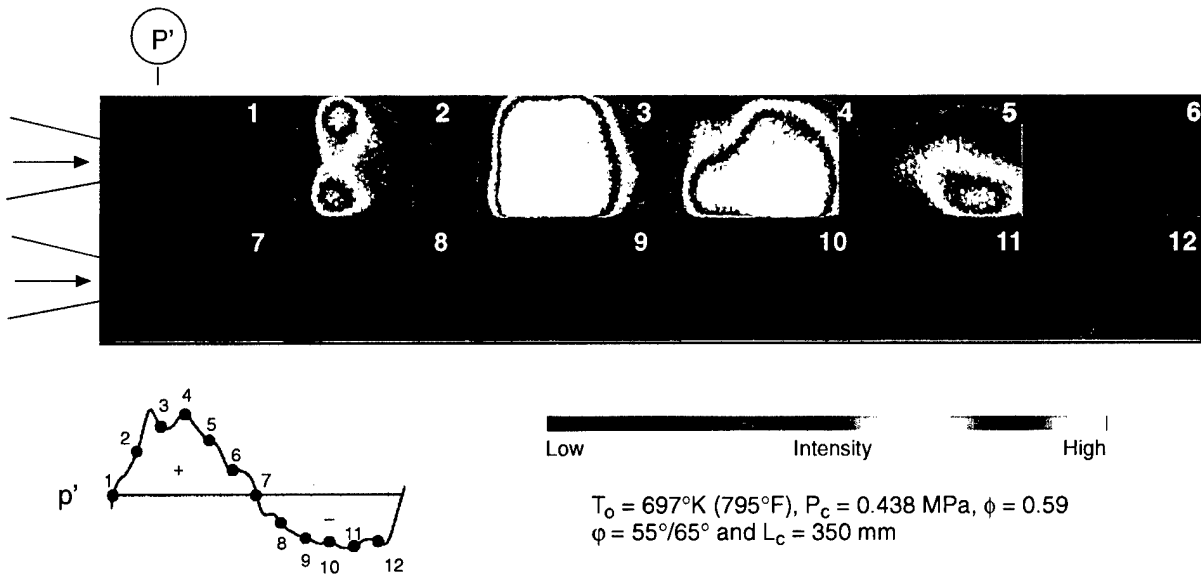


Figure 31. Phase-locked Average OH PLIF Images.



(a) 45°/55° DACRS Injector



(b) 55°/65° DACRS Injector

Figure 32. Phase-resolved Chemiluminescence Images (DACRS 45°/55°).

4.1.5 Emissions

In order for a combustion instability study to be really meaningful, great care must also be given to engine performance and pollutant emission. High engine efficiencies and low emissions were both absolute requirements. Hence, NO, NO₂, CO₂, O₂ and CO emission values have been systematically monitored in the study. Plots of NO_x and CO concentrations versus ϕ are presented in Figure 33. The trends displayed were typical of those observed in actual LPM gas turbine engines. At lean conditions, NO_x and CO concentrations were below 10 ppm and sharply increase with ϕ to reach 100 ppm levels at richer conditions ($\phi > 0.75$). Both injectors behave very similarly, only the 55/65° injector generates very slightly lower emissions, which was probably due to its ability to premix air and fuel somewhat better as indicated in the PLIF acetone mixing studies (Figures 28 and 29).

4.2 3X DACRS

4.2.1 Stability Regimes

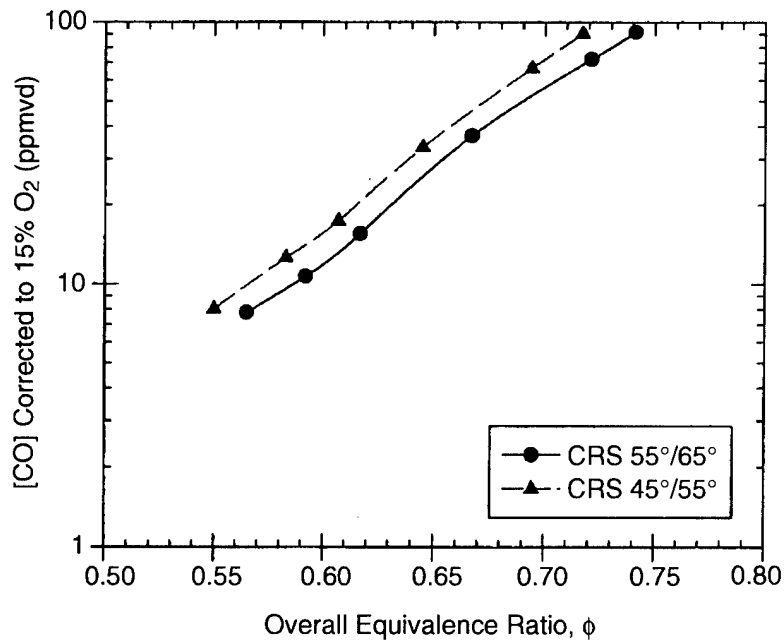
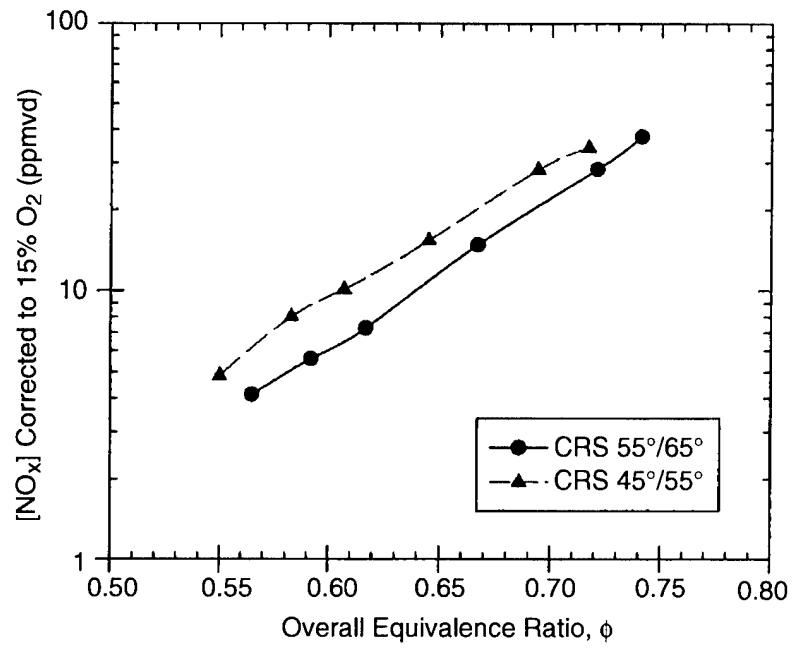
The stability characteristics of the single-injector combustor with the 3X DACRS injector were presented in the form of stability maps, which were plots of the relative rms pressure fluctuation ($p_{rms}/p_{mean} \times 100$) versus equivalence ratio at specific inlet air temperatures and combustor velocities. The test conditions that were varied are as follows:

Combustor velocity:	5 m/s, 10 m/s
Inlet air temperature:	400°C, 450°C
Equivalence Ratio:	LBO – 0.90

While mapping the stability characteristics of the combustor at the above conditions, the combustor velocity and inlet air temperature were fixed and the equivalence ratio was varied. To avoid hysteresis effects, the equivalence ratio was always varied from LBO to 0.90.

Figure 34 shows the relative rms pressure fluctuation plotted versus equivalence ratio at the various conditions studied. As can be seen in this figure, there were distinct regions of both stable and unstable combustion over this range of operating conditions. For example, the strongest instabilities were observed at the 5 m/s, 400°C operating condition (open circles) when the equivalence ratio was near 0.7. In this case the relative rms pressure fluctuations were near 17%. The strength of the instability though falls off at both lower and higher equivalence ratios, such that combustion was relatively stable at equivalence ratios below 0.6 and above 0.8. The effect of equivalence ratio on the stability characteristics, however, was not repeated at other inlet temperatures and combustor velocities. For example, by simply increasing the inlet temperature to 450°C there was a marked change in the stability characteristics. In this case combustion appears to be stable from LBO to an equivalence ratio of 0.9, except for two regions of relatively weak instabilities near equivalence ratios of 0.62 and 0.83. Similarly, there were changes in the stability characteristics when the combustor velocity and again the inlet temperature were changed. Unfortunately, there was no apparent pattern to these changes. For example, the effect of increasing the inlet temperature at a combustor velocity of 5 m/s was not the same as it was for 10 m/s. Clearly the critical challenge in understanding combustion dynamics was developing a phenomenological model that can explain such complex behavior.

The complexity of this phenomenon was further illustrated by the frequency spectra of the pressure fluctuations at the different operating conditions. Two dominant frequencies, i.e.; 130Hz and 670Hz,



$T_0 = 710\text{K}$, $P_c = 0.454\text{ MPa}$, $\bar{m}_{\text{air}} = 50\text{g/s}$, $U_0 = 47\text{ m/sec}$, and $L_c = 235\text{ mm}$

Figure 33. NO_x and CO Emissions of DACRS Injectors.

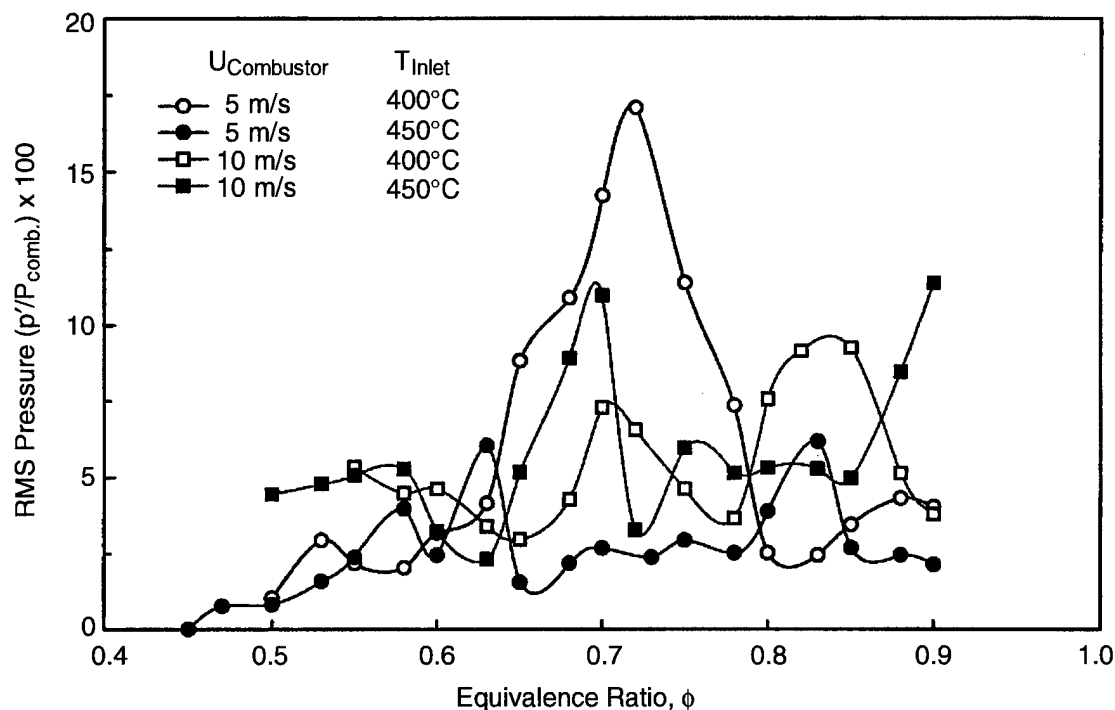


Figure 34. Pressure Fluctuation vs. Equivalence Ratio. Variation in sound levels with equivalence ratios at the different combustor conditions to determine the stability regimes of the combustor.

were found to occur in the frequency spectra over the range of equivalence ratios, inlet temperatures and combustor velocities tested. Cross-correlation between the pressure signals from the dump-plane transducer and the transducer located at $3/4 L$ from the dump-plane show that the two signals were nearly in phase at the lower frequency. This suggests that the lower frequency corresponds to a bulk mode pressure oscillation. Phase differences at the higher frequency indicate that the pressure oscillations at this frequency correspond to a longitudinal mode instability. The 670 Hz frequency also agrees well with the estimated frequency of the fundamental, half-wave, longitudinal mode in the combustor. Typical frequency spectra of the pressure signal at the dump plane were plotted in Figures 35 and 36, for an operating condition of 400°C and 5 m/s at two different equivalence ratios, 0.65 and 0.72 respectively. In the 400°C , 5 m/s, equivalence ratio 0.72 case, which corresponds to the strongest instability which was observed over the range of test conditions studied, the strongest pressure fluctuations were associated with the 670 Hz longitudinal mode. However, when the equivalence ratio was changed to 0.65, not only did the overall strength of the instability decrease by approximately a factor of two (see Figure 34), but the strongest pressure fluctuations were then associated with the 130 Hz bulk mode instability.

Also shown in Figure 35 and 36 are the frequency spectra for the fuel supply pressure measurements. Fuel supply pressure oscillations at 130 Hz were observed at all unstable operating conditions, however, at some equivalence ratios a somewhat weaker oscillation was also observed at 670 Hz. Fluctuations in the fuel supply pressure suggest that fuel system coupling may be driving the observed instabilities. Fluctuations in the fuel supply pressure cause fluctuations in the fuel flow rate which can lead to temporal fluctuations in the local equivalence ratio in the combustion zone, which in turn cause heat release fluctuations and also local flame extinction. In order to assess the impor-

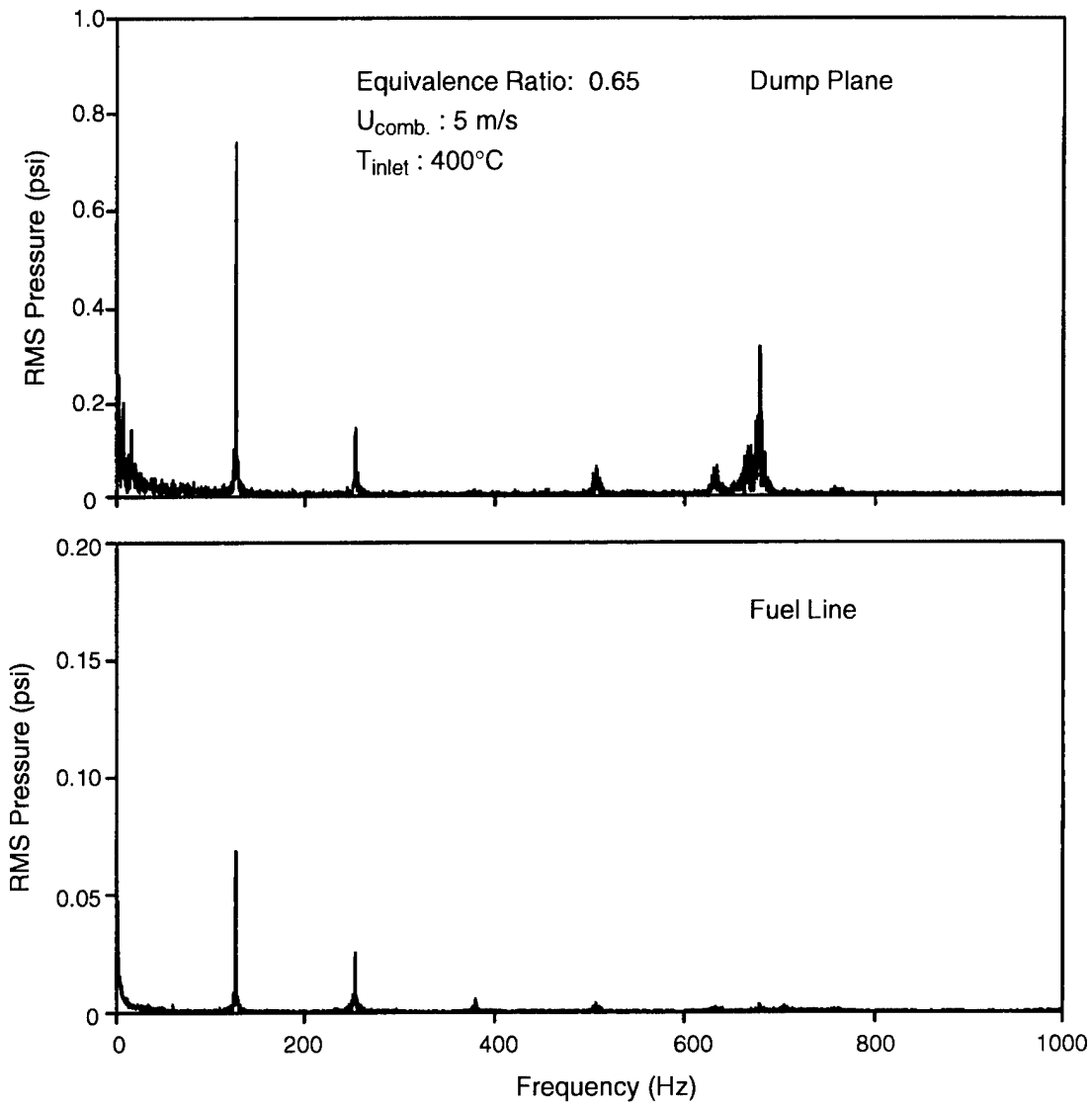


Figure 35. Pressure Signal Frequency at the Dump Plane and Fuel Line – Equivalence Ratio 0.65.

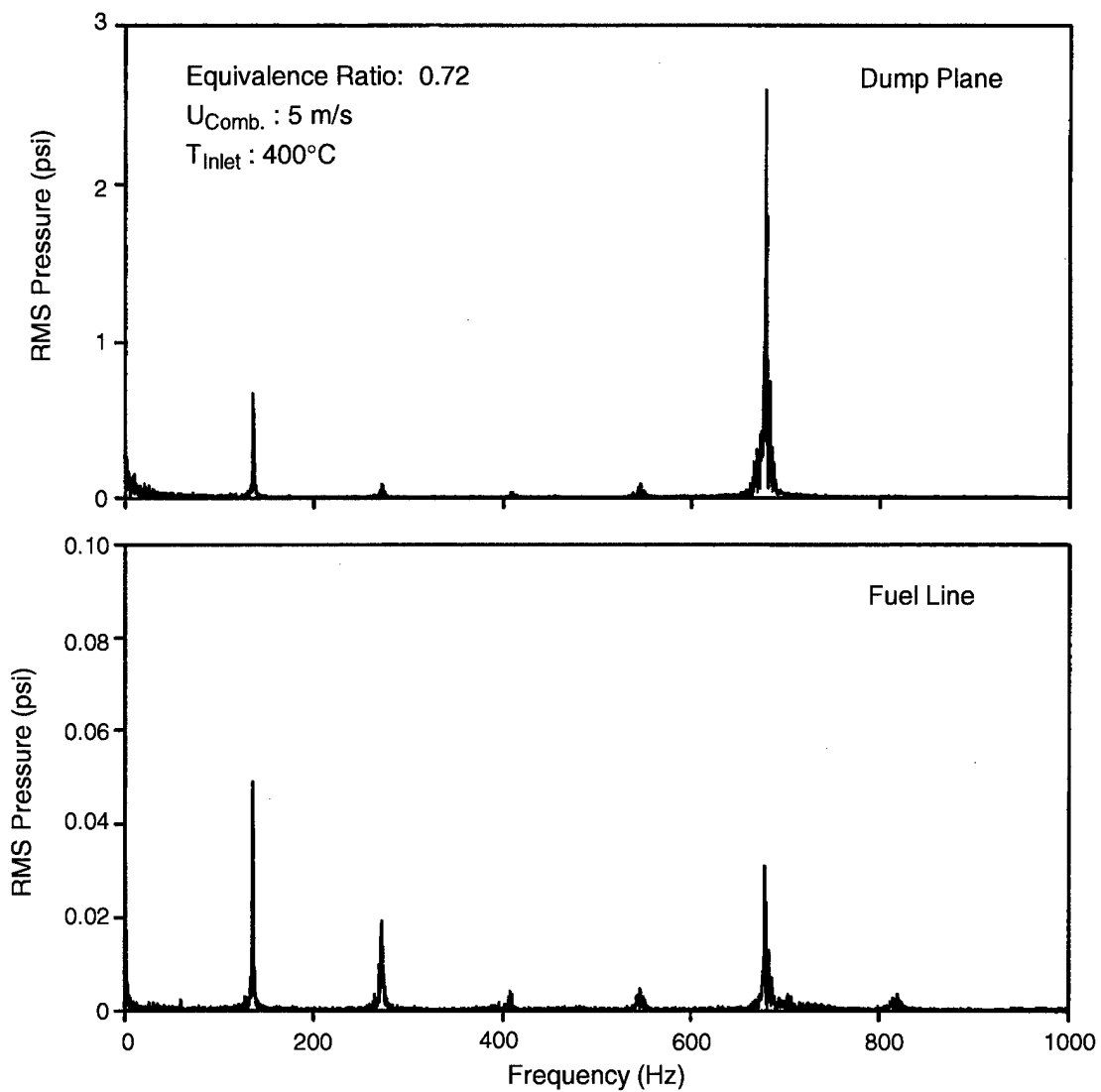


Figure 36. Pressure Signal Frequency at the Dump Plane and Fuel Line – Equivalence Ratio 0.72.

tance of the observed fuel system coupling to the observed instabilities, a time-lag analysis can be performed (Reference 18). In order to estimate the time required for the fuel flow rate fluctuations to travel from the injector holes to the flame zone, one must identify the location in the combustion chamber where the heat release and pressure fluctuations were most strongly coupled. In order to such an analysis, measurements of the flame structure during unstable combustion were made which are discussed in the Section 4.2.2.

4.2.2 Flame Chemiluminescence Measurements

Flame chemiluminescence from a number of species, such as OH^* , CH^* and CO_2^* , has been used as a qualitative measure of the heat release from lean premixed flames (Reference 7). Imaging of the flame chemiluminescence can also provide valuable insight regarding the structure and evolution of the regions of heat release in the combustor during unstable combustion, which can shed light on the underlying mechanisms that were driving the instability.

The first chemiluminescence measurements were made of the total CH. In this case the flame emission was measured using a PMT, which was positioned to collect light from the entire optical section of the combustor. Measurements were made at a combustor velocity of 5m/s and an inlet air temperature of 400°C at several equivalence ratios. The dump-plane pressure was also simultaneously recorded. Figure 37 shows the time traces of flame intensity and pressure fluctuations at an equivalence ratio of 0.72. This was the condition where the strongest instabilities were observed. Both the low frequency (~130 Hz) and the high frequency (~670 Hz) pressure oscillations are evident in Figure 37. Note, however, that only the low frequency fluctuation was evident in the chemiluminescence intensity measurement. This indicates that the heat release fluctuations that drive the instability only occur at the lower frequency, i.e.; the frequency of the bulk mode instability. Therefore the longitudinal mode instability was not directly driven by the heat release fluctua-

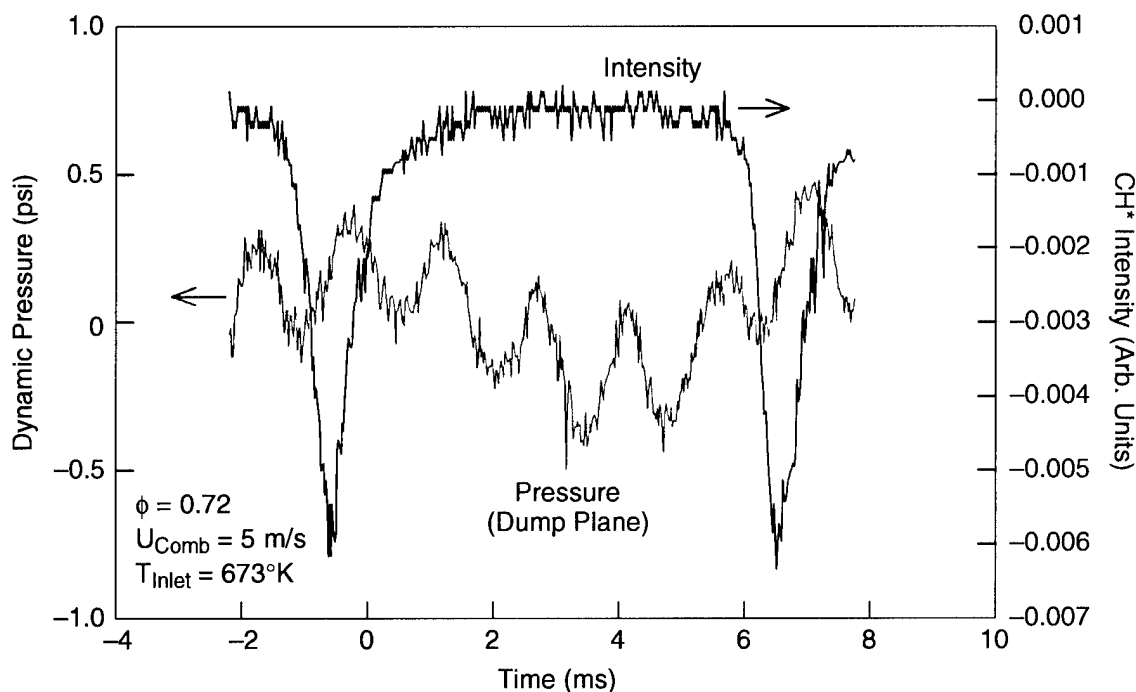


Figure 37. Time Trace of Pressure and Total Flame Cumiluminescence Fluctuation at Equivalence Ratio of 0.72.

tions, but appears to be a parasitic acoustic oscillation that was driven by the low frequency bulk mode instability. It should also be noted that as expected the heat release fluctuations and the pressure fluctuations were very nearly in-phase as predicted by Rayleigh's criterion (Reference 20).

Next, two-dimensional images of the CH chemiluminescence were obtained at equivalence ratios of 0.65 and 0.72, a combustor velocity of 5 m/s and an inlet air temperature of 400°C. These measurements were recorded using an intensified CCD camera which was phase-synchronized with the pressure fluctuation to obtain phase-averaged images of the flame structure. The dump-plane pressure signal was passed through a low-pass filter, to remove the higher frequency component, before being fed to the camera triggering circuit. This was done to synchronize image acquisition with the bulk-mode oscillation, since the total intensity measurements show that chemiluminescence intensity fluctuates at this frequency.

Figures 38 and 39 show the phase-resolved, flame chemiluminescence images at equivalence ratios of 0.65 and 0.72, respectively. Note that these were not the original line-of-sight images, but were the deconvoluted images which show the actual two-dimensional structure of the flame. Each figure is a set of 12 images, and images in a set were scaled similarly to accurately depict the flame structure differences during the oscillation cycle. Note, however, that the two sets of images were scaled differently, and therefore comparisons between the two sets should be made with caution. The field of view of the individual images was 18.75 cm x 12.5 cm, and the flow was from left to right. It should be noted that there were two major artifacts in the deconvoluted images which were a result of the deconvolution procedure. One of these was that the deconvoluted images were perfectly axisymmetric. This was a result of the fact that the deconvolution procedure required an axisymmetric line-of-sight image, which was obtained by calculating a line-of-sight image which was an average of the upper and lower halves of the original, slightly asymmetric, line-of-sight image. A second artifact was associated with the removal of noise that was produced by the Abel inversion procedure from along the centerline of the deconvoluted images.

Qualitatively, the phase-averaged images at the two equivalence ratios were very similar. They both show that the flame intensity, and not the flame shape, changes significantly during the instability. Thus flame-vortex interaction (Reference 3, 21, and 22), which has been found to be an important instability mechanism in other studies, appears to not be important in these instabilities. The chemiluminescence intensity shown in these images was observed to change by more than an order of magnitude, and it appeared that the flame was actually undergoing a periodic extinction and re-ignition process. This was consistent with the occurrence of equivalence ratio fluctuations resulting from pressure fluctuations in the fuel line as discussed previously.

If the intensity of the deconvoluted chemiluminescence images was assumed to be proportional to the local heat release, the phase-averaged images can be used to calculate the local Rayleigh index distribution. The local Rayleigh index was the correlation between the local heat release and pressure fluctuations in the combustor, where a positive Rayleigh index indicates that the heat release was driving the pressure fluctuations and a negative Rayleigh index indicates that the heat release was damping the pressure fluctuations. The Rayleigh index plots corresponding to the images shown in Figures 38 and 39 are shown in Figures 40 and 41. At both operating conditions, no significant region of damping was observed, and the region where the Rayleigh index was largest, i.e.; where the instability was most strongly driven, lies about one combustor diameter downstream of the dump plane along the combustor wall.

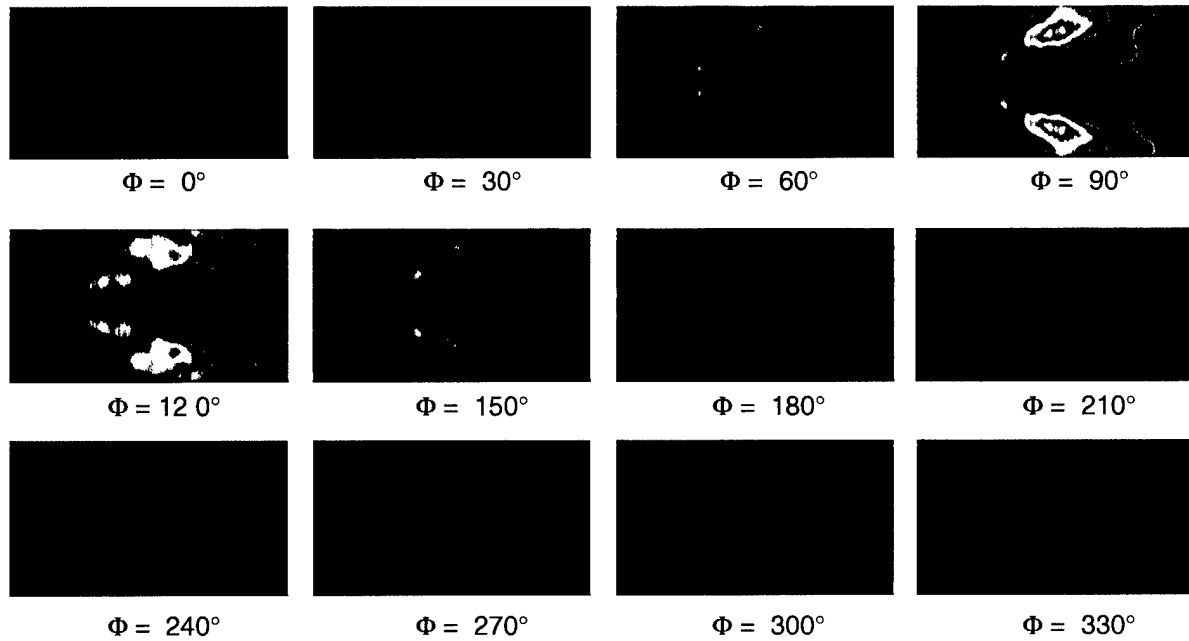


Figure 38. Flame Intensity Variations During a Pressure Oscillation Cycle – Equivalence Ratio 0.65, $U_{\text{Comb}} = 5 \text{ m/s}$, $T_{\text{inlet}} = 400^\circ\text{C}$.

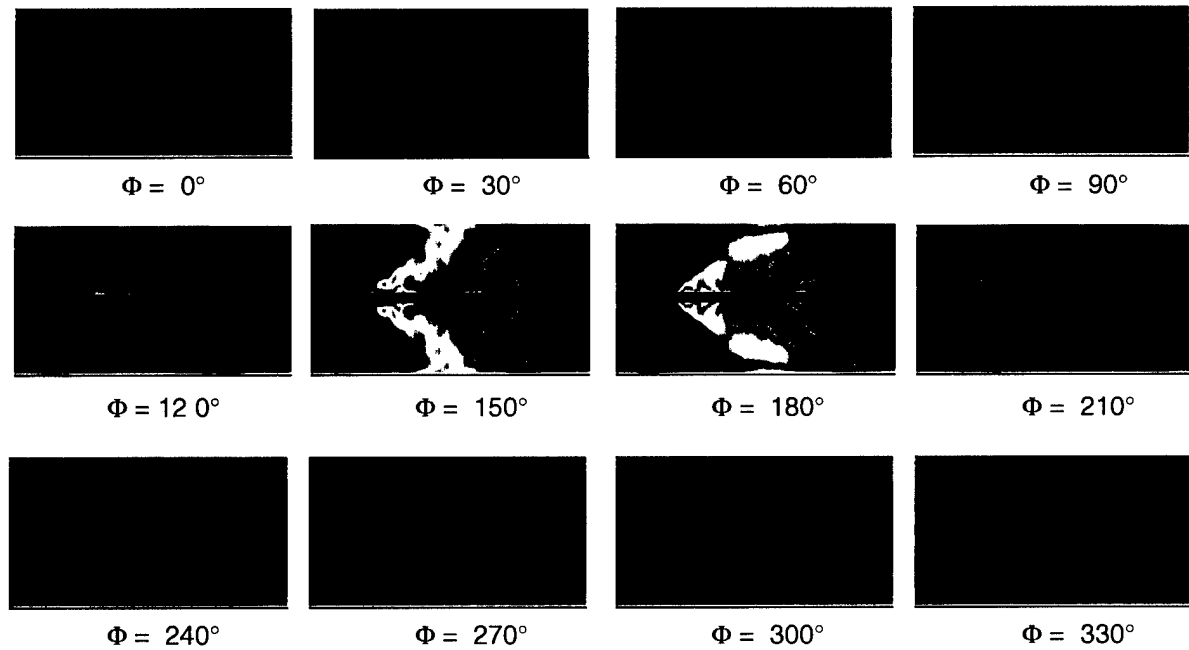


Figure 39. Flame Intensity Variations During a Pressure Oscillation Cycle – Equivalence Ratio 0.72, $U_{\text{Comb}} = 5 \text{ m/s}$, $T_{\text{inlet}} = 400^\circ\text{C}$.

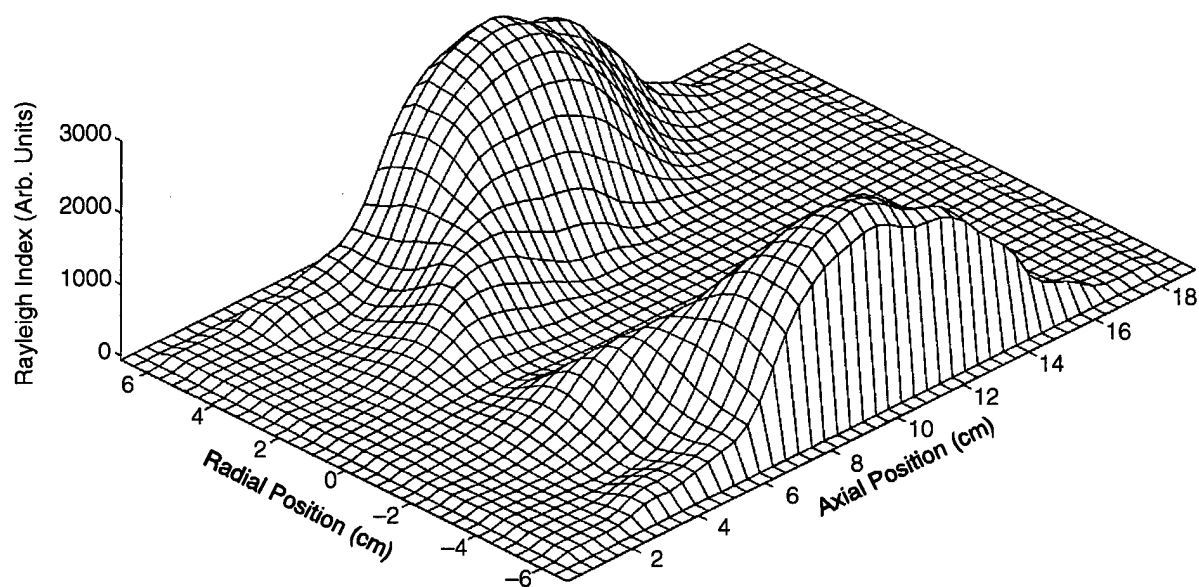


Figure 40. Flame Intensity Variations During a Pressure Oscillation Cycle – Equivalence Ratio 0.65, $U_{\text{Comb}} = 5 \text{ m/s}$, $T_{\text{inlet}} = 400^\circ\text{C}$.

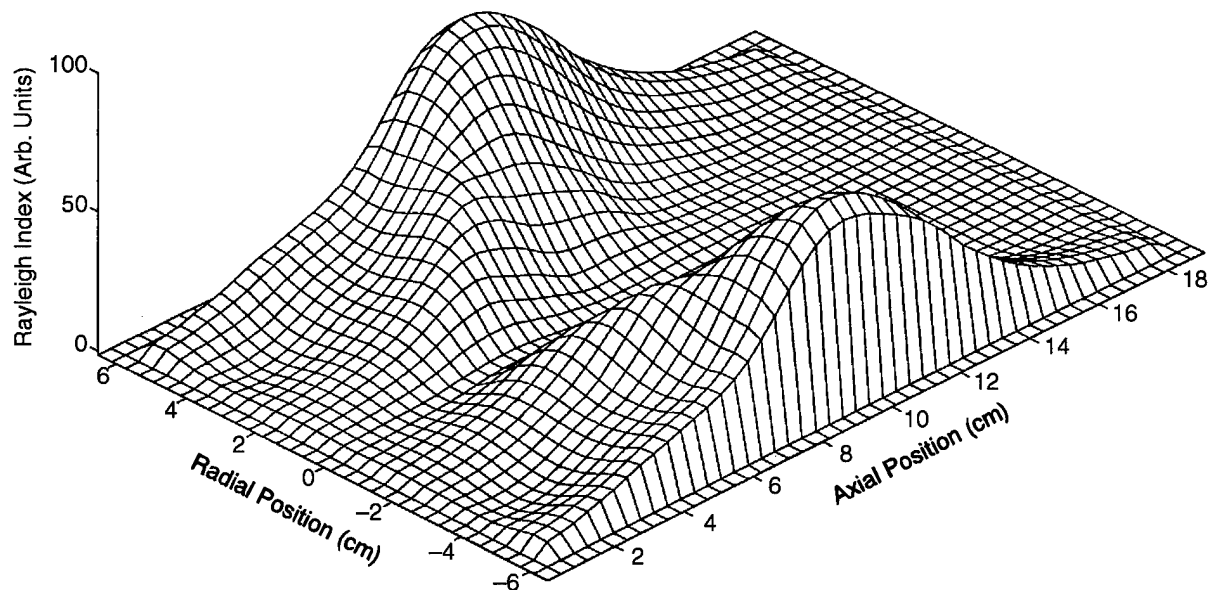


Figure 41. Flame Intensity Variations During a Pressure Oscillation Cycle – Equivalence Ratio 0.72, $U_{\text{Comb}} = 5 \text{ m/s}$, $T_{\text{inlet}} = 400^\circ\text{C}$.

5.0 Summary and Conclusions

In the previous chapter the results of a series of combustion instability studies that have been conducted to investigate the stability characteristics of the GE Dual Annual Counterrotating Swirl (DACRS) injector were described. These studies have investigated the effects of inlet air temperature, equivalence ratio, combustion chamber length and swirl vane configuration on the DACRS injector stability characteristics. Since these were carried out at sub-scale conditions, the effect of injector scale (i.e.; size) was addressed by considering two DACRS injectors that differed in size by a factor of three (referred to as the 1X and 3X DACRS injectors).

5.1 1X DACRS Injectors

Studies of the 1X DACRS injector were conducted at pressures as high as five atmospheres and for two combustion chamber lengths, 235 mm (9.25 in) and 350 mm (13.78 in). The shorter 235 mm long chamber corresponded to a combustor chamber length appropriate for actual operational conditions. Under these conditions the DACRS injector showed excellent combustion stability characteristics over a wide range of equivalence ratios and inlet temperature conditions. Comparisons to a simple single swirl injector, which was fabricated in-house at Penn State, indicated that under identical operating conditions the PSU single swirl element exhibited significant combustion instability with rms pressure amplitudes of approximately 12.5% as compared to the much more stable operation exhibited by the 1X DACRS injectors. Mixing studies of the 1X DACRS injectors using planar laser-induced fluorescence (PLIF) to excite acetone seeded into the flow showed conclusively that the DACRS injectors had superior mixing characteristics to the PSU single swirl injector. The mixing performance of the 1X DACRS injector was also observed to be sensitive to the swirl angle combination employed. Two swirl angle combinations were studied: 45°/55° and 55°/65° swirler configurations. The 55°/65° swirler combination displayed the best mixing characteristics, but at the expense of pressure drop, which increased from 4% for the 45°/55° swirler combination to 8% for the 55°/65° configuration. However both swirler combinations exhibited similar combustion stability and emissions characteristics, thus, indicating the suitability of the lower pressure drop 45°/55° swirler combination.

The comparisons between the Penn State single swirl element injector and the 1X DACRS injector allowed an examination of the effects of unmixedness and fluid mechanics on the initiation and sustenance of combustion instability. The mixing studies clearly showed that greatly improved mixing occurs for the 1X DACRS injector. Previous studies of the Penn State single swirl injector had shown that increasing unmixedness, that was poorer mixing, enhances the occurrence of combustion instability in terms of its dependence on equivalence ratio [Reference 1]. Thus, to some degree, the improved mixing achieved by the 1X DACRS can be argued to account for the improved combustion stability behavior of the 1X DACRS injector. However, studies of the Penn State single swirl element also showed that under perfectly premixed conditions, combustion instability was still observed although over a narrower range of equivalence ratio than observed for less well mixed conditions. Therefore, improved mixing can not be the sole mechanism responsible for the improved stability characteristics of the 1X DACRS injector. The use of a counterrotating swirl configuration may also contribute to the stability through effects on the fluid mechanics occurring in the region of the dump plane and the bluff body. Evidence for such an effect was observed in the video and phase-resolved chemiluminescence images obtained under unstable operating conditions. The 1X

DACRS injector exhibited a more uniformly distributed flame that extended over a greater portion of the combustion chamber as compared to the flame produced using the Penn State single swirl injector. It was argued that this longer, better mixed flame, spreads out the energy release over a larger volume and was less capable of coupling to the 1L mode of the combustor, which has a pressure node near the dump plane. In contrast, the Penn State single swirl injector showed a compact flame that easily sustained the 1L mode. For the Penn State single swirl injector, phase-resolved chemiluminescence measurements clearly showed that the energy release and chamber pressure oscillations were in-phase, in agreement with Rayleigh's condition for driving combustion instability. Thus, it can be concluded that both the superior mixing performance of the 1X DACRS injector and the improved fluid mechanic characteristics of the counterrotating swirl configuration, through its stretching of the flame volume, contributed to the improved combustion stability of the 1X DACRS injector.

To test this hypothesis, the results of the study involving the longer chamber length must be considered. For the 350-mm (13.78 in.) long combustion chamber, significant combustion instability was observed for both the 1X DACRS and the Penn State single swirl injectors. In fact, the 1X DACRS injector had slightly larger pressure oscillations as compared to the Penn State single swirl injector for the longer chamber length case. This result argues strongly that the previous explanation regarding the coupling between the 1L mode and the flame energy release volume was creditable. The basis for this statement was that under the longer combustion chamber conditions, the region over which the 1L mode can be influenced, that was driven, extends further from the dump plane than in the shorter chamber length case. Thus, more of the flame energy release was capable of coupling to the pressure sensitive response region. The observation that both mixing and fluid mechanic effects were contributing to the stability behavior of the 1X DACRS injector was also confirmed by the longer chamber results. Combustion instability continued to be observed even in the studies for which fully premixed conditions existed. These fully premixed conditions were achieved for the 1X DACRS injector by injecting the fuel upstream of the inlet venturi. For these conditions, the amplitude of the observed pressure oscillations were reduced by only a factor of two, thus, indicating that unmixedness was not solely responsible for the observed combustion instability. The effects of the counterrotating swirling flow also plays a role in the mechanism accounting for combustion instability in the 1X DACRS injector. Thus, the stability or instability behavior of the 1X DACRS injector has elements of both unmixedness and fluid mechanic effects as the mechanism control the stability behavior of the injector.

Other aspects of the behavior of the 1X DACRS and Penn State single swirl injector with respect to their combustion instability behavior, however, were not clear at this point and will rely on future modeling efforts for an explanation. Most of these effects were related to the role of temperature on the initiation and amplitude of the pressure oscillations observed. The 1X DACRS injector exhibited the onset of combustion instability for the longer chamber length studies as the inlet air temperature was increased and the amplitude of the instability typically remained nearly constant with further increases in the inlet air temperature. In contrast, the Penn State single swirl injector displayed improved combustion instability behavior at elevated inlet air temperatures and as the inlet air temperature decreased the amplitude of the combustion instability was observed to increase. This temperature behavior was opposite to that observed for the Penn State single swirl injector in the shorter 235-mm long combustion chamber, where the behavior was similar to that of the 1X DACRS injector in the longer 350-mm long chamber. The specific mechanism responsible for this behavior

was not evident from the studies conducted to date, but may be resolved from the modeling studies that GEAE will conduct in the future. In this regard, the current experiments with the 1X DACRS injectors clearly have met the original objective of the study to provide a robust and diverse data set on combustion instability for model development and validation.

5.2 3X DACRS Injectors

1. Regions of stable and unstable combustion were observed over the range of operating conditions studied with the 3X DACRS injector. Both combustor velocity and inlet temperature were found to affect the stability characteristics of this injector, however, no consistent pattern to these was discerned. The strongest instability observed exhibited an RMS pressure fluctuation that was equal to 17% of the mean pressure.
2. During unstable combustion, two dominant frequencies were observed in the frequency spectrum of the pressure fluctuations. The lower frequency, around 130 Hz, corresponded to a bulk mode oscillation in the combustor, and the higher frequency, around 670 Hz, corresponded to a half-wave longitudinal mode instability.
3. Although the pressure fluctuations in the combustor exhibited both a bulk mode (~130 Hz) and a half-wave longitudinal mode (~670 Hz), simultaneously recorded CH* flame-chemiluminescence intensity fluctuations indicated that the heat release fluctuations were only occurring at the frequency of the bulk mode oscillation.
4. Pressure fluctuations were measured in the fuel supply line during unstable combustion with frequencies that matched those in the combustor. This suggests that fuel system coupling may be causing equivalence ratio fluctuations which were driving the observed instabilities.
5. Deconvoluted, phase-averaged images of the chemiluminescence emission from the flame showed that flame-vortex interaction was not an important mechanism in the observed instabilities. This observation, plus the fact that the flame appeared to be undergoing periodic extinction and re-ignition, further supports the conjecture that equivalence ratio fluctuations were driving the instabilities observed in the 3X DACRS injector.

6.0 References

6.1 Cited References

- 1 Broda, J. C.; Seo, S.; Santoro, R. J.; Shirhattikar, G.; and Yang, V.; "An Experimental Study of Combustion Dynamics of a Premixed Swirl Injector", *27th Symposium (International) on Combustion*, The Combustion Institute, pp. 1849–1856, 1998.
- 2 Gaydon, A. G. and Wolfhard, H. G.; *Flames: Their Structure, Radiation and Temperature*, Chapter 9, Chapman and Hall, London, 1978.
- 3 Poinso, T. J.; Trouvé, A. C.; Veynante, D. P.; Candel, S. M.; and Esposito, E. J.; "Vortex-driven Acoustically Coupled Combustion Instabilities," *Journal of Fluid Mechanics*, vol. 177, pp. 265–292, 1987.
- 4 Gütmark, E.; Parr, T. P.; Hanson-Parr, D. M.; and Schadow, K. C.; "Use of Chemiluminescence and Neural Networks in Active Combustion Control," *Twenty-Third Symposium (International) on Combustion*, The Combustion Institute, pp. 1101–1106, 1990.
- 5 Yu, K. H.; Trouvé, A.; and Daily, J. W.; "Low-frequency Pressure Oscillations in a Model Ramjet Combustor," *Journal of Fluid Mechanics*, vol. 232, pp. 47–72, 1991.
- 6 Samaniego, J. M.; Yip, B.; Poinso, T.; and Candel, S.; "Low-Frequency Combustion Instability Mechanisms in a Side-Dump Combustor," *Combustion and Flame*, vol. 94, pp. 363–380, 1993.
- 7 Samaniego, J.-M.; Egolfopoulos, F. N.; and Bowman, C. T.; "CO*₂ Chemiluminescence in Premixed Flames," *Combustion Science and Technology*, vol. 109, pp. 183–203, 1995.
- 8 Hanson, R. K.; "Combustion Diagnostics: Planar Imaging Techniques," *Twenty-first Symposium (International) on Combustion*, The Combustion Institute, pp. 1677–1691, 1986.
- 9 Lozano, A.; "Laser-excited Luminescent Tracers for Planar Concentration Measurements in Gaseous Jets," High Temperature Gasdynamics Laboratory, Stanford University, HTGL Rept. T-284, 1992.
- 10 Lozano, A.; Yip, B.; and Hanson, R. K.; "Acetone: a Tracer for Concentration Measurements in Gaseous Flows by Planar Laser-Induced Fluorescence," *Experiments in Fluids*, vol. 13, pp. 369–376, 1992.
- 11 Lozano, A.; Smith, S. H.; Mungal, M. G.; and Hanson, R. K.; "Concentration Measurements in a Transverse Jet by Planar Laser-Induced Fluorescence of Acetone," *AIAA Journal*, vol. 32, pp. 218–221, 1993.
- 12 Yuen, L. S.; Peters, J. E.; and Lucht, R. P.; "Pressure Dependence of Laser-Induced Fluorescence from Acetone," *Applied Optics*, vol. 36, pp. 3271–3277, 1997.
- 13 Eckbreth, A. C.; *Laser Diagnostics for Combustion Temperature and Species*, Abacus Press, Kent, UK, 1988.
- 14 Dimotakis, P. E. and Miller, P. L.; "Some Consequence of the Boundedness of Scalar Fluctuations," *Physics of Fluids A*, vol. 2, pp. 1919–1920, 1990.

- 15 Sivasegaram, S. and Whitelaw, J.; "Oscillations in Axisymmetric Dump Combustors," *Combustion Science and Technology*, vol. 52, pp. 413–426, 1987.
- 16 Shih, W–P, Lee, J.G. and Santavicca, D. A.; "Stability and Emissions Characteristics of a Lean Premixed Gas Turbine Combustor," Twenty–Sixth Symposium (International) on Combustion, 1996.
- 17 Dasch, C.J.; "One–Dimensional Tomography: A Comparison of Abel, Onion–Peeling and Filtered Back Projection Methods", *Applied Optics*, vol.31, No.8, 1992.
- 18 Straub, D. L. and Richards, G. A.; "Effects of Fuel Nozzle Configuration on Premix Combustion Dynamics", submitted for presentation at the 1998 ASME/IGTI Turbo Expo Meeting, 1998.
- 19 Lieuwen, T.; Neumeier, Y. and Zinn, B. T.; "The Role of Unmixedness and Chemical Kinetics in Driving Combustion Instabilities in Lean Premixed Combustors," *Combustion Science and Technology*, Vol. 135, No. 1–6, pp. 193–211, 1998.
- 20 Rayleigh, J. W. S.; *The Theory of Sound*, The Macmillan Company, 1984.
- 21 Schadow, K. C.; Gütmark, E.; Parr, T.P.; Parr, D. M.; Wilson, K. J. and Crump, J.E.; "Large Scale Coherent Structures as Drivers of Combustion Instability," *Combustion Science and Technology*, Vol. 64, 1989.
- 22 Venkataraman, K. K.; Preston, L.H.; Simons, D.W.; Lee, B.J, Lee, J.G. and Santavicca, D. A.; "Sources of Heat Release Fluctuation During Unstable Combustion in a Lean Premixed Dump Combustor," First Joint Meeting of the U.S. Sections, The Combustion Institute, Washington DC, March 14–17, 1999.

6.2 Relevant Papers

Shih, W–P, Lee, J.G. and Santavicca, D. A.; "The Effect of Incomplete Fuel–Air Mixing on the Lean Blowout Limit, Lean Stability Limit and NO_x Emissions of Lean Premixed Gas Turbine Combustors," Fall Technical Meeting, The Eastern States Section of the Combustion Institute, 1994.

6.3 Contributing Professionals

Participating PSU professionals were:

Dr. Domenic A. Santavicca, Professor of Mechanical Engineering

Dr. Robert J. Santoro, Professor of Mechanical Engineering

Dr. Jean–Christophe Broda, Research Associate

Dr. Jongguen Lee, Research Associate

Dr. Christophe Brossard, Post–doctoral Fellow

Dr. Byeong–Jun Lee, Post–doctoral Fellow

Mr. Ramarao Bandaru, Research Assistant

Dr. Seong Seo Ph.D. degree student (graduated Fall 1998)

Mr. Krishna Kumar Venkataraman, Ph. D. degree student

Mr. Derrick Simons, M.S. degree student (graduated Fall 1997)

Mr. Lon Preston, M.S. degree student (graduated Fall 1997)

Mr. Larry Horner, Technician

6.4 Publications, Meetings, and Presentations

In addition to the references cited, the following papers are germane to the discussions in this addendum.

Publications

Santoro, R. J.; "Applications of Laser-Based Diagnostics to High Pressure Rocket and Gas Turbine Combustor Studies," AIAA 98-2698, 20th AIAA Advanced Measurement and Ground Testing Technology Conference, June 15-18, 1998, Albuquerque, NM.

Broda, J.-C.; Seo, S.; Santoro, R. J.; Shirhattikar, G.; and Yang, V.; "An Experimental Study of Combustion Dynamics of a Premixed Swirl Injector," 27th Symposium (International) on Combustion, The Combustion Institute, pp. 1849-1856, 1998.

Lee, J. G. and Santavicca, D. A.; "Fiber-Optic Probe for Laser-Induced Fluorescence Measurements of the Fuel-Air Distribution in Gas-Turbine Combustors," *Journal of Propulsion Engineering*, 13:384-387 (1997).

Lee, J.G.; Hong, B. S.; Kim, K.; Yang, V. and Santavicca D. A.; "Optimization of Active Control Systems for Suppressing Combustion Instability," Proceedings of the RTO Symposium on Gas Turbine Engine Combustion, Emissions and Alternative Fuels, Lisbon, Portugal (1998).

Santavicca, D. A.; "Combustion Instabilities in Lean Premixed Gas Turbine Combustors," *Nensho Kenkyu (Combustion Research)*, vol. 113, pp. 1-10, 1998.

Jones, C. M.; Lee, J.G. and Santavicca, D. A.; "Closed-Loop Active Control of Combustion Instabilities Using Sub-Harmonic Secondary Fuel Injection," *AIAA Journal of Propulsion and Power*, vol. 15, no. 2, March-April, 1999.

Venkataraman, K.K.; Preston, L.H.; Simons, D.W.; Lee, B.J.; Lee, J.G. and Santavicca, D. A.; "A Study of the Mechanism of Combustion Instability in a Lean Premixed Dump Combustor," *AIAA Journal of Propulsion and Power*, vol. 15, No. 6, November-December 1999.

Meetings and Presentations

Santoro, R. J.; "Combustion Instability," invited presentation at the Workshop on Turbine Engine Combustion Issues, Integrated high Performance Turbine Engine Technology, Sept. 12, 1996, Dayton, OH.

Lee, S.-Y.; Pal, S. and Santoro, R. J.; "Temperature and Unmixed Fuel Measurements in Turbulent Jet Flames by Using Coherent Anti-Stokes Raman Spectroscopy," presented at the Fall Technical Meeting of The Eastern States Section of The Combustion Institute, October 27, 1997, Hartford, CT.

Lee, S.-Y.; and Santoro, R. J.; "Imaging Studies of Soot Formation in Turbulent Ethylene Jet Flames," presented at the Fall Technical Meeting of The Eastern States Section of The Combustion Institute, October 27, 1997, Hartford, CT.

Broda, J. C.; Seo, S. and Santoro, R. J.; "Recent Experimental Results in High Pressure Gas Turbine Combustion Instabilities," presented at the Fall Technical Meeting of The Eastern States Section of The Combustion Institute, October 27, 1997, Hartford, CT.

Santoro, R. J.; "Applications of Laser-Based Diagnostics to High Pressure Rocket and Gas Turbine Combustor Studies," presented at the 20th AIAA Advanced Measurement and Ground testing Technology Conference, June 15-18, 1998, Albuquerque, NM.

Seo, S.; Lee, S.-Y.; Broda, J. C. and Santoro, R. J.; "Effects of the Degree of Premixing on Combustion Instabilities in a Model Gas Turbine Combustor," presented at the Tenth Annual Symposium, Propulsion Engineering Research Center, NASA Marshall Space Flight Center, October 26-27, 1998, Huntsville, AL.

Broda, J. C. and Santoro, R. J.; "High Pressure Flow Reactor Combustion Instability Experiments," presented at the Advanced Turbine System Conference, November 2-4, 1998, Washington, DC.

Lee, S.-Y.; Santoro, R. J.; Watkins, W. B. and Kincaid, K.; "Statistical Determination of Fuel Regimes and its Implication Using CARS System in Turbulent Ethylene Jet Flames," presented at the Tenth Annual Symposium, Propulsion Engineering Research Center, NASA Marshall Space Flight Center, October 26-27, 1998, Huntsville, AL.

Lee, S.-Y. and Santoro, R. J.; "Observation of Length Scales of Soot Particles, OH Radicals and PAH In Turbulent Diffusion Flames," presented at the First Joint Meeting of the U. S. Sections of The Combustion Institute, March 14-17, 1999, Washington, DC.

Seo, S.; Lee, S.-Y.; Broda, J. C. and Santoro, R. J.; "Effects of the Degree of Premixing on Combustion Instabilities in a Model Gas Turbine Combustor," presented at the First Joint Meeting of the U. S. Sections of The Combustion Institute, March 14-17, 1999, Washington, DC.

Santoro, R. J.; "Non-Intrusive Diagnostics in High Pressure Combustion Environments," invited presentation presented at 1999 National Heat Transfer Conference, August 15-17, 1999, Albuquerque, NM.

Lee, J. G.; C.-H. Jeon and Santavicca, D. A.; "Flame Evolution Imaging and Its Application to Control of Combustion Instability in a Coaxial Dump Combustor," presented at the 1996 Eastern States Section of The Combustion Institute Fall Meeting (1996).

Shih, W.-P.; J. G. Lee and Santavicca, D. A.; "Stability and Emissions Characteristics of a Lean Premixed Gas Turbine Combustor," presented at the 26th Symposium (Int'l.) on Combustion, Naples, Italy (1996).

Lee, B.-J.; L. Preston, D. Simons, K. K. Venkataraman and Santavicca, D. A.; "Combustion Instabilities in Lean Premixed Combustors," presented at the 1997 Joint Meeting of the French and Belgian Sections of The Combustion Institute, Lille, France (1997).

Santavicca, D. A.; "Lean Premixed Gas Turbine Combustors," plenary lecture presented at the 1997 Meeting of the Italian Section of The Combustion Institute, Cagliari, Italy (1997).

Ondas, M. S. and Santavicca, D. A. "A Study of Droplet Vaporization in a Longitudinal Acoustic Field Using Exciplex Vapor/Liquid Visualization," presented at the ASME Symposium on Dispersed Flows in Combustion, Incineration and Propulsion Systems, Dallas, Texas (1997).

Venkataraman, K.K.; L.H. Preston, D.W. Simons, B.-J. Lee, J.G. Lee and Santavicca, D. A.; "An Optical Study of Unstable Combustion," presented at the 9th NASA Propulsion Engineering Research Center Symposium, Cleveland, Ohio (1997).

Addendum C

**Large-Eddy Simulations of Turbulence-Chemistry Interactions in
Low NO_x Gas Turbine Engines**

AFOSR Focused Research Initiative
Low Emissions, High Performance Gas Turbine Engines

Contract 200-IQ-14N44080
General Electric Aircraft Engines
Cincinnati, Ohio

Principal Investigator
Suresh Menon

Georgia Institute of Technology
Atlanta, GA 30332

July, 1999

Table of Contents

	<u>Page</u>
1.0 Introduction	1
2.0 Objective	2
3.0 Approach	6
3.1 Simulation Model	6
3.1.1 Equations of LES	6
3.1.2 Flame Propagation Model	9
3.2 Subgrid Combustion Models	9
3.3 Linear-Eddy Single Phase Model	10
3.4 Subgrid Implementation of LEM	11
4.0 Results	13
5.0 Conclusions	14
6.0 Acknowledgements	15
7.0 References	16
7.1 Cited References	16
7.2 Relevant Papers	17
7.3 Contributing Professionals	17
7.4 Publications, Meetings, and Presentations	17

1.0 Introduction

Large-Eddy simulation (LES) of turbulent combustion in a full-scale combustor is very challenging for a variety of reasons. Resolution of the flow field in both space and time is essential to capture the dynamics of the flow-combustion interactions. However, since the flow in the gas turbine is at a high Reynolds number, severe constraints are imposed on the LES approach in order to achieve a solution even when massively parallel systems are employed. High accuracy in the predicted results is required using relatively coarse grid resolution (in order to obtain solution within a reasonable time frame). This requirement implies that the classical subgrid closure based on algebraic model cannot be used and a higher order subgrid closure is required even for momentum and energy transport. In addition, for combustion modeling, small-scale mixing and molecular diffusion processes need to be resolved in order to achieve accurate predictions, especially of pollutant emissions. This requirement is in contradiction with conventional LES approach which is to resolve scales larger than the grid and to model the small scales using an eddy viscosity/diffusivity approach. The physics of species mixing and combustion which evolves within the small (unresolved) subgrid scales clearly suggest that the conventional eddy diffusivity closure is inappropriate. The LES requirements also imply that conventional Reynolds-Averaged Navier-Stokes (RANS) codes cannot be simply extended for LES applications by making the scheme time-accurate (or unsteady) unless special constraints are imposed on the spatial/temporal accuracy and appropriate subgrid models are incorporated. In this research, a new subgrid turbulence model based on the subgrid kinetic energy is combined with an innovative subgrid turbulent mixing and combustion simulation methodology within each LES cell for application to high Reynolds number flow. The advantage of using advanced subgrid models is that coarse-grid LES can be used for engineering analysis without compromising excessively on accuracy. Simulations of premixed, partially premixed, and non-premixed combustion in a variety of configurations including full-scale General Electric combustors have been performed to validate this new capability. Results show that the present approach is capable of capturing the finer details of combustion process at a level of accuracy that is not possible using conventional methods. These studies also demonstrate that using advanced physics-based subgrid model that captures the small-scale physics within a coarse grid LES results in a computationally efficient simulation methodology. With the advent of massively parallel systems including PC-clusters, it is envisioned that the application of this type of LES engineering design of gas turbine combustors could be attempted in the near future.

Desirable features for the next generation gas turbine engines are combustion efficiency, reduced emissions and stable combustion in the lean limit. All these features are mandated by real concerns regarding the long-term impact of constantly increasing number of aircraft flights in the upper troposphere especially in the highly travelled Atlantic and Pacific flight corridors. At present, it appears likely that propulsion systems in aircraft engines for the conceivable future will remain fossil fuel based. Thus, reducing emissions from combustion systems using fossil fuels such as gas turbine combustors remains a high priority.

2.0 Objective

The exhaust emission from gas turbine combustors consists of the combustion products, CO₂ and H₂O and depending upon the efficiency of the engine, pollutants such as CO, NO_x, unburned hydrocarbons (UHC), SO_x and soot particulates. Although restrictions on the level of pollutant emission in the engine exhaust have been imposed in many countries, the actual levels allowed are considerably high in order to minimize economic impact also due to the inability to achieve stricter limits. However, the increasing environmental concerns are expected to significantly tighten these restrictions in the near future and as a result, the next generation aircraft engines will have to be more efficient with significantly lower emissions.

At present, achieving orders of magnitude reduction in pollutant emissions from gas turbine engines is nearly impossible for a variety of reasons. Although the chemical mechanism of CO, NO_x, UHC and SO_x formation has been well understood for sometime, finding an optimum solution to mitigate or drastically reduce these emissions has been very difficult since the source of these pollutant formations are quite different. For example, although CO and NO_x are formed in the bulk gas, the formation of UHC is more complex and many locations such as the exhaust, incomplete mixing or local unmixedness, flame quenching near the wall and deposition in crevices etc. have all been identified as potential sources of UHC. A potentially feasible method to control all these emissions is to reduce the equivalence ratio (lean mixture combustion) since both CO and NO reduces with reduction in equivalence ratio. However, as the equivalence ratio decreases beyond a critical limit localized flame extinction occurs resulting in a rapid increase in UHC. Thus, flame stability in the lean limit has become one of the major unresolved issues in the development of low emission gas turbine combustors.

A possible concept that may be able to deliver low CO and NO emission is a lean, premixed prevaporized (LPP) combustor. In this combustor, the fuel-air is premixed and combustion occurs in a premixed mode. In this approach fuel-air mixing is not relevant (although molecular diffusion of some key radical may not be negligible). Furthermore, even though lean combustion is possible in this approach, there remains many unresolved issues. For example, it is not fully understood what impact near-wall flame quenching and partial oxidation of UHC has on the total CO emissions since past measurements in lean mixtures suggest that the measured values of CO are higher than the partial equilibrium limit. The effect of lean combustion on NO emission is also not fully resolved since it appears that in addition to the local stoichiometry and fuel temperature, system parameters such as the shape of the chamber, operating conditions of the engine, local fuel-air mixing (including the effect of wall air cooling) all appear to play roles in the eventual magnitude of the NO emission. Formation of NO in the highly turbulent reaction zone (when turbulence-flame interactions can impact flame propagation and stability) is also an area that is not very well understood. Finally, elimination of UHC is the most problematic since it is related to the formation of quench layers near the wall and the deposition of HC into crevices (which is a system design issue). Another fluid dynamic issue is that the mechanism of this deposition process may be related to the formation of a turbulent fuel-rich boundary layer on the wall of the combustor. The interaction of this reacting boundary layer with cooling wall air jets that are injected into the combustor is also a complex process that needs to be well understood under lean burn conditions.

In the premixed limit, the resolution of the propagating flame front is critical to accurately capture the heat release effect. Thus, a numerical tool is needed that can deal with premixed combustion in the flamelet regime and can capture the flame front without numerical diffusion. The computational requirement to capture thin flames is not a trivial issue since thermodynamic variables such as temperature, density, and pressure undergo major jumps across the flame (as in shock waves) and capturing such high gradients using conventional schemes is impossible. The conventional approach is to employ a very high grid resolution to resolve this thin flame. However, under flow conditions of practical interest the flame thickness is much smaller than the scale of the smallest eddy (i.e., the Kolmogorov scale) and thus, the required resolution far exceeds the computational power available. Tracking thin flames in highly turbulent flow without resorting to very high grid resolution requires a new approach.

In reality, to achieve premixed state, fuel and air have to be mixed upstream of the combustor. In most premixing devices, a fully-mixed state is very difficult to achieve. Results in the past have shown that partially premixed mixture with significant spatial and temporal variation of the equivalence ratio can exist in the combustor. Under such conditions, combustion may occur in fully premixed, partially premixed, and diffusion conditions all within a small region. Numerical models must be able to deal with these multiple states (non-premixed, partially premixed, and premixed mixtures within the same computational domain) without requiring ad hoc fixes.

Even when a fully premixed state is achieved, the combustion process can be quite complex and depends upon the turbulent scales in the flow. Under certain conditions (that can be characterized using Reynolds, Damkohler, and Karlovitz numbers, as discussed in the papers listed in Section 7), premixed combustion occurs in the flamelet regime where the turbulent scales are much larger than the flame thickness. Under this condition, turbulence just wrinkles the flame and the degree of wrinkling increases with the intensity of turbulence. As a result, the propagation speed of the premixed flame (or the mass consumption rate) is modified resulting in an effective turbulent flame speed. Most premixed combustion devices under the right conditions will exhibit flamelet burning. In the past many models have been developed to predict flame behavior in this regime, especially to estimate the turbulent burning rate. However, as the turbulence intensity can spatially vary quite widely in a combustor other burning regimes may become dominant locally. For example, under certain conditions, the distributed burning can occur. In this distributed reaction regime, turbulent scales are smaller than the flame thickness and therefore, can penetrate into the preheat zone thereby modifying the flame speed. Models developed for the flamelet regime cannot be used in the distributed reaction zone. Thus, simulation of full-scale combustor even under fully premixed mode requires development of a model that can seamlessly deal with flamelet and distributed reaction regimes without requiring ad hoc fixes. At present, other than the model developed here, no other model has been developed to deal with this entire regime.

Although LPP concept is one possible approach, current gas turbine engines depend upon liquid fuels for providing the chemical energy. When liquid fuel is employed, fuel spray atomization, vaporization, and mixing with ambient air all need to be taken into consideration. To achieve efficient combustion with liquid fuel injection, research was focused on improving the liquid fuel atomization process and to increase fuel-air mixing downstream of the fuel injector. However, structure of a complex three-dimensional, swirling fuel-air mixing layers is very difficult to resolve using current experimental and numerical methods. Since, fuel atomization and fuel-air mixing are both highly unsteady, conventional steady-state methods cannot be used to elucidate the finer

details. Therefore, numerical simulation methodology that can resolve both the spatial and time scales of fuel–air mixing and the resulting combustion process is needed.

In addition to the inability to deal with complex spatio–temporal features of turbulence–chemistry interaction, there are other limitations of steady–state RANS methods that are currently used for combustion modeling. In addition to omitting (or modeling using ad hoc global models) important aspects of the small–scale unsteady mixing process most RANS models have to employ closure for the chemical reaction source term which can result in major error in prediction of emissions (in particular). More advanced models based on probability density functions (pdf) transport equations treat the reaction rate term exactly, but employ somewhat ad hoc mixing sub models in addition to using the standard RANS closure for the conservation equations. Thus, the limitations of the baseline RANS model for the fluid dynamics cannot be avoided in scalar–pdf methods.

The difficulties encountered in modeling the scalar mixing process is due to the inability of conventional models to deal with the interaction among turbulent stirring, molecular diffusion, and chemical reaction that occur at the smallest scales of the flow. These small scales are never resolved in any conventional numerical treatment. As a result, the subtle mixing effects that impact combustion (such as differential molecular diffusion and compositional variations within fluid that is nominally fully mixed) cannot be included. Differential diffusion can influence the thermochemical state within a flame and thus, impact ignition, extinction, and formation of toxic pollutants, such as NO_x. Furthermore, since NO_x is produced locally, due to the presence of transient key radicals in high temperature regions, the local unsteady mixing process has to be accurately modeled. In addition, the sensitivity of local chemistry to the relative abundance of fuel and air (e.g., the propensity to form soot in fuel–rich zones) requires accurate modeling of small deviations from complete mixing. Incomplete premixing can produce unanticipated results in the combustion dynamics which need to be accurately predicted.

In this project a new approach has been developed to address the aforementioned issues. This research has focused on characterizing the unsteady mixing process and to determine accurately the effects of local time– and length–scales on the combustion process. Turbulent mixing may be envisioned as a two–step process consisting of: 1) turbulent stirring and length–scale reduction of initially unmixed species and, 2) molecular diffusion that brings species into contact before combustion can take place. In many classical approaches to modeling turbulent mixing at high Reynolds (Re) numbers it is assumed that the first step is rate–limiting and the second step can therefore, be omitted. Recent experimental observations are first, the mixing rate appears quite sensitive to the molecular diffusivity for a given Reynolds number and second, the spatial structure of the mixing field cannot be explained solely in terms of large–scale gradient diffusion. These observations indicate that a) molecular diffusion accounts for a significant portion of the total mixing time and, b) there are complex interplay between large–scale and fine–scale processes.

In this study, a simulation methodology based on Large Eddy Simulations (LES) has been developed to address these issues. LES resolves all large–scales (that is configuration–dependent, and therefore, cannot be modeled) using a space– and time–accurate scheme while scales smaller than the grid are modeled using a subgrid model. For momentum transport, the small scales provide an effective dissipative mechanism and therefore, simple eddy viscosity models can be employed. Even with this simplification, simple algebraic models cannot be used for practical simulations, since such models require an equilibrium between subgrid kinetic energy production and dissipation. This requirement is only valid if most of the inertial range is resolved (at a very high computational cost, since the

number of grid points required to resolve all scales is proportional to Re^3). Therefore, advanced subgrid closures (such as the one used in this study) are required that allow reduction of the grid resolution without losing numerical accuracy.

Extending the eddy viscosity concept to scalars is even more problematic. Since small-scale mixing and diffusion processes are essential for the accurate prediction of the chemical processes, subgrid eddy diffusivity models cannot be employed. In this study, a novel subgrid combustion model has been developed that allows accurate treatment of the unsteady subgrid mixing, diffusion, and combustion process without ad hoc modeling. The key features of this LES approach are:

1. Unsteady turbulent mixing, molecular diffusion, and chemical kinetics evolve at the local time-scale within the subgrid where all relevant length-scales are resolved.
2. The small-scale processes are coupled to the large-scale motion simulated by LES providing a two-way interaction between local processes and global motion.
3. Chemical kinetics and molecular diffusion in the small scales can be implemented without any closure assumptions thereby providing a means for accurate prediction of the local production of key radicals and hence pollutant formation.
4. The local subgrid scalar fields and species production/destruction terms can be statistically averaged to obtain mean values that can be used to evaluate conventional closure models and for comparison with experiments.
5. Since this methodology is uniquely suited for parallel processing, the resulting simulation procedure is optimized for parallel machines to take advantage of the future scale-up of these machines.

This report summarizes the results obtained in this research. Since most of the results have been presented in the publications listed in Section 7 of this Addendum, they are not repeated here. This addendum briefly summarizes the key modeling issues in both conventional and the new LES approaches and then the highlights of the studies are summarized.

3.0 Approach

3.1 Simulation Model

The numerical method solves the full 3D, compressible Navier–Stokes equations using a finite volume scheme that is second–order accurate in time and fourth–order accurate in space. These equations are supplemented by the one–equation dynamic model for the subgrid kinetic energy. In some of the LES studies of premixed combustion, a flamelet model is used to track the thin premixed flame in the combustor. The turbulent propagation speed of this flame is determined using a subgrid model for the flame speed in terms of the subgrid turbulence intensity and the laminar flame speed. The key advantage of this approach is that only one more equation is solved along with the LES Navier–Stokes equations. For more detailed chemical processes, reduced reaction kinetics has been employed.

3.1.1 Equations of LES

The equations describing the conservation of mass, momentum and total energy are given by the full three–dimensional, unsteady, compressible Navier–Stokes equations. In LES, the flow variables are decomposed into the resolved scale and subgrid scale components. The large scales are computed explicitly while the effects of the subgrid scales on the large scales are modeled. Dynamics of large–scale structures (which contain most of the energy) is dictated by the geometry of the flow and the Reynolds number, while the small scales (which primarily dissipate energy transferred from the large scales) are relatively unaffected by the geometry except near walls.

The flow variables are decomposed into the resolved (supergrid scale) and unresolved (subgrid scale) components by a spatial filtering operation such that: $f = \tilde{f} + f''$ where the Favre filtered variable (with tilde) is defined as $\tilde{f} = \overline{\rho f} / \bar{\rho}$ and the bar represents spatial filtering given by

$$\bar{\rho f} = \int_D \rho f(\bar{x}) G(\bar{x} - \bar{x}', \Delta) d^3x' \quad (1)$$

Here, G is the filter kernel, D is the domain of the flow, and Δ is a characteristic grid size. The filtering operation is normalized by requiring that

$$\int_D G(\bar{x} - \bar{x}', \Delta) d^3x' = 1 \quad (2)$$

Filtering reduces the high wave number content in the flow variables and separates the resolved scale component from the subgrid (unresolved) scales. In this study, a box filter is employed which is appropriate for finite volume schemes. Contrary to the more traditional Favre temporal averaging, $\tilde{f} \neq \bar{f}$ and in general, $\tilde{f}'' \neq 0$. Applying the filtering to the Navier–Stokes equations results in the following LES equations:

$$\frac{\partial \bar{\rho}}{\partial t} + \frac{\partial \bar{\rho} \bar{u}_i}{\partial x_i} = 0 \quad (3a)$$

$$\frac{\partial \bar{\rho} \bar{u}_i}{\partial t} + \frac{\partial}{\partial x_j} [\bar{\rho} \bar{u}_i \bar{u}_j + \bar{p} \delta_{ij} - \bar{\tau}_{ij}] + \frac{\partial \tau_{ij}^{sgs}}{\partial x_j} = 0 \quad (3b)$$

$$\frac{\partial \bar{\rho} \bar{E}}{\partial t} + \frac{\partial}{\partial x_i} [(\bar{\rho} \bar{E} + \bar{p}) \bar{u}_i + \bar{q}_i - \bar{u}_j \bar{\tau}_{ij}] + \frac{\partial H_i^{sgs}}{\partial x_i} + \frac{\partial \sigma_{ij}^{sgs}}{\partial x_j} = 0 \quad (3c)$$

In the above equations, ρ is the density, E is the total energy per unit mass, p is the pressure, u_i ($i = 1, 3$) are the velocity components, τ_{ij} and q_i are, respectively, the viscous stresses and heat conduction, and τ_{ij}^{sgs} , H_i^{sgs} , and σ_{ij}^{sgs} are the subgrid stresses that have to be modeled. The above equations are supplemented by the filtered equation of state $\bar{p} = \bar{\rho} R \bar{T}$ and other relevant thermodynamic relations. The filtered viscous stresses and heat conduction terms are defined as:

$$\bar{\tau}_{ij} = \bar{\mu} \left(\frac{\partial \bar{u}_i}{\partial x_j} + \frac{\partial \bar{u}_j}{\partial x_i} \right) - \frac{2}{3} \bar{\mu} \frac{\partial \bar{u}_k}{\partial x_k} \delta_{ij} \quad (4a)$$

and

$$\frac{\partial \bar{q}_i}{\partial x_i} = -\bar{\lambda} \frac{\partial \bar{T}}{\partial x_i} \quad (4b)$$

where $\bar{\mu}$ and $\bar{\lambda}$ are respectively the filtered coefficient of molecular viscosity and thermal conductivity. In this study, the Sutherland's law of viscosity is used to determine molecular viscosity and $\bar{\lambda} = \bar{\mu} C_p / \text{Pr}$, where Pr is the Prandtl number and C_p is specific heat at constant pressure (assumed to be a constant in this study). The filtered total energy per unit volume is given by

$$\bar{\rho} \bar{E} = \bar{\rho} \bar{e} + \frac{1}{2} \bar{\rho} \bar{u}_i \bar{u}_i + \frac{1}{2} \bar{\rho} [u_i u_i - \bar{u}_i \bar{u}_i] \quad (4c)$$

Here, $\bar{e} = C_p \bar{T}$ is the internal energy per unit mass and the last term in Eq. (4c) is a contribution due to the unresolved kinetic energy, hereafter referred to as the subgrid kinetic energy and is defined as $k = \frac{1}{2} [u_i u_i - \bar{u}_i \bar{u}_i]$.

The exact subgrid terms are given by

$$\tau_{ij}^{sgs} = \bar{\rho} [u_i u_j - \bar{u}_i \bar{u}_j] \quad (5a)$$

$$H_i^{sgs} = \bar{\rho} [E u_i - \bar{E} \bar{u}_i] + [\bar{p} u_i - \bar{p} \bar{u}_i] \quad (5b)$$

$$\sigma_{ij}^{sgs} = [\bar{u}_j \bar{\tau}_{ij} - \bar{u}_j \bar{\tau}_{ij}] \quad (5c)$$

In order to solve this system of equations, models must be found for the above noted subgrid terms τ_{ij}^{sgs} , H_i^{sgs} , and σ_{ij}^{sgs} . In addition, it is necessary to obtain the subgrid turbulence intensity to evaluate the flame speed model (which is discussed in the next section). Subgrid models for compressible flows are still relatively new (References 1, 2 and 3) and no best choice exists. In this study, we employ the one-equation model for the subgrid kinetic energy proposed by Reference 4. The equation is:

$$\frac{\partial \bar{\rho} k}{\partial t} + \frac{\partial (\bar{\rho} \tilde{u}_i k)}{\partial x_i} = P_k - D_k + \frac{\partial}{\partial x_i} \left(\bar{\rho} v_t \frac{\partial k}{\partial x_i} \right) \quad (6)$$

Here, P_k and D_k are the rate of production and dissipation of subgrid kinetic energy, respectively. An advantage of this model is that unlike in algebraic eddy viscosity models (e.g., Smagorinsky's model), the production and the dissipation of the subgrid kinetic energy need not be in equilibrium. The above model however, neglects the pressure dilatation term that appears in the original exact k -equation for two reasons. First, it is still unclear how to model the pressure dilatation in terms of the resolved flow field variables, and second, at low fluctuating Mach numbers, its influence may be negligible. The production and dissipation of the subgrid kinetic energy are modeled respectively as:

$$P_k = - C_k \tau_{ij}^{sgs} \frac{\partial \tilde{u}_i}{\partial x_j} \quad (7a)$$

$$D_k = C_\epsilon \bar{\rho} \frac{k^{3/2}}{\Delta_g} \quad (7b)$$

where Δ_g is a characteristic grid size and v_t is the subgrid eddy viscosity given by $v_t = C_v K^{1/2} \Delta_g$. The three constants appearing in the above equations have been prescribed as:

$$C_k = 1.0, C_\epsilon = 0.916, C_v = 0.0854.$$

A new dynamic k -equation model is used here as a possible replacement to the constant coefficient model described above. The dynamic approach uses a new method for local evaluation of the coefficients so that the algebraic identity of Reference 5 is no longer necessary. The dynamic model has been shown to perform significantly better than the constant coefficient model and the Germano et al.'s eddy viscosity model for incompressible, homogeneous isotropic turbulence, Taylor–Green flow and temporal mixing layers (Reference 6, 7, and 8).

The k -equation is solved simultaneously with the rest of the flow equations. With k and v_t determined, the subgrid stresses are evaluated as:

$$\tau_{ij}^{sgs} = - 2 \bar{\rho} v_t \left(\tilde{S}_{ij} - \frac{1}{3} \tilde{S}_{kk} \delta_{ij} \right) \quad (8a)$$

where $\tilde{S}_{ij} = \frac{1}{2} \left(\frac{\partial \tilde{u}_i}{\partial x_j} + \frac{\partial \tilde{u}_j}{\partial x_i} \right)$ is the resolved scale stress tensor and H_i^{sgs} is given by

$$H_i^{sgs} = - C_\epsilon \bar{\rho} v_t \frac{\partial \tilde{H}}{\partial x_i} = - C_\epsilon \bar{\rho} v_t \left(C_p \frac{\partial \tilde{T}}{\partial x_i} + \tilde{u}_j \frac{\partial \tilde{u}_j}{\partial x_i} \right) \quad (8b)$$

and $C_e = 1/Pr_t$. Pr_t is the turbulent Prandtl number and σ_{ij}^{sgs} is modeled by

$$\sigma_{ij}^{sgs} = \tilde{u}_j \tau_{ij}^{sgs} \quad (9)$$

Note that in Eq. (8a) no attempt has been made to separate the Leonard and Cross terms from the subgrid Reynolds stresses since it has been noted earlier (Reference 9) that in doing so, the modeled LES equations no longer satisfies Galilean invariance. It should also be noted that third order correlation arise as a result of this modeling approach but are neglected here.

3.1.2 Flame Propagation Model

To simulate the propagating surface in the premixed case, a thin-flame model Reference 10 is used in which a progress variable G is defined that is governed by the equation:

$$\frac{\partial G}{\partial t} + \mathbf{u} \cdot \nabla G = -u_F |\nabla G| + \frac{v_t}{C_G} \nabla^2 G \quad (10)$$

where \mathbf{u} is the fluid velocity and u_F is the local propagation speed. This equation is solved simultaneously with the LES equations. This equation describes the convection of a level surface, described by $G = \text{constant}$, by the fluid velocity while simultaneously undergoing propagation normal to itself at a speed u_F . In the flow field, the value of G is in the range $[0,1]$ and in flame front modeling, G exhibits a step function-like behavior, separating the burned region from the unburned region. G is assigned the value of unity in the unburned region and zero in the burned region with the thin flame identified by a fixed value of G in the range $[0,1]$. Since no heat release is included in the present study, any value of $G = \text{constant}$ can be used to identify the flame front. Thus, the physical interpretation is that an evolving G -level for any level G represents the simulated propagation of the constant property surface of that level. Thus, statistics from all values of $G = \text{constant}$ can be combined; in effect, each simulation corresponds to a family of simulations parameterized by G .

The second term on the right hand side of equation (10) does not appear in the original equation, however it was added here in order to avoid false minima from occurring in the flow. A false minimum is not physically meaningful and results from a lack of resolution of the scalar field. Reference 10 and 11 both added a similar term to the above equation in their simulations of isotropic turbulence. The constant $C_G = 4$ was used in all simulations reported here. It was determined by analyzing the simulation data that this term does not affect the key results of this study and further, in most of the simulated cases, less than 10% of the grid points exhibited these false minima.

In LES of premixed combustion, u_F is considered the turbulent flame speed u_t averaged over a characteristic volume. The turbulent flame speed is not known explicitly and must be modeled. For example, the RNG model of Yakhot (Reference 12):

$$\frac{u_t}{S_L} = \exp \left[\frac{(u'/S_L)^2}{(u_t/S_L)^2} \right] \quad (11)$$

is used for some of the simulations. In other cases, a model based of Pocheau has been used in high turbulence cases (Reference 13). Here, S_L is the laminar flame speed and $u' = \sqrt{2k}$ is the subgrid turbulence intensity. Thus, the solution of the one-equation model for the subgrid kinetic energy is necessary to obtain the subgrid intensity to close Eq. (11). This is another reason for the choice of the subgrid model in the present study. Yakhot (Reference 12) found that Eq. (11) correlates quite well with various experimental observations at least in the low to moderate turbulence intensity cases. The laminar flame speed S_L contains information about the chemical kinetics and molecular diffusion and, once the local subgrid turbulence intensity is determined, Eq. (11) can be used to find u_F for a given fuel mixture.

3.2 Subgrid Combustion Models

The principle difficulty in reacting LES simulations is the proper modeling of the combustion-related terms involving the temperature and species, for example, the convective species fluxes such as due to subgrid fluctuations and the filtered species mass production rate. Probability density function (pdf) methods, when applied within LES either in the assumed shape or evolution equation form, may be used to close, and, in principle, any temperature-species correlations. However, the treatment of molecular mixing and small scale stirring using phenomenological models as in pdf methods have been only partially successful in predicting the mixing effects. Problems have also

been noted when gradient diffusion assumption based eddy viscosity model is used to approximate the species transport terms. Use of this type of assumption for reactive species is dubious, as noted earlier (Dimotakis, 1989; Pope, 1979). Frankel et al. (1993) attributed the use of this assumption as the source of errors in the comparison of reacting LES simulations with direct numerical simulation (DNS) data.

Earlier, Kerstein (Reference 4) developed a mixing model termed the linear eddy mixing (LEM) model and demonstrated its ability to separately treat the molecular diffusion and turbulent convective stirring processes at all relevant fluid mechanical length scales of the flow. The scalar fields are simulated within a 1D domain, which represents a stochastic slice through the local scalar field. Within the context of LES, the LEM model is used to represent the effect of only the unresolved scales on the scalar fields while the larger resolved turbulent scales of the flow are calculated directly from the LES equations of motion. To accomplish this, the mixing model is implemented within each LES cell. In the present investigation, the procedure for coupling the LEM model to the LES equations is essentially identical to the method developed earlier for gas-phase combustion (Reference 14, 15, 16, 17, and 18) and therefore, is only summarized here.

As noted in earlier studies, the subgrid LEM approach has several advantages over conventional LES of reacting flows. In addition to providing a fundamentally accurate treatment of the small-scale turbulent mixing and molecular diffusion processes, the present method avoids gradient diffusion modeling of scalar transport. As a result, both co- and counter-gradient diffusion processes can be simulated without requiring any model changes.

3.3 Linear-Eddy Single Phase Model

The details of the baseline gas phase LEM model have been summarized earlier (References 4 and 14). Briefly, the exact reaction-diffusion equations (without any LES filtering and without the convective term) are numerically solved using standard finite-difference scheme in the local 1D domain using a grid fine enough to resolve the Kolmogorov and/or the Batchelor microscales. Consequently, the species production rate can be expressed in terms of the raw temperature and species fields without any modeling. This is a particularly attractive feature of the present model since it obviates the need for any modeling of the highly non-linear production terms.

Simultaneous to the deterministic evolution of the reaction-diffusion processes, turbulent convective stirring within the 1D domain is modeled by a stochastic mapping process (Reference 4). This procedure models the mixing effect of turbulent eddies on the scalar fields and is implemented as an instantaneous rearrangement of the scalar fields without changing the magnitudes of the individual fluid elements, consistent with the concept of turbulent stirring. An underlying assumption employed here is that the subgrid turbulence is homogeneous and isotropic. Within the context of the LES, this is a reasonable assumption and is generally invoked for subgrid modeling.

The implementation of the stirring process requires (randomly) determining the eddy size from a length scale pdf $f(l)$ in the range between the Kolmogorov scale and the characteristic subgrid length scale which is currently assumed to be the local grid resolution. A key feature of this approach is that the range of scales is determined from inertial range scaling as in 3D turbulence for a given subgrid Reynolds number. Thus, the range of eddy sizes and the stirring frequency (or event time) incorporates the fact that the small scales are 3D even though it is still implemented on the 1D stochastic domain. This feature is one of the major reasons for the past successes of LEM in diffusion

flame studies. The details of the method to determine these parameters and the mapping procedure are given in (References 16, 17, and 18).

3.4 Subgrid Implementation of LEM

Since the filtered species is calculated directly by filtering the subgrid fields, there is no need to solve the LES filtered equations for the species. Consequently, use of conventional (gradient diffusion) models is avoided. However, since the subgrid fields are also influenced by large-scale convection (due to the LES-resolved velocity field and the subgrid turbulent fluctuation estimated from subgrid kinetic energy), additional subgrid-supergrid coupling processes are required. Here, supergrid denotes the resolved scale field as computed by the LES equations.

The convection of the scalar fields by the supergrid field (supergrid-to-subgrid coupling) across LES cell faces is modeled by a "splicing" algorithm developed earlier (References 14, 16, and 17). Details of this process are given in the cited references and, therefore, avoided here.

Briefly, the subgrid and supergrid processes involve the following processes. Given the initial subgrid scalar fields and void fraction in each LES cell, molecular diffusion, chemical reaction, turbulent stirring, and large-scale convection processes are implemented as discrete events occurring in time. The epochs of these processes are determined by their respective time scales. This type of discrete implementation is similar to the fractional step method used to solve differential equations.

As the subgrid scalar fields evolve under the action of these processes, the resolved LES fields (the filtered equations of mass, momentum, and energy) are solved concurrently on the LES time scale (the CFL time step). The resolved scales influence the evolution of the subgrid scalar fields via the specification of the subgrid length scale and the subgrid Reynolds number. The subgrid scalar fields in turn influence the development of the resolved scales (subgrid-to-supergrid coupling) by providing the filtered scalar fields and any temperature-species correlations calculated from the subgrid scalar fields.

The splicing algorithm employed in the study transported subgrid fluid elements from one LES cell to another based on the local velocity field. The local velocity consisted of the resolved velocity plus a fluctuating component (estimated from the subgrid kinetic energy). The splicing events were implemented discretely on the convective time scale (which is also the time-step for the gas phase LES). Each splicing event involved 1) the determination of volume transfer between adjacent LES grid cells, 2) the identification of the subgrid elements to be transferred, and 3) the actual transport of the identified fluid elements. The underlying rationale for this procedure has been discussed elsewhere (Reference 14). Some changes to the splicing algorithm are needed to simulate premixed combustion using the G-equation thin flame model. Details of these modifications are reported in Reference 19 and 20.

An important property of the splicing algorithm is that the species convection was treated as in Lagrangian schemes. Thus, convection was independent of the magnitude or gradient of the species that were transported and depended only on the velocity field. As a result, subgrid elements were transported without changing their species and temperature magnitudes. This property allowed this algorithm to avoid the classic difficulty of false numerical diffusion associated with the numerical approximation of convective terms in differential equations. By avoiding both numerical diffusion and gradient diffusion assumptions, the splicing algorithm allows an accurate picture of the small-scale effects of molecular diffusion to be captured, including differential diffusion effects.

In this project, the subgrid combustion model previously noted has been implemented both as a stand-alone model and as a subgrid model with the LES approach. Results obtained using these methods are reported in the References listed in Section 7.

4.0 Results

The detailed discussion of the results obtained in this study is given in the papers listed in Section 7. Here, we briefly summarize the key findings of this study and comment on their implications.

4.1 Model predictions in non-premixed combustion

Simulation using the subgrid model developed in this research has demonstrated that this approach was capable of capturing Re , Da , and Sc number dependencies without requiring any ad hoc fixes. Comparison with experimental data (reported in References 16, 21, and 22) showed that if this approach was used, accurate quantitative agreement with experimental data could be achieved. In contrast, conventional eddy diffusivity model results in erroneous prediction of the mixedness and hence, product formation.

4.2 Model predictions in premixed combustion

Many studies were conducted for premixed combustion using both the G -equation model and finite-rate kinetics model. Results reported in References 23, 24, and 25 demonstrate the ability of the present approach.

4.3 LES of premixed combustion with and without flame broadening

A new approach for conventional LES using the G -equation with the dynamic model has been developed for engineering level simulations. This model has also been extended to deal with flame broadening effects which is likely to occur in full-scale combustors due to the wide range of turbulence in the flow field. Model development and application to problems are discussed in References 25, 26, 27, and 28.

4.4 Application to full-scale combustors

The baseline LES model developed in this research was applied to simulate premixed combustion in a full-scale combustor such as the GE LM 6000. Results were compared with experimental data and excellent results were obtained in both the mean and turbulence flow fields. Results are discussed in References 30, 8, 27, and 13. Overview of these results were recently reported in References 28, and 29.

5.0 Conclusions

The results obtained under this research project have demonstrated a unique simulation methodology that is capable of capturing fundamental physics of scalar mixing and chemical reactions without any ad hoc model adjustments. Application in premixed and non-premixed combustion problems is discussed in the papers in Section 7. Extension of this method to deal with two-phase combustion as in spray combustion has already been carried out. Future studies of turbulent-chemistry interactions in full-scale combustors will employ this two-phase LES approach. Simplifications of the subgrid model for computational expediency is also being addressed. It was expected that with the advent of next generation massively parallel systems, LES of combustion in full-scale combustors could be attempted in a routine manner. However, the accuracy of the predictions depended significantly on the physics incorporated within the subgrid models. Simply increasing the grid resolution to improve the predictions was not likely to prove successful in the long run since typical test conditions in full-scale combustors would require grid resolution that is beyond the limit of then current (and perhaps future) computer systems.

The application of advanced physics-based mixing and combustion models within in the context of LES is the key to the development of simulation tools that can be used for engineering research. The LES methodology developed in this research has already demonstrated its unique capability since its predictions compared quite well with experimental data (this agreement was not achievable using conventional LES closures). Furthermore, this agreement was achieved using a relatively coarse grid when compared to conventional approaches reported in the past. The success of this approach could be directly attributed to the physics-based subgrid closures developed under this study. The application and validation of this methodology for engineering design of full-scale combustor remains to be demonstrated.

6.0 Acknowledgements

The computational effort under this project was carried out at the various DoD High Performance Computing (HPC) Centers and the NSF Supercomputer Center at Pittsburgh. Earlier (1996–97) support was provided on the Intel Paragon at WPAFB, OH, the SGI Power Challenge at Army Research Laboratory, MD and the Cray at the NSF center. Recently (1997–99), support was provided on the Cray T3E at NAVOCEANO, MS and the Origin 2000 at ASC (WPAFB), OH HPC centers in part under a Grand Challenge Project initiated through Wright Patterson Air Force Base with B.Sekar as a Co-PI. This computational support is gratefully acknowledged.

7.0 References

7.1 Cited References

- 1 Erlebacher, G. Hussaini, M. Y. Speziale, C. G. and Zang, T. A., (1987) "Toward the Large-Eddy Simulation of Compressible Turbulent Flows," Institute for Computer Applications in Science and Engineering, Hampton, VA, ICASE 87-20.
- 2 Squires, K. and Zeman, O., (1990) "On the Subgrid-Scale Modeling of Compressible Turbulence," Center for Turbulence Research, Proceedings of the Summer Program, pp. 47-59.
- 3 Moin, P., Squires, K., Cabot, W., and Lee, S., (1991) "A Dynamic Subgrid-Scale Model for Compressible Turbulence and Scalar Transport," *Phys. Fluids A*, Vol. 11, pp. 2746-2754.
- 4 Menon, S., and Kerstein, A.R. (1992) "Stochastic Simulation of the Structure and Propagation Rate of Turbulent Premixed Flames," *24th Symp. (Int.) on Combustion*, 24, pp. 443-450.
- 5 Germano, M., Piomelli, U., Moin, P., and Cabot, W. H., (1991) "A Dynamic Subgrid-Scale Eddy viscosity Model," *Phys. Fluids A*, Vol. 3, pp. 1760-1765.
- 6 Kim, W.-W. and Menon, S. (1995) "A New Dynamic One-Equation Subgrid-Scale Model for Large-Eddy Simulations," AIAA Paper No. 95-0356, 33rd Aerospace Sciences Meeting.
- 7 Kim, W.-W. and Menon, S. (1997) "Application of a localized dynamic subgrid-scale model to turbulent wall-bounded flows," AIAA 97-0210, 35th AIAA Aerospace Sciences Meeting.
- 8 Kim, W.-W., Menon, S. and Mongia, H., (1999) "Large-Eddy Simulation of a Gas Turbine Combustor Flow," *Combustion Science and Technology*, 1999 (to appear).
- 9 Speziale, C. (1985) "Galilean Invariance of Subgrid Scale Stress Models in Large-Eddy Simulations of Turbulence," *J. Fluid Mechanics*, Vol. 156, pp. 55-62.
- 10 Kerstein, A. R., Ashurst, W. T., and Williams, F. A., (1988) "The Field Equation for Interface Propagation in an Unsteady Homogeneous Flow field," *Phys. Rev. A*, 37, pp. 2728.
- 11 Smith, T. M., Menon, S., and McMurtry, P. A., (1994) "The Structure of Premixed Flames in Isotropic and Shear Driven Turbulent Flows," AIAA 94-0677, 32nd Aerospace Sciences Meeting, Reno, NV.
- 12 Yakhot, V. (1988) "Propagation Velocity of Premixed Turbulent Flame," *Combustion Science and Technology*, Vol. 60, pp. 191-214.
- 13 Kim, W.-W. and Menon, S. (1999b) "Large-Eddy Simulation of Turbulent Premixed Flames in the Thin Reaction Zone Regime," AIAA Paper 99-2816, 35th AIAA/ASME/ASEE/SAE Joint Propulsion Conference, Los Angeles, CA, June 20-23, 1999.
- 14 Menon, S., McMurtry, P., and Kerstein, A.R. (1993a) "A Linear Eddy Mixing Model for LES of Turbulent Combustion," in *Large-Eddy Simulations of Complex Engineering and Geophysical Flows*, (B. Galperin and S.A.Orszag, Eds.), Cambridge University Press, pp. 278-315, 1993.
- 15 Menon, S., McMurtry, P. and Kerstein, A. R. (1993b) "A Linear-Eddy Subgrid for Turbulent Combustion: Application to Premixed Combustion", AIAA Paper No. 93-0107.

-
-
- 16 Menon, S and Calhoon, W., (1996) "Subgrid Mixing and Molecular Transport Modeling for Large-Eddy Simulations of Turbulent Reacting Flows", *Symposium (International) on Combustion*, 26, 59-66, 1996.
 - 17 Calhoon, W.H. and Menon, S. (1996) "Subgrid Modeling for Reacting Large-Eddy Simulations," AIAA 96-0516, 34th AIAA Aerospace Sciences Meeting, Reno, NV, Jan. 15-18, 1996
 - 18 Calhoon, W. H. and Menon, S., (1997) "Linear Eddy Subgrid Modeling for Reacting Large-Eddy Simulations: Heat Release Effects," AIAA-97-0368, 35th Aerospace Sciences Meeting, Reno, NV, January 6-9, 1997.
 - 19 Smith, T. and Menon, S., (1998a) "Subgrid Combustion Modeling for Premixed Turbulent Flows," AIAA Paper No. 98-0242, 36th Aerospace Sciences Meeting and Exhibit, Reno, NV, January 12-15, 1998.
 - 20 Smith, T. and Menon, S., (1998b) "Flame/Turbulence Interactions in Premixed Stagnating Flows," AIAA Paper No. 98-2978, 29th Fluid Dynamics Conf., Albuquerque, NM, June 15-18, 1998.
 - 21 Goldin, G. and Menon, S. (1997) "A Scalar PDF Construction Model for Turbulent Non-Premixed Combustion," *Combustion Science and Technology*, Vol. 125, 47-72, 1997
 - 22 Goldin, G. and Menon, S., (1998) "A Comparison of Scalar PDF Turbulent Combustion Models," *Combustion And Flame*, Vol. 113, 442-453, 1998.
 - 23 Smith, T. and Menon, S. (1996) "Model Simulations of Freely Propagating Turbulent Premixed Flames", *Symposium (International) on Combustion*, 26, 1996.
 - 24 Smith, T. and Menon, S., (1997a) "One-dimensional Simulations of Freely Propagating Turbulent Premixed Flames," *Combustion Science and Technology*, Vol. 128, 99-130, 1997.
 - 25 Smith, T. and Menon, S., (1998a) "Subgrid Combustion Modeling for Premixed Turbulent Flows," AIAA Paper No. 98-0242, 36th Aerospace Sciences Meeting and Exhibit, Reno, NV, January 12-15, 1998.
 - 26 Smith, T. and Menon, S., (1998b) "Flame/Turbulence Interactions in Premixed Stagnating Flows," AIAA Paper No. 98-2978, 29th Fluid Dynamics Conf., Albuquerque, NM, June 15-18, 1998.
 - 27 Kim, W.-W. and Menon, S., (1999a) "Numerical Modeling of Fuel-Air Mixing in a Dry Low-Emission Premixer," to appear in the *Proceedings of the Second AFOSR International Conference on DNS and LES*, New Brunswick, New Jersey, June 7-9, 1999.
 - 28 Menon, S., Kim, W.-W., Stone, C. and Sekar, B. (1999b) "Large-Eddy Simulation of Fuel-Air Mixing and Chemical Reactions in Swirling Flow Combustor," AIAA Paper No. 99-3440, 30th Plasmadynamics and Lasers Conference, Norfolk, VA, 28th June - July 1, 1999.
 - 29 Menon, S., Kim, W.-W., Stone, C., Henry, W. and Sekar, B. (1999a) "Simulation of Fuel-Air Mixing and Reactions in Full-Scale Gas Turbine Combustors," presented at the 1999 DoD High Performance Computing Modernization Conference, Monterey, CA, June 7-10, 1999.
 - 30 Kim, W.-W., Menon, S. and Mongia, H. C., (1998) "Large-Eddy Simulations of Reacting Flow in a Dump Combustor," AIAA Paper No. 98-2432, 29th Fluid Dynamics Conf., Albuquerque, NM, June 15-18, 1998.

7.2 Relevant Papers

In addition to the references cited, the following papers are germane to the discussions in this addendum.

Menon, S. and Kim, W.-W. (1996) "High Reynolds Number flow Simulations using the Localized Dynamic Subgrid-Scale Model," AIAA 96-0425, 34th AIAA Aerospace Sc., Reno, NV.

Menon, S., Yeung, P.-K. and Kim, W.-W. (1996) "The Effect of Subgrid Models on the Computed Interscale Energy Transfer in Isotropic Turbulence", *Computer and Fluids*, Vol. 25, pp. 165-186.

Piomelli, U., Moin, P., and Ferziger, J. H., (1988) "Model Consistency in Large Eddy Simulation of Turbulent Channel Flows," *Phys. Fluids*, Vol. 31, pp. 1884-1891.

Pope, S.B., Yeung, P. K., and Girimaji, S. S., (1989) "The curvature of material surfaces in isotropic turbulence," *Phys. Fluids*, Vol. 1, pp. 2110-2018.

Rutland, C. J. and Trouvé, A., (1993) "Direct Simulations of Premixed Turbulent Flames with Nonunity Lewis Numbers," *Combustion and Flame*, Vol. 94, pp. 41-57.

Smith, T. and Menon, S., (1997b) "Large-Eddy Simulations of Turbulent Reacting Stagnation Point Flows," AIAA-97-0372, 35th Aerospace Sciences Meeting, Reno, NV, January 6-9, 1997.

Menon, S. , Pannala, S., Kim, W.-W., Smith, T. M. and Arunajatesan, S. (1998) "Parallel Simulations of Reacting Two-Phase Flows: A DoD Grand Challenge Progress Report," AIAA Paper No. 98-2928, 29th Plasmadynamics and Lasers Conference, Albuquerque, NM, June-15-18, 1998.

Addendum D

**Spray Modeling Based Upon Physically Accurate Models
at all Scales**

AFOSR Focused Research Initiative
Low Emissions, High Performance Gas Turbine Engines

Contract 200-IQ-14N44080
General Electric Aircraft Engines
Cincinnati, Ohio

Principal Investigator
Dr. Josette Bellan,
Visiting Associate

California Institute of Technology
Pasadena, California 91125

September, 1999

Table of Contents

	<u>Page</u>
1.0 Summary	1
2.0 Introduction	2
3.0 Results and Discussion	4
3.1 Liquid Spray Studies	4
3.2 Supercritical Fluid Disintegration Studies	7
4.0 Recommendations	9
4.1 Follow-Up Investigation	9
4.1.1 Model for the Prediction of Turbulent Two-Phase Flow with Phase Change	9
4.1.1.1 Behavior of a Priori Developed Models in <i>a Posteriori</i> Simulations.	9
4.1.1.2 Experimental Validation of the Best Behaved <i>a Posteriori</i> Models	9
4.1.2 Supercritical Fluid Disintegration	10
4.1.2.1 LES of Supercritical Mixing Layers for Binary Fluids (Heptane-Nitrogen)	10
4.1.2.2 LES of Supercritical Mixing Layers for Multicomponent Mixtures.	10
5.0 References	12
5.1 Cited References	12
5.2 Relevant Papers	12

1.0 Summary

Fundamental research was performed under the guidelines of the Air Force Office of Scientific Research (AFOSR) Announcement and under the technical guidance of General Electric Aircraft Engines (GEAE). The research described here was aimed at controlling combustion in gas turbine engines so as to achieve increased efficiency and pollutant reduction. The California Institute of Technology (Caltech) was one of the members of a team assembled by GEAE.

The Caltech effort focussed on the modeling of both liquid sprays for the purpose of understanding what were the control parameters in various regions of the spray, and on fluid drop disintegration at realistic chamber pressures.

Traditional modeling did not account from first principles for the microscale turbulent mixing occurring at the smallest scales and affecting drop dispersion as well as mixing of gas; and therefore governing combustion and pollutant reduction. The novelty of the present approach was to categorize all two phase flow length scales into macroscales and microscales for the realistic case of an inhomogeneous flow laden with evaporating drops. The macroscales were the length scales of engineering relevance whereas the microscales were the length scales of scientific relevance; all phenomena occurring at the microscale had a serious impact on observations performed at the macroscale and vice-versa. We describe here the utilization and enhancement of models previously developed at Caltech - Jet Propulsion Laboratory (Caltech/JPL) in order to represent the microscale, and then we discuss the derivation from these models of submodels that could be used at the macroscale. These microscale models will be tested in further eventual investigations by coupling them to macroscale models accounting only for the large scales, and thus inherently devoid of the smallest scales effects.

Combustor design codes used in the aircraft industry invariably need initial and boundary conditions. The spray size distribution was one of the crucial items of information that was used as input to these codes; yet this information was based on empirical/computational information obtained from subcritical (i.e. low pressure) liquid atomization instead of the supercritical (i.e. the high pressure conditions of the advanced design) fluid disintegration that would prevail in the new generation of engines. For this reason, part of our study was devoted to a preliminary investigation relevant to supercritical fluid disintegration.

Within the course of this investigation, we used the Caltech/JPL supercomputing facilities, including the CRAY C90 and the HP-Exemplar parallel computer. The contribution of this computational facility was crucial to the accomplishment of the task.

Future work was also described which was not included under this contract's funding. This future work addresses two different issues. First, we want to validate the microscale model in two steps as follows: 1) inclusion of several microscale models into a macroscale model to determine which of the submodels gives the most accurate results by comparison with the original all-scale simulation from which the submodels were derived, and 2) validation of the most accurate model found in Step 1 by comparing it with experimental data. Second, future work was described that will lead to the prediction of fluid jet disintegration under the realistic high pressure conditions of the new gas turbine engines.

2.0 Introduction

Improvements in civil and military transport required the development of new concepts for gas turbine engines. Before these new concepts could be adopted for engine design, it had to be demonstrated that the engines complied with the limits for pollutant emissions. In particular, NO_x and CO emissions had to be reduced from the then-current levels during flight; and unburned hydrocarbons had to be reduced during idling, takeoff, and landing operations because of proximity to urban areas.

Three low-NO_x combustor concepts have been proposed: lean-premixed-prevaporized (LPP), lean direct injection (LDI), and rich burn/quick quench/lean burn (RQL). It was impossible to promote one of these proposed concepts over the others because the experimental evidence showed that each had advantages and disadvantages in their original configuration. Further testing and optimization of these configurations was not proposed due to the prohibitively large financial resources which would be needed to completely define the design of mass production engines. The reason for this situation was the wide range of time and length scales associated with drop evaporation, mixing of fuel and oxidizer (in the highly turbulent environment prevailing in the engine), ignition and combustion. Before being able to design such an engine, it was crucial to understand the contributions of these different phenomena and relevance of all these scales to soot, NO_x and CO production.

The only practical path to controlling and optimizing the three aforementioned systems and to comparing their performance was to use results obtained with codes based upon physically-accurate models. As practice has shown at the Boeing Aircraft Co., such a strategy can be far more economical than empirically-based testing.

However, current models of spray evaporation, ignition, and combustion lack many of the features necessary for making accurate predictions. The state-of-the-art codes were still based upon steady conservation equations, single isolated drop evaporation, $k-\epsilon$ turbulence model or assumed probability density function (PDF) methods untested under two-phase flow conditions, and 2D axisymmetric geometry. As a result, these models cannot account for the multitude of scales identified earlier.

One systematic way to categorize the multitude of length scales associated with multiphase flows was to group them into *macroscales* and *microscales*. Macroscales, grouped the scales of engineering relevance, the scales at which measurements of temperature and species in the engine were made. Depending upon the size of the engine, the macroscales were $O(10)$ – $O(100)$ cm. In contrast, microscales were scales which were not available for engineering observations because they were $O(0.1)$ – $O(0.001)$ cm. These were the scales at which drops interact either dynamically or thermodynamically, at which the Kolmogorov scales dissipate momentum through the action of viscosity, and the scales at which molecular diffusion mixes reactants. Since mixing of fuel and oxidizer was critical to both performance and emission control of commercial and military engines, clearly, these microscales have enormous impact upon the characteristics measured at the macroscale. In fact, it was the two-way coupling between microscale and macroscale events which determined the characteristics of combustion and pollutant formation.

Conventional modeling of spray combustion has focused upon the modeling of the macroscale without regard to the microscale. Phenomena such as flow penetration between drops, limitations on heat and mass transfer due to drop proximity, dispersion of drops by microscale turbulence, drop

collisions and occasional coalescence, and the impact of molecular diffusion upon combustion through mixing have all been ignored. On the other hand, extremely detailed models describing the behavior of a small number of drops in matrices or streams have never been considered to be practical enough for incorporation into macroscale models. This was because these models were based upon many unrealistic assumptions and the information they provide was geometry-dependent.

Moreover, since the advanced generation of gas turbine engines were to operate at pressures of up to 60 atm, the jet fuels used would be at supercritical conditions with respect to the combustion chamber conditions. Therefore, the question arose regarding the applicability under these realistic conditions of the many existing models and correlations describing fuel atomization. For example, experimental evidence from the Air Force Research Laboratory at Edwards Air Force Base conclusively demonstrated that supercritical fluid disintegration no longer resembled subcritical atomization that was dominated by primary atomization yielding ligaments and by further secondary atomization yielding drops; instead finger-like protuberances (wisps) emerged from the jet and quickly dissolved into the surrounding fluid. It should be realized that because the critical point of a mixture was a function of the composition, the above-described interest in liquid drop sprays was relevant because the combustion chamber could harbor both regions of subcritical and supercritical conditions. However, the ultimate goal should have been to have models embedding both types of behavior: subcritical and supercritical.

3.0 Results and Discussion

Our approach was to build upon the existing California Institute of Technology – Jet Propulsion Laboratory (Caltech/JPL) models both in the area of subcritical liquid drop behavior and supercritical fluid drop behavior. A separate description of these two approaches follows; although the general fluid model that was used to describe supercritical conditions has been validated in both subcritical and supercritical regimes. However, this validation occurred after the crucial database for the liquid drop spray related study was generated, and therefore, the more general model could not be used in that part of the study. The following description was the general approach, its progression, and the most important findings.

3.1 Liquid Spray Studies

The main objective of this investigation was to use the promising protocol of Direct Numerical Simulation (DNS) followed by a Large Eddy Simulation (LES) as a guideline. Because of the limited funding, it was not expected to reach the stage of LES, but to obtain the necessary information to perform LES in future studies. The following explains the underlying rationale of the DNS/LES approach that must be followed rigorously in order to ensure that the investigation was correct.

DNS was a method whereby all scales of the flow, down to the Kolmogorov scale, were resolved; given the then-current state of the art in computing power, this method could be applied only to very small physical domains and for Reynolds numbers that were smaller than those typical of the turbulent regime. A different approach from DNS was Large Eddy Simulation in which the governing equations rather than being resolved down to the Kolmogorov scale were instead filtered locally in either physical or wave number space (the wave number space was not recommended for inhomogeneous flows); therefore, the effects of the small scales of the flow field were removed through filtering, and had to be modeled and further reinserted into the equations in a consistent manner. Practically, LES applied to turbulent flows were methods whereby the flow equations were first filtered and then solved at the larger scale (than the smallest scale of the flow), with the missing detailed information being reintroduced through Subgrid Scale (SGS) models. The success of LES in the accurate portraying of the flow depended to a great extent on the employed SGS model. For this reason, a large effort was devoted to the derivation of SGS models that either emulate experimental data, or that were based on results from DNS that resolve all the scales of the flow (albeit in a very small volume and for Reynolds numbers smaller than those characteristic to the turbulent regime). When SGS models were derived from either experimental data or from DNS, they were called *a priori*, a term implying that there was an uncertainty associated with them; indeed, the uncertainty was that of their performance in a LES. In contrast to *a priori* models, *a posteriori* models test the performance of *a priori* models in LES by comparing the LES results either with the observations, or with the filtered (with the same filter as that used in the LES) DNS results, depending on the origin of the *a priori* model. Only when this comparison was satisfactory could a SGS model be considered to have good potential for a more general application.

There were many examples of appropriate *a priori* models that did not perform satisfactorily in *a posteriori* tests even for relatively simple flows where the only necessary model was that of the SGS stresses; however, in this study one additionally needed to model the SGS heat and mass fluxes.

There were several reasons for this lack of performance: Constant coefficient models (wherein the adopted functional form of the SGS was proportional to a constant that was either empirically determined or calculated from *a priori* analysis) were necessarily flow dependent, and therefore could not be expected to be applicable to flows different from their originators. Therefore, in order for models to be of general value, dynamic models wherein the proportionality coefficient was determined as a function of space and time, were needed. Our study culminated with the development of several dynamic models; which of these models have the correct behavior in a LES study remains to be determined in a follow-up investigation.

Since DNS for mixing layers laden with evaporating drops was not available, we first proceeded to develop such a database. However, the preliminary step was to insure that our drop model was experimentally validated. Therefore, a comparison of several drop models existing in (Reference 1), showed that the JPL derived model that constitutes the basis of all our studies was superior to all other models. The validation was conducted both for hydrocarbon and water drops, and for a temperature range relevant to evaporation.

Using this drop model, a three-dimensional mixing layer having one stream laden with as many as 7.3×10^5 evaporating drops was simulated using DNS; the pre-transitional study described in (Reference 2) yielded a preliminary understanding of drop behavior in mixing layers. The simulations showed that at low gas temperatures the droplet laden stream rapidly saturates due to the buildup of evaporated vapor and cooling of the gas temperature resulting from latent heat effects. After this saturation occurs, the droplets in the free stream essentially cease vaporizing; however, droplets near the mixing region become engulfed into the layer where they come into contact with higher temperature carrier gas and continue to evaporate. This results in a large disparity between the droplet size distributions found in the interior and laden stream portions of mixing layers.

We also used the same simulation database to address assumed probability density function (PDF) modeling of non-premixed combustion in Reynolds averaged Navier-Stokes (RANS) simulations; this study is described in (Reference 3). In that investigation we derived the necessary mixture fraction moment transport equations, analyzed their budgets and observed that the assumed β probability density function (PDF) poorly represents the simulated scalar fields. This observation was very important as the β PDF was currently used in turbulence models of single phase flows, and was also used by investigators to model two phase flows, albeit without justification. Our findings suggest that great caution must be exercised to blindly extending successful single phase flow methods to two phase flows without prior validation.

Although generally employed for single phase flow predictions, LES was also used to study particle dispersion. In reality, particles were convected by the superimposed effects of both the resolved (filtered) velocity field and the unresolved subgrid velocity fluctuations. However, in most studies the subgrid effects were neglected under the assumption that the particle inertia was sufficiently large; under this assumption the particles should not significantly interact with the small scale flow motions. This assumption has never been tested against either DNS or experimental data, and the actual influence of subgrid fluctuations may have a significant effect on dispersion even for particles with Stokes numbers ~ 1 depending on the flow Reynolds number and the relative filter width. The situation becomes more complex for evaporating droplets due to the additional effects of subgrid thermodynamic fluctuations which affect both the droplet heating and the vaporization rates. One exception to the above mentioned studies was that of Pannala and Menon (citation in Reference 4) who performed LES of droplet laden turbulence using a modified eddy interaction model (EIM) to

account for subgrid velocity (but not thermodynamic) fluctuations. The subgrid variance was provided by an additional transport equation for the subgrid kinetic energy; however, the EIM was simply extended without further comment, and no *a priori* testing was mentioned. Also, using the subgrid kinetic energy equation for the fluctuation variances was not directly applicable to flows in which the subgrid velocity may be anisotropic.

Therefore the objectives of our next study was to: 1) extend our pre-transitional simulations to sufficiently high Reynolds numbers to capture the transition to mixing turbulence for multiphase flows where both evaporation and complete two-way coupling were important, 2) use the simulated database to perform an *a priori* investigation of the role of subgrid fluctuations on the transport, heating and vaporization of droplets in the context of LES, and 3) to propose a model for these subgrid effects. This part of our investigation was described in (Reference 4). The results include a detailed description of the transition to turbulence and the corresponding effects of the flow Reynolds number and droplet mass loading ratio. Subgrid fluctuations were then investigated based on filtering the resolved DNS fields using both spherical and cubic spatial filter kernels. An extension of the EIM, which was tested *a priori*, was then proposed to model both velocity and thermodynamic subgrid fields for LES which was based on a Scale-Similarity (SS) model to predict subgrid variances. Results obtained for two different initial Reynolds numbers and two different loading ratios showed that increasing the loading ratio at fixed initial Reynolds number produces a more natural turbulence and increases the preferential concentration of the drops (i.e. drop clustering). One of the most important results of this study was to show that the drops follow closely the subgrid fluctuations indicating that any model neglecting this aspect might be highly in error.

Based upon the knowledge that the subgrid information might be crucial, we proceeded with the development of the LES equations and a model to infer information from the larger scale resolved quantities (LES grid) to the smaller scale which in a LES was unresolved; this investigation is discussed in (Reference 5). We first evaluated the terms in the LES equations and showed that several assumptions embedded in their derivation were justified. Then, we proposed a model for inferring small scale information from the large scale and showed using the database developed in the publication of (Reference 4) that our model predicted the small scale variables at the droplet locations considerably better than simple interpolation of the large scale variables would do it; this result was obtained for the SGS stresses as well as for the SGS heat and mass fluxes. Finally, we used three constant coefficient SGS models and the transitional database (for two different initial Reynolds numbers and two different mass loading ratios) to determine if the functional form of these models was appropriate for the present flow. Our findings indicated that the classical Smagorinsky (SM) model was inadequate to describe this flow (consistent with numerous studies of single phase flows), but that the Gradient (GR) and the SS models in which the proportionality constant was properly calculated, were excellent representations of the database.

Constant coefficient models were by construction flow dependent, and in order to generalize the value of the constant coefficient SGS models to a variety of flows, dynamic SGS models were necessary. The accomplishment of a dynamic model was to effectively infer information at the subgrid scale from the information at the smallest resolved scales based upon the assumption that the main interaction between the SGS and resolved scales occurs with the smallest resolved scales. In the context of particle laden flows, this subgrid scale information might be essential as shown by the studies presented in References 4 and 5. Therefore, we proceeded with the development of dynamic SGS models; this study was described in (Reference 6). Similarly to our other studies

described above, not only did we develop dynamic subgrid models, but we also carefully checked the underlying assumptions of dynamic studies to evaluate their validity for the present flow. Our findings indicated that the similarity assumption that was the cornerstone of dynamic modeling was satisfied as far as the SGS stresses were concerned for all four models tested; these included two single models (SM and GR), and two mixed models (GRDSM and SSDSM). In the GRDSM and SSDSM models the GR and SS part of the model has a coefficient that was kept at its constant theoretical value, whereas the SM coefficient was determined dynamically (i.e. as a function of time and spatial position). Based on this evaluation, we find that the GR model was the only one that correlated well with the stresses and reasonably satisfied assumptions of dynamic modeling. For this reason, we extended the dynamic GR model to the SGS heat and mass fluxes, and further proposed a model wherein the coefficient was only a function of time with the spatial dependence being provided by the functional form of the model. We also noted that it was well known that *a priori* studies were only indicative of the prospects of models, that in fact models with inferior *a priori* prospects might eventually be better behaved in an actual LES, and that the final conclusions could be made only after a LES, *a posteriori* simulation; (Reference 6) contains a thorough discussion on this topic. Therefore, we proposed a follow-up *a posteriori* study to first determine which of the derived models was most accurate, and second to validate the model by comparison with experiments.

3.2 Supercritical Fluid Disintegration Studies

This part of the investigation was devoted to the study of high pressure effects in the context of fluid jet disintegration. The approach was use the DNS technique to simulate a shear layer between two fluids; the chosen fluids were heptane–nitrogen, as the supercritical fluid model had been validated with Japanese microgravity experimental data in a different but related research program. Of particular concern was the value of the thermal diffusion factor entering the calculation of the additional transport terms that may become important at supercritical conditions: the Soret and Dufour terms. Thermal diffusion factor databases do not exist (we have this information from the National Institute of Standards and Technology); however, in our validation study we were able to use part of the database to determine the value of the thermal diffusion factor, and once the value was set, we used the complement of the database for model validation.

The supercritical mixing layer study was presented in (Reference 7). Because thermal diffusion factor values did not exist for most mixtures of interest in the gas turbine engine context, and because there were two possibilities for defining thermal diffusion factors (as shown in a paper produced under the related aforementioned study, where it was also shown that the difference of the two thermal diffusion factors was a thermodynamic function that was simply evaluated from the equation of state), one of the first tasks in this work was to identify the contributions of each definition of the thermal diffusion factors as if they were not known. The purpose of this first part of the study was to ascertain the different trends, if any, that the two different thermal diffusion factors would predict under the assumption that they were constant. Our findings showed that knowledge of the thermal diffusion factors was paramount in producing correct predictions since the qualitative behavior of the solution was different under the assumption of each defined type being constant. Following this exploratory study, we used the thermal diffusion factor calculated under the related study for heptane–nitrogen to investigate now the behavior of a three dimensional supercritical mixing layer at 60 atm where the lower heptane stream was at 600 K and the upper nitrogen stream was at 1000 K, this parametric regime being chosen to portray injection conditions in future gas

turbine engines. From the practical point of view, the most important finding was the identification of the formation of strong density gradient regions (Reference 7), in complete qualitative agreement with experimental observations from the Air Force Laboratory that were also included in the manuscript (Reference 7). Moreover, the fact that in those regions the compression ratio (measuring departures from the perfect gas behavior) in less than unity and the mass diffusion factor (measuring departures from an ideal mixture) was also less than unity, were both consistent with the experimental observations that fluid disintegration under supercritical conditions no longer resembled liquid atomization characterized by primary breakup (ligament formation) and followed by secondary breakup (drop formation); instead the wisps of fluid emerging from the jet dissolved into the surrounding fluid. This pointed to the fact that current drop size distributions that were used as input to computational fluid dynamic (CFD) codes, and which were invariably based upon subcritical studies, did **NOT** portray the real fluid disintegration under the new high pressure chamber conditions. In the follow-up investigation described in Section 4.1 there was an outline of further work to be undertaken to extend this study to the prediction fluid disintegration such as needed for input to CFD codes.

4.0 Recommendations

4.1 Follow-Up Investigation

Since the investigations under Sections 3.1 and 3.2 could not be completed under this current contract. What follows are two separate efforts that could bring the research to completion. The deliverable items under each effort are specified.

4.1.1 Model for the Prediction of Turbulent Two-Phase Flow with Phase Change

Several issues remained at the end of our investigation as follows:

4.1.1.1 Behavior of *a Priori* Developed Models in *a Posteriori* Simulations.

To resolve this issue one must perform LES with a variety of models and compare the results with those of the filtered DNS; this was called an *a posteriori* study. In particular, one must address the question of how to accurately model at the larger scale the source terms associated with mass (and species), momentum and energy that couple the two phases. In fact this opens the question of the so called "computational particles" that were generally used in most CFD calculations without the support of accurate justification. The question is: How many real particles can be represented by a computational particle without losing accuracy (the accuracy must be defined, for example, at 90% of source term representation)? Using the DNS database, we now have the ability to quantitatively answer this question.

Additionally, because in a LES one must inherently use computational rather than real particles, this opens up another issue: that of dense regions of the spray. In other words, we want to explore in a well defined protocol, with supporting justification, the use of dense cluster of drops models (such as developed at JPL over the last two decades if it turns out that a large number of drops may be represented by a computational drop, or other, even more detailed models if it turns out that only a small number of drops may be represented by a computational drop with the defined accuracy), to represent the "computational particles" that in any event must be utilized in LES. This was a crucial issue that has so far eluded all investigations and could not be addressed in the funded study due to the need to first develop a well defined protocol and understanding associated with dilute spray regions (note that although we performed DNS calculations for mass loading ratios as large as 0.5, the highest volume fraction was no larger than 7.2×10^{-4} despite the 5.7×10^6 drops used in that calculation).

4.1.1.2 Experimental Validation of the Best Behaved *a Posteriori* Models

To resolve this issue one must identify well characterized experiments that were simple enough to duplicate computationally, and yet have the significant ingredients necessary for validation of the important elements of the model: turbulence-drop two-way interactions, both dynamic and thermodynamic; and mixing of the evaporated fuel with the surrounding gas. One such experiment was that of Kiger and Lasheras, and other experiments could be performed at GEAE to provide a database

for comparison. Such prospective experiments could be coordinated with JPL to ensure that calculations and measurements of the same quantities were performed in the same spray regimes in order to ensure uncontroversial comparisons.

The deliverable of this investigation could be a validated SGS model to be used in LES of two-phase flows with phase change.

4.1.2 Supercritical Fluid Disintegration

As discussed previously, there now exists experimental evidence that fluid disintegration in the regime of interest for future gas turbine engines does not resemble even qualitatively the liquid atomization that was the basis of all drop size distributions currently used as inputs in CFD codes. Our preliminary pre-transitional study was in qualitative agreement with the experimental observations. To derive practical benefit (information that can be incorporated into a GEAE CFD code) from the supercritical study, we must extend it in two directions:

4.1.2.1 LES of Supercritical Mixing Layers for Binary Fluids (Heptane–Nitrogen)

This investigation could emulate the strategy of liquid spray investigation:

- Extend the pre-transitional DNS computation to the transitional regime; this will be more difficult than in the two phase flow situation because of the strong density stratification of the layer, as well as because of the regions of strong density gradients that act akin to solid surfaces and hinder entrainment and transfer of energy from large to small-scale eddies. This last mechanism may suppress transition, and this suppression was amplified by the effect of mixture non ideality which reduces molecular mixing.
- Perform an *a priori* study to develop SGS models. Note that in this study, the presence of the Soret and Dufour terms in the species and energy equations will lead to a more complicated form of the LES equations, and thus to different models of the SGS terms.
- Perform an *a posteriori* study to ascertain which of the *a priori* developed models was the most accurate.
- Perform a model validation with the most promising *a posteriori* identified model by comparing with existing experimental data.

The information thus produced could be incorporated into CFD codes to produce initial and boundary conditions to describe fuel jet disintegration for a single species fuel mixture in nitrogen and will constitute the deliverable of this investigation.

4.1.2.2 LES of Supercritical Mixing Layers for Multicomponent Mixtures (Two Hydrocarbon Species, Oxygen and Nitrogen to Represent Jet Fuel in Air).

To investigate the behavior of multicomponent fuels such as JP-8, the following strategy could be adopted. The high pressure properties of all single species fuels entering the composition of the multicomponent fuel would be listed. We would identify two of the mixture components that were

most likely to influence fluid disintegration (careful attention would be devoted to identifying an appropriate criterion based upon the study in Section 4.1.2.1). This procedure would circumvent the impossible task of taking into account each pure component of the fuel.

Based on information derived under a continuation of the present related study for multicomponent fuels, we would calculate the necessary thermal diffusion factors, and proceed with a study following the same protocol as in Section 4.1.2.1. The deliverable of this portion of the investigation would be information that could be incorporated into CFD codes to produce initial and boundary conditions for a two component fuel mixture in air to describe fuel jet disintegration.

5.0 References

5.1 Cited References

- 1 Kim W-W., Menon S., Mongia H., (1999) "Large-Eddy Simulation of a Gas Turbine Combustor – Flow," *Combustion Science and Technology*, 1999, Vol. 143, p. 25
- 2 Menon S., Kim W-W., Stone C., Sekar B., (1999) "Large-Eddy Simulation of Fuel-Air Mixing and Chemical Reactions in Swirling Flow Combustor," AIAA 99-3440, 30th Plasmadynamics and Lasers Conference, 28 June – July 1, 1999 / Norfolk VA,
- 3 Kim W-W., Menon S., (1999) "Numerical Modeling of Fuel/Air Mixing in a Dry Low-Emission Premixer," Second AFOSR International Conference on Direct Numerical Simulation and Large Eddy Simulation; June 7-9, 1999; Rutgers University, New Brunswick, NJ
- 4 Menon S., Kim W-W., Stone C., Henery W., Sekar B., (1999) "Simulation of Fuel-Air Mixing and Reactions in Full-Scale Gas Turbine Combustors," 1999 DoD High Performance Computing Modernization Program Conference, Monterey, CA June 7-10, 1999
- 5 Kim W-W., Menon S., (1999) "Large-Eddy Simulation of Turbulent Premixed Flames in the Thin Reaction Zone Regime," AIAA 99-2816, 35th AIAA/ASME/SAE/ASEE Joint Propulsion Conference and Exhibit, June 20-23, 1999 / Los Angeles, CA
- 6 Smith T.M., Menon S., (1998) "Flame/Turbulence Interactions in Premixed Staging Flows," AIAA 98-2978, 29th AIAA Fluid Dynamics Conference, June 15-18, 1998 / Albuquerque, NM
- 7 Kim W-W., Menon S., Mongia H., (1999) "Large Eddy Simulations of Reacting Flow in a Dump Combustor," AIAA 98-2432, 29th AIAA Fluid Dynamics Conference, June 15-18, 1998 / Albuquerque, NM

5.2 Relevant Papers

Menon S., Pannala S., Kim W-W., Smith T.M., Arunajatesan S., (1998) "Parallel Simulations of Reacting Two-Phase Flows: A DoD Grand Challenge Progress Report," AIAA 98-2928, 29th Plasmadynamics and Lasers Conference, June 15-18, 1998 / Albuquerque, NM

Smith T.M., Menon S., (1998) "Subgrid Combustion Modeling for Premixed Turbulent Reacting Flows," 36th Aerospace Sciences Meeting & Exhibit, January 12-15, 1998 / Reno, NV

Goldin G.M., Menon S., (1998) "A Comparison of Scalar PDF Turbulent Combustion Models," *Combustion and Flame*, 113:442-453

Calhoun W.H. Jr., Menon S., (1997) "Linear-Eddy Subgrid Model for Reacting Large-Eddy Simulations: Heat Release Effects," AIAA 97-0368, 35th Aerospace Sciences Meeting & Exhibit, January 6-10, 1997 / Reno, NV

Smith T.M., Menon S., (1997) "Large-Eddy Simulations of Turbulent Reacting Stagnation Point Flows," AIAA 97-0372, 35th Aerospace Sciences Meeting & Exhibit, January 6-10, 1997 / Reno, NV

Goldin G.M., Menon S., (1997) "A Scalar PDF Construction Model for Turbulent Non-Premixed Combustion," *Combustion Science and Technology*, 1997, Vol. 125, pp. 47-72

Smith T.M., Menon S., (1997) "One-Dimensional Simulations of Freely Propagating Turbulent Premixed Flames," *Combustion Science and Technology*, 1997, Vol. 128, pp. 99-130

Menon S., Calhoun W.H. Jr., (1996) "Subgrid Mixing and Molecular Transport Modeling in a Reacting Shear Layer," Twenty-Sixth Symposium (International) on Combustion / The Combustion Institute, 1996, pp. 59-66

Addendum E

Lagrangian Simulation of Gas Turbine Engine Combustion

AFOSR Focused Research Initiative
Low Emissions, High Performance Gas Turbine Engines

Contract 200-IQ-14N44080
General Electric Aircraft Engines
Cincinnati, Ohio

Principal Investigator
Ahmed F. Ghoniem

Massachusetts Institute of Technology

August, 1999

This addendum is replicated directly from the submission from MIT.

Table of Contents

	<u>Page</u>
Abstract	1
Objectives	1
Summary of Results	1
Students and Post Doctors	5
Publications	5
 Appendix I – A redistribution method for axisymmetric diffusion	
1 Introduction	1
2 Governing equations	1
3 Vortex method	2
4 Redistribution method	3
5 Properties of the redistribution method	5
6 Numerical results	6
6.1 Stokes flow	6
6.1 Navier–stokes flow	6
7 Conclusions	7
Acknowledgements	8
References	8
 Appendix II – The Effect of Flow and Mixture Inhomogeneity on the Dynamics of Strained Flames	
Abstract	2
Acknowledgements	3
Contents	4

Lagrangian Simulation of Gas Turbine Engine Combustion

Ahmed F. Ghoniem

Massachusetts Institute of Technology

Abstract

This report summarizes progress made at the Massachusetts Institute of Technology on Lagrangian simulation of combustion as part of the General Electric effort on developing high efficiency, low emission, gas turbine engine technology. The effort at MIT focused on (1) developing Lagrangian algorithms to simulate directly the convection-diffusion-reaction equation governing flow and combustion at high Reynolds number, (2) developing complementary large-eddy simulation approaches to allow the incorporation of detailed chemistry and transport into the simulations, (3) simulating several important generic problems in these engines such as highly swirling flows and reacting vortical structures in shear layers. We are assembling a reacting jet code using these methodologies.

Objectives

The objectives of this project are to:

1. Develop an axisymmetric reacting flow algorithm to simulate a reacting jet using Lagrangian grid-free schemes based on the vortex method and transport-element method. The schemes allow both direct-numerical simulation and large-eddy simulation, using fast chemistry or one-step chemistry, of a low-Mach number, compressible, high Reynolds number flow.
2. Develop a flame embedding method for the large-eddy simulation of multi-step chemistry and transport which is compatible with the approaches used for the numerical simulation of the flow. The method employs an unsteady strained wrinkled flame code with detailed fuel chemistry and transport, and achieves computational efficiency by using advanced linear algebra techniques for large non linear systems.
3. Simulate a number of flows which represent dynamically relevant and technologically significant problems for engine development, and for which data are available. Of particular interest is the high swirl flow case used for enhancing mixing downstream the air-fuel section.

Summary of the Results

Vortex simulation of turbulent reacting flow is an efficient direct or large-eddy simulation approach since it allows one to capture, without closure modeling, the large scales of turbulence, their transition to small scales via stretching and folding of vorticity lines, and their dissipation through viscous diffusion at the small scales, as well as their interaction with combustion, in a grid-free, self-adaptive numerical approach. The approach is compatible with high Reynolds number and large Damkohler number conditions which are expected to prevail in a high performance, low emission gas turbine engine combustors since it relies on following the evolution of the vorticity

field which, in this case, is concentrated within a small fraction of the flow field. When extended to the case of a reacting flow, then one must solve the equations governing the transport of chemical species and energy, all treated as scalars.

We have developed two approaches to perform such extension, the transport element method in which the scalar gradients are transported using the appropriate equations, and the second is direct numerical simulation in which the scalar transport equation is solved using a particle scheme. The transport element method is based on neglecting diffusion along the instantaneous streamline direction, and hence can be regarded as a large eddy simulation. Its efficiency is achieved from the fact that one follows material lines along which the flow gradients are non zero, and that the diffusion in the cross streamline direction can be modeled using the core expansion approach. We have used this method to develop combustion codes for the simulation of reacting flows in shear layers, jets and combustion plumes and the results have been used extensively. Results have been used to predict the rate of burning, assuming fast chemistry or a single step Arrhenius reaction, the impact of density variation on the shear flow dynamics, the impact of upstream mixing, and the role of the splitter plate thickness in mixing and burning.

On the other hand, in applications of this methodology to jet simulation over large times, we observed that, within large vortical structure, and especially at later times, the material lines can continue to spiral after mixing has been completed. This can be computationally costly, and there is no obvious way to discard the material lines across which mixing has been achieved. Moreover, to reduce the computational cost, a "subgrid" type diffusion model is used to reduce the number of computational elements and alleviate the need for using computational elements whose scale is comparable to Kolmogorov scale. This, while efficient, can cause conceptual difficulty when applied to the scalar gradients instead of the scalars. This prompted us to develop a new particle method for the transport of the scalar which relies on computational elements that carry fractions of the scalar itself, and implement a new grid free diffusion scheme to overcome the inaccuracies in the core expansion method. The method has fully been developed during the course of this work and represents a significant improvement over all other currently utilized numerical approaches.

The particle method which is described in more detail in Appendix I is a direct simulation of the convection-diffusion equation using computational elements which transport fractions of the volume integral of the scalar concentration along the trajectories and exchange these fractions locally to simulate diffusion. Superior accuracy is achieved by concentrating computational elements in zones with non zero variation and with a distance in between elements of the order of the diffusion length scale. The convective transport is still implemented by moving conserved fractions along particle trajectories in a way which is compatible with the vortex method. Diffusive transport is formulated as a weak solution of the conservation equation in which a number of moments of the scalar field to ensure high order accuracy. The method has been validated by comparing its solution for a propagating vortex ring with that obtained using other methods [1,2]. Due to the adaptive nature of this method, in which computational elements are introduced where diffusion has moved the species and energy from where they were concentrated, the solution can be obtained using the least possible number of computational elements. We have recently extended this method to include a source term, due to baroclinic effects in the vorticity transport equation and chemical reactions in the energy and species transport equations [3]. This extension required developing a strategy to solve the equations concurrently in the physical domain and a transformed domain in which the source terms are integrated accurately (similar to pseudo spectral approaches). This extension is

currently being tested and will be incorporated in the simulation routines in the near future. We hope to have a jet/plume code for the simulation of reacting flow in an axisymmetric domain soon using this approach. We should also mention that this method has been shown to represent a "grid free weighted residual approach" for solving Navier Stokes equations, i.e., it belongs a class of "grid free finite element methods".

When extended to reacting flows with complex chemistry and transport, the computational requirement of direct numerical simulations can be overwhelming. This is because of the number of species involved and the very small time steps required to integrate the resulting stiff equations. It is impossible in the near or far future to imagine that computer power will grow to allow direct numerical simulation of reacting flows in engineering systems, and as such effort to construct large eddy simulation approaches must be intensified. A rational solution toward this goal has been devised by us in which the solution domain is divided into two zones, an inner zone around the reaction fronts where the reacting flow equations are solved, and an outer zone where the non reacting flow equations are integrated [4]. This approach models the combustion zone as generalized elemental flames sandwiched between two nonreacting flow zones, where the flow impacts the flame by imposing curvature and strain which vary in time while the flame impacts the flow via volumetric expansion and vorticity generation. While restricted to the flamelet regime of combustion, the power of our approach stems from the fact that it allows for unsteady effects to be captured, and in fact for strain rates whose length scale are comparable with the length scale of the flame thickness to be incorporated. In this sense, it models cases in which the flame thickness is of the same order of magnitude as the small eddies affecting its structure.

We have constructed such model and tested its validity by comparing its results with those obtained using direct simulation [5]. The detail of this work and more results are described in Appendix II. Essentially, an efficient unsteady strained flame code has been written to solve for the burning rate given an arbitrary, time dependent boundary conditions, defining the incoming flow equivalence ratio and temperature, and time dependent strain. An improvement in the computational efficiency of more than two orders of magnitudes has been achieved by applying several innovations in the linear algebra including a Newton iteration method with back tracking to solve the non linear algebraic equations, a Krylov space iteration solver to solve the linear equation, and matrix preconditioning. The first approximates the Newton method when exact solutions are unnecessary and hence saves the iterations required to get an exact Newton solution. The second is a version of conjugate gradient methods which replaces direct solutions of a dense linear system by an iterative one, taking advantage of the fact that the solution changes rather slowly between time steps. The preconditioning step ensures fast convergence even when the linear system is nearly singular. The new formulation and numerical algorithm allow simulation under complex conditions such as extinction.

By applying this methodology, we found that the flow strain which affects a flame must be measured near the reaction front, and developed schemes for defining where in a multi dimensional computation should this strain be defined. We also developed algorithms for extrapolating the strain rate outside the flame zone into the flame structure. These are useful in cases where the flow gradient are on the same order of magnitude as the flame thickness. We also developed an algorithm for imposing time dependent boundary conditions on this flame solution to capture cases in which the equivalence ratio, temperature and pressure ahead of the flame change due to mixing or control. The code works for premixed flames, diffusion flames, and partially premixed flames, and for both

single and double flame configurations. The code has been tested against existing codes, such as PREMIX and OPPDIF, and the results match very well. Our code is however much more robust and efficient.

The code has been used to fully validate the concept of flame embedding by showing that when strain rate histories generated by multi dimensional flame–vortex interaction simulations are used in this 1D unsteady flame code, the burning rates predicted match very well those obtained in the multi dimensional simulations. The level of agreement depends on where the strain rate is measured in the multi dimensional simulation. Results show that one must measure the strain rate at the reaction front, or extrapolate the “non reacting” strain rate which would have prevailed towards the anticipated location of the reaction front. We developed equations for such extrapolation whose form depend on the expected flow elements ahead of the flame. The decay of the strain rate within the flame structure essentially violate the basic assumptions of flamelet modeling. Nevertheless, we showed that using the appropriate averaging within the flame structure one can construct a value for the strain which, in the 1D model, reproduces accurately the flame structure and burning rate.

We also used the code to investigate the impact of unsteadiness and the effect of mixture inhomogeneity on the burning rate and flame structure. These results are very important in many applications in gas turbine combustion in which mixture equivalence ratio can not be guaranteed to remain within the design values, or is forced to change to affect a certain problems such as instability or emission control. For instance we found that in cases when the fuel concentration is reduced at certain rate, flames continue to burn even when the equivalence ratio drops below the “flammability limit”. We analyzed the associated mechanism in detail and labeled it as “back support” where the higher temperature of the products on the “richer” mixture support the burning of the “leaner” mixture. This study will appear in an upcoming paper [6]. If the equivalence is perturbed in a controlled, oscillatory manner, using the above result, one can maintain flames burning under their nominal lean burnout limit, and hence maintain low emission, without risking the danger of extinction.

We have initiated the effort of developing an axisymmetric reacting jet code, and have obtained results for the non reacting flow. Due to the lack of sufficient funding, this part of the effort has not been completed, although it is very well underway. Different parts of the code are currently being tested for convergence and efficiency, and a fast solver which will allow a long time simulation of the reacting jet flow out to 100 jet diameters downstream is being coupled with the simulations. Also a massively parallel version of the entire package is being developed. The objective here is to develop a large eddy simulation package for reacting shear flows in shear layer/jet flow configurations, in which the impact of the large scales are captured without modeling while the small scales are introduced via subgrid modeling or flame embedding. Preliminary results of this work will be presented at the Jan–2000 Aerospace Sciences Meeting in Reno, NV [8].

Meanwhile we have used our codes to study, through numerical simulations, a number of generic problems of significance to gas turbine combustion. The 3D vortex code has been applied to simulate a swirling flow, and the results have been used to examine the mechanism of mixing enhancement downstream a swirler. Results indicate that vortex breakdown and the formation of a strong recirculation zone occur as the circulation number exceeds a critical value. The dynamics leading to the breakdown are self sustaining and are associated with the creation of azimuthal vorticity via the divergence of the axial vortex lines due to the unfavorable pressure gradient and natural instabilities. The recirculation zone is unsteady and experiences periodic oscillations leading to the forma-

tion of an unsteady wake behind the breakdown zone. The size, location, and frequency of oscillations are strong functions of the swirl number. While the size of the mixing bubble increases as the amount of streamwise circulation increases in the initial flow, its location moves closer to the inlet section. The unsteadiness is manifested in two aspects: the stream oscillation of the recirculation bubble, and the formation of an unsteady wake behind it where large vortices are shed. Results also show that while the average flow is axisymmetric, the instantaneous is not, with strong helical motion observed there within and downstream the mixing zone. Results agree well with experimental measurements, and were presented in detail in Ref. [9].

Students and Post doctors

Funding has been used to partially support the following students:

1. Constantine Petrov, Ph.D., completed 1997.
2. Jean Claude Saghbini, M.Sc., completed 1997.
3. Youssef Marzouk, M.Sc., finished 1999.
4. Shankar Subramaniam, post doctor, finished 1999.

Publications

1. Shankar, S. and Ghoniem, A.F., "Vortex Methods for Axisymmetric Reacting Flows, a New Redistribution Algorithm for Diffusion," 3rd Int. Workshop on Vortex Flows and related Numerical Methods, Toulouse, France, Aug 24–27, 1998.
2. Shankar, S. and A.F. Ghoniem, "Grid Free Methods for Vorticity and Scalar Transport in Axisymmetric Flows, to be submitted to the J. Comput. Phys.
3. Shankar, S., "Progress in Lagrangian Simulation of Axisymmetric Flow, Anisotropic Diffusion and the Reaction Diffusion Equation, Reacting Gas Dynamics Report, Oct. 1999.
4. Ghoniem, A.F. and Petrov, C., "Numerical Simulation of Reacting Flows with Multi-Step Kinetics", *the 35th Aerospace Sciences Meeting and Exhibit*, Reno, Nevada, January, 1997, AIAA-97-0291
5. Marzouk, Y., The effect of flow and mixture inhomogeneity on the dynamics of strained flames, M.Sc. thesis, MIT, August 1999.
6. Marzouk, Y., and Ghoniem, A.F., "Development of Flame Embedding Techniques for Turbulent Combustion Simulations", for presentation at the 38th Aerospace Science Meeting, Reno, NV, Jan 10–33, 00.
7. Marzouk, Y., and Ghoniem, A.F., "Impact of mixture inhomogeneity on flame propagation speed and limits in premixed system," to be submitted for presentation at the 28th International Combustion Symposium,
8. Lakkis and Ghoniem, "Lagrangian Simulation of Flame Vortex Interactions", for presentation at the 38th Aerospace Science Meeting, Reno, NV, Jan 10–33, 00.
9. Ghoniem, A.F. and J. Saghbini, "Numerical Simulation of the Dynamics and Mixing in a Swirling Flow," *the 35th Aerospace Sciences Meeting and Exhibit*, Reno, Nevada, January, 1997, AIAA-97-0507.

APPENDIX I

A redistribution method for axisymmetric diffusion

S. Shankar and A. F. Ghoniem

Department of Mechanical Engineering
Massachusetts Institute of Technology
Cambridge, Massachusetts, 02139, U.S.A.
subram@centaurus.mit.edu
ghoniem@mit.edu

Abstract

We develop grid-free numerical procedures to compute axisymmetric incompressible flows. In particular, we formulate a grid-free ‘redistribution method’ to handle diffusion processes accurately on a disordered collection of computational elements. We validate the numerical procedures by computing the Stokes flow and the Navier-Stokes flow of a vortex ring.

1 Introduction

Vortex methods simulate fluid flows by following a collection of computational elements (‘vortex elements’) which transport of vorticity, and other conserved scalars such as energy and chemical species [4, 6, 7]. Often, those quantities are transported due to convection and diffusion. The convection process is handled accurately in a grid-free manner by moving the computational points according to the local velocity field. The diffusion process must also be implemented accurately using grid-free procedures to maintain the advantages of a Lagrangian computation.

In this paper we formulate grid-free methods to compute the evolution of the vorticity and temperature for axisymmetric incompressible flows in free-space. A fractional-step method [2, 5] is used to solve the governing equations. In this context, the diffusive effects are governed by the unsteady Stokes equations. To compute the Stokes equations accurately on a disordered distribution of computational elements is our primary objective.

We present the governing equations in Section 2. In Section 3 we formulate a vortex method to solve those equations. In Section 4 we briefly describe the extension of the redistribution method [11] to solve the Stokes equations for the vorticity and temperature in an axisymmetric domain; details of the formulation are given in [9]. In Section 5 we discuss the properties of the method. The numerical procedures are validated in Section 6 by computing the Stokes flow and the Navier-Stokes flow of a vortex ring. Conclusions and further work are discussed in Section 7.

2 Governing equations

We consider the free-space flow of a homogenous, incompressible fluid of constant density in an axisymmetric domain; we assume that the kinematic viscosity, ν , and the thermal diffusivity, κ , are constant. Let r and z be the radial and axial directions of the flow in the $r-z$ plane so that $-\infty < r, z < \infty$. The location of a point in this plane is denoted by $\vec{x} = (r, z) = r\hat{r} + z\hat{z}$; the symbols \hat{r} and \hat{z} are the unit vectors. Let t be the time. The velocity field is denoted by $\vec{u}(\vec{r}, t) = (u_r, u_z) = u_r(\vec{r}, t)\hat{r} + u_z(\vec{r}, t)\hat{z}$. The vorticity field, which is the curl of the velocity, is denoted by $\omega(\vec{r}, t)$; it points in the direction $\hat{z} \times \hat{r}$ into the plane. Let $T(\vec{r}, t)$ be the temperature that is transported as a passive scalar; since the density and specific heat are

constant, the temperature is proportional to the internal energy of the fluid. The governing equations for the vorticity and temperature are [1, 3]:

$$\frac{1}{r} \frac{\partial(r u_r)}{\partial r} + \frac{\partial u_z}{\partial z} = 0 \quad , \quad (1)$$

$$\frac{D\omega}{Dt} = \frac{\omega u_r}{r} + \nu \left(\frac{\partial^2 \omega}{\partial r^2} + \frac{1}{r} \frac{\partial \omega}{\partial r} - \frac{\omega}{r^2} + \frac{\partial^2 \omega}{\partial z^2} \right) \quad , \quad (2)$$

$$\omega \equiv \frac{\partial u_r}{\partial z} - \frac{\partial u_z}{\partial r} \quad , \quad (3)$$

$$\frac{DT}{Dt} = \kappa \left(\frac{\partial^2 T}{\partial r^2} + \frac{1}{r} \frac{\partial T}{\partial r} + \frac{\partial^2 T}{\partial z^2} \right) \quad , \quad (4)$$

where

$$\frac{D}{Dt} \equiv \frac{\partial}{\partial t} + \left(u_r \frac{\partial}{\partial r} + u_z \frac{\partial}{\partial z} \right) \quad (5)$$

is the material derivative.

To solve the above equations, the initial vorticity and the temperature distributions must be specified. The boundary conditions along the axis of symmetry are discussed in Section 4. In the next section we formulate a vortex method to solve the above equations numerically.

3 Vortex method

The vortex method presented here is based on a fractional-step algorithm [2, 5], that separates the inviscid and viscous processes at each time-step. To do this, the conservation equations (2) and (4) are approximated by the following two steps:

Inviscid step:

$$\frac{d\vec{X}}{dt} = \vec{u} \quad , \quad (6)$$

$$\frac{d\Gamma_\omega}{dt} = 0 \quad , \quad (7)$$

$$\frac{d\Gamma_T}{dt} = 0 \quad . \quad (8)$$

Viscous step:

$$\frac{d\vec{X}}{dt} = 0 \quad , \quad (9)$$

$$\frac{\partial \omega}{\partial t} = \nu \left(\frac{\partial^2 \omega}{\partial r^2} + \frac{1}{r} \frac{\partial \omega}{\partial r} - \frac{\omega}{r^2} + \frac{\partial^2 \omega}{\partial z^2} \right) \quad , \quad (10)$$

$$\frac{\partial T}{\partial t} = \kappa \left(\frac{\partial^2 T}{\partial r^2} + \frac{1}{r} \frac{\partial T}{\partial r} + \frac{\partial^2 T}{\partial z^2} \right) \quad . \quad (11)$$

In the above equations, \vec{X} is the location of a fluid element, \vec{u} is its velocity,

$$\Gamma_\omega \equiv \iint \omega \, dr \, dz \quad (12)$$

is the circulation, and

$$\Gamma_T \equiv \iint T r \, dr \, dz \quad (13)$$

is the internal energy per unit mass divided by the specific heat. The integrals in (12) and (13) are taken over the area of the fluid element in the half-plane $0 \leq r$. For the Stokes equations, the circulation of an element decays in time, while the energy is still conserved.

Equations (7) and (8) are obtained by integrating over the half-plane the equations (2) and (4) without the diffusion terms. The velocity is obtained from the vorticity ([1], eqn. 2.4.10).

To solve (6) through (11) using a vortex method, the initial vorticity and temperature are first represented by computational elements. To do this, we divide the flow region into small cells, and assign an element to each cell. The mathematical representation is then

$$\omega(\vec{x}, 0) = \sum_{i=1}^N \Gamma_{\omega_i}(0) \delta(\vec{x} - \vec{x}_i(0)) \quad , \quad (14)$$

$$T(\vec{x}, 0) = \sum_{i=1}^M \Gamma_{T_i}(0) \delta(\vec{x} - \vec{x}_i(0)) \quad , \quad (15)$$

where, i is the index for the element, $\vec{x}_i(t)$ is its position at time t , $\Gamma_{\omega_i}(t)$ is its circulation, $\Gamma_{T_i}(t)$ is its internal energy, and $\delta(\cdot)$ is the Dirac delta function. According to equations (12) and (13), the initial circulation of an element is taken to be the vorticity at the element location times the area of the cell; the initial internal energy is the product of the temperature at the element location, the radial location of the element and the cell area. Each computational element, however, need not carry both the circulation and energy, although saving in computational time may be achieved if they did.

During the inviscid step, we move each computational element according to the local velocity field (6) while keeping its circulation and energy unchanged (7,8). The velocity of each element is computed by summing up all the velocities induced at its location by all the vorticity carrying elements including itself ([1], eqns. 2.2.11 & 7.2.13). The velocity is desingularized [5, 13] using a small smoothing parameter of size $\sqrt{0.5 \nu \Delta t}$, where Δt is the time-step in the computation.

At the end of the inviscid step, we perform the viscous step to account for diffusion. During the viscous step we do not move the computational elements (9), but change their circulations (10) and the energies (11) using the redistribution method. We formulate the redistribution method in the next section to solve the Stokes equations (10) and (11).

We reverse the sequence of the inviscid and viscous steps at every time-step to improve accuracy [2].

4 Redistribution method

The effect of diffusion is simply to spread out the circulation and energy of each computational element. The redistribution method is based on this idea: it spreads the circulation and energy of an element to its neighboring elements located within a chosen radius, R , according to the Stokes equations. This radius is proportional to the diffusion length scale $h_\lambda = \sqrt{\lambda \Delta t}$; the diffusivity λ being either the kinematic viscosity or thermal diffusivity, and Δt is the time-step. In our computations, the average distance between the computational elements is taken to be $\sqrt{8}h_\lambda$; and the neighborhood radius R is taken to be $4h_\lambda$. These two parameters are chosen so that a solution to the system of equations, derived below, becomes possible [11].

More precisely, let i be an element located at (r_i, z_i) , whose circulation (or energy) needs to be diffused, and $j = 1, \dots, m$ be its neighboring elements located within the radius R . Let f_{ij}^n be the fraction of the circulation (or energy) moved from i to its neighbor j to advance the vorticity (or temperature) from time level n to the next time level $n + 1$. Then the vorticity field at time level n ,

$$\omega^n = \sum_i \Gamma_i^n \delta(\vec{x} - \vec{x}_i) \quad (16)$$

becomes

$$\omega^{n+1} = \sum_i \sum_j f_{ij}^n \Gamma_i^n \delta(\vec{x} - \vec{x}_j) \quad (17)$$

at the next time level.

Now the question is how do we find those fractions f_{ij}^n . To do that, we will ensure that the Fourier modes of the numerical solution are correctly damped [11]. This is accomplished by matching the Hankel-Fourier transform [12] of the the numerical solution (17) given by

$$\hat{\omega}^{n+1} = \sum_i \sum_j f_{ij}^n \Gamma_i^n r_j J_1(k_r r_j) e^{-i k_z z_j} \quad (18)$$

with that of the exact solution

$$\hat{\omega}_e^{n+1} = \sum_i \Gamma_i^n r_i J_1(k_r r_i) e^{-i k_z z_i} e^{-k^2 \nu \Delta t} \quad (19)$$

to desired order of accuracy $O(h_\lambda^M)$, as described below; and M is a positive integer. The exact solution (19) is obtained by solving the Stokes equation (10) with initial vorticity (16). In the above equations, $J_1(\cdot)$ is the Bessel function of first kind and order one; and the wave number is denoted by $\vec{k} = k_r \hat{r} + k_z \hat{z}$, and its magnitude by k . For the diffusion of internal energy, the above procedure is the same except that the radial modes are now Bessel functions of first kind and order zero.

We next expand (18) and (19) using Taylor's series around \vec{x}_i for small times and ensure that the truncation errors vanish to desired accuracy; the distances between the vortices within the neighborhood are scaled by h_λ . This results in a system of linear equations for the fractions f_{ij}^n :

$$\sum_j f_{ij}^n = 1 \quad ; \quad (20)$$

$$\sum_j f_{ij}^n \Delta r_{ij} = \frac{\varepsilon}{r_i/h_\lambda} \quad , \quad (21)$$

$$\sum_j f_{ij}^n \Delta z_{ij} = 0 \quad ; \quad (22)$$

$$\sum_j f_{ij}^n \Delta r_{ij} \Delta r_{ij} = 2 \quad , \quad (23)$$

$$\sum_j f_{ij}^n \Delta r_{ij} \Delta z_{ij} = 0 \quad , \quad (24)$$

$$\sum_j f_{ij}^n \Delta z_{ij} \Delta z_{ij} = 2 \quad , \quad (25)$$

where $\Delta \xi_{ij} \equiv (\xi_j - \xi_i)/h_\lambda$. The equations (20)-(25) are $O(h_\lambda)$ approximation to the Stokes equations (10) and (11). Higher-order spatial accuracy can be achieved by including additional redistribution equations that are obtained by retaining higher-order terms in the Taylor's series expansion.

The value of the parameter ε in (21) is -1 for the diffusion of circulation, and 1 for the diffusion of energy. When $\varepsilon = 0$, however, the same equations represent the diffusion of circulation and energy in Cartesian two-dimensional flows. The above redistribution equations maintain the conservation laws of the Stokes equations exactly.

The above system of linear equations is usually underdetermined, since the number of elements within the neighborhood is often more than the number of equations. There is, however, a restriction on the values of the fractions f_{ij}^n . For stability, all fractions must be nonnegative. The linear system can be solved using any standard simplex method program from IMSL for example. When no nonnegative solution can be found, it is an indication that 'holes' may be present in the distribution of the computational elements. These holes are filled

until an acceptable solution is obtained. This automatic addition of computational elements maintains the chosen resolution at all times, and further ensures that the vorticity diffuses correctly into the surrounding irrotational flow.

In our computations, we use elements only in the half-plane $0 \leq r$. Then the axis of symmetry is a boundary of the computational domain, and appropriate boundary conditions must be applied there. To do so, we place a layer of 'mirror elements' on the negative side of r . The mirror elements are simply reflections of the elements on the positive side, whose radial locations are less than the neighborhood radius R mentioned above.

The vorticity is antisymmetric in r , and hence vanishes on the axis. Therefore while diffusing the vorticity of the elements near the axis, the amounts of circulation moved to the mirrors are considered 'lost'. This ensures the correct decay of the circulation the half-plane.

The temperature is symmetric in r , and hence there is no heat flux across axis. Therefore, the energy received by a mirror element is given back to its mirror located on the positive side. This conserves the energy in the half-plane.

We must also point out a numerical difficulty caused by the equation (21): the righthand side becomes singular whenever the element to be diffused is very close to the axis. To avoid this singularity, we keep a thin strip near the axis free of computational elements. Of course, convection could still move some of the elements inside this strip due to numerical errors. However, those elements are moved back onto the edge of the strip and at the same time maintaining the appropriate conservation laws. The numerical results presented in the next section show that these procedures indeed reproduce the vorticity and temperature fields accurately.

We next discuss the theoretical properties of the method.

5 Properties of the redistribution method

In this section, we give a summary the properties of the method. Further discussion of the following properties is given in [9, 11]. The advantages of the method achieved for cartesian two-dimensional flows successfully carry over to the axisymmetric case as well.

1. The redistribution equations spread the conserved quantities over only a finite number of neighbors inside a small area. This allows the method to resolve sharp gradients in the flow fields accurately [10].
2. The redistribution method does not require a uniform distribution of computational elements, or even an ordering of the elements. In particular, even if convection disorders the initial uniformity of the elements, the adaptive addition of new elements allows the computation to continue without loss of accuracy.
3. The redistribution method does not use any smoothing function to perform diffusion; the resulting desirable properties, especially the resolution of short scales, are discussed in [11], Sec. 9.1.
4. The conservation laws of the Stokes equations are *exactly* maintained using only a finite number of elements within the neighborhood, even if the elements are disordered.
5. The sign of a uniformly positive or negative vorticity field is preserved for any finite order of accuracy by the method, at least for the Stokes equations ([11], Sec. 9.5).
6. The redistribution method can, in principle, have any order of accuracy. At the same time, the splitting error of the fractional-step algorithm must be considered for spatial accuracy beyond fourth-order.

The advantages of the above properties have been demonstrated for the computation of two-dimensional unsteady separated flows at high Reynolds numbers [10]. In the next section we present numerical results to verify that those properties can be achieved for axisymmetric flows also.

6 Numerical results

To validate the method, we computed the Stokes flow and the Navier-Stokes flow of a vortex ring. We present the numerical results in the next two subsections. We verified the results using various time-steps and corresponding spatial resolutions. The results presented here correspond to the smallest time-step used in our convergence study. The computations were carried out in single-precision on SGI/IRIX-6.1 with an average speed of 15Mflops and with a machine zero of about 6.0×10^{-8} .

6.1 Stokes flow

The redistribution method is tested on the Stokes flow due to a point source of circulation and energy. For these two cases, exact solutions are available that are simply the free-space Green's functions of the Stokes equations (10) and (11).

For the diffusion of vorticity, an initial point source of unit circulation, represented by a single computational element, is placed at $(r, z) = (2.5, 0.0)$. The time-step is $\Delta\tau = 0.004$, with the corresponding spatial resolution $R \approx 0.2530$. The computation was continued until time $\tau = 1.0$ when the circulation in the half-plane had decayed to about eighty percent of the initial value; by this time it was clear that the handling of the axis boundary condition is accurate. The number of computational elements is about 3600 at this time. The impulse is conserved with a relative error less than 10^{-6} at all times, and the axial center of vorticity is conserved with a relative error less than 10^{-5} . At the end of the computation, the relative error in mean square axial expansion is about 2.55×10^{-3} , and the error in the circulation in the half-plane is about 1.17×10^{-3} . More importantly, the high wave numbers that are most susceptible to dissipative errors are also correctly damped: the relative error in the maximum vorticity at $\tau = 0.50$ is about 2.47×10^{-4} , and at $\tau = 1.00$ the error is about 3.47×10^{-4} . In figure 1(a) the computed vorticity contours at time $\tau = 0.50$ are compared with the exact solution.

For the diffusion of heat, an initial point source of unit internal energy, represented by a single computational element, is placed at $(r, z) = (2.5, 0.0)$. The time-step and spatial resolution is the same as that for the vorticity. The computation is performed until time $\tau = 1.30$, long enough to verify that the axis boundary condition works correctly; at this time, the maximum temperature is already attained on the axis. The number of computational elements is about 4100 at this time. The energy in the half-plane is conserved to machine precision. The axial center of temperature is conserved with a relative error less than 10^{-6} at all times. The mean square radial and axial expansions of the temperature field grow linearly with time as predicted theoretically, and the relative error in both is less than 10^{-5} throughout the computation. Further, the relative error in the maximum vorticity at $\tau = 0.70$ is about 1.66×10^{-3} and at $\tau = 1.30$ the error is about 4.43×10^{-4} . The higher error at the earlier time is due to the high gradients arising from the transition of the temperature from a local minimum on the axis to the maximum value at the source location. In figure 1(b) the computed temperature contours at time $\tau = 0.70$ are compared with the exact solution.

The numerical errors in the above conserved quantities are primarily due to round-off errors, and due to the truncation of the exponentially small vorticity and temperature fields determined a priori by a cut-off value of circulation and energy. The circulation or the energy of an element is not diffused if it falls below this cut-off; in the computations, a cut-off value of 10^{-6} is used.

In the next subsection we include convection as well to verify that the numerical procedures can handle the flow just as accurately as it did for the Stokes flow.

6.2 Navier-Stokes flow

When convection is present, the computational elements become disordered due to the straining of the flow. In this section we show that the method still maintains high accuracy under these conditions. As a nontrivial test case, we compute the Navier-Stokes flow of the propagation of a vortex ring in free-space. At the same time, we wanted to verify that our vortex method produces the pointwise values of the vorticity and temperature fields correctly at all times. Since

we did not find suitable data in the literature, we computed this flow using a finite-difference method also. A convergence study of the finite-difference solution was performed based on the mesh-size, time-step, and domain size. In our finite-difference computations, we verified the convergence, not only of the various global moments of vorticity and temperature fields, but also the pointwise values of the fields themselves at different times. The best resolution used as many as 512×1024 computational points distributed uniformly over the domain $0 \leq r \leq 8$, $-8 \leq z \leq 8$; and a time-step of 0.0005.

The redistribution computation starts from a vortex ring of small core located radially a unit distance from the axis of symmetry. The ring has unit circulation and unit energy. The Reynolds number is $Re = 50$ based on the initial circulation and ring radius. The Prandtl number is $Pr = 1$.

The initial vorticity distribution over the core of the vortex ring is obtained by allowing a point source to diffuse out as a Stokes flow (no convection) until the scaled time $\tau \equiv t/Re = 0.002$. At this time, the vorticity distribution is almost a two-dimensional Gaussian with a core radius of about 0.18; just outside the core, the vorticity is less than one percent of the maximum. The initial temperature distribution is obtained similarly.

The figure 2 shows the distribution of computational elements. Notice that the points are disordered and denser near the center of the vortex due to the straining of the flow. New elements are automatically added only where the conserved quantities spread out. We replaced elements very close to each other, located within a radius $\sqrt{0.5} \Delta\tau$, by a single element [10]. The scaled time-step $\Delta\tau$ is 0.0005, and the corresponding spatial resolution $R \approx 0.0894$. The small circle in figure 1(c) indicates the size of the spatial resolution. The number of computational elements initially is about 400, and grow almost linearly to roughly 5000 elements at scaled time $\tau = 0.15$. At this time, the circulation in the half-plane had reduced to about eighty percent of its initial value.

The figure 3 provides a clear evidence of the accuracy of the method: it correctly reproduces the vorticity and temperature fields. We also verified that they are correct at several intermediate times. The vorticity is obtained by convolving the circulations with an infinite-order axisymmetric smoothing function; the temperature is obtained similarly. Notice in figure 3(a) that the vorticity and temperature fields have evolved very differently although they were identical initially; the maximum temperature is attained on the axis, while the vorticity vanishes there. The impulse of the vortex ring is conserved with a relative error less than 2.0×10^{-5} at all times. The internal energy in the half-plane is conserved with a relative error less than 4.0×10^{-5} . The relative error in the circulation is less than 2.11×10^{-3} . The relative error in the velocity of the vortex ring [8] is about 2.35×10^{-4} at the end of the computation.

The accuracy of the above numerical results is excellent considering that the computational elements are disordered and that a relatively coarse spatial resolution was used in the computations.

7 Conclusions

We have developed numerical procedures that are truly mesh-free for computing axisymmetric flows. The axisymmetric redistribution method simulates diffusion accurately even if convection causes strong distortions in the distribution of computational elements. The ability of the method to satisfy various conservation laws exactly by construction, together with other properties, provide reliable and accurate simulations of more complex flow fields. In fact, we are developing these procedures for the direct numerical simulation of jet diffusion flames. The redistribution method is an explicit time-stepping scheme, and we are working to obtain an implicit formulation to relax stability restrictions. The procedures can also be used to simulate many reacting flows based on coupling functions [14]. To compute an even wider class of flows, however, we need to handle diffusivities that vary spatially; that is also necessary to compute incompressible flows based on large eddy simulations. In this direction, our preliminary numerical results for one-dimensional diffusion are just as accurate as the constant diffusivity computations.

Acknowledgements

This work was supported by the US Department of Energy, Basic Energy Sciences, mics, DE-F602-98ER25355. S. Shankar appreciates the helpful discussions with Professor L. van Dommelen, Department of Mechanical Engineering, FAMU-FSU College of Engineering.

References

- 1 BATCHELOR, G. K.: *An Introduction to Fluid Dynamics* (Cambridge Univ. Press, Cambridge), (1987).
- 2 BEALE, J. T. & MAJDA, A.: Rates of convergence for viscous splitting of the Navier-Stokes equations, *Math. Comput.* **37**, (1981), 243–259.
- 3 BIRD, R. B., STEWART, W. E., & LIGHTFOOT, E. N.: *Transport phenomena* (John Wiley, New York), (1960).
- 4 CHORIN, A. J.: Vortex Methods, PAM Report 593, Department of Mathematics, University of California, Berkeley, (1993).
- 5 CHORIN, A. J.: Numerical study of slightly viscous flow, *J. Fluid Mech.* **57**, (1973), 785–796.
- 6 GHONIEM, A. F.: Computational methods in turbulent reacting flow, in *Lectures in Applied Mathematics*, Vol. 24, edited by G. S. S. Ludford, (American Mathematical Society, Providence), (1986), 199–265.
- 7 LEONARD, A.: Vortex methods for flow simulation, *J. Comput. Phys.* **37**, (1980), 289–335.
- 8 SAFFMAN, P. G.: The velocity of viscous vortex rings, *Stud. Appl. Math.* **49**, (1970), 371–380.
- 9 SHANKAR, S. & GHONIEM, A. F.: A grid-free vortex method for axisymmetric flows, to be submitted to *J. Comput. Phys.*
- 10 SHANKAR, S.: A new mesh-free vortex method, Ph.D. thesis, Florida State University, 1996.(unpublished).
- 11 SHANKAR, S. & VAN DOMMELEN, L.: A new diffusion procedure for vortex methods, *J. Comput. Phys.* **127**, (1996), 88–109.
- 12 SNEDDON, I. N.: *The use of integral transforms* (McGraw-Hill, New York), (1972).
- 13 VAN DOMMELEN, L. & RUNDENSTEINER, E. A.: Fast, adaptive summation of point forces in the two-dimensional Poisson equation, *J. Comput. Phys.* **83**, (1989), 126–147.
- 14 WILLIAMS, F. A.: *Combustion theory* (Addison-Wesley, New York), (1985).

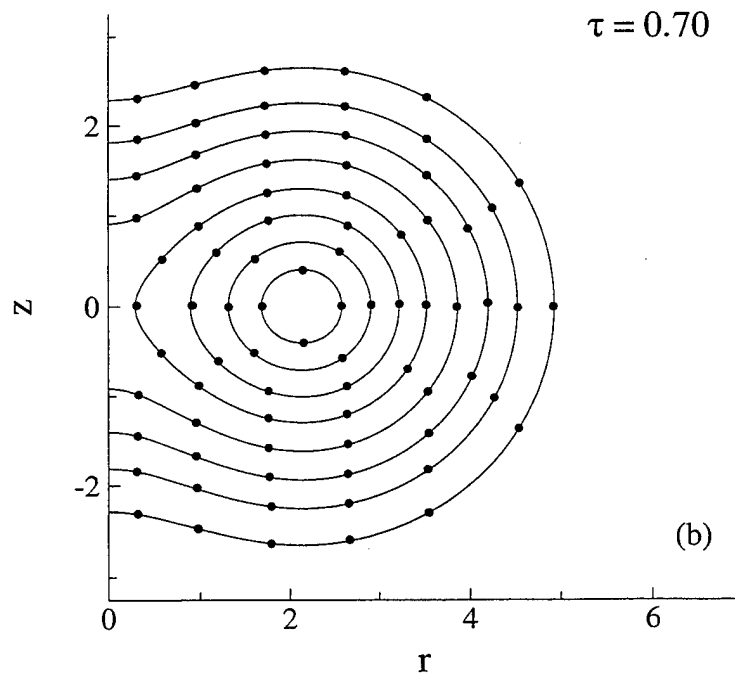
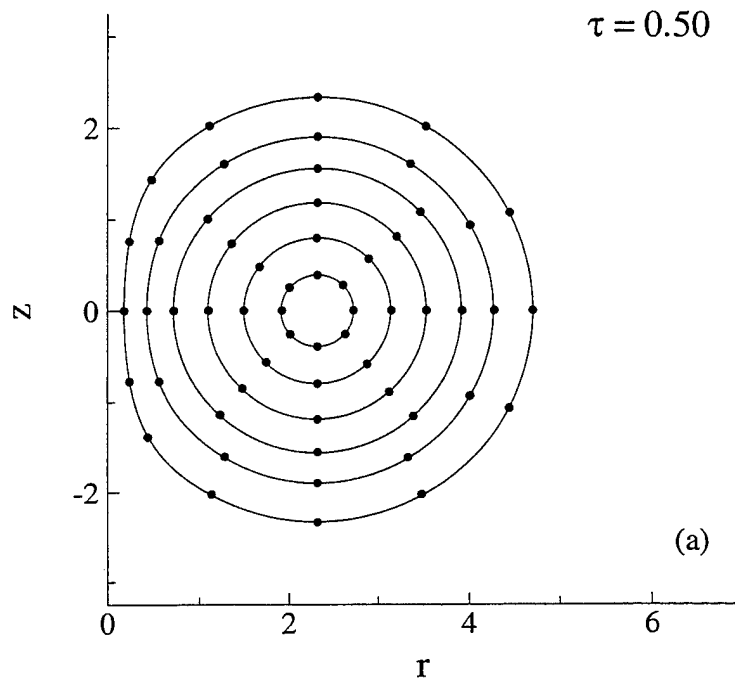


Figure 1: Stokes flow of point source: (a) Vorticity contours at $\tau = 0.50$: $\omega = 0.010, 0.025, 0.045, 0.075, 0.110, 0.140$. (b) Temperature contours at $\tau = 0.70$: $T = 0.010, 0.020, 0.032, 0.048, 0.067, 0.085, 0.102, 0.115$. Solid lines are exact and symbols are redistribution solutions.

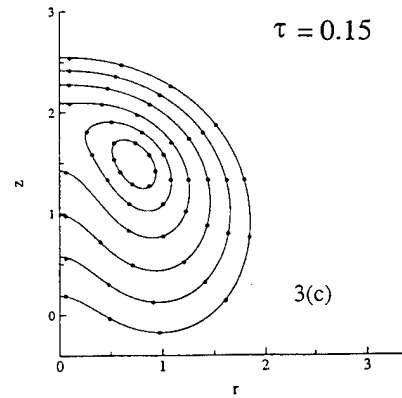
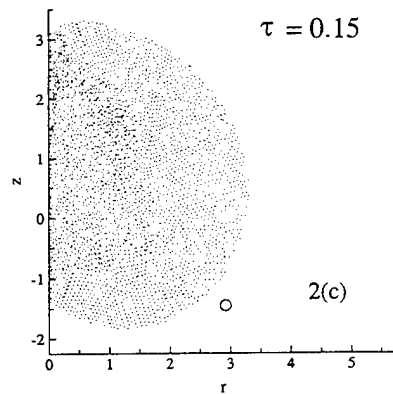
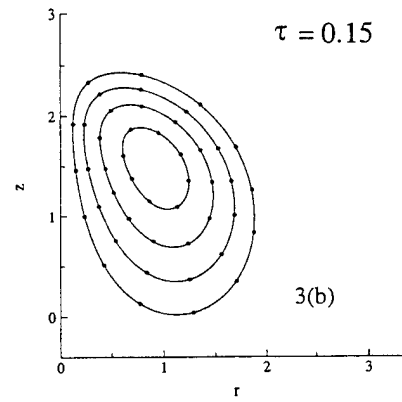
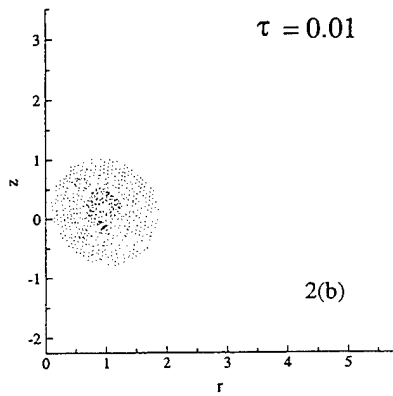
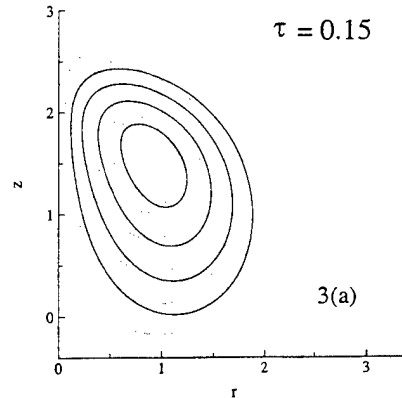
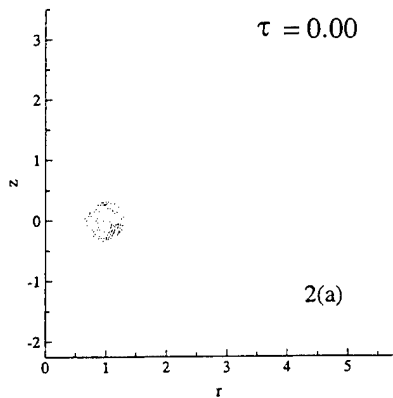


Figure 2: Computational elements for the flow of a vortex ring at $Re = 50$ and $Pr = 1$. The small circle in 2(c) represents the spatial resolution.

Figure 3: (a) Solid lines are vorticity contours, $\omega = 0.08, 0.15, 0.25, 0.375$; dotted lines are temperature contours, $T = 0.08, 0.15, 0.25, 0.375, 0.475, 0.54$. (b) & (c) are vorticity and temperature contours; solid lines are finite-difference solutions and symbols are redistribution solutions.



APPENDIX II

The Effect of Flow and Mixture Inhomogeneity on the Dynamics of Strained Flames

by

Youssef Mohamed Marzouk

Submitted to the Department of Mechanical Engineering
on August 23, 1999, in partial fulfillment of the
requirements for the degree of
Master of Science in Mechanical Engineering

Abstract

Changes in flow strain and mixture composition on the order of a flame time scale are characteristic of many practical combustion processes. Accurately predicting the unsteady response of burning to these changes requires detailed modeling of species transport and chemical kinetics. This thesis formulates a detailed one-dimensional computational model for arbitrary unsteady conditions of strain and mixture, demonstrating its applicability to subgrid modeling of turbulent combustion. A novel numerical formulation, based on a globalized Newton iterative method and a preconditioned Krylov subspace linear solver, ensures efficient and robust convergence despite the stiffness of detailed chemistry. The model is validated via comparison with OP-PDIF, a well-benchmarked steady-state strained flame code. The model is then used to characterize the fundamental interactions of flow and mixture inhomogeneity—examining the dynamic response of flame structure and burning to linear variations in mixture equivalence ratio, and capturing the effect of unsteady strain on a flame surface interacting with a vortex in two dimensions. The latter example leads to a redefinition of the appropriate subgrid strain for flame embedding simulation of premixed turbulent combustion.

Thesis Supervisor: Ahmed F. Ghoniem
Title: Professor of Mechanical Engineering

Acknowledgments

Thanks are first due to my thesis advisor, Professor Ahmed Ghoniem. His guidance and insight have brought coherence and rigorous thinking to this work, as well as a strong awareness of its context and implications. I would also like to thank Dr. Habib Najm, who hosted me at Sandia National Laboratories in August of 1998, during the early stages of this effort. His attention to detail and his practical know-how, shared in many discussions over the past year, helped speed the progress of my research. Also, Habib generously provided the data from simulations of flame-vortex interaction that are used in this thesis.

I owe a debt of gratitude to my family, who have been constant and supportive throughout my education; my appreciation of their support continues to grow. Thanks are also due to my fellow students (and postdocs) at the Reacting Gas Dynamics Lab—Jean-Pierre Hathout, Issam Lakkis, Shankar Subramaniam, and Mahmoud Fleifil. I have relied on them for friendship, technical advice, and a healthy share of lunchtime diversion. I also thank Constantin Petrov, a laboratory alumnus, for introducing me to the elemental flame code.

Finally, I would like to acknowledge the support of the Fannie and John Hertz Foundation, which has sponsored me as a graduate fellow for the past two years. Numerical simulations in this thesis were performed at Sandia National Laboratories, through a collaboration supported by the United States Department of Energy.

Contents


1	Introduction	9
1.1	Turbulent Combustion Simulation	10
1.2	Flame Response to Unsteady Strain	13
1.3	Flame Response to Unsteady Mixture	14
1.4	Scope and Goals	16
2	Model Formulation	17
2.1	Kinematics of Flame Front Stretching	17
2.2	Governing Equations for the Elemental Flame	21
2.3	Transport and Kinetics	26
2.3.1	Transport Model	26
2.3.2	Chemical Mechanism	27
3	Numerical Solution	29
3.1	Finite-difference Discretization	29
3.2	Inexact Newton Method	34
3.3	Krylov Subspace Iterative Solver	36
3.3.1	BiCGSTAB	37
3.3.2	ILUTP Preconditioning	38
3.4	Initialization Conditions	41
3.4.1	Starting Case	41
3.4.2	Mass Flux Projection Method	42

4	Steady-State Validation	44
4.1	OPPDIF Formulation	44
4.2	Comparison of Results	46
5	Unsteady Applications	52
5.1	Burning in a Stratified Mixture	52
5.1.1	Dynamic Effect of Equivalence Ratio Variation	54
5.1.2	Back-support of the Elemental Flame	54
5.2	Unsteady Strain in a Flame-Vortex Interaction	57
5.2.1	Matching the Leading Edge Strains	57
5.2.2	Matching Average Strains	60
6	Conclusions and Further Work	74
	Bibliography	76

List of Figures

1-1	Full numerical simulation of flame-vortex interaction.	11
1-2	Flame surface in homogeneous turbulence.	12
1-3	Phase diagram of turbulent combustion.	12
1-4	Schematic of equivalence-ratio driven combustion instability.	16
2-1	Deformation of material element on a flame front.	18
2-2	Flow-induced deformation in the reference frame of a flame element.	19
2-3	Flame strained in a stagnation point flow; the elemental flame model.	22
4-1	Flow configuration modeled by OPPDIF.	48
4-2	Flow velocity through the flame, elemental flame code vs. OPPDIF.	48
4-3	Distribution of effective strain, elemental flame code vs. OPPDIF.	49
4-4	Temperature and major species profiles in the flame region, elemental flame code vs. OPPDIF.	50
4-5	Minor species profiles in the flame region, elemental flame code vs. OPPDIF.	51
5-1	Heat release rate vs. time for linear changes in ϕ ; $\epsilon = 300$	63
5-2	Heat release rate vs. time, back-support and no back-support.	64
5-3	Heat release rate vs. reactants equivalence ratio, back-support and no back-support.	65
5-4	Temperature profiles with changing ϕ , back-supported flame; $\Delta t = 3$ ms.	66

5-5	Temperature profiles with changing ϕ , non-back-supported flame; $\Delta t = 3$ ms.	67
5-6	OH profiles with changing ϕ , back-supported flame; $\Delta t = 3$ ms.	68
5-7	OH profiles with changing ϕ , non-back-supported flame; $\Delta t = 3$ ms.	69
5-8	Strain histories extracted from the flame-vortex interaction.	70
5-9	One- and two-dimensional heat release rates vs. time for various strain-matching schemes.	71
5-10	Strain profile in the two-dimensional flame element; $t = 2$ ms.	72
5-11	Structure of the one- and two-dimensional flame elements; $t = 2$ ms.	73



List of Tables

2-1	Smooke-46 chemical mechanism for methane-air combustion.	28
-----	--	----

Chapter 1

Introduction

Combustion is a dynamically complex process, reliant on the interplay of fluid flow, diffusive transport, and chemical kinetics, all occurring over a wide range of length and time scales. Computational simulation of combustion in practical devices necessarily applies simplifying assumptions to these physical processes. Indeed, full numerical simulation of multi-dimensional reacting flow—simulation that resolves all spatial and temporal scales of turbulence and chemistry—is far beyond the reach of current computer technology, and will not be feasible in the foreseeable future.

A classical practice in combustion simulation has been to assume instantaneous response of the flame to dynamic changes in flow or mixture composition, using such devices as a flamelet library or some other closure scheme based on steady-state flame properties. Yet there is a whole range of combustion processes for which this assumption is not valid; combustion instability, combustion at high turbulence intensity, and combustion in stratified charges are but a few phenomena in which flow and mixture composition changes on the order of a flame time scale do occur. Capturing the dynamic, *unsteady* response of flames is thus essential to a physical understanding of these phenomena. Modeling the effect of such flow and mixture inhomogeneities is the focus of work in this thesis.

1.1 Turbulent Combustion Simulation

Combustion in a turbulent flow may take the form of a flame surface convoluted over a range of length scales by vortical structures. The area and burning rate of this flame surface is primarily affected by the hydrodynamic strain, i.e., the continually varying strain rate imposed by turbulent eddies. Figures 1-1 and 1-2 demonstrate the interaction of turbulence with a two-dimensional flame front. Figure 1-1 shows snapshots of a premixed flame interacting with a vortex at 0.5 ms intervals, extracted from a direct numerical simulation; Figure 1-2 shows a flame front in a sea of homogeneous turbulence, also obtained via direct numerical simulation. In both cases, the flame is a thin surface wrapped around vortical structures, and the evolutions of the flame surface and the flow structures are dynamically linked.

Of course, this model is not applicable to all regimes of turbulent combustion. Turbulent combustion processes may be classified by Damköhler and Karlovitz numbers, as seen in Figure 1-3. The Damköhler number is the ratio of the flow (integral) time scale to chemical time scale

$$Da = \frac{\tau_F}{\tau_R} \quad (1.1)$$

while the Karlovitz number is taken as the ratio of the flame stretch rate to a critical stretch rate, using l_F as a flame thickness and s_L as the laminar flame speed:

$$Ka = \frac{\frac{1}{A} \frac{dA}{dt}}{s_L/l_F} \quad (1.2)$$

The limit of fast chemistry corresponds to $Da \gg 1$, while one expects local quenching and distributed reaction zones for $Ka > 1$. Thus the model of a continuous flame surface wrinkled or corrugated by turbulence, as described above, is valid in the regime $Da \gg 1$, $Ka \leq 1$.

In this “flamelet” regime of turbulent combustion, the flame surface occupies only a fraction of the total volume of reacting flow. Yet solving the fully coupled equations of reacting flow with detailed chemistry, as in Figures 1-1 and 1-2 is computationally very expensive, prohibitive for all but the most idealized cases. It would be

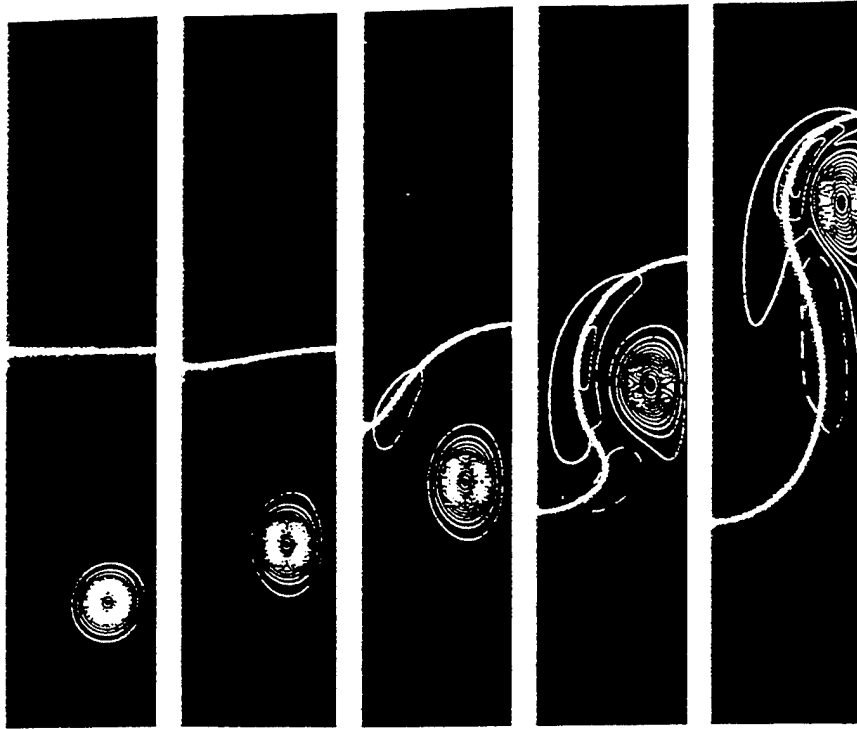


Figure 1-1: Full numerical simulation of flame-vortex interaction.

desirable—for the purposes of computational efficiency, and as a fundamental modeling advance—to decouple the flame surface from the non-reacting portions of the flow, to develop a *subgrid model* for the flame, specifically, one that captures the unsteady effects of strain imposed by the flow. Modeling a turbulent reacting flow in the flamelet regime would thus consist of dynamically coupling a non-reacting flow solver with this subgrid model, the flow straining the flame and changing its burning rate, the flame acting as a source of volumetric expansion and a baroclinic source of vorticity in the flow. This idea is known as flame embedding, and has been explored in its initial stages [22]. A detailed and accurate subgrid model is central to the success of the flame embedding technique and will be developed in subsequent chapters.



Figure 1-2: Flame surface in homogeneous turbulence.

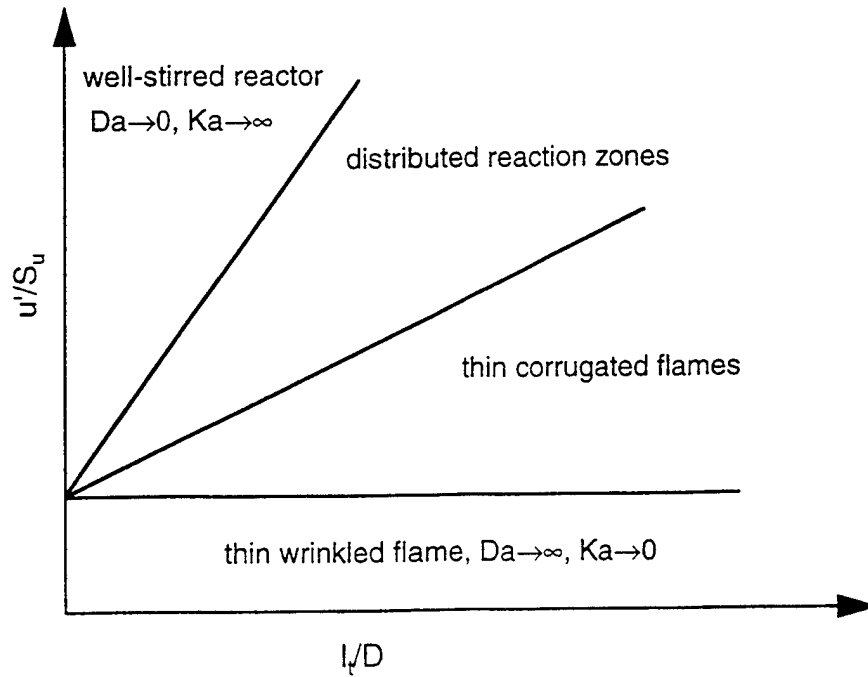


Figure 1-3: Phase diagram of turbulent combustion.

1.2 Flame Response to Unsteady Strain

Many studies have examined the response of premixed or non-premixed laminar flames to unsteady strain rates, most often for the purposes of understanding the effect of turbulence on burning [34, 12, 23, 25, 3, 9, 26, 24, 11, 13, 5]. Strain affects a flame by changing scalar gradients and thus the rates of diffusive transport feeding the flame. Accurately predicting the effects of strain therefore requires detailed models for chemistry and species transport. However, certain qualitative results can be summarized:

Consider a premixed flame in which, for simplicity, a single Lewis number ($Le \equiv \alpha/D$) describes the transport of all species. The direct impact of strain is on the convection-diffusion zone of the flame, but the actual effect of strain on burning, i.e., on the reaction zone, depends closely on the Lewis number. For a unity Lewis number, mass and heat diffusion rates are equal, and the reaction-diffusion zone is essentially unaffected over a range of weak to intermediate strains. Once the flow time scale imposed by the strain becomes comparable to the chemical time scale, however, the temperature in the reaction zone begins to fall and the burning rate decreases. Here the Karlovitz number is of order unity; at even higher strains (and values of Ka), flame extinction may be observed.

For nonunity Lewis number, the imbalance between mass and heat flux leads to changes in flame structure at weak and intermediate strains. Strain shifts values of temperature and fuel mass fraction relative to one another, thus altering the conditions in the reaction zone. For $Le > 1$, heat diffuses more quickly than mass; a smoother temperature profile reduces the temperature in the reaction zone, and the burning rate decreases monotonically with strain. For $Le < 1$, fuel diffuses more quickly than heat, and temperature actually increases at the location of the maximum reaction rate; the burning rate thus increases with weak to intermediate strain.

At high strain, Lewis number effects become less important. As described above for unity Lewis number, the burning rate at $Ka > 1$ must decrease for nonunity and unity Lewis number flames alike. Flame extinction occurs as the influx of cold

reactants exceeds the rate of heat release from chemical reaction and the reaction zone falls below the ignition temperature. Numerical results supporting these trends can be found in [23].

Of course, a single Lewis number applied to all species cannot describe a real reacting flow. This simplified discussion of strain at varying Lewis numbers emphasizes the importance of detailed chemistry and transport in accurately modeling a flame, even to predict the steady-state effect of a given strain rate. In a realistic flame, the diffusive flux of each mixture component reacts differently to a change in strain rate, and the superposition of these diffusive fluxes changes the composition and temperature of the reaction zone, where, in turn, a complex set of chemical pathways determines the burning rate.

Now consider unsteady strain rates: The effect of oscillatory strain on a flame depends on the frequency of the applied oscillations. At low frequency the flame may respond in a quasi-steady manner; at moderate frequency, the flame responds with a time lag, and thus a phase shift; while at even higher frequency, a flame may be unresponsive to oscillations in strain. The bounds between these regimes depend on the relative sizes of the flame time scale and the period of strain oscillations. It is also important to note that a flame may survive at higher unsteady strains than it would in a steady-state environment, a result reported by Najm [16] and others. Moreover, flames in a turbulent environment can undergo quenching and subsequent re-ignition. All these effects must be captured to model the effects of flow inhomogeneity on combustion.

1.3 Flame Response to Unsteady Mixture

The response of flames to unsteady changes in mixture composition, or more specifically, to unsteady changes in equivalence ratio, has not been studied extensively. However, spatial or temporal stratification of a reacting mixture occurs in numerous practical devices. An outstanding example of this—with unsteadiness on the order of a flame time scale—occurs in combustion instability and its control.

Consider the combustor shown schematically in Figure 1-4. Perturbations in the heat release rate of the flame will lead to pressure perturbations in the combustion chamber. If the fuel flow is choked or constant, as with a fuel injector, pressure perturbations will affect only the air flow and thus create variation in the equivalence ratio of the mixture reaching the flame. This perturbation in ϕ then affects the heat release in the flame, and a positive feedback can occur, leading to instability. Equivalence-ratio driven combustion instabilities like this have been observed in practice, and discussed in the literature [29].

The preceding argument may be cast in a more rigorous, mathematical form. The heat release rate \dot{q} acts as a source term in the standard wave equation:

$$\frac{\partial^2 p'}{\partial t^2} - c^2 \frac{\partial^2 p'}{\partial x^2} = (\gamma - 1) \dot{q} \quad (1.3)$$

Now using a Galerkin expansion and focusing on only one acoustic mode, we obtain an oscillator equation.

$$p' = \eta(t)\psi(x) \longrightarrow \ddot{\eta} + \omega^2 \eta = c\dot{q} \quad (1.4)$$

The heat release rate \dot{q} depends on both the velocity and equivalence ratio perturbations, and the equivalence ratio perturbation is some function of p' and \dot{p}' . The first of these relationships must incorporate the character of unsteady flame response. Under appropriate conditions, the functional form of \dot{q} will introduce a negative term in \dot{p}' on the left-hand side of the oscillator equation; this negative damping is indicative of combustion instability.

Combustion instability is typically observed at frequencies of 100–1000 Hz, implying mixture inhomogeneity on the order of a flame time scale. Moreover, even when combustion instability is not driven by equivalence ratio, control actuation mechanisms such as fuel injection can still introduce equivalence ratio variation at similar frequencies.

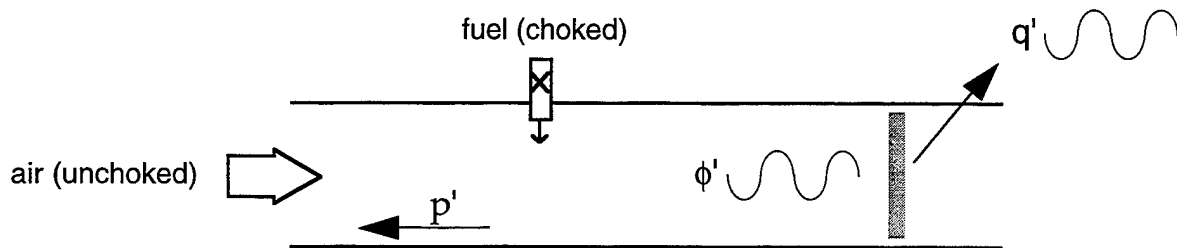


Figure 1-4: Schematic of equivalence-ratio driven combustion instability.

1.4 Scope and Goals

Motivated by the physical problems presented above, this thesis will develop a simple computational model applicable to flame embedding and to arbitrary unsteady conditions of strain and mixture. The formulation of this model is presented in Chapter 2.

To accurately predict unsteady flame response, our model must incorporate detailed chemical kinetics and species transport. Many detailed-chemistry flame codes are currently available, but most of these codes are aimed at steady-state problems. Also, these codes tend to lack numerical robustness and to exhibit poor efficiency. Thus an important thrust of this work will be to develop more robust, computationally efficient numerical methods for stiff, multi-species reacting flow. Implementation of these numerical methods is described in Chapter 3.

The remainder of the thesis will focus on applications of the computational model. Validation of the model, through direct comparison with a well-benchmarked steady-state flame code (Sandia's OPPDIF) is presented in Chapter 4. Chapter 5 finally uses the code to examine several unsteady problems discussed in the preceding sections: first, the burning of a stratified mixture, and second, a comparison with direct numerical simulation of two-dimensional turbulent combustion, thereby refining the concepts of flame embedding.

Chapter 2

Model Formulation

Turbulent combustion in the “flamelet” regime, as described in §1.1, takes the form of a thin flame surface strained by turbulent eddies. Our goal is to develop a model that captures the effect of flow strain and changing mixture composition on this surface—in other words, an unsteady subgrid model applicable to flame embedding. Though motivated by a physical picture of turbulent flow, this model also will lend itself to more idealized studies of arbitrary strain and mixture inhomogeneity.

2.1 Kinematics of Flame Front Stretching

The first assumption of our model is suggested by the thinness of a turbulent flame surface in the flamelet regime. Fast chemistry ($Da \gg 1$) and a high rate of heat release insure that scalar gradients normal to the flame surface are much larger than those tangential to it. Neglecting the tangential gradients, one obtains a locally one-dimensional flame structure.

Now consider the kinematics of a material element on a two-dimensional flame front, as shown in Figure 2-1. The motion of any such fluid line segment may be decomposed into translation, rotation, and strain. In flame coordinates—that is, in the reference frame of the fluid line segment—the only effect of motion that will be apparent is that of strain. Translation and rotation may change the mixture that the flame front encounters, but only strain will alter the flame’s internal structure. The

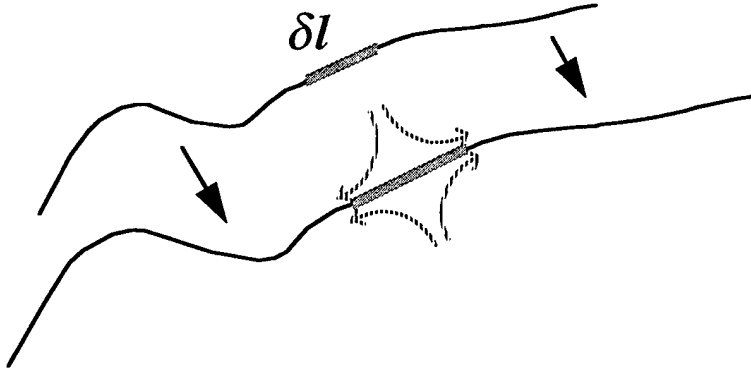


Figure 2-1: Deformation of material element on a flame front.

strain is given by the relative change in length of the line segment:

$$\epsilon = \frac{1}{|\delta \mathbf{l}|} \frac{d\delta \mathbf{l}}{dt} = \frac{\delta \mathbf{l} \cdot \nabla \mathbf{u}}{|\delta \mathbf{l}|} \quad (2.1)$$

Further insight may be obtained by decomposing the flow local to the flame front. Figure 2-2 shows two initially perpendicular line segments, l and m , in a reference frame \mathcal{F} chosen to follow a flame element. The x-axis of this reference frame is always parallel to the flame surface, while the y-axis is always perpendicular to it. The line segment l is a material element of the flame front and thus always lies on the x-axis, while the line segment m is initially coincident with the y-axis. At an initial time t , the projections of the the line segments on the axes are

$$l_x(t) = l(t), \quad l_y(t) = 0 \quad (2.2)$$

$$m_x(t) = 0, \quad m_y(t) = m(t) \quad (2.3)$$

After an elapsed time dt , the projections become

$$l_x(t + dt) = \left(1 + \frac{\partial u}{\partial x} dt \right) l(t) \quad (2.4)$$

$$l_y(t + dt) = \left(\frac{\partial v}{\partial x} dt \right) l(t) = 0 \quad (2.5)$$

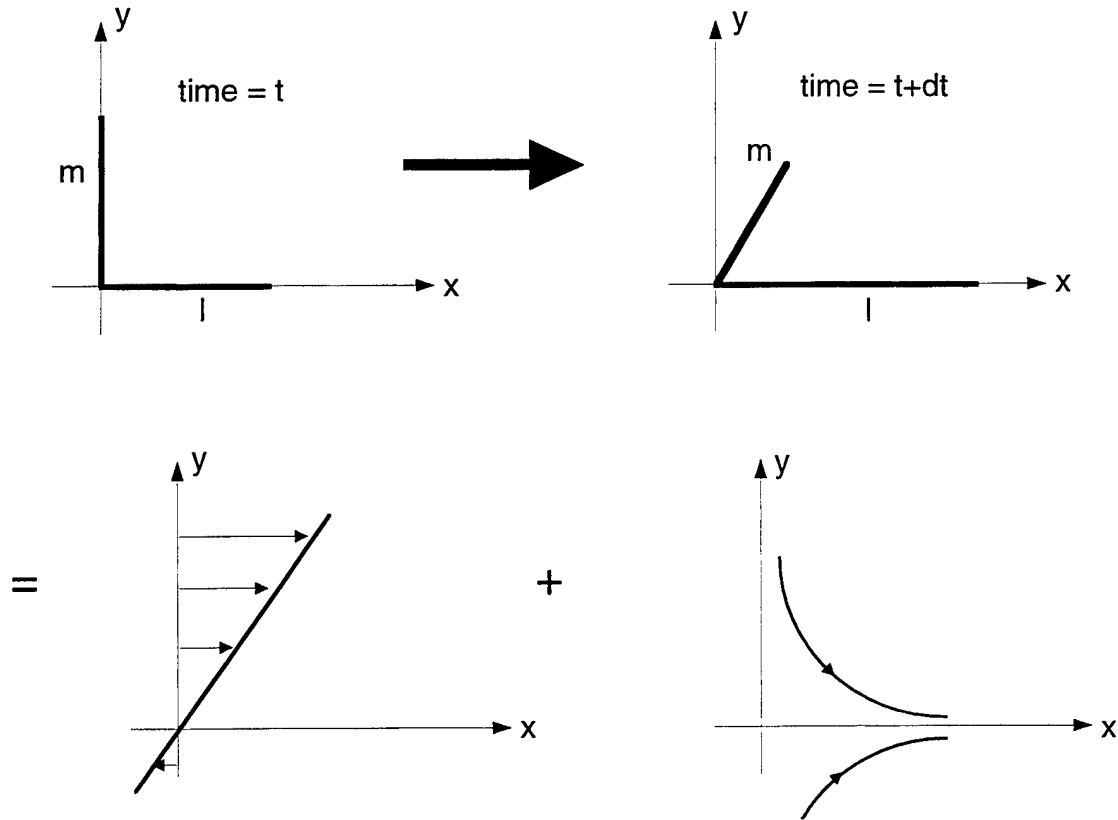


Figure 2-2: Flow-induced deformation in the reference frame of a flame element.

$$m_x(t + dt) = \left(\frac{\partial u}{\partial y} dt \right) m(t) \quad (2.6)$$

$$m_y(t + dt) = \left(1 + \frac{\partial v}{\partial y} dt \right) m(t) \quad (2.7)$$

where u and v are the flow velocities in the x and y directions, respectively. Note that our choice of reference frame requires the derivative in Equation 2.5 to equal zero.

As expressed in Equation 2.6, the projection m_x grows at the rate $\partial u/\partial y$; the segment initially in the y -direction thus rotates without changing its length. This deformation is consistent with a *pure shear flow*, corresponding to off-diagonal components of the strain rate tensor:

$$\tau_{xy} = \frac{1}{2} \left(\frac{\partial u}{\partial y} + \frac{\partial v}{\partial x} \right) \quad (2.8)$$

The second component of flow local to the flame element is a *stagnation point flow*,

observed in Equations 2.4 and 2.7. Both line segments are strained along the principal axes, and because of continuity in an incompressible flow, the rates of strain are equal and opposite in sign:

$$\epsilon = \frac{\partial u}{\partial x} = -\frac{\partial v}{\partial y} \quad (2.9)$$

Decomposition of the flow in the vicinity of a flame element is shown schematically in Figure 2-2.

What does this flow decomposition imply for modeling the effect of inhomogeneities on a flame surface? As stated earlier, scalar gradients (e.g., gradients of temperature, density, species concentrations) normal to the flame are much larger than those tangential to the flame. In the reference frame \mathcal{F} , this can be written

$$\frac{\partial}{\partial x} \ll \frac{\partial}{\partial y} \quad (2.10)$$

Now consider the transport equation for a scalar in \mathcal{F} ; this equation must contain the following differential operator:

$$\mathcal{L} \equiv \frac{\partial}{\partial t} + u \frac{\partial}{\partial x} + v \frac{\partial}{\partial y} - \frac{\partial^2}{\partial x^2} - \frac{\partial^2}{\partial y^2} \quad (2.11)$$

The velocity of the shear flow, $u_{shear} = cy$, contributes only to the u in the second term of Equation 2.11. Following Equation 2.10, this second term can be neglected entirely, rendering the shear component of the velocity field unimportant in local transport of scalars. Physically, this can be understood from Figure 2-2; the shear field simply advects constant values of scalars parallel to the flame surface and cannot alter the distribution of scalars normal to the flame. As a result, the instantaneous burning of a turbulent flame surface is locally similar to that of a stagnation point flow with an appropriately chosen strain rate. Our subgrid model for the effect of strain and mixture inhomogeneity on burning will center on this stagnation point flow.

It is important to note that the preceding analysis does not account for curvature of the flame surface. (The line segments displaced in Figures 2-1 and 2-2 are perfectly

straight.) Propagation of a curved flame contributes to the total stretch rate as follows:

$$\frac{1}{|\delta\mathbf{l}|} \frac{d\delta\mathbf{l}}{dt} = \epsilon + 2s_d h_m \quad (2.12)$$

where ϵ is the ordinary hydrodynamic strain, given by the surface divergence of the velocity field, s_d is the speed of the flame surface normal to itself, and h_m is the mean curvature. This effect is relevant only to premixed flames ($s_d \neq 0$), and typically becomes important only in regions of high curvature (where the radius of curvature is small relative to the flame thickness)—in the cusp of a vortical structure, for example. For simplicity, the flame models used in this thesis will ignore curvature effects.

Finally, it is instructive to contrast our subgrid model with traditional flamelet models for turbulent combustion, as developed by Bray [2]. Both models represent local burning conditions of the flame surface with a stagnation point flow, but the model developed here will have the distinction of being *unsteady*. As discussed in Chapter 1, the effects of unsteadiness are fundamental to the dynamics of flame-flow interaction, and modeling them takes an important step towards accurate simulation of reacting flow.

2.2 Governing Equations for the Elemental Flame

The unsteady combustion zone model developed in this chapter is known as the *elemental flame* model, distinguishing it from the quasi-steady flamelet approach [22]. Consider a flame strained in a planar stagnation point flow, with coordinates and flow velocities shown in Figure 2-3. The flame introduces directionality to this figure and enables use of the boundary layer approximation; for any scalar φ , gradients parallel to the flame $\partial^2\varphi/\partial x^2$ are negligible compared to those perpendicular to the flame, $\partial^2\varphi/\partial y^2$. We thus write unsteady boundary layer equations for transport of species, energy, momentum, and mass:

$$\rho \frac{\partial Y_k}{\partial t} + \rho u \frac{\partial Y_k}{\partial x} + \rho v \frac{\partial Y_k}{\partial y} = \frac{\partial}{\partial y} \left(\rho D_k \frac{\partial Y_k}{\partial y} \right) + \dot{w}_k W_k \quad (2.13)$$

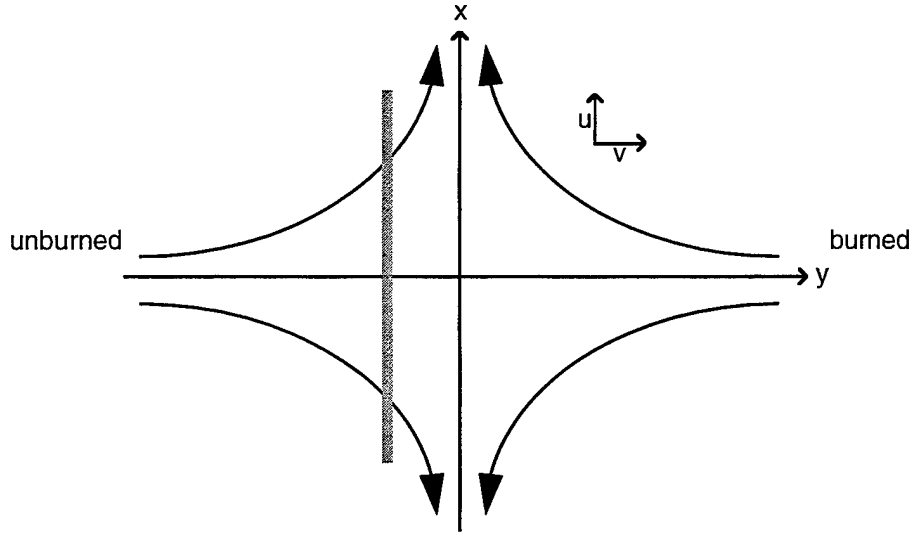


Figure 2-3: Flame strained in a stagnation point flow; the elemental flame model.

$$\rho \frac{\partial T}{\partial t} + \rho u \frac{\partial T}{\partial x} + \rho v \frac{\partial T}{\partial y} = \frac{1}{C_p} \frac{\partial}{\partial y} \left(\lambda \frac{\partial T}{\partial y} \right) + \sum_k \frac{\dot{w}_k h_k}{C_p} \quad (2.14)$$

$$\rho \frac{\partial u}{\partial t} + \rho u \frac{\partial u}{\partial x} + \rho v \frac{\partial u}{\partial y} = -\frac{\partial p}{\partial x} + \frac{\partial}{\partial y} \left(\mu \frac{\partial u}{\partial y} \right) \quad (2.15)$$

$$\frac{\partial \rho}{\partial t} + \frac{\partial (\rho u)}{\partial x} + \frac{\partial (\rho v)}{\partial y} = 0 \quad (2.16)$$

Here Y_k is the mass fraction of species k , D_k is the mixture-averaged diffusion coefficient for species k , while W_k and \dot{w}_k are the molecular weight and molar production rate for species k , respectively. In the remaining equations, C_p is the mixture-averaged specific heat, λ is the thermal conductivity, h_k is the molar specific heat of species k , p is the hydrodynamic pressure, and μ is the absolute viscosity of the mixture. Note that the enthalpy flux term is neglected in the energy equation (Equation 2.14) while thermal diffusion velocity is neglected in each species transport equation (Equation 2.13). Smooke [33] and others have shown that both effects are unimportant to the laminar strained flame.

The pressure gradient dp/dx inside the boundary layer is identical to that in the outer stagnation point flow, since by the usual boundary layer assumption, Δp across the boundary layer is negligible. Substituting the stagnation point flow velocity

profile $u_\infty = \epsilon(t) x$, $v_\infty = -\epsilon(t) y$ into the general x-direction momentum conservation equation, we obtain the pressure gradient as a function of the imposed strain:

$$\frac{\partial p}{\partial x} = -\rho_{ub} u_\infty \epsilon - \rho_{ub} \frac{u_\infty}{\epsilon} \frac{\partial \epsilon}{\partial t} \quad (2.17)$$

The notation ρ_{ub} above emphasizes that the density of the *unburned* mixture is used to define the pressure gradient. In the diffusion flame, densities outside of the boundary layer are equal, $\rho_{ub} = \rho_{-\infty} = \rho_\infty$, so this distinction is moot. In the premixed flame, however, heat release within the flame leads to a products-side stream entering with lower density—and to maintain a constant pressure gradient, a higher effective strain. Defining the global strain ϵ on the unburned side, in accordance with the expression for pressure gradient above, thus insures consistency and clarity across all flame configurations.

Introducing the notation $U \equiv u/u_\infty$, $V \equiv \rho v$, and substituting the pressure gradient expression into the equation for momentum conservation inside the boundary layer (Equation 2.15), Equations 2.13–2.16 can be rewritten as follows:

$$\rho \frac{\partial Y_k}{\partial t} + \rho u_\infty U \frac{\partial Y_k}{\partial x} + V \frac{\partial Y_k}{\partial y} = \frac{\partial}{\partial y} \left(\rho D_k \frac{\partial Y_k}{\partial y} \right) + \dot{w}_k W_k \quad (2.18)$$

$$\rho \frac{\partial T}{\partial t} + \rho u_\infty U \frac{\partial T}{\partial x} + V \frac{\partial T}{\partial y} = \frac{1}{C_p} \frac{\partial}{\partial y} \left(\lambda \frac{\partial T}{\partial y} \right) + \sum_k \frac{\dot{w}_k h_k}{C_p} \quad (2.19)$$

$$\begin{aligned} \rho u_\infty \frac{\partial U}{\partial t} + \rho u_\infty U \frac{1}{\epsilon} \frac{\partial \epsilon}{\partial t} + \rho u_\infty^2 U \frac{\partial U}{\partial x} + \rho u_\infty U^2 \epsilon + u_\infty V \frac{\partial U}{\partial y} = \\ \rho_{ub} u_\infty \left(\frac{1}{\epsilon} \frac{\partial \epsilon}{\partial t} + \epsilon \right) + u_\infty \frac{\partial}{\partial y} \left(\mu \frac{\partial U}{\partial y} \right) \end{aligned} \quad (2.20)$$

$$\frac{\partial \rho}{\partial t} + u_\infty U \frac{\partial \rho}{\partial x} + \rho U \epsilon + \rho u_\infty \frac{\partial U}{\partial x} + \frac{\partial V}{\partial y} = 0 \quad (2.21)$$

Now consider the solution of the boundary layer equations along the stagnation streamline, $x = 0$. Along this streamline, $u = u_\infty U = 0$ and by symmetry, $\partial \varphi / \partial x = 0$, where φ is a passive scalar—namely, T , Y_k , U , or ρ . Thus, we can eliminate

the x-direction convective terms in Equations 2.18–2.21. Note, however, that $\partial u/\partial x$ and $\partial u_\infty/\partial x$ are nonzero on the stagnation streamline, and that this flow divergence should be reflected in the momentum and continuity equations. Every term in the momentum conservation equation (Equation 2.20) is proportional to u_∞ , so to retain this equation in the system, we divide by u_∞ . The resulting equation governs the strain rate through the reaction zone, where ϵU can be thought of as the effective strain. The final set of governing equations takes the following form:

$$\rho \frac{\partial Y_k}{\partial t} + V \frac{\partial Y_k}{\partial y} - \frac{\partial}{\partial y} \left(\rho D_k \frac{\partial Y_k}{\partial y} \right) - \dot{w}_k W_k = 0 \quad (2.22)$$

$$\rho \frac{\partial T}{\partial t} + V \frac{\partial T}{\partial y} - \frac{1}{C_p} \frac{\partial}{\partial y} \left(\lambda \frac{\partial T}{\partial y} \right) - \sum_k \frac{\dot{w}_k h_k}{C_p} = 0 \quad (2.23)$$

$$\rho \frac{\partial U}{\partial t} + \rho U \frac{1}{\epsilon} \frac{\partial \epsilon}{\partial t} + \rho U^2 \epsilon + V \frac{\partial U}{\partial y} - \frac{\partial}{\partial y} \left(\mu \frac{\partial U}{\partial y} \right) - \rho_{ub} \left(\frac{1}{\epsilon} \frac{\partial \epsilon}{\partial t} + \epsilon \right) = 0 \quad (2.24)$$

$$\frac{\partial \rho}{\partial t} + \frac{\partial V}{\partial y} + \rho U \epsilon = 0 \quad (2.25)$$

Note that the low Mach number assumption has been used in the governing equations above. Density is calculated as a function of the temperature, species mass fractions, and thermodynamic pressure (assumed constant) via the ideal gas equation of state.

At various times, it will be useful to consider a flame strained in an axisymmetric stagnation point flow rather than in the planar configuration used above. Denoting the radial coordinate with r and the axial coordinate with y , the velocity profile of an axisymmetric stagnation point flow is $u_\infty = \epsilon(t) r$, $v_\infty = -2\epsilon(t) y$. The governing equations for this configuration are identical to those derived above (Equations 2.22–2.24) with the exception of the continuity equation. The revised continuity equation is:

$$\frac{\partial \rho}{\partial t} + \frac{\partial V}{\partial y} + 2\rho U \epsilon = 0 \quad (2.26)$$

Boundary conditions for the species and energy equations consist of defining the composition and temperature of the two incoming streams of the stagnation point

flow.

$$\begin{aligned}
 y = -\infty : Y_k &= Y_{k,-\infty}, \quad T = T_{-\infty} \\
 y = +\infty : Y_k &= Y_{k,+\infty}, \quad T = T_{+\infty}
 \end{aligned}
 \tag{2.27}$$

The continuity equation requires only one boundary condition, which specifies zero velocity at the stagnation point:

$$y = 0 : V = 0 \tag{2.28}$$

The momentum conservation equation requires two boundary conditions. At an unburned stream, $u = u_\infty$, so the boundary condition is by definition $U = 1$. Setting the spatial gradients in Equation 2.24 to zero gives the boundary condition burned stream. This far-field boundary condition places an important requirement on the size of the computational domain; the flame must be far enough from the $+\infty$ and $-\infty$ boundaries for spatial gradients in U to vanish. In the case of steady strain, the burned-stream boundary condition on U is

$$U_b = \sqrt{\frac{\rho_{ub}}{\rho_b}} \tag{2.29}$$

where ρ_b is the density of the burned mixture. For unsteady strain, we must integrate the resulting ODE for U_b :

$$\frac{\partial U_b}{\partial t} = -U_b^2 \epsilon - U_b \left(\frac{1}{\epsilon} \frac{\partial \epsilon}{\partial t} \right) + \frac{\rho_{ub}}{\rho_b} \left(\frac{1}{\epsilon} \frac{\partial \epsilon}{\partial t} + \epsilon \right) \tag{2.30}$$

For a premixed flame, the effective strain rate in the incoming products-side mixture thus responds dynamically to the imposed strain rate.

2.3 Transport and Kinetics

To solve the system of governing equations derived in the preceding sections, every term must be expressed in terms of the fundamental variables: temperature, pressure, flow velocities, and mixture composition. Conductivity, viscosity, and species diffusion coefficients vary across the flame according to a prescribed transport model. The chemical source terms \dot{w}_k —molar production rates for each species—are complex functions of the local mixture conditions and thus depend on some chosen scheme of chemical kinetics, whether it is global or detailed. The models used to evaluate these terms are discussed below.

2.3.1 Transport Model

The transport coefficients μ , λ , and D_k could be evaluated exactly using Sandia's TRANSPORT package, an extension to CHEMKIN based on polynomial fits to empirical data. This approach is slow and cumbersome, however; instead we use the approximations validated by Smooke [33].

Smooke showed that the Lewis number of any given species does not vary significantly across the profile of a strained laminar flame. A fixed Lewis number $Le_k \equiv \alpha/D_k$ is thus chosen for each species, capturing the effects of multicomponent differential diffusion. The Prandtl number is chosen constant and equal to 0.75, while a curve fit is used to calculate the ratio λ/C_p in cgs units:

$$\frac{\lambda}{C_p} = 2.58 \times 10^{-4} \left(\frac{T}{298} \right)^{0.7} \quad (2.31)$$

This curve fit provides excellent results over a wide range of temperatures and pressures. The thermodynamic properties C_p and h_k are evaluated by CHEMKIN subroutines, polynomial functions of local mixture conditions.

For reference, the governing equations are restated below to incorporate the transport approximations just developed. Subsequent chapters will solve the equations in

this form.

$$\rho \frac{\partial Y_k}{\partial t} + V \frac{\partial Y_k}{\partial y} - \frac{\partial}{\partial y} \left(\frac{1}{Le_k} \frac{\lambda}{C_p} \frac{\partial Y_k}{\partial y} \right) - \dot{w}_k W_k = 0 \quad (2.32)$$

$$\rho \frac{\partial T}{\partial t} + V \frac{\partial T}{\partial y} - \frac{1}{C_p} \frac{\partial}{\partial y} \left(\lambda \frac{\partial T}{\partial y} \right) - \sum_k \frac{\dot{w}_k h_k}{C_p} = 0 \quad (2.33)$$

$$\rho \frac{\partial U}{\partial t} + \rho U \frac{1}{\epsilon} \frac{\partial \epsilon}{\partial t} + \rho U^2 \epsilon + V \frac{\partial U}{\partial y} - Pr \frac{\partial}{\partial y} \left(\frac{\lambda}{C_p} \frac{\partial U}{\partial y} \right) - \rho_{ub} \left(\frac{1}{\epsilon} \frac{\partial \epsilon}{\partial t} + \epsilon \right) = 0 \quad (2.34)$$

$$\frac{\partial \rho}{\partial t} + \frac{\partial V}{\partial y} + \rho U \epsilon = 0 \quad (2.35)$$

2.3.2 Chemical Mechanism

The kinetic pathways of a combustion process typically consist of hundreds of elementary reactions among major and minor species, each with its own rate expression. These reactions together constitute a chemical mechanism, and can be simplified, or reduced, to an arbitrary level of detail. For example, if the steady-state heat release rate of a flame is the only variable of interest, a global mechanism with a single Arrhenius rate expression is sufficient. For detailed flame structure and for proper modeling of unsteady effects, however, a detailed kinetics mechanism is necessary (along with multicomponent transport), as discussed in Chapter 1. The reduction of chemical mechanisms is a field unto itself, and is beyond the scope of this discussion.

The detailed mechanism used for most of the simulations in this thesis is designed for methane-air combustion and consists of 46 reactions among 16 species. It is a C1 chemical mechanism, and thus is most appropriate to stoichiometric and lean flames. The larger GRIMech mechanisms use both C1 and C2 chemistry and are perhaps the most detailed mechanisms available for hydrocarbon combustion, but we eschew them in favor of computational efficiency. For stoichiometric and lean flames, the simpler 46-reaction mechanism provides excellent predictions, as reported by Smooke [33]. The mechanism is shown in Table 2-1.

REACTIONS CONSIDERED		(k = A T**b exp(-E/RT))		
		A	b	E
1.	CH3+H=CH4	1.90E+36	-7.0	9050.0
2.	CH4+O2=CH3+HO2	7.90E+13	0.0	56000.0
3.	CH4+H=CH3+H2	2.20E+04	3.0	8750.0
4.	CH4+O=CH3+OH	1.60E+06	2.4	7400.0
5.	CH4+OH=CH3+H2O	1.60E+06	2.1	2460.0
6.	CH2O+OH=HCO+H2O	7.53E+12	0.0	167.0
7.	CH2O+H=HCO+H2	3.31E+14	0.0	10500.0
8.	CH2O+M=HCO+H+M	3.31E+16	0.0	81000.0
9.	CH2O+O=HCO+OH	1.81E+13	0.0	3082.0
10.	HCO+OH=CO+H2O	5.00E+12	0.0	0.0
11.	HCO+M=H+CO+M	1.60E+14	0.0	14700.0
12.	HCO+H=CO+H2	4.00E+13	0.0	0.0
13.	HCO+O=OH+CO	1.00E+13	0.0	0.0
14.	HCO+O2=HO2+CO	3.00E+12	0.0	0.0
15.	CO+O+M=CO2+M	3.20E+13	0.0	-4200.0
16.	CO+OH=CO2+H	1.51E+07	1.3	-758.0
17.	CO+O2=CO2+O	1.60E+13	0.0	41000.0
18.	CH3+O2=CH3O+O	7.00E+12	0.0	25652.0
19.	CH3O+M=CH2O+H+M	2.40E+13	0.0	28812.0
20.	CH3O+H=CH2O+H2	2.00E+13	0.0	0.0
21.	CH3O+OH=CH2O+HO2	1.00E+13	0.0	0.0
22.	CH3O+O=CH2O+OH	1.00E+13	0.0	0.0
23.	CH3O+O2=CH2O+HO2	6.30E+10	0.0	2600.0
24.	CH3+O2=CH2O+OH	5.20E+13	0.0	34574.0
25.	CH3+O=CH2O+H	6.80E+13	0.0	0.0
26.	CH3+OH=CH2O+H2	7.50E+12	0.0	0.0
27.	HO2+CO=CO2+OH	5.80E+13	0.0	22934.0
28.	H2+O2=2OH	1.70E+13	0.0	47780.0
29.	OH+H2=H2O+H	1.17E+09	1.3	3626.0
30.	H+O2=OH+O	2.00E+14	0.0	16800.0
31.	O+H2=OH+H	1.80E+10	1.0	8826.0
32.	H+O2+M=HO2+M	2.10E+18	-1.0	0.0
	H2O	Enhanced by	2.100E+01	
	CO2	Enhanced by	5.000E+00	
	H2	Enhanced by	3.300E+00	
	CO	Enhanced by	2.000E+00	
	O2	Enhanced by	0.000E+00	
	N2	Enhanced by	0.000E+00	
33.	H+O2+O2=HO2+O2	6.70E+19	-1.4	0.0
34.	H+O2+N2=HO2+N2	6.70E+19	-1.4	0.0
35.	OH+HO2=H2O+O2	5.00E+13	0.0	1000.0
36.	H+HO2=2OH	2.50E+14	0.0	1900.0
37.	O+HO2=O2+OH	4.80E+13	0.0	1000.0
38.	2OH=O+H2O	6.00E+08	1.3	0.0
39.	H2+M=H+H+M	2.23E+12	0.5	92600.0
	H2O	Enhanced by	6.000E+00	
	H	Enhanced by	2.000E+00	
	H2	Enhanced by	3.000E+00	
40.	O2+M=O+O+M	1.85E+11	0.5	95560.0
41.	H+OH+M=H2O+M	7.50E+23	-2.6	0.0
	H2O	Enhanced by	2.000E+01	
42.	H+HO2=H2+O2	2.50E+13	0.0	700.0
43.	HO2+HO2=H2O2+O2	2.00E+12	0.0	0.0
44.	H2O2+M=OH+OH+M	1.30E+17	0.0	45500.0
45.	H2O2+H=HO2+H2	1.60E+12	0.0	3800.0
46.	H2O2+OH=H2O+HO2	1.00E+13	0.0	1800.0

NOTE: A units mole-cm-sec-K, E units cal/mole

Table 2-1: Smooke-46 chemical mechanism for methane-air combustion.

Chapter 3

Numerical Solution

The evolution of the elemental flame is governed by a set of one-dimensional partial differential equations, as derived in the previous chapter. Difficulty in the numerical solution of these PDEs stems from the inclusion of detailed chemistry. The chemical source terms \dot{w}_k are composites of elementary rate expressions, where each rate expression is a strong, usually exponential, function of temperature. Together, these source terms introduce a wide range of time scales to the governing equations, extending to the order of nanoseconds. Overcoming the stiffness of detailed chemistry has been a long-standing challenge in numerical combustion simulation, one which here necessitated the use of several novel numerical tools.

3.1 Finite-difference Discretization

The governing equations of the elemental flame (Equations 2.32–2.35) must be integrated implicitly, as required by stiffness. A first-order, backward Euler formulation is used, discretizing the time derivatives as follows:

$$\rho \frac{\partial T}{\partial t} = \mathcal{F}(T, V, Y_k, \dots) \rightsquigarrow \rho^{n+1} \frac{T^{n+1} - T^n}{\Delta t} = \mathcal{F}(T^{n+1}, V^{n+1}, Y_k^{n+1}, \dots) \quad (3.1)$$

Here and in all subsequent discretizations, the superscript indicates the time layer; the time derivative in the energy equation is used as an example. In contrast to previ-

ous formulations [22], all the governing equations—energy conservation, momentum conservation, species conservation, and continuity—are solved simultaneously.

To prevent the formation of numerical instabilities, convective terms in the species, energy, and momentum conservation equations are discretized with a first-order upwind stencil. This stencil thus depends on the sign of the convective velocity:

$$V_j < 0 : V \frac{\partial T}{\partial y} \approx V_j \frac{T_{j+1} - T_j}{h_j} \quad (3.2)$$

$$V_j > 0 : V \frac{\partial T}{\partial y} \approx V_j \frac{T_j - T_{j-1}}{h_{j-1}} \quad (3.3)$$

Here, the subscript represents the point on the spatial grid, while h is the grid spacing: $h_j \equiv y_{j+1} - y_j$. Diffusion terms are approximated to second-order accuracy. Again, the energy equation (2.33) is used as an example:

$$\frac{1}{C_p} \frac{\partial}{\partial y} \left(\lambda \frac{\partial T}{\partial y} \right) \approx \frac{1}{C_{p,j}} \frac{2}{y_{j+1} - y_{j-1}} \left(\lambda_{j+1/2} \frac{T_{j+1} - T_j}{h_j} - \lambda_{j-1/2} \frac{T_j - T_{j-1}}{h_{j-1}} \right) \quad (3.4)$$

The continuity equation (2.35) must be carefully discretized to avoid numerical oscillations in the mass flux profile. Without an appropriate stencil, oscillations are observed during translation of the flame with respect to the spatial grid; susceptibility to oscillations is high since the continuity equation is the only governing equation without physical dissipation. Thus, an upwind discretization is used. The term ‘upwind’ is written with some qualification, since the continuity equation is not properly a transport equation and $\partial V / \partial y$ is not a convective term per se. Nonetheless, taking the positive sign of $\partial V / \partial y$ to suggest a positive upwind velocity, the following discretization of the continuity equation adds dissipation of the appropriate sign:

$$\begin{aligned} \frac{\partial \rho}{\partial t} + \frac{\partial V}{\partial y} + \rho U \epsilon = 0 \rightsquigarrow \\ \frac{\rho_j^{n+1} - \rho_j^n}{\Delta t} + \frac{V_j^{n+1} - V_{j-1}^{n+1}}{h_{j-1}} + \rho_j^{n+1} U_j^{n+1} \epsilon^{n+1} = 0 \end{aligned} \quad (3.5)$$

This discretization of $\partial V / \partial y$ prevents direct implementation of the stagnation point boundary condition, Equation 2.28. Instead, a boundary value on the mass flux V

must be chosen at $y = -\infty$. The boundary value is arbitrary provided that it is large enough for a flame to stabilize at a lower mass flux, since V decreases in the direction of the stagnation point. If the boundary value is too large, on the other hand, the flame (or for that matter, the stagnation point) may not fall within the computational domain. The boundary value can thus be set to any reasonable number based on the size of the computational domain and the strain rate. The solution to the problem matches the mass flux profile to the flame location, as reflected in the profiles of T , Y_k , ρ , and U . In computations with changing strain rate, the boundary condition on V must be updated periodically, a process detailed in §3.4.2.

Spatial discretization of the governing equations is performed on a non-uniform adaptive grid. Non-uniform grid spacing permits a greater clustering of grid points in regions where spatial gradients are strong, thus ensuring adequate resolution through the reaction-diffusion zone; a fine grid resolution tends to offset the fact that convective discretizations are only first-order accurate. Grid points are more sparsely spaced away from the flame, in regions of constant gradient. This non-uniform allocation of grid points provides accuracy without sacrificing computational efficiency.

As the flame translates in space or as its internal structure changes, adaptivity of the grid becomes important. Several criteria for grid resolution are enforced at the end of each time step, and where these criteria are not met, grid points are added or removed appropriately. First, the gradient of each scalar must be adequately resolved, relative to its range:

$$|\varphi_{j+1} - \varphi_j| < \alpha \left| \max_j \varphi - \min_j \varphi \right| \quad (3.6)$$

Here, φ is chosen to include all the dependent variables (T , Y_k , U , and V) as well as each chemical source term \dot{w}_k ; α is a tolerance parameter on the order of 0.1. Second gradients are subject to an analogous criterion:

$$\left| \left(\frac{\partial \varphi}{\partial y} \right)_{j+1} - \left(\frac{\partial \varphi}{\partial y} \right)_j \right| < \beta \left| \max_j \left(\frac{\partial \varphi}{\partial y} \right) - \min_j \left(\frac{\partial \varphi}{\partial y} \right) \right| \quad (3.7)$$

The final criterion forces the grid to be relatively uniform:

$$\gamma < \frac{h_j}{h_{j-1}} < 1/\gamma \quad (3.8)$$

Linear interpolation is used to calculate the value of the dependent variables at any new grid point.

At the end of each time step, the thickness of the flame's temperature profile is compared to the distance from each boundary to the nearest end of the flame. If the flame comes to within two thermal thicknesses of the boundary, the computational domain is extended and values of each dependent variable are extrapolated to the new grid points. This criterion for grid extension is most important on the products side of a premixed flame, where the boundary conditions expect the mixture to have reached equilibrium, with all spatial gradients in T , Y_k , and U falling to zero.

The time step for integration is constant, typically chosen in the range of 1–10 μs . At each time step, discretization reduces the governing PDEs to a set of nonlinear algebraic equations. The nonlinear system can be written as:

$$F(x) = 0, \quad F: \mathbb{R}^n \rightarrow \mathbb{R}^n \quad (3.9)$$

The output of the function F is a column vector containing residuals of the discretized governing equations, while x is the solution vector, containing profiles of each fundamental variable, Y_k , T , U , and V . The organization of the values within these column vectors is important, as it affects the bandwidth and structure of the Jacobian matrix,

$F'_{ij} \equiv \partial F_i / \partial x_j$. Variables and residuals are thus grouped by grid point:

$$x = \begin{pmatrix} \vdots \\ Y_{(k=1),j} \cdots Y_{(k=K),j} \\ T_j \\ U_j \\ V_j \\ Y_{(k=1),j+1} \cdots Y_{(k=K),j+1} \\ T_{j+1} \\ U_{j+1} \\ V_{j+1} \\ \vdots \end{pmatrix} \quad (3.10)$$

$$F = \begin{pmatrix} \vdots \\ res_{spec(k=1),j} \cdots res_{spec(k=K),j} \\ res_{energy,j} \\ res_{mntm,j} \\ res_{cont,j} \\ res_{spec(k=1),j+1} \cdots res_{spec(k=K),j+1} \\ res_{energy,j+1} \\ res_{mntm,j+1} \\ res_{cont,j+1} \\ \vdots \end{pmatrix} \quad (3.11)$$

Here, $res_{energy,j}$ denotes the residual of the energy conservation equation discretized at grid point j ; similar notation applies to the residuals of the conservation equation for species k ($res_{spec(k),j}$), the momentum conservation equation ($res_{mntm,j}$), and the continuity equation ($res_{cont,j}$).

3.2 Inexact Newton Method

The most basic means of solving nonlinear equations is Newton's method. The solution is approached by iteration; a linear model is constructed at each trial solution to yield a step, or correction, towards a more accurate solution. For a nonlinear system of equations as in (3.9), the Newton step is given by

$$F'(x_k)s_k = -F(x_k) \quad (3.12)$$

where x_k is the current approximate solution and s_k is the step towards the next solution, $x_{k+1} = x_k + s_k$. As defined in the previous section, $F'(x_k)$ is the Jacobian computed at x_k , $F'_{ij} \equiv \partial F_i / \partial x_j$.

Newton's method converges quadratically in the neighborhood of a solution, a desirable feature when the trial solution is accurate. Far away from a solution, however, Newton's method is not robust, converging poorly if at all. Directly solving Equation 3.12 for a Newton step—a computationally expensive undertaking in any large scale problem—is not effective in this situation. Replacing the Newton condition of Equation 3.12, we introduce the more flexible *inexact Newton condition*:

$$\|F(x_k) + F'(x_k)s_k\| \leq \eta_k \|F(x_k)\| \quad (3.13)$$

This modification of the Newton equation is at the core of the Inexact Newton Backtracking (INB) method, developed by Eisenstat and Walker [7].

The key parameter in Equation 3.13 is η_k , known as the forcing term. The inexact Newton condition essentially restates the exact Newton condition from the perspective of an iterative linear solver. An iterative method is used to find an approximate solution to (3.12), and η_k specifies the tolerance to which this solution (s_k) is found. For η_k equal to zero, the Newton condition is solved exactly, reducing Equation 3.13 to Equation 3.12, while as η_k approaches 1, computational effort falls to zero.

Proper specification of η_k can vastly enhance efficiency and convergence of the nonlinear solver. Far away from a solution, where the linear model of Equation 3.12

may poorly describe the nonlinear surface of the function F , it makes little sense to calculate each Newton step exactly. Doing so is computationally expensive and may result in little or no progress toward a solution; indeed, a less accurate solution of (3.12) may be more effective in reducing $\|F\|$. The forcing term is thus chosen close to 1. If the linear model becomes accurate, however, a precise Newton step is likely to provide fast reduction in $\|F\|$; the forcing term is thus chosen close to zero. Explicit formulas governing the choice of η_k at each iteration will be given, but first let us outline the entire Inexact Newton Backtracking algorithm:

Algorithm 3.1 (Inexact Newton Backtracking Method)

Let $x_o, \eta_{max} \in [0, 1)$, $t \in (0, 1)$, and $0 < \theta_{min} < \theta_{max} < 1$ be given.

For $k = 0, 1, \dots$, until convergence:

Choose initial $\eta_k \in [0, \eta_{max}]$ and s_k such that

$$\|F(x_k) + F'(x_k)s_k\| \leq \eta_k \|F(x_k)\|.$$

While $\|F(x_k + s_k)\| > [1 - t(1 - \eta_k)] \|F(x_k)\|$ do:

Choose $\theta \in [\theta_{min}, \theta_{max}]$.

Update $s_k \leftarrow \theta s_k$ and $\eta_k \leftarrow 1 - \theta(1 - \eta_k)$.

Set $x_{k+1} = x_k + s_k$.

This algorithm augments the inexact Newton condition with a globalization known as *safeguarded backtracking*. Sufficient reduction in the norm of F is enforced at the ‘while’ loop; if the step s_k of the inexact Newton condition does not sufficiently reduce $\|F\|$, the step is reduced by a scalar factor θ , essentially ‘backtracking’ along the search direction. Backtracking continues until the condition on $\|F\|$ is met, for in a sufficiently small neighborhood of the trial solution x_k , the linear model must indicate the correct downward path; the Newton equation is consistent. The backtracking process is considered ‘safeguarded’ because limits are placed on the choice of θ , and it is known as a ‘globalization’ because it vastly improves the domain of convergence of Newton’s method. Indeed, in exact arithmetic, the INB algorithm is guaranteed to converge from an arbitrary initial guess unless x_k has no limit points or x_k only has limit points at which F' is singular [7].

As described above, the forcing term η_k is updated at each iteration to reflect the accuracy of the local linear model. Two schemes that provide fast local convergence while minimizing oversolving are given by Pernice and Walker [19]. For the first, we select $\eta_o \in [0, 1)$ and choose subsequent values of η_k as follows:

$$\eta_k = \frac{\| \|F(x_k)\| - \|F(x_{k-1}) + F'(x_{k-1})s_{k-1}\| \|}{\|F(x_{k-1})\|}, \quad k = 1, 2, \dots \quad (3.14)$$

The second scheme updates η_k based on the norm reduction of the previous Newton iteration, a more indirect measure of the accuracy of the local linear model:

$$\eta_k = \gamma \left(\frac{\|F(x_k)\|}{\|F(x_{k-1})\|} \right)^\alpha, \quad k = 1, 2, \dots \quad (3.15)$$

The scaling γ is chosen in $[0, 1]$ and the exponent α is chosen in $(1, 2]$.

In our implementation of the INB method, convergence is declared when $\|F(x_k)\|_2$ or $\|F(x_k)\|_\infty$ falls below a specified tolerance, usually 10^{-9} . Equation 3.14 is typically used to specify the forcing terms, with $\eta_o = 0.5$. The remaining parameters are adjusted arbitrarily to enhance convergence.

3.3 Krylov Subspace Iterative Solver

Iterative solution of the Newton equation (3.12) is a rather large scale problem. For a typical grid of 150 points and a detailed mechanism of 16 species, the Jacobian matrix F' is of dimension $m \approx 3000$. Given that the Newton equation is solved repeatedly in the course of a single time step, an efficient linear iterative method is essential to the performance of the code. Here we turn to a modern class of iterative methods known as Krylov subspace methods, and we develop preconditioners to accelerate their convergence.

3.3.1 BiCGSTAB

Krylov subspace methods are based on the idea of projecting an m -dimensional problem onto a lower-dimensional Krylov subspace [36]. For a linear system $Ax = b$, a Krylov subspace of dimension n is defined as follows:

$$\mathcal{K}_n = \langle b, Ab, \dots, A^{n-1}b \rangle \quad (3.16)$$

At each iteration, the trial solution x_n is chosen from the subspace \mathcal{K}_n ; iteration increases the size of the Krylov subspace and thus the accuracy of the solution. GMRES (*Generalized Minimum Residual*) is probably the simplest and best-known Krylov method, and its workings are illustrative: At each step, Arnoldi iterations construct an orthonormal basis for \mathcal{K}_n . A least-squares approximation then finds the $x_n \in \mathcal{K}_n$ that minimizes the norm of the residual $b - Ax$.

In our implementation of the INB algorithm, we use a variant Krylov subspace method known as BiCGSTAB—*Bi-Conjugate Gradients Stabilized*. The details of this method are more complex, and are left better-described elsewhere [36, 10, 30]. BiCGSTAB is based on Lanczos iteration, which, in contrast to the Arnoldi iterations of GMRES, uses a three-term recurrence relation to construct an orthonormal basis for \mathcal{K}_n . BiCGSTAB does not strictly minimize the residual norm at each iteration, and its convergence is not monotonic. However, it requires less storage space, and in our experience, provides greater numerical stability.

An important attribute of Krylov subspace methods is that they do not operate directly on the matrix A . All that is required is matrix-vector products Ax , making it simple to design procedures that exploit the sparsity of A . For a matrix of dimension m with only ν nonzero entries per row, one can easily compute Ax in $O(\nu m)$ rather than $O(m^2)$ operations. In the context of the INB algorithm, our matrix A is the Jacobian, F' , and a finite-difference formula is used to calculate the product of F' with an arbitrary vector v :

$$F'(x_k)v \approx \frac{1}{2\delta} [F(x_k + \delta v) - F(x_k - \delta v)] \quad (3.17)$$

The scalar perturbation δ is chosen as follows:

$$\delta = \frac{[(1 + \|x_k\|) \epsilon_{mach}]^{1/3}}{\|v\|} \quad (3.18)$$

where ϵ_{mach} denotes machine epsilon.

3.3.2 ILUTP Preconditioning

The inclusion of detailed chemistry in the governing equations (2.32–2.35) creates scalar entries of the Jacobian that span several orders of magnitude relative to one another. Stiffness on the continuous scale thus manifests itself as an extremely ill-conditioned linear algebra problem. Indeed, the condition number $\kappa(F')$ is typically on the order of 10^9 . The convergence properties of BiCGSTAB and other Krylov methods are not completely understood, but it is known that they hinge on the eigenvalue or singular value distribution of the matrix. As a rule of thumb, closely and uniformly distributed eigenvalues produce fast convergence, and an ill-conditioned matrix has a spectrum that is quite the opposite. The question then arises of how to improve the properties of our Jacobian matrix so that BiCGSTAB converges rapidly? In principle, a Krylov subspace method must converge in $n \ll m$ steps if it is to be useful. The answer lies in preconditioning—subjecting the matrix to operations that improve its eigenvalue spectrum from the perspective of the Krylov subspace solver.

The basic procedure of preconditioning is outlined as follows.¹ The linear system $Ax = b$ is replaced by two equations:

$$AM^{-1}y = b \quad (3.19)$$

$$Mx = y \quad (3.20)$$

The Krylov subspace solver is applied to the first equation, while x is calculated from the second. To accelerate convergence of the Krylov solver, M is chosen so

¹Actually, this is just *right* preconditioning. A preconditioner may also be applied on the left ($M^{-1}Ax = M^{-1}b$), or on both sides, to preserve hermitian positive definiteness ($[C^{-1}AC^{-*}] C^* = C^{-1}b$).

that AM^{-1} is not too far from normal and its eigenvalues are clustered; AM^{-1} is the well-behaved matrix that the Krylov solver “sees.” On the other hand, M must also be chosen so that Equation 3.20 is simple to solve. The preconditioner M must lie somewhere between A and I on a spectrum of approximation; choosing $M = A$ or $M = I$ would render Equation 3.20 or Equation 3.19, respectively, equivalent to the original ill-conditioned problem.

The right preconditioner implemented here is based on the idea of *incomplete LU factorization*, ILU for short. An exact LU factorization of a sparse matrix like F' produces two dense matrices L and U ; the replacement of zero entries in F' with nonzero entries in L and U is known as fill-in. Suppose, however, that fill-in were prevented, that \tilde{L} and \tilde{U} could have nonzero entries only where F' was nonzero. Then, \tilde{L} and \tilde{U} are the incomplete LU factors of F' , and

$$M = \tilde{L}\tilde{U} \approx F' \tag{3.21}$$

becomes a useful preconditioner.

Several refinements of ILU factorization have been developed by Saad [30] and published in his SPARSKIT sparse matrix toolkit. Using this package, we implement an ILUTP preconditioner, a more accurate ILU factorization that allows some fill-in. ILUTP preconditioning regulates fill-in in L and U on the basis of two parameters: one, called *lfil*, is the absolute number of fill-in elements that are allowed in each row of L or U ; the second, called *droptol* is threshold value below which a potential fill-in element is set to zero. The ILUTP approach also provides for pivoting, in which the original matrix is permuted to insure diagonal dominance. Details of the ILUTP algorithm are more fully described elsewhere [30].

To improve the stability of the factorization process, we scale each column of the matrix by its 1-norm prior to computing the preconditioner. The entire preconditioning process can now be summarized as follows, where A is understood to be the Jacobian F' :

$$ASP \approx LU \equiv M \tag{3.22}$$

$$Ax = b \longrightarrow$$

$$ASP(LU)^{-1}y = b \quad (3.23)$$

$$S^{-1}P^{-1}LUx = y \quad (3.24)$$

S is a diagonal matrix containing the column-scaling parameters and P is the permutation matrix. The Jacobian is scaled and permuted, then factored into L and U . The original linear problem then consists of solving (3.23) and (3.24). BiCGSTAB is applied to Equation 3.23; in Equation 3.24, S and P are inverted by inspection, and back-substitution is used to invert L and U .

Implementing this preconditioning scheme in the context of the INB algorithm is relatively simple. The preconditioning factors L , U , S , and P are computed and stored at the start of each Newton iteration. The BiCGSTAB algorithm requires only matrix-vector products, specifically the product of $ASP(LU)^{-1}$ with arbitrary vectors z . Equation 3.24 is thus used to compute $v = SP(LU)^{-1}z$, and the output v is sent to Equation 3.17. Applying the preconditioner thus consists of repeatedly inverting Equation 3.24. In practice, the preconditioning factors need not be computed at the start of *each* Newton iteration, as the Jacobian may not change significantly, and preconditioning is, after all, approximate. The optimal frequency for updating the preconditioner rests on a balance of computational times: the additional time required to recalculate L , U , S , and P versus the time this saves by speeding the convergence of BiCGSTAB.

In contrast to the matrix-free formulation of the Krylov subspace solver, computing the preconditioner by the methods described in this section requires an explicit Jacobian. At each preconditioner update, entries of the block-tridiagonal Jacobian are constructed according to the definition, $F'(x_k)_{ij} \equiv \partial F(x_k)_i / \partial x_{k,j}$. Most of these derivatives can be computed analytically, but those involving chemical source terms are computed via finite-difference approximation:

$$\frac{\partial \dot{w}_k}{\partial Y_{k*}} = \frac{\dot{w}_k(T, Y_1, \dots, Y_{k*} + \delta Y_{k*}, \dots, Y_K) - \dot{w}_k(T, Y_1, \dots, Y_{k*}, \dots, Y_K)}{\delta Y_{k*}} \quad (3.25)$$

where δ is usually chosen around 10^{-3} ; here the derivative with respect to species mass fraction was chosen as an example. To compute derivatives of \dot{w}_k analytically would entail decomposing the chemical rate expressions within CHEMKIN—a difficult undertaking—and would compromise the modularity of the code with respect to kinetic schemes. In addition, derivatives of the transport coefficients with respect to T or Y_k cannot be computed easily, since they involve polynomial approximations within CHEMKIN for C_p . These derivatives are omitted from the explicit Jacobian; the resulting inaccuracy is generally insignificant, since L and U are approximate factors.

3.4 Initialization Conditions

Despite the robust convergence properties of the INB method, it will not converge quickly from a completely arbitrary profile. At every time step, the Newton solver requires a starting point for its iterations, an initial guess x_o . Ingenuity in creating these initialization conditions can yield large computational savings. We analyze this process in two cases: creating a starting condition for the code at $t = 0$, and selecting the initial guess at each time step while the code is running, i.e., for $t > 0$.

3.4.1 Starting Case

When applying the elemental flame code to a new chemical mechanism or a new flame configuration, an initial solution vector is assembled to approximate the expected flame structure as closely as possible. This guess is both x at the $n = 0$ time step and the initial guess for $x^{n=1}$. A reasonable procedure for creating such an initial guess is as follows: Hyperbolic tangent functions are used to approximate $T(y)$, $U(y)$, and the mass fraction profiles of major species. Gaussians are used to approximate the profiles of minor species. In a premixed flame, an equilibrium code such as STANJAN provides product-side boundary conditions on T and Y_k , and in all cases, a steady-state version of the continuity equation (2.35) is integrated to find V . The thickness and height of each profile must be estimated based on knowledge of the

kinetic mechanism and of typical flame structure at the desired strain rate.

Clearly, this ad hoc scheme cannot predict the flame structure very closely. To create a more accurate starting condition for the elemental flame, the initial guess is subjected to a *continuation* scheme for gradually introducing the chemical source terms. Chemistry is the root of stiffness in the governing equations, and thus is the primary cause of difficult convergence. The continuation scheme places damping terms—arbitrary scalar factors θ —in front of the chemical source terms in the energy and species equations (2.33 and 2.32), converting the elemental flame into a weakly-reacting or non-reacting mixture as follows:

$$\rho \frac{\partial Y_k}{\partial t} + V \frac{\partial Y_k}{\partial y} - \frac{\partial}{\partial y} \left(\frac{1}{Le_k} \frac{\lambda}{C_p} \frac{\partial Y_k}{\partial y} \right) - \theta \dot{w}_k W_k = 0 \quad (3.26)$$

$$\rho \frac{\partial T}{\partial t} + V \frac{\partial T}{\partial y} - \frac{1}{C_p} \frac{\partial}{\partial y} \left(\lambda \frac{\partial T}{\partial y} \right) - \theta \sum_k \frac{\dot{w}_k h_k}{C_p} = 0 \quad (3.27)$$

The initial guess is used to start the code in a weakly-reacting form, and as time integration proceeds, the damping terms θ are gradually increased to unity. Once the solution vector reaches steady-state, it becomes a physically accurate starting case.

The continuation scheme typically begins with damping terms on the order of 10^{-3} and brings them to 1.0 in about 10 ms of integration. Precise values depend on the stiffness of the kinetic scheme, the accuracy of the initial guess, and the flame time scale.

3.4.2 Mass Flux Projection Method

When $t > 0$, creating the initial guess for the solution vector at each time step is much simpler; the initial guess at $t = n+1$ is just x^n . This procedure creates difficulty in the case of unsteady strain, however. Recall that to aid in discretization, the boundary condition on V is imposed at $y = -\infty$. The strain rate ϵ can easily vary one or two orders of magnitude in a given simulation, however; such a change in strain, with a fixed boundary value on the mass flux through the flame, causes the flame to translate rapidly with respect to the grid. The flame nears the boundary of the

computational domain, and successive regriddings become necessary. This outcome is not only cumbersome, but computationally taxing; when the flame translates quickly, x^n is a poor guess for x^{n+1} .

To avoid this situation while retaining the boundary condition $V(y = -\infty)$, we implement a projection method to update the mass flux profile in the case of unsteady strain. At the start of time step $n + 1$, an initial guess for V^{n+1} is obtained by integrating the continuity equation with ϵ^{n+1} , U^n , and ρ^n :

$$\frac{\rho_j^n - \rho_j^{n-1}}{\Delta t} + \frac{V_j^{n+1, guess} - V_{j-1}^{n+1, guess}}{h_{j-1}} + \rho_j^n U_j^n \epsilon^{n+1} = 0 \quad (3.28)$$

In one step, this projection updates the boundary value on V at $y = -\infty$ and generates a new guess for V^{n+1} . Updating the boundary value on V minimizes flame translation for fast convergence.

Chapter 4

Steady-State Validation

The numerical solution of the elemental flame assembles a number of novel mathematical techniques. Before the resulting code is applied to problems of flow and mixture inhomogeneity, it is important to model a standard, well-understood flame configuration and check the accuracy of the results, thus validating the numerical methods, the transport model, and the underlying formulation of the elemental flame. This chapter presents a direct comparison of the elemental flame code with Sandia's steady-state OPPDIF (Opposed Flow Diffusion Flame) solver; both codes are used to compute the detailed structure of a strained, premixed methane-air flame.

4.1 OPPDIF Formulation

OPPDIF is designed to compute the steady-state structure of an axisymmetric flame between two opposed nozzles, as shown in Figure 4-1. Though its name suggests otherwise, OPPDIF models reacting flow between two jets of arbitrary composition; thus premixed combustion may be represented in both single-flame and two-flame configurations. The flow conditions are defined by the distance between the two nozzles and the mass flux of each species through each nozzle, along with the density of each stream. The flow leaving each nozzle is divergence-free, i.e., the radial velocity component at the nozzle equals zero. A similarity solution reduces this two-dimensional flow to a single dimension, along the centerline. The resulting governing equations

form a two-point boundary value problem. To satisfy the radial momentum equation, the radial pressure gradient $\frac{1}{r} \frac{\partial p}{\partial r}$ is constant across the domain; it must be computed as an eigenvalue. Further detail on this formulation may be found in [15].

The OPPDIF formulation differs significantly from that of the elemental flame, which imposes an outer flow solution for stagnation flow from a point source at minus-infinity onto a compressible boundary layer. The elemental flame uses a single strain rate, useful in parametrizing solutions for flamelet modeling, but *imposes* no length scale on the problem. (The only length scale is the flame thickness, and this value is calculated, not imposed.) In contrast, the OPPDIF formulation imposes a length scale—the nozzle separation—but does not define a characteristic strain; a strain must be backed out of the final solution. This formulation is better suited to modeling the experimental configurations actually used to study strained laminar flames, which physically do create a stagnation plane between opposed jets of uniform flow. A detailed discussion contrasting one- and two-parameter formulations for the strained laminar flame may be found in [34, 12].

The species transport model used in OPPDIF is more detailed than that of the elemental flame (see §2.3.1). At each point in the domain, OPPDIF computes diffusion velocities by a multicomponent formulation; thermal diffusion velocities are not neglected. For the purposes of comparison, both OPPDIF and the elemental flame code are run with Smooke's 46-reaction C1 mechanism (Table 2-1), however. The kinetic scheme has too important an effect on flame structure not to be conserved in the comparison.

OPPDIF uses a finite-difference discretization on a uniform grid, reserving up-wind differencing for convective terms, as in the elemental flame. Several iterations are necessary to obtain a well-resolved solution, however. OPPDIF is first made to converge on a coarse grid, then this solution is used as the starting condition on a finer grid. Successively finer grids, typically three or four, are introduced until the reaction zone of the flame is clearly resolved.

4.2 Comparison of Results

Though OPPDIF does not model a true stagnation point flow, the flow field local to the stagnation plane approaches that of a stagnation point. The strain rate effectively applied to the flame is found by examining the axial velocity profile immediately ahead of the flame, on the reactants side. Before any expansion due to burning has occurred, the “cold” hydrodynamic strain is obtained from the usual relation:

$$\epsilon = -\frac{\partial v}{\partial y} \quad (4.1)$$

Figure 4-2 shows the velocity profile v for both an OPPDIF solution and the elemental flame, where both codes have been used to compute an axisymmetric premixed flame at a strain rate of 100 s^{-1} . The common centerline coordinate has been defined such that both flames reach their stagnation point at $y = 0$. Note that the slopes $\partial v/\partial y$ are identical immediately ahead of the flame, where expansion is then manifested as a sharp rise in axial velocity. The strain rate of 100 s^{-1} was imposed *a priori* on the elemental flame, but achieved through an appropriate choice of nozzle velocities and nozzle separation for the OPPDIF flame.

Of course, the strain fields of the two flames cannot match over the entire domain. The strain rate in the OPPDIF flame must equal zero at the nozzles, where flow is divergence-free, and rise towards the center of the domain due to both expansion within the flame and hydrodynamic, stagnation point, effects. This expectation is borne out in Figure 4-3, where the dimensionless U of the elemental flame is plotted along the common centerline coordinate together with a U for the OPPDIF solution. The equivalent U for the OPPDIF solution is defined as follows:

$$U = \frac{1}{\epsilon} \left(\frac{u}{r} \right)_{r=0} \quad (4.2)$$

where ϵ is our reactants-side strain, 100 s^{-1} .

Now let us examine the temperature and species profiles through the flame region. Figure 4-4 shows temperature and selected major species in both flames, with the

heat release rate in the elemental flame plotted for reference. In this plot and in subsequent plots of flame structure, the OPPDIF flame has been shifted with respect to its coordinate so that it lies directly on top of the elemental flame; a point along the rise of each temperature profile was used to select the appropriate translation. Because of differences in the flow fields of the two flames, the elemental flame sits further from the stagnation point. This does not factor negatively in our comparison; it is the *local* structures and the burning velocities of the flames that we expect to agree.

Indeed, close agreement is observed in the temperature and major species profiles of the OPPDIF solution and the elemental flame. The temperature profile is characteristic of the premixed flame: a fast rise in the peak reaction zone, followed by a slower rise as CO oxidation proceeds. Figure 4-5 extends the comparison to selected minor species. Again, close agreement of profile shape, peak value, and peak location is observed between the two models. The peak in Y_{CH_2O} occurs ahead of the peak in Y_{OH} , since CH_2O is formed earlier in the breakdown of methane. Small and persistent differences in species mass fraction on the products side of the flame may be due to the fact that the products stream composition in the OPPDIF flame deviated slightly from equilibrium.

In sum, the steady-state flame structure predicted by the elemental flame code matches well with that of a well-benchmarked model. Differences in the profiles can be attributed to the distinct flow fields of the two flames, as well as differences in the transport models and in grid spacing. It is significant, particularly in the context of the next chapter, to note that detailed agreement between combustion in the pure stagnation point flow and combustion in the more experimentally realistic opposed-jet flow was obtained by matching strains at the reactants-side leading edge of the flame.

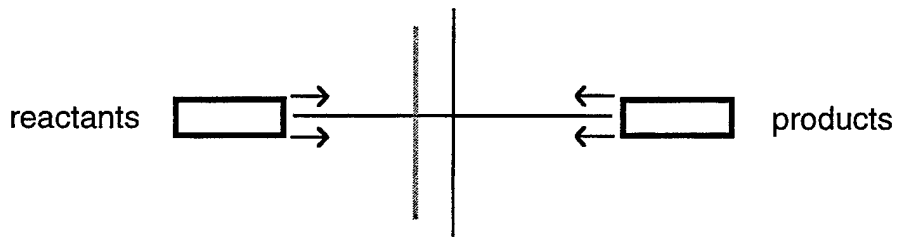


Figure 4-1: Flow configuration modeled by OPPDIF.

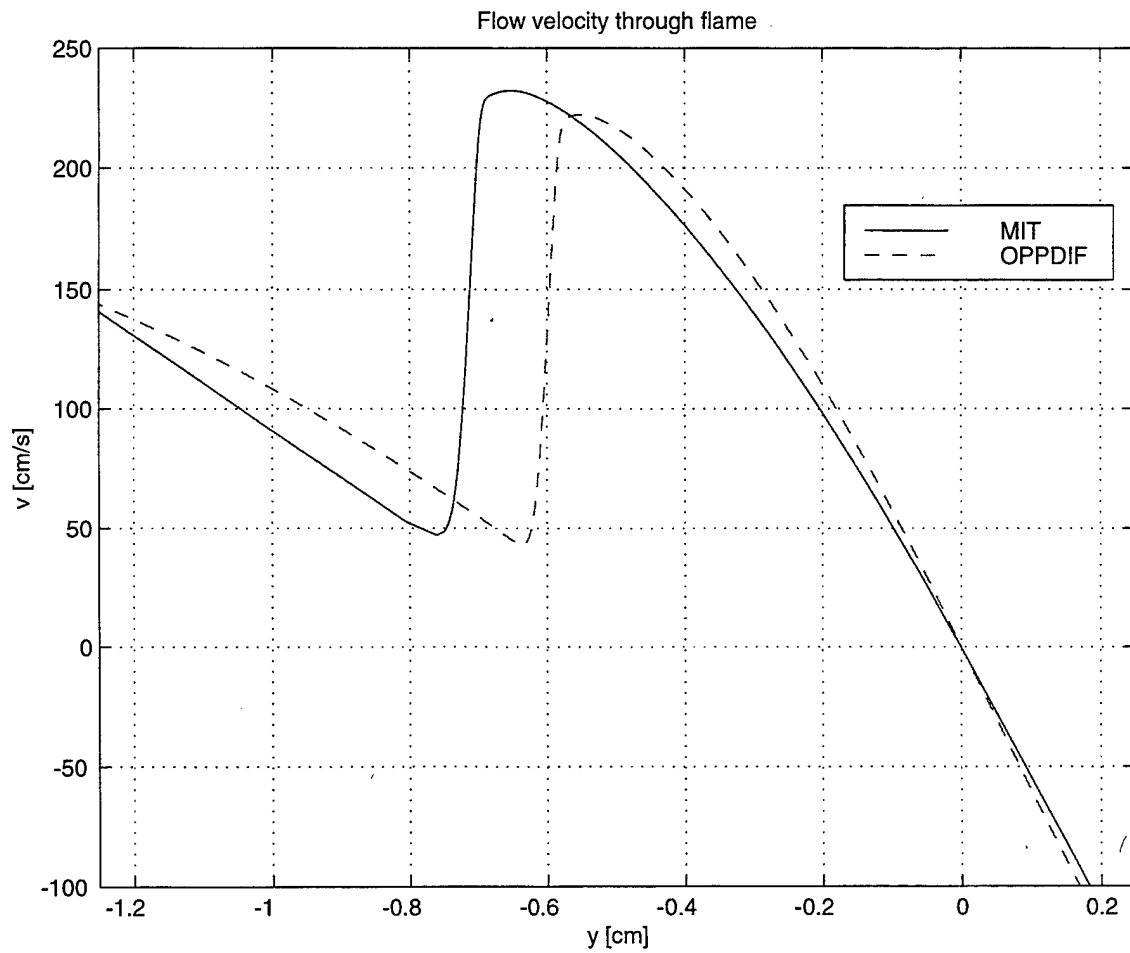


Figure 4-2: Flow velocity through the flame, elemental flame code vs. OPPDIF.

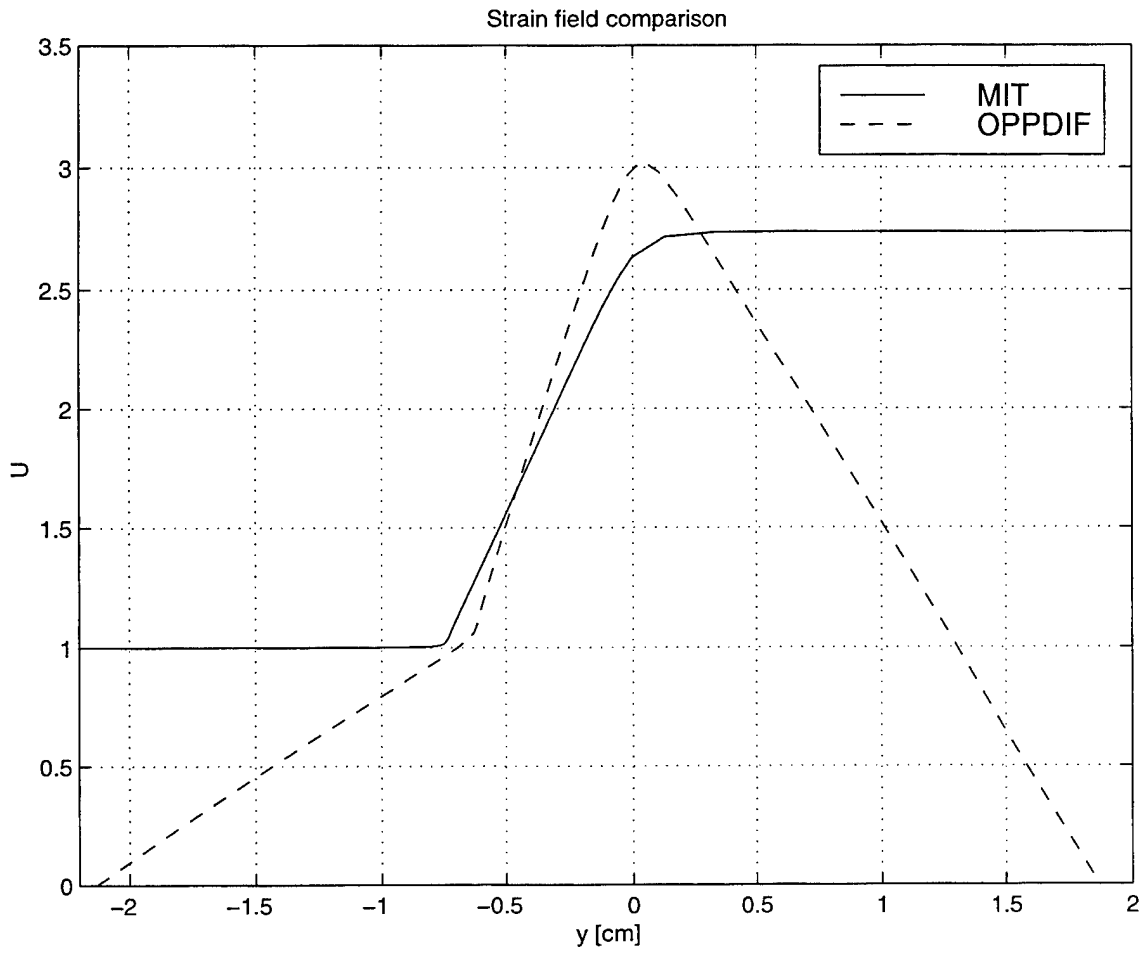


Figure 4-3: Distribution of effective strain, elemental flame code vs. OPPDIF.

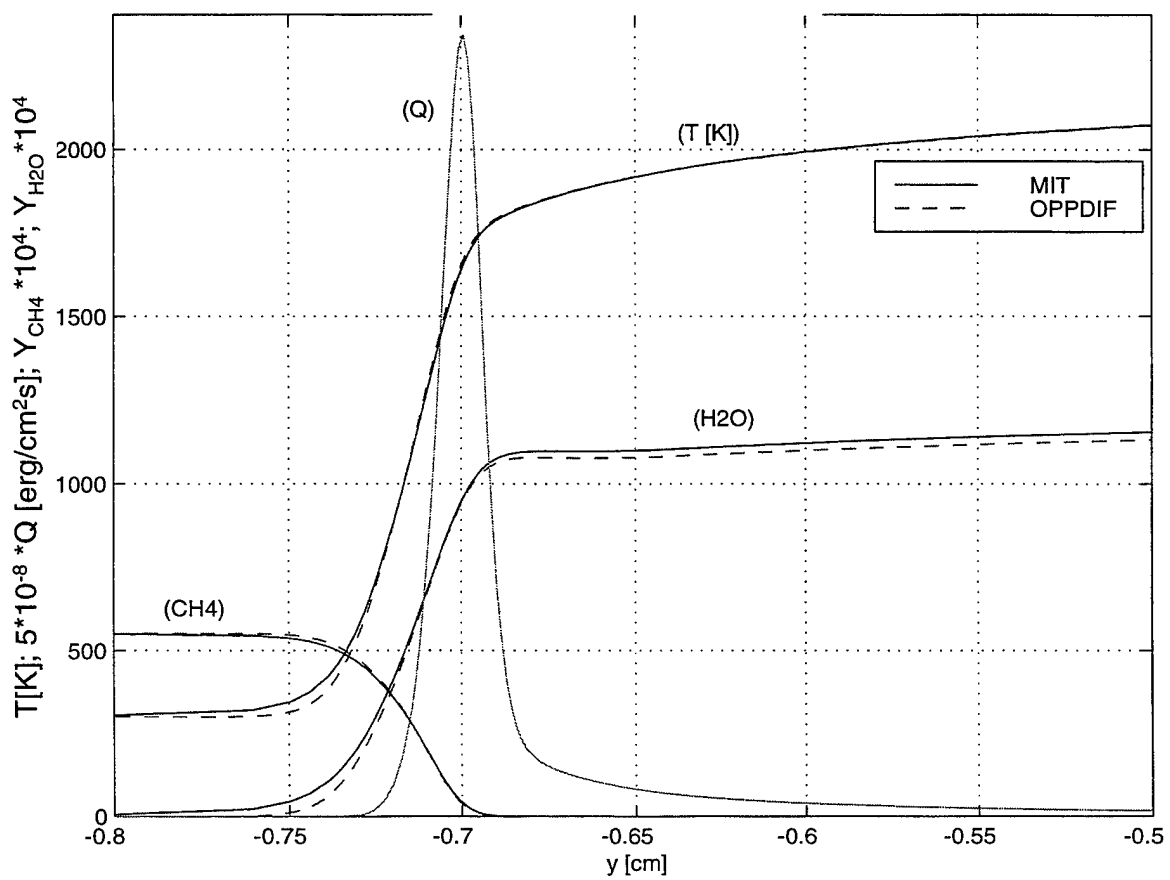


Figure 4-4: Temperature and major species profiles in the flame region, elemental flame code vs. OPPDIF.

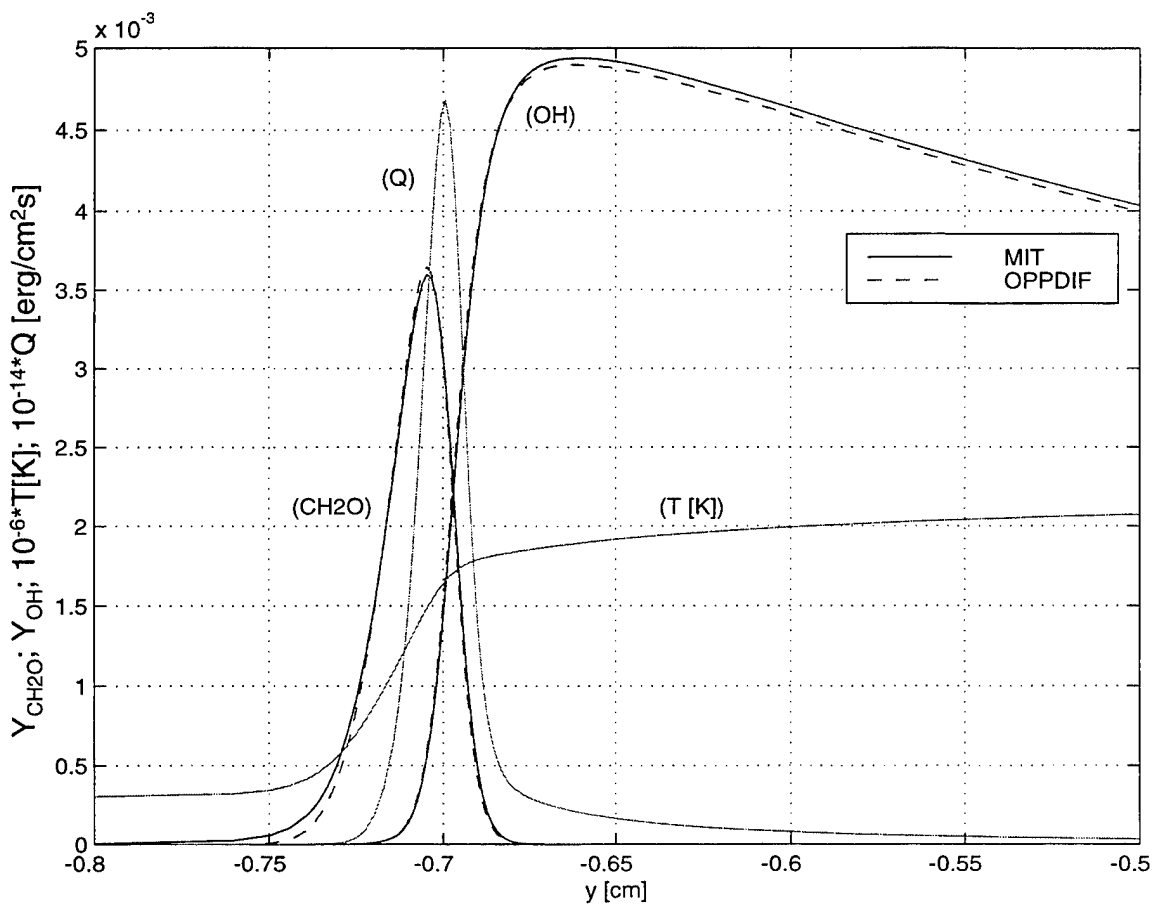


Figure 4-5: Minor species profiles in the flame region, elemental flame code vs. OPPDIF.

Chapter 5

Unsteady Applications

Our focus now returns to the modeling of flow and mixture inhomogeneities. The combustion zone model developed in the preceding chapters is used to examine and expand upon the fundamental unsteady interactions presented in Chapter 1. For clarity, two broad regimes of unsteadiness are treated in separate examples. The first, unsteady variation in equivalence ratio, is presented in terms of the burning of a stratified mixture. The second, unsteady variation in strain, is set in the environment of two-dimensional premixed turbulent combustion: the elemental flame is used to model the burning and structure of a flame surface interacting with a vortex. Because this example effectively tests the ability of a subgrid model to capture a complex turbulent interaction, its analysis holds important implications for the flame embedding technique described in §1.1.

5.1 Burning in a Stratified Mixture

Fast temporal or spatial stratification of a reacting mixture is present in numerous practical phenomena. One of these phenomena is combustion instability, as described in §1.3; another is burning in a direct-injection engine, where the equivalence ratio of the mixture decreases away from the fuel injection port. The goal of this section is to develop a computation that captures the essential features of both of these phenomena, one that answers the following question: how does a temporal change in

ϕ on the order of a flame time scale affect flame structure and burning?

We begin by choosing a strain rate of 300 s^{-1} , a reasonable value for burning in an internal combustion engine [38]. To simulate propagation through a stratified mixture, a change in equivalence ratio from 1.0 to 0.6 is imposed on the reactants stream. Temporal and spatial stratification are rendered equivalent by the Lagrangian frame of the elemental flame; the model simply follows the flame surface as new mixture is encountered.

In the elemental flame model, control of the reactants stream composition comes from the boundary condition on Y_k at $y = -\infty$. An imposed $\phi(t)$ at this boundary will not produce the same change $\phi(t)$ at the flame, however. The flame typically sits some distance away from the edge of the computational domain, so changes in ϕ at the boundary will be subject to a propagation delay as they travel to the flame; during this propagation, the change in ϕ will also be smoothed out via diffusion. The stagnation flow geometry thus makes it difficult to impose an exact $\phi(t)$ on the flame. Fortunately, there is no restriction on the location of the reactants-side edge of the computational domain. To impose a $\phi(t)$ at the flame, the computational domain is resized so that the $y = -\infty$ boundary occurs precisely at the flame's leading edge, thus avoiding the difficulties of propagation delay and its associated diffusion. The leading edge of the flame is defined at the initial rise of the temperature profile. This shortened computational domain can be seen in Figures 5-4 through 5-7.

A second challenge in modeling propagation of the strained flame lies in defining the composition of the products stream. The choice of products-side boundary condition is aided by two physical interpretations: If the products mixture behind the propagating flame is well-mixed, then its composition will not change appreciably during a perturbation in ϕ . This leads to constant boundary conditions on T and Y_k at $y = \infty$, corresponding to, for instance, the products of combustion at $\phi = 1.0$. For reasons that will become clear in §5.1.2, this case is known as the back-supported flame. If, on the other hand, the products mixture is not well-mixed—if it is itself stratified—then the products-side of the flame will be affected only by the instantaneous products of burning. Now the products stream composition must be updated

to reflect the changing reactants-side ϕ ; such a flame is deemed to lack back-support.

5.1.1 Dynamic Effect of Equivalence Ratio Variation

Before investigating differences in burning with and without back-support, we focus on the dynamic effect of equivalence ratio variation—how a flame responds to changing ϕ , and how the time scale of this change affects the response. Figure 5-1 shows the heat release rate histories $\dot{Q}(t)$ of two back-supported flames, both subject to the same absolute change in ϕ , as chosen in the discussion above ($\phi = 1.0 \rightarrow \phi = 0.6$). The solid line corresponds to a linear change in ϕ over a 10 ms period, while the dashed line results from a linear change in ϕ over 2 ms. As expected, both flames reach the same steady-state rate of heat release. For reference, the linear changes in ϕ are plotted on the same scale.

The heat release rate $\dot{Q}(t)$ corresponding to the faster change in ϕ exhibits a greater degree of unsteadiness than its slower counterpart. At the end of the 2 ms change, \dot{Q} has traversed only 40% of its total range; this behavior is not surprising, since 2 ms is approximately a flame time scale. The asterisks in Figure 5-1 represent the steady-state heat release rates corresponding to the same 2 ms change in ϕ , underscoring the fact that the response of the flame to this fast change in ϕ is not steady-state. The heat release rate corresponding to the 10 ms change in ϕ , however, is more quasi-steady; at the conclusion of the ϕ change, only a 10% correction in heat release rate is observed.

5.1.2 Back-support of the Elemental Flame

Updating the composition of the products stream for the non-back-supported flame presents difficulties similar to those encountered in updating the composition of the reactants stream. The flame ordinarily sits far from the products-side boundary, leading to propagation delay and diffusion of the mixture conditions imposed at the products stream. To avoid these problems, the $y = \infty$ boundary cannot be placed arbitrarily, however; consistency with respect to the boundary conditions (Equations 2.29–2.30)

dictates that the computational domain must extend to the point where gradients on U relax to zero. Here, then, is where the mixture boundary conditions are imposed. Based on an interpolation table of equilibrium values for combustion at a given reactants-side ϕ , T and Y_k are updated¹ to reflect the appropriate stream of burned products.

How to time these updates of the products mixture is yet another matter. The mixture should reflect the instantaneous products of burning, but dynamic effects insure that the instantaneous burning is not determined by the current reactants-side ϕ . A reasonable, though approximate, solution to this problem is constructed as follows. The composition of the products stream should reflect burning at an equivalence ratio—call this ϕ_b —equal to the equivalence ratio ϕ_r imposed on the reactants side of the flame *one flame time scale earlier*. For simplicity, we choose a fixed flame time scale, here equal to 2 ms, though in reality the flame time scale will itself change with ϕ_r and ϕ_b .

Using this construction, the effect of back-support is examined by again applying a 10 ms change in ϕ_r from 1.0 to 0.6. Heat release rates for both the back-supported and non-back-supported flame are plotted in Figure 5-2. The products side ϕ_b follows the same linear path as ϕ_r , merely shifted forward in time by 2 ms. Back-support strengthens the burning in the flame, and the flames reach appreciably different steady-state heat release rates. Note that the heat release history of the non-back-supported flame equilibrates more slowly because its product side boundary conditions continue to change until $t = 12$ ms, one flame time scale after the change in ϕ_r is complete.

Figure 5-3 uses the same time-dependent calculations but plots the heat release rates in terms of ϕ_r , emphasizing that the effect of back-support is not inherently a dynamic one. Each \dot{Q} is really a function of both ϕ_r and ϕ_b ; for the back-supported flame, ϕ_b is always 1.0, while for the non-back-supported flame, ϕ_b lags behind ϕ_r but follows it. Thus the divergence of paths as ϕ_r approaches 0.6: the difference in ϕ_b between the two flames is increasing. The convergence of data points into vertical

¹ U is also updated, indirectly, through Equation 2.30.

groups at $\phi_r = 0.6$ occurs as heat release rates settle from their dynamic values to equilibrium.

Understanding the mechanism of back-support requires an examination of flame structure. Figures 5-4 through 5-7 show temperature and Y_{OH} profiles for the 10 ms change in ϕ_r . Six profiles are shown in each plot, beginning at $t = 0$ and separated by 3 ms intervals. Focusing first on the temperature profiles of the back-supported flame, one can identify high-temperature points at which the slope of the profile sharply decreases; these points generally correspond to the temperature in the reaction zone of the flame. Thus as ϕ_r decreases, the reaction zone temperature decreases, an effect consistent with trends observed in \dot{Q} . However, as the reaction zone temperature decreases, the slope on the products side of the reaction zone increases. A diffusive heat flux from the high-temperature, $\phi_b = 1.0$ products stream feeds the reaction zone. In the non-back-supported flame (Figure 5-5), this heat flux is not present. As the reaction zone temperature drops, the products-stream temperature drops accordingly. No high-temperature reservoir of heat is present to strengthen the flame.

The burning of the back-supported flame may also be enhanced by radicals in the products stream, an effect examined with regard to OH in Figures 5-6 and 5-7. The concentration of OH is certainly higher in the reaction zone of the back-supported flame than in the reaction zone of the non-back-supported flame. This could be due to the higher temperature of the back-supported reaction zone, but it may also result, in part, from a change in diffusive fluxes. The concentration of OH in the products stream falls with ϕ_b , and the diffusive flux of OH out of the reaction zone into the products may thus be larger in the non-back-supported flame than in the back-supported flame. This significance of this mechanism is not clear from the given data. Plotting the profile of each term in the OH species conservation equation—reaction and diffusion, in particular—would elucidate the effects of radical back-support.

It is important to note that in all the plots of flame structure (Figures 5-4 through 5-7), the flame tends to shift slightly over time with respect to the computational grid. The location of the reactants-side and products-side boundaries remains fixed in time, however; though initially chosen to closely surround the flame, as described above,

the current formulation does not update the boundary coordinates to account for flame movement. The total range of flame movement does not exceed 0.25 mm, so this inaccuracy is probably quite negligible.

5.2 Unsteady Strain in a Flame-Vortex Interaction

The impact of flow inhomogeneity on burning is studied in the context of the flame-vortex interaction of Figure 1-1. The figure shows four snapshots, separated by 1 ms intervals, of a counterrotating vortex pair moving towards a freely propagating premixed flame. Since the domain is symmetric, only the left half of the interaction is shown. The grayscale indicates temperature and the contour lines indicate vorticity. As discussed in §1.1, the flame surface is stretched and reshaped by the vortex. Data for this figure comes from a direct numerical simulation of two-dimensional reacting flow, performed with detailed chemistry and transport [17, 16].

Now consider the flame element on the centerline of the flame-vortex interaction. As the vortex approaches, strain on the flame element rapidly increases and the burning rate changes as a result. We would like to model the time-dependent burning of this flame element using our elemental flame, thus testing the applicability of the elemental flame as a subgrid model as well as its ability to capture the effects of unsteady strain.

5.2.1 Matching the Leading Edge Strains

The primary input to the elemental flame model must be the strain history of the flame element at the centerline of the two-dimensional simulation. A natural idea is to match the strain at the reactants-side leading edge of the two-dimensional flame with the leading edge strain (ϵ) of the elemental flame. According to the flamelet hypothesis, we should expect the profiles in the elemental flame and the profiles normal to the two-dimensional flame surface to have similar structures; this structural similarity includes profiles of strain (or ϵU , in the elemental flame case). Also, matching of the leading edge strains led to favorable comparison of the elemental flame with

OPPDIF.

The strain tangential to a 99% contour of Y_{CH_4} is thus extracted from the centerline of the flame-vortex interaction. This contour is a reliable indicator of the flame leading edge, so it follows the flame element in a Lagrangian sense. The leading edge strain history is plotted as the solid line in Figure 5-8. This strain and its corresponding Karlovitz number rise 1.6 orders of magnitude over a period comparable to the time scale of the premixed flame. The burning of the flame element clearly will not respond quasi-steadily.

With an input strain history $\epsilon(t)$ in hand, the elemental flame requires only a starting condition and appropriate mixture boundary conditions matching those in the flame-vortex interaction. The premixed flame in the flame-vortex interaction is a stoichiometric methane-air flame with an additional 20% N_2 dilution by volume present in both the reactants and products. This dilution lowers the adiabatic flame temperature from 2230 K to approximately 1900 K, thus reducing the burning rate and lengthening the flame time scale. Dilution is included in the flame-vortex calculation both to reduce the stiffness of the chemistry and to amplify the effects of unsteady strain. Mixture boundary conditions on the elemental flame reflect this dilution but remain fixed in time. Smooke's 46-reaction mechanism (Table 2-1) is used in computing both the flame-vortex interaction and evolution of the elemental flame. The flame-vortex interaction uses a more detailed transport model, identical to that of OPPDIF, but in light of §4.2, the resulting discrepancy should be minimal.

The computed heat release rate of the elemental flame, obtained by matching the leading edge strain histories, is shown by the solid line in Figure 5-9. Circles represent the heat release rate of the two-dimensional flame element, computed by integrating \dot{w}_T along the centerline coordinate of Figure 1-1. Note that the comparison of heat release rates does not extend past $t = 4$ ms; beyond this time, the vortex in the two-dimensional simulation comes within a diameter of the convective boundary conditions at the top of the domain, and the results become numerically questionable. The heat release rate falls with increasing strain in both the one-dimensional (elemental flame) and two-dimensional results—an expected trend—but the elemental

flame clearly underpredicts the heat release rate at the two-dimensional flame surface. This discrepancy widens at higher strains and larger times; the elemental flame even undergoes quenching near $t = 3.5$ ms.

Underprediction of \dot{Q} suggests that the strain in the elemental flame is too high in comparison to that of the two-dimensional flame element. Suspicion of such a strain mismatch is confirmed in Figure 5-10. Here, the solid line represents the strain profile across the centerline element of the two-dimensional flame surface at $t = 2$ ms; the open circle indicates the location and strain of the flame leading edge. The average strain in this flame element, particularly the strain around the reaction zone (indicated by \dot{w}_T), is significantly lower than the leading edge strain. Indeed, the strain rate generally seems to fall when moving across the flame from reactants to products, excepting a small hump around the reaction zone. This strain profile differs markedly from that of the elemental flame, as exemplified in Figure 4-3. Strain in the elemental flame rises due to expansion in the reaction zone—from a reactants-side value of ϵ to a products-side value of ϵU_b .

An explanation for the unusual strain profile in the two-dimensional flame element is advanced as follows. Ahead of the flame in Figure 5-10, the strain is observed to decay quite rapidly. This strain profile comes only from the vortex (which sits to the left of the figure boundary), not from the flame. Extrapolating this non-reacting strain into the flame region, the dashed line continues to represent the strain profile in the absence of reaction, due only to decay around the vortex. The vortex-induced non-reacting strain is in a sense the *underlying strain* in the flame region. Expansion within the flame *adds* to the underlying strain to produce the measured strain profile (the solid line), but the underlying decay in strain insures that the measured strain falls towards the products side.

This flame-vortex interaction may thus be on the boundary of the flamelet regime. The strain imposed by the vortex on the flame is varying over the length scale of the flame, while an essential flamelet assumption is that the flame should be thin with respect to length scales in the flow. In the elemental flame, developed under these flamelet assumptions, the underlying strain is constant and equal to ϵ , for in the

absence of reaction, the velocity field would collapse to that of a pure stagnation point flow.

5.2.2 Matching Average Strains

Though the flame-vortex interaction of Figure 1-1 may not be an ideal test case for the flamelet concept, it still represents a flow regime of practical importance. A correction is thus proposed to extend the accuracy of our subgrid model. Rather than matching strains at the leading edges, the *average strain* in the two-dimensional flame element should be matched to the average strain in the elemental flame.

The average strain in the elemental flame, $\bar{\epsilon}_{1d}$, is defined arithmetically

$$\bar{\epsilon}_{1d} = \epsilon \left(\frac{1 + U_b}{2} \right) \quad (5.1)$$

where ϵ is the usual reactants-side strain. (Use of the geometric mean was also investigated, but found to give less accurate results.) Two methods are proposed for extracting the two-dimensional average strain, $\bar{\epsilon}_{2d}$. The first method supposes the average strain to equal the strain at the heat release peak. Because the 10% contour of Y_{CH_4} has been found to follow the heat release peak fairly closely [17], the strain tangent to the 10% contour of Y_{CH_4} is extracted from the centerline and deemed the ‘center’ average. The second method for extracting $\bar{\epsilon}_{2d}$ takes the arithmetic mean of two strains at each timestep: the leading edge strain, again calculated at the 99% contour of Y_{CH_4} , and the trailing edge strain, calculated at the 90% contour of Y_{CO_2} . This mean value is deemed the ‘two-point’ average strain. Both of the resulting strain histories $\bar{\epsilon}_{2d}(t)$ are shown in Figure 5-8. To confirm that the 10% contour of Y_{CH_4} does indeed follow the reaction zone center, the figure plots \times marks periodically, denote the strain directly measured at the \dot{w}_T maximum. The 10% criterion matches well with these marks, slightly overestimating the center strain only for $t > 3$ ms.

The elemental flame requires the reactants-side strain ϵ as an input to each time step. The inversion of Equation 5.1 to calculate ϵ from $\bar{\epsilon}_{1d} = \bar{\epsilon}_{2d}$ is not as straightforward as it may seem, however. For unsteady strains, U_b is a function of ϵ and $\frac{1}{\epsilon} \frac{\partial \epsilon}{\partial t}$,

according to the instantaneous solution of the ODE in Equation 2.30. Consequently, Equations 5.1 and 2.30 must be combined to yield a single ODE, which is then integrated implicitly to find U_b from $\bar{\epsilon}_{1d}(t)$. The solution for U_b is substituted back into Equation 5.1 to yield ϵ .

Outputs from the elemental flame code obtained by matching the average strain histories are shown in Figure 5-9. The dashed line, corresponding to the center average, tends to overpredict the heat release rate at initial times, implying that the heat release peak may under-represent the optimal strain. The dash-dotted line, corresponding to the two-point average, shows closer agreement with the actual two-dimensional heat release rate, diverging only at high strains and large time. In general, both methods of defining the average strain on the two-dimensional flame surface and matching it to the average strain on the elemental flame show a marked improvement over the matching of leading edge strains explored in the previous section.

To illustrate the unsteady response of burning to these rapid changes in strain, steady-state reference points are included in Figure 5-9. These points, computed with the elemental flame, are the steady-state values of the heat release rate at average strains corresponding to the instantaneous two-point averages extracted from the two-dimensional simulation. For $t \geq 3.5$ ms, burning persists under the dynamically applied strain, though at steady-state the flame would have undergone quenching. With the average strain as an input, the elemental flame model captures this important unsteady effect.

Figure 5-11 compares the instantaneous structure of the elemental flame using the two-point average with the structure of the two-dimensional flame; both sets of profiles are taken at $t = 2$ ms, where the heat release rates match closely. This comparison highlights the inherent difficulty of making the elemental flame exactly predict the two-dimensional burning. Though the average strains in the two flame regions are equal, the strain distributions are profoundly different. Disagreement in the strain distributions causes the remaining scalar profiles to differ in shape, as demonstrated here by the temperature. These differences in shape in turn affect the diffusive fluxes, which feed into the complex mechanics of the reaction zone.

It is notable that the strain at center of the reaction zone, i.e. at the peak of \dot{w}_T , did not provide the best characterization of the two-dimensional burning. This result is tempered by the fact that strain at the *true* reaction zone center falls below our continuous strain history at later times. Still, examining all the computed burning rate histories in light of the two-dimensional flame structure suggests a path to more accurate application of the elemental flame: as strain on the premixed flame increases, the reaction zone moves further into the products side, where in the two-dimensional flame, the strain is lower. Overprediction of the strain at $t > 3$ ms may really be a symptom of overpredicting the strain at higher strains. A weighted average of strain over the reaction zone, always following the reaction zone in time, may thus provide the best characterization of two-dimensional burning. Weighing the strain over the entire reaction zone rather than just at its peak should better capture the diffusive fluxes feeding chemical reaction and perhaps avoid overestimating the burning at low strains.

Finally, an important addition to this analysis would involve applying the elemental flame subgrid model to a flame surface strained by a weaker vortex—a vortex for which the length scale of the underlying strain rate variation is large. Equivalently, one could examine slices of the current two-dimensional flame surface farther from the vortex than the centerline flame element examined here.

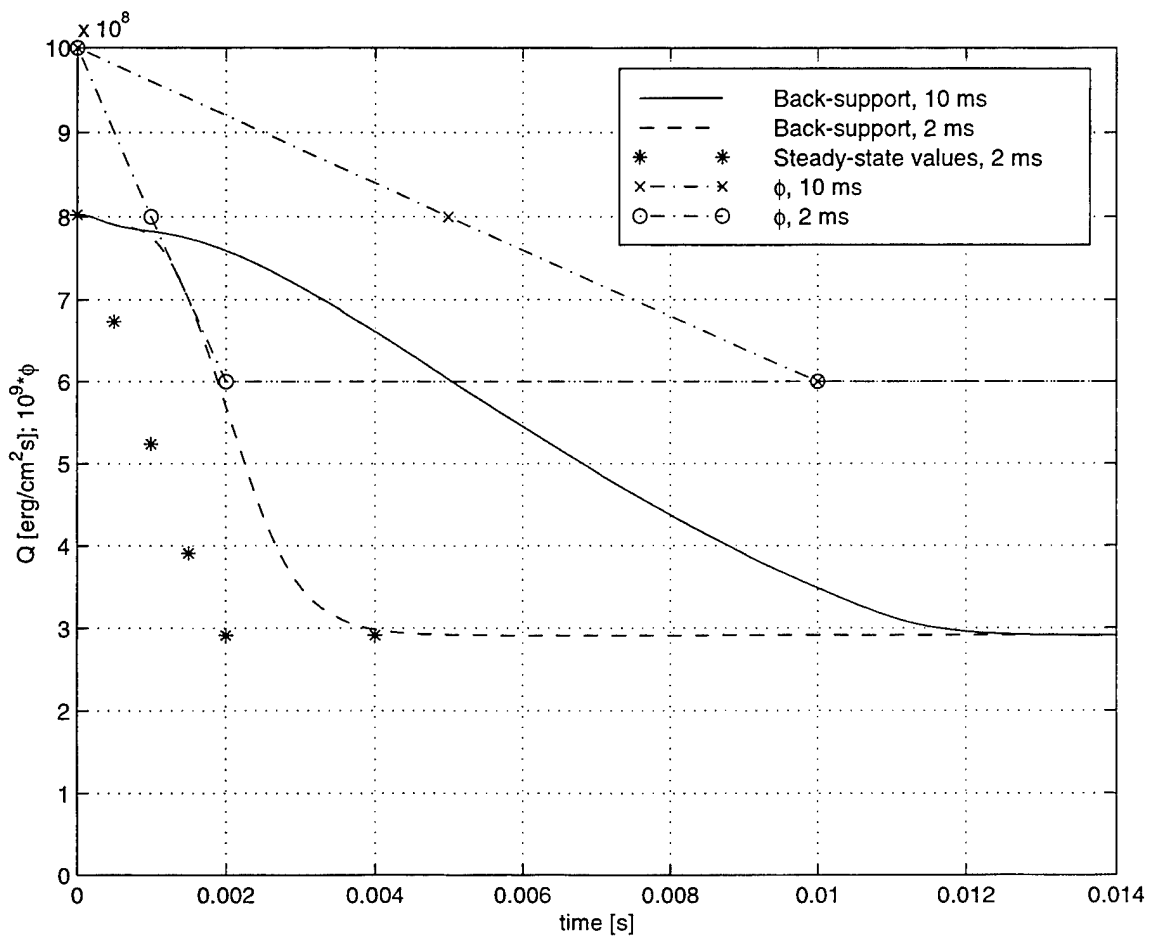


Figure 5-1: Heat release rate vs. time for linear changes in ϕ ; $\epsilon = 300$.

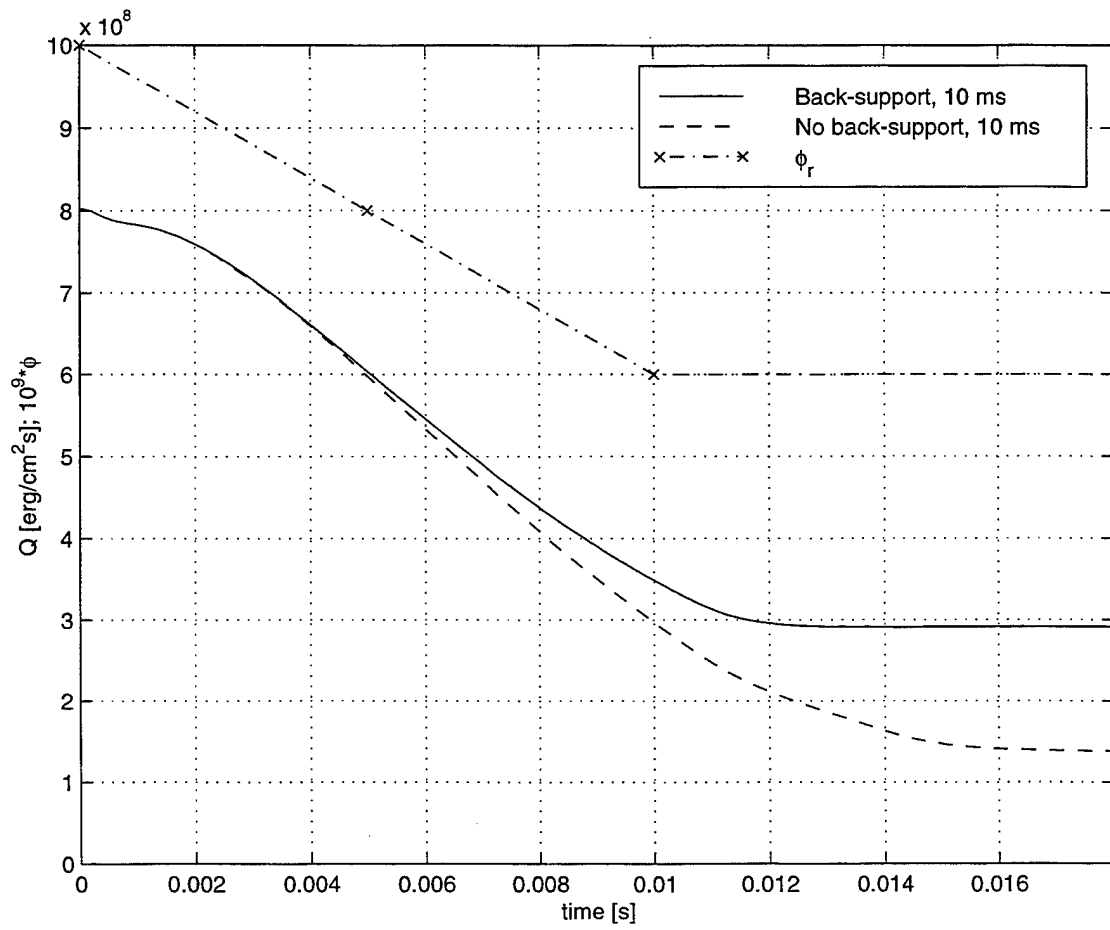


Figure 5-2: Heat release rate vs. time, back-support and no back-support.

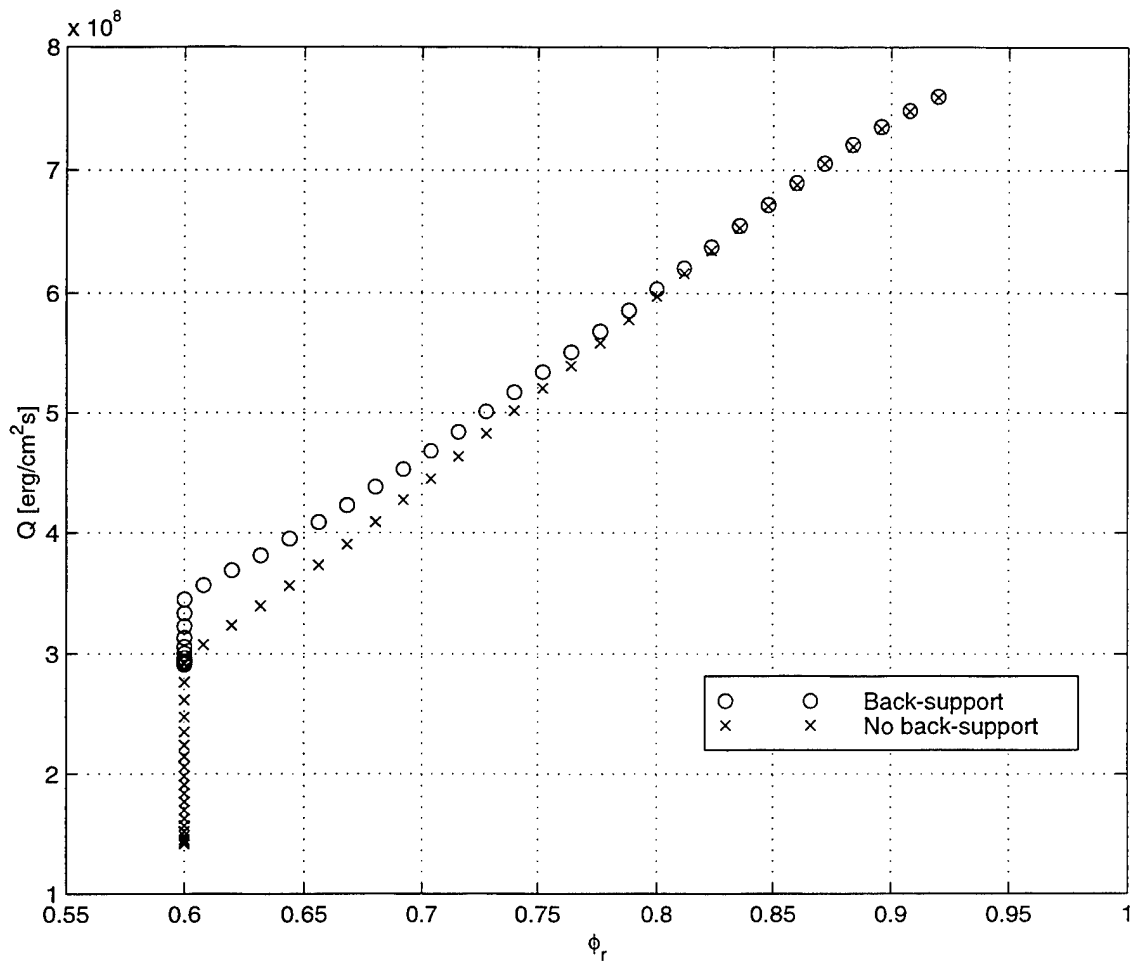


Figure 5-3: Heat release rate vs. reactants equivalence ratio, back-support and no back-support.

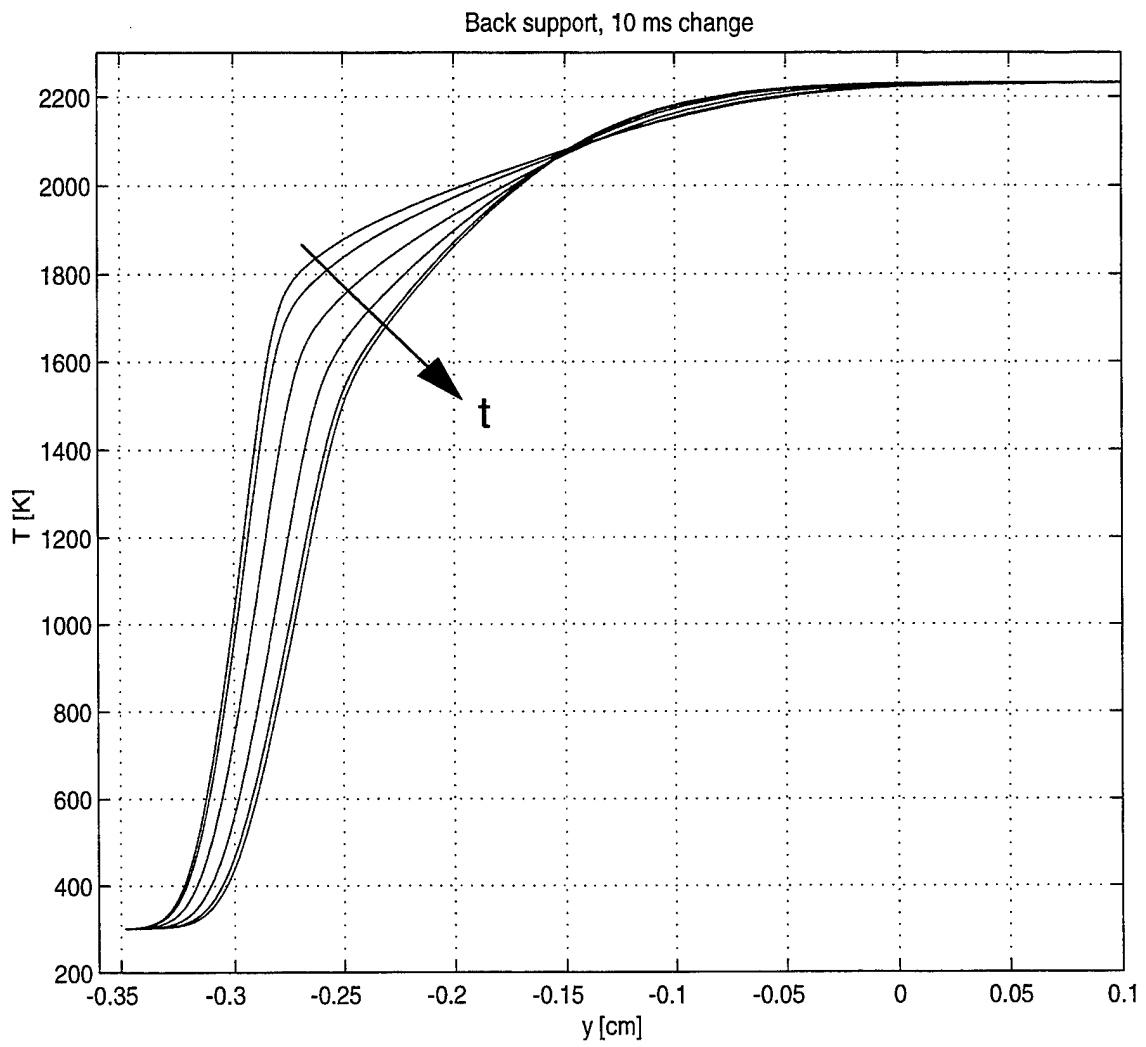


Figure 5-4: Temperature profiles with changing ϕ , back-supported flame; $\Delta t = 3$ ms.

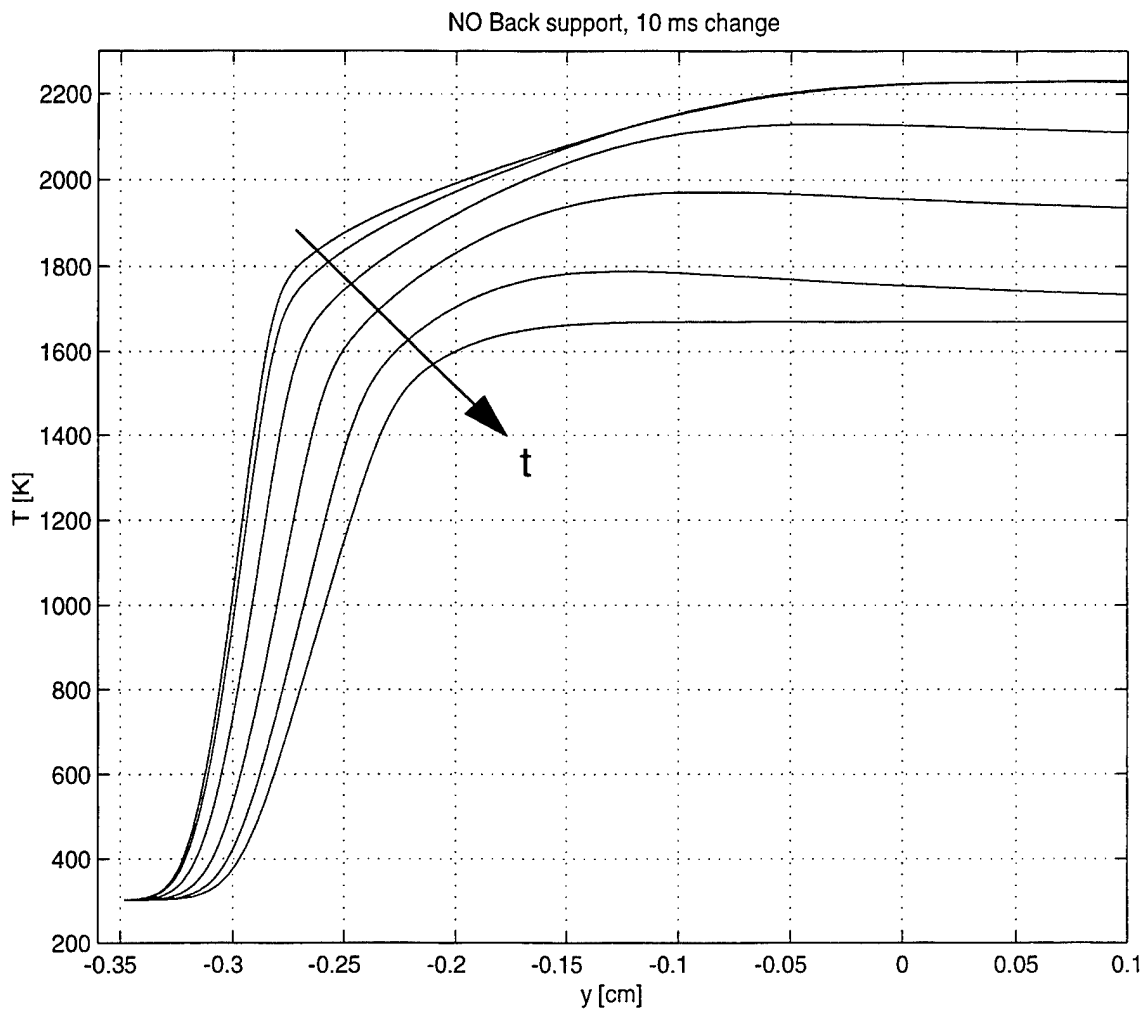


Figure 5-5: Temperature profiles with changing ϕ , non-back-supported flame; $\Delta t = 3$ ms.

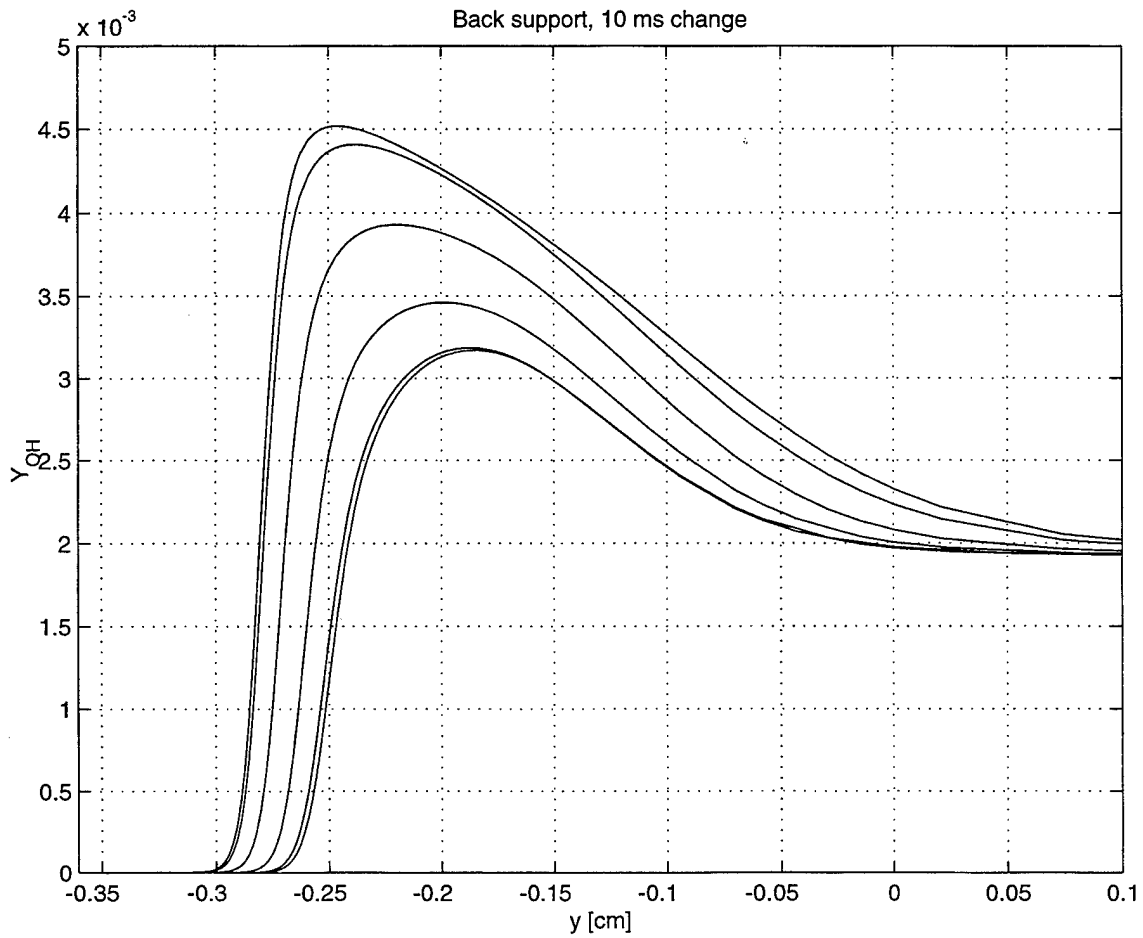


Figure 5-6: OH profiles with changing ϕ , back-supported flame; $\Delta t = 3$ ms.

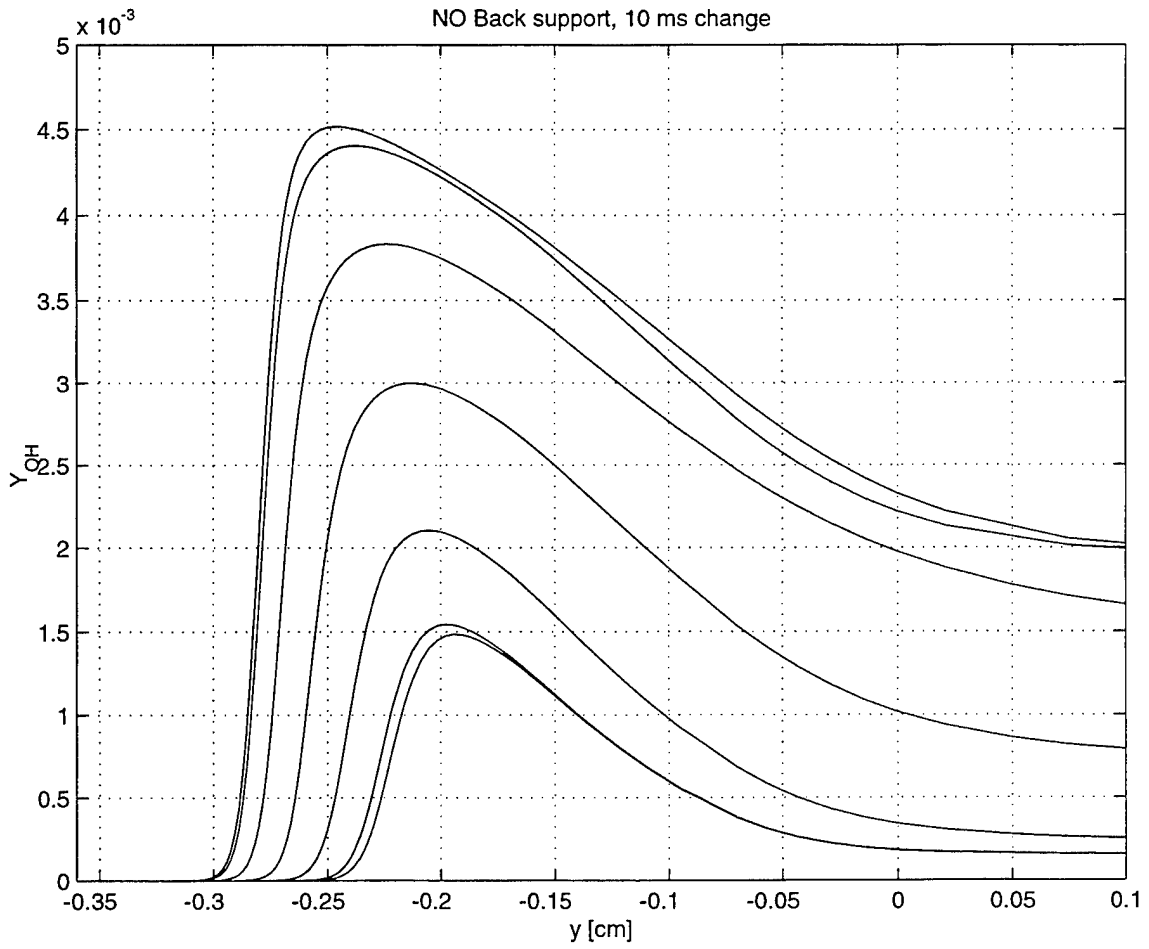


Figure 5-7: OH profiles with changing ϕ , non-back-supported flame; $\Delta t = 3$ ms.

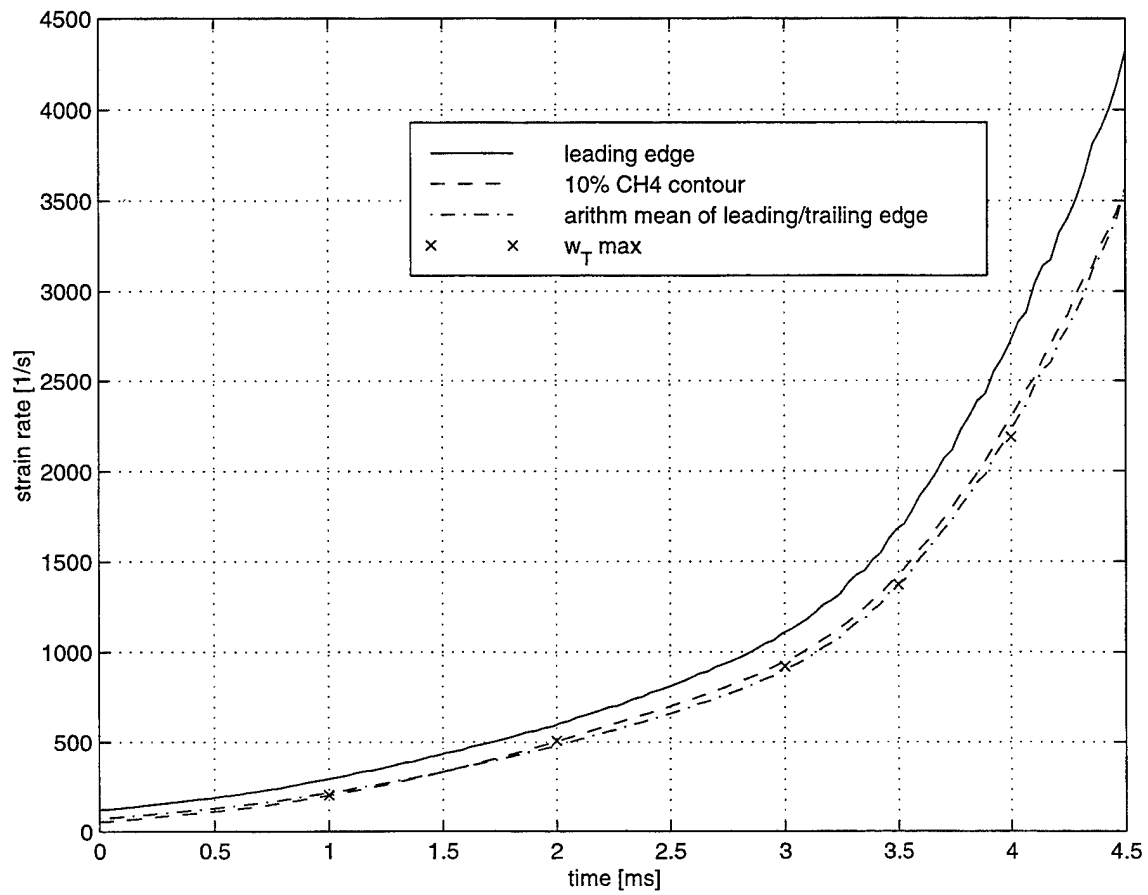


Figure 5-8: Strain histories extracted from the flame-vortex interaction.

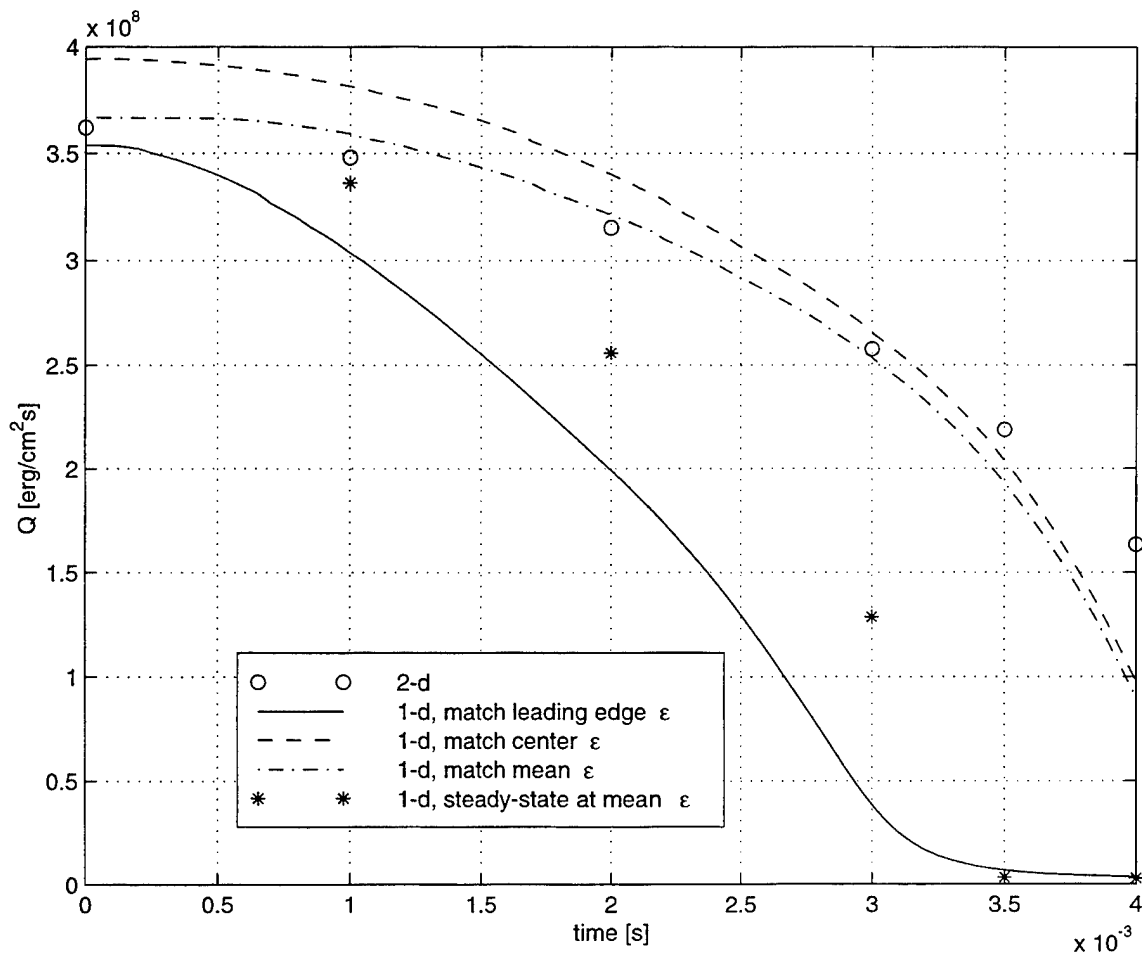


Figure 5-9: One- and two-dimensional heat release rates vs. time for various strain-matching schemes.

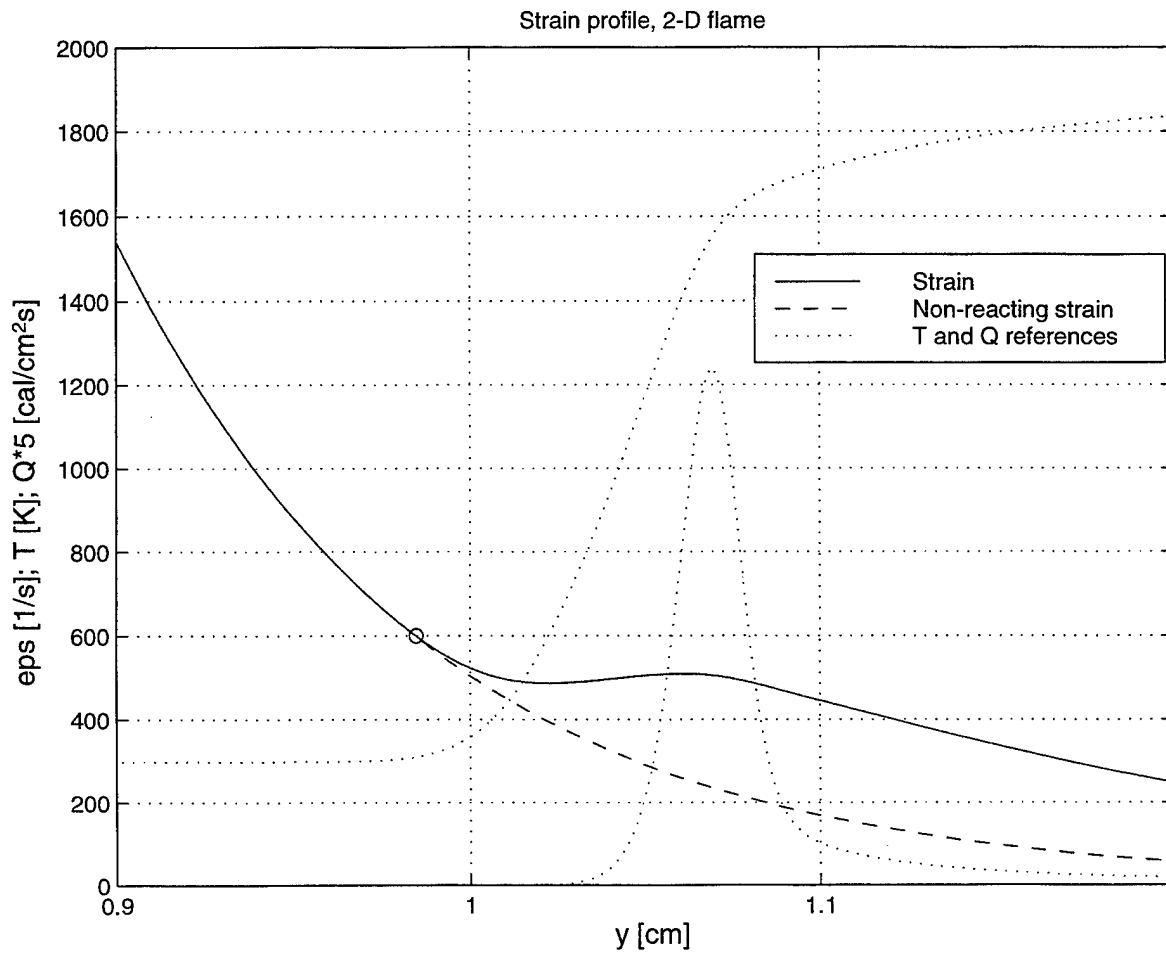


Figure 5-10: Strain profile in the two-dimensional flame element; $t = 2$ ms.

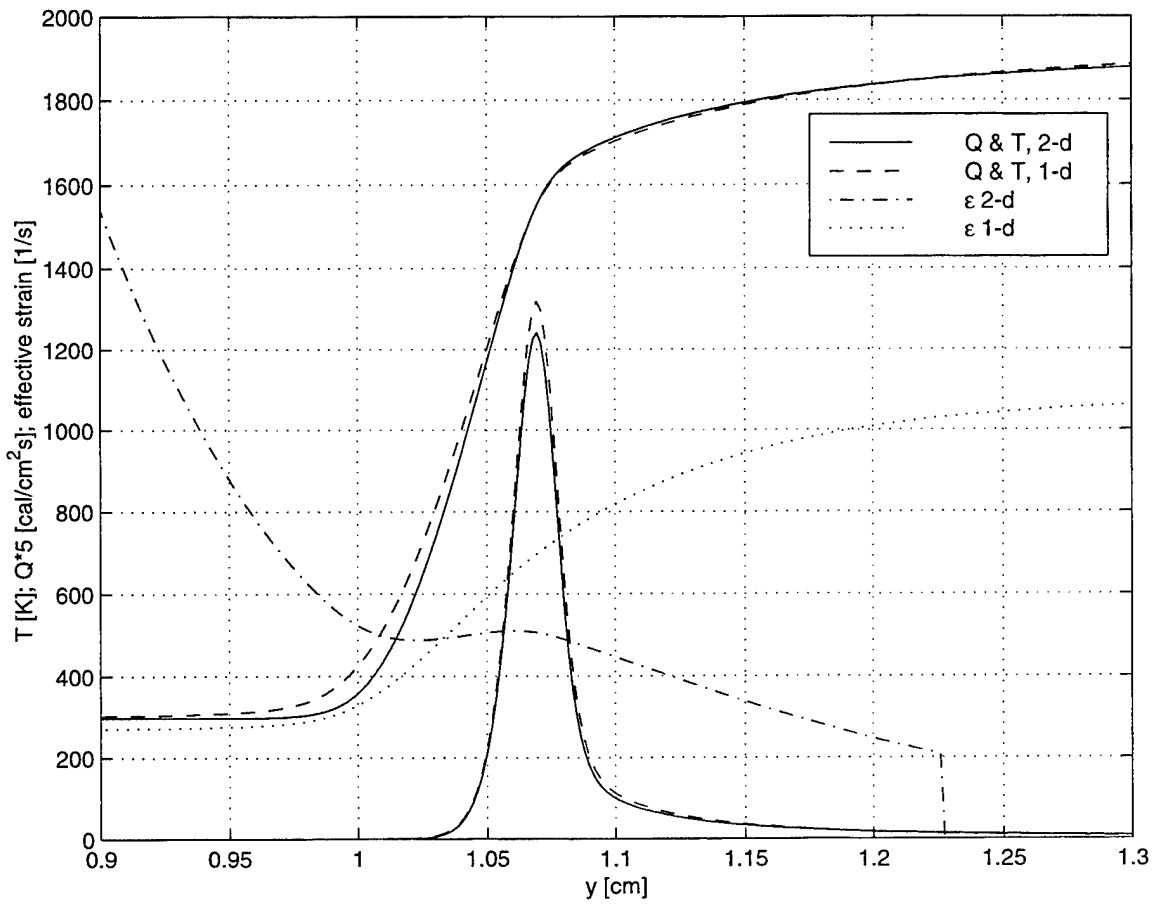


Figure 5-11: Structure of the one- and two-dimensional flame elements; $t = 2$ ms.

Chapter 6

Conclusions and Further Work

The preceding chapters have developed a robust and efficient computational model for combustion under arbitrarily varying strain rate and mixture composition. In its most basic form, the elemental flame model provides a rich data set for analyzing kinetic and transport processes within flames. Reduction of this data set can yield fundamental insights into the mechanisms of unsteady flame response, by linking detailed flame structure to the modeling of flame dynamics.

The unsteady interactions described at the outset of this research were examined in carefully-defined but practical contexts. Equivalence-ratio variation on the order of a flame time scale produced a dynamic burning response and modified the flame structure. It remains to develop a more elegant method of updating the composition of the products stream of the non-back-supported flame, one that reformulates the role of the products stream in the context of a Lagrangian transformation. The unsteady strain applied by a vortex to a two-dimensional flame surface allowed burning to persist at strains far higher than the steady-state values at quenching. Use of the elemental flame as a subgrid model in this context concluded with an important refinement to the flame embedding and flamelet approaches: the key parameter governing burning at a premixed flame surface is the average strain, not the cold strain at the reactants-side leading edge. Further development must clarify how to best define this average.

The simplicity of the elemental flame model makes possible numerous extensions,

with wide applicability. Radiation or some other heat loss term can be included to more realistically model flame extinction. Adding the appropriate chemical kinetics could lead to accurate NO_x predictions, based on the detailed flame structure. The unsteady evolution of the elemental flame could be used to simulate control feedback and actuation; instantaneously computed burning parameters of the elemental flame could be used within an arbitrary control law. Additionally, the detailed computation of the elemental flame can be used to develop and validate lower-order models for the control of flame dynamics.

Bibliography

- [1] A. M. Bruaset, A. Tveito, and R. Winther. On the stability of relaxed incomplete LU factorizations. *Mathematics of Computation*, 54:701–719, 1990.
- [2] R. S. Cant, K. N. C. Bray, L. W. Kostiuk, and B. Rogg. Flow divergence effects in strained laminar flamelets for premixed turbulent combustion. *Combustion Science and Technology*, 95:261–276, 1994.
- [3] N. Darabiha. Transient behaviour of laminar counterflow hydrogen-air diffusion flames with complex chemistry. *Combustion Science and Technology*, 86:163–181, 1992.
- [4] Tarek Echekki and Jacqueline H. Chen. Unsteady strain rate and curvature effects in turbulent premixed methane-air flames. *Combustion and Flame*, 106:184–202, 1996.
- [5] Fokion N. Egolfopoulos. Dynamics and structure of unsteady, strained, laminar premixed flames. In *25th Symposium (International) on Combustion*, pages 1365–1373. The Combustion Institute, 1994.
- [6] Fokion N. Egolfopoulos and Charles S. Campbell. Unsteady counterflowing strained diffusion flames: diffusion-limited frequency response. *Journal of Fluid Mechanics*, 318:1–29, 1996.
- [7] Stanley C. Eisenstat and Homer F. Walker. Globally convergent inexact Newton methods. *SIAM Journal on Optimization*, 4:393–422, 1994.

- [8] Howard C. Elman. A stability analysis of incomplete LU factorizations. *Mathematics of Computation*, 47:191–217, 1986.
- [9] Ahmed F. Ghoniem, Marios C. Soteriou, Omar M. Knio, and Baki Cetegen. Effect of steady and periodic strain on unsteady flamelet combustion. In *24th Symposium (International) on Combustion*, pages 223–230. The Combustion Institute, 1992.
- [10] Gene H. Golub and Charles F. van Loan. *Matrix Computations*. The Johns Hopkins University Press, Baltimore, third edition, 1996.
- [11] H. G. Im, J. K. Bechtold, and C. K. Law. Counterflow diffusion flames with unsteady strain rates. *Combustion Science and Technology*, 106:345–361, 1995.
- [12] Robert J. Kee, James A. Miller, Gregory H. Evans, and Graham Dixon-Lewis. A computational model of the structure and extinction of strained opposed-flow premixed methane-air flames. In *22nd Symposium (International) on Combustion*, pages 1479–1494. The Combustion Institute, 1988.
- [13] J. S. Kistler, C. J. Sung, T. G. Kreutz, C. K. Law, and M. Nishioka. Extinction of counterflow diffusion flames under velocity oscillations. In *26th Symposium (International) on Combustion*, pages 113–120. The Combustion Institute, 1996.
- [14] Randall J. LeVeque. *Numerical Methods for Conservation Laws*. Birkhauser Verlag, Basel, second edition, 1992.
- [15] A. E. Lutz, R. J. Kee, J. F. Grcar, and F. M. Rupley. OPPDIF: A Fortran program for computing opposed-flow diffusion flames. Technical Report SAND96-8243, Sandia National Laboratories, May 1997.
- [16] H. N. Najm, R. W. Schefer, R. B. Milne, C. J. Mueller, K. D. Devine, and S. N. Kempka. Numerical and experimental investigation of vortical flow-flame interaction. Technical Report SAND98-8232, Sandia National Laboratories, February 1998.

- [17] Habib N. Najm, Phillip H. Paul, Charles J. Mueller, and Peter S. Wyckoff. On the adequacy of certain experimental observables as measurements of the flame burning rate. *Combustion and Flame*, 113:312–332, 1998.
- [18] Habib N. Najm, Peter S. Wyckoff, and Omar M. Knio. A semi-implicit numerical scheme for reacting flow; stiff chemistry. *Journal of Computational Physics*, 143:381–402, 1998.
- [19] Michael Pernice and Homer F. Walker. NITSOL: A Newton iterative solver for nonlinear systems. *SIAM Journal on Scientific Computing*, 19:302–318, 1998.
- [20] N. Peters and R. J. Kee. The computation of stretched laminar methane-air diffusion flames using a reduced four-step mechanism. *Combustion and Flame*, 68:17–29, 1987.
- [21] Norbert Peters. Length scales in laminar and turbulent flames. In Elaine S. Oran and Jay P. Boris, editors, *Numerical Approaches to Combustion Modeling*, chapter 6, pages 155–182. AIAA, Washington, DC, 1991.
- [22] Constantin Petrov. *Numerical Simulation of Reacting Flows with Complex Chemistry Using Flame Embedding*. Ph.D. thesis, Massachusetts Institute of Technology, Department of Mechanical Engineering, February 1997.
- [23] Constantin Petrov and Ahmed Ghoniem. An unsteady strained flame model for turbulent combustion simulations. In *32nd Aerospace Sciences Meeting and Exhibit*, number AIAA-94-0776. AIAA, January 1994.
- [24] Constantin Petrov and Ahmed Ghoniem. The transient response of strained laminar-premixed flames. *Combustion and Flame*, 102:401–417, 1995.
- [25] Constantin Petrov and Ahmed Ghoniem. An unsteady strained flame model with multi-step chemical kinetics for turbulent combustion simulations. In *33rd Aerospace Sciences Meeting and Exhibit*, number AIAA-95-0380. AIAA, January 1995.

- [26] Constantin Petrov and Ahmed Ghoniem. A uniform strain model of elemental flames in turbulent combustion simulations. *Combustion and Flame*, 111:47–64, 1997.
- [27] T. Poinso, D. Veynante, and S. Candel. Diagrams of premixed turbulent combustion based on direct simulation. In *23rd Symposium (International) on Combustion*. The Combustion Institute, 1990.
- [28] Alberto Pueyo and David W. Zingg. Efficient Newton-Krylov solver for aerodynamic computations. *AIAA Journal*, 36:1991–1997, 1998.
- [29] G. A. Richards, M. C. Janus, and E. H. Robey. Control of flame oscillations with equivalence ratio modulation. *Journal of Propulsion and Power*, 15(2):232–240, 1999.
- [30] Yousef Saad. *Iterative Methods for Sparse Linear Systems*. PWS Publishing, Boston, 1996.
- [31] K. Sardi, A. M. K. P. Taylor, and J. H. Whitelaw. Mixing model for the calculation of extinction in oscillating flames. *AIAA Journal*, 37(6):751–758, 1999.
- [32] John Shadid, Raymond S. Tuminaro, and Homer F. Walker. An inexact Newton method for fully-coupled solution of the navier-stokes equations with heat and mass transport. Technical Report SAND97-0132, Sandia National Laboratories, February 1997.
- [33] Mitchell D. Smooke, editor. *Reduced Kinetic Mechanisms and Asymptotic Approximations for Methane-Air Flames*. Lecture Notes in Physics. Springer-Verlag, Berlin, 1990.
- [34] G. Stahl and J. Warnatz. Numerical investigation of time-dependent properties and extinction of strained methane- and propane-air flamelets. *Combustion and Flame*, 85:285–299, 1991.

- [35] C. J. Sung, J. B. Liu, and C. K. Law. Structural response of counterflow diffusion flames to strain rate variations. *Combustion and Flame*, 102:481–492, 1995.
- [36] Lloyd N. Trefethen and David Bau. *Numerical Linear Algebra*. SIAM, Philadelphia, 1997.
- [37] Forman A. Williams. *Combustion Theory*. Addison-Wesley, Reading, MA, second edition, 1985.
- [38] A. O. zur Loye and F. V. Bracco. Two-dimensional visualization of premixed-charge flame structure in an IC engine. Technical Report 870454, Society of Automotive Engineers, February 1987.